Bayesian analysis of burst gravitational waves from galactic neutron stars

Mikel Bastarrika

Submitted in fulfilment of the requirements for
the Degree of Ph.D

University of Glasgow

Institute of Gravitational Research

Department of Physics and Astronomy

September 2010

Abstract

This thesis summarises the work done by myself in the period Oct 2006 - Aug 2010 in relation to data analysis for gravitational wave detection. Most of the personal contribution relates to the assessment of the detectability of potential burst-type gravitational wave signals from the galactic population of neutron stars and to the parameter estimation of the models used to represent these signals. A small part of the work, contained in the last chapter, describes the experimental work carried at the beginning of the research period and aimed to measure the shot-noise level of the modulated laser-light in the gravitational wave detectors.

Chapter 1 is introductory and presents generic information about gravitational wave radiation, a postulate of the theory of general relativity. The polarisation of the radiation and the approximate values of amplitudes and frequencies of the signals expected from astrophysical events are presented together with most important gravitational radiation sources for ground-based detectors. General information about the second and third generation detectors is included and the astrophysical prospects for the new detectors are reviewed. Physical mechanisms expected to make compact stars oscillate and the subsequent generation of short-lived gravitational wave bursts are introduced, bringing the focus onto the oscillation frequency values and damping times expected.

Chapter 2 presents the study on the detectability of burst-type gravitational wave signals incoming from neutron stars located in our galaxy. Three differently shaped galactic neutron star populations are introduced and the detectability of ground-based detectors to signals

of different polarisation degree incoming from these source populations is investigated. Based on the time- and polarisation-averaged antenna pattern and antenna power values, approximated by Monte Carlo methods, detectability is measured in terms of a) the geographical location and orientation of hypothetical detectors, and b) the current detectors, either working individually or as a part of a network. Also, the sidereal times at which each detector is more sensitive to the sources of the neutron star populations defined are inferred.

Detectors located in the equator and with geographical orientation '$\times$' were found to have the maximum detectability to galactocentric populations. The orientation factor becomes negligible for latitudes higher than $|\beta| > 60^{\circ}$. This contrasts with a previous study for signals from the Virgo cluster resulting in a most favourable geographical '+' orientation for equatorial latitudes and orientation factor becoming negligible for latitudes bigger than $|\beta| > 45^{\circ}$. The constrast or maximum differences between the antenna power values in the equator and the poles is smaller for the galactic centre (18%) than for the Virgo cluster (46%), indicating that changes in latitude and orientation are not so drastic for the detection of sources located towards the galactic centre.

The mean ($\bar{x}$-value) has been used to compare time- and polarisation-averaged histograms of antenna factor values and in order to sort out current detectors in decreasing order of detectability to galactocentric populations: PERTH, LIGO-L, LIGO-H, VIRGO, TAMA300, GEO600. The sidereal times at which each detector is most suitable for the detection of signals from a galactocentric population have been calculated based on the evolution of the $\bar{x}$-value along one rotation of the Earth. The times at which the sensitivity is maximum differ slightly for signals of different polarisation degree and all fall within a maximum uncertainty of 15 minutes. Time intervals between the peaks of $\bar{x}$-value curves showing its diurnal evolution match well with the geographical longitude differences between detectors. Although in

a less quantitatively form that the study of $\bar{x}$-value, detection probability curves have shown that it is advantageous to have a detector located in the southern hemisphere (PERTH), working on its own or included in a network of detectors, for the detection of signals from neutron stars in the southern celestial hemisphere.

Chapter 3 introduces a mathematical model of the burst-type gravitational wave ringdown signal investigated in this work. It represents a short-lived gravitational polarised radiation generated by an oscillating neutron star: an exponentially damped sinusoid comprising a sine and a cosine component, of the same frequency and different amplitude, as the two polarisation components of the signal. The model of the signal both in the time- and in the frequency-domain are given. The relation between the discrete Fourier transform (DFT) and the close-form of the discrete time Fourier transform (DTFT) is presented, together with their relation to the z-transform of discrete signals in the time-domain. The derived analytical expression of the modeled signal in the frequency-domain provides the possibility of avoiding the lengthy computation of a DFT, to obtain the coefficients of each frequency point considered, by focusing in the bandwidth of interest and thus speeding up the calculation of the evidence of the model in presence of the data. The z-transform and its properties ease the calculation of the Fourier coefficients for shifted signals based on z-transforms of non-shifted signals.

3) through Bayesian model comparison and parameter estimation of signals injected into synthetic noise as seen by a network comprised of three second generation detectors.

Chapter 4 is devoted to present the Bayesian probability tools necessary to carry out *model comparison* and *parameter estimation* for the study of our particular burst-type signal. Comparing models allows chosing that one that represents the data best and then focusing on by computing of the most likely parameter values of that model. Also, in this section, the way in which the detector data can be simulated

in the frequency domain, combining the signal and a noise realisation corresponding to the power spectrum of the noise that characterizes the detector, is explained. The likelihood function for a signal corresponding to one oscillation mode and seen by one detector is derived both in the time- and in the frequency-domain. The nested sampling algorithm is summarised, a very useful tool used to compute effectively the marginal likelihood of the hypotheses considered.

Chapter 5 presents the results of the model selection and the parameter estimation exercise. The expression of the likelihood is generalised so that it can adopt more than one oscillation mode and seen by various detectors of a network. Depending whether one, f-mode, or two oscillation modes, f and p, are suspect, two different scenarios of various hypotheses are considered. For each hypothesis the minimum strength of the signal to claim a detection is studied and a parameter estimation exercise is carried out to characterise the signal and define the location of the source in the sky.

Signals of known parameters and differing strengths were injected (once modulated in relation to the relative orientation of the detector and the source location) into the synthetic noise of three advanced detectors comprising a network. There is little understanding of the energy channeled into the f and p oscillation modes. This may provoke making assumptions that are not too realistic. The values of the parameters were estimated using Bayesian inference for two different scenarios: when only the f-mode is suspect (scenario 1), or when both f- and p-modes are suspect (scenario 2). To begin with, the strengths of signals for which the signal hypothesis favour the noise hypothesis are calculated, and the Bayes factors for 1% false-alarm rates are established for both scenarios. Penalization of models containing more parameters than necessary in the underlying physical model in the Bayesian approach was demonstrated.

Posterior probabilities of the parameters in Scenario 1 are better defined and constrained than those for Scenario 2, due to the added

uncertainty of including another oscillation mode. As expected, the uncertainty of the probability distributions of the parameter values decreases and the mode shifts toward the exact injected value as the signal strength increases. For both scenarios the frequency value can be accurately estimated, not so well the damping times, especially for the p-mode oscillation, which have longer time durations than f-modes of typically several seconds. The ability to estimate the polarisation degree of the signal is also quite limited and strong signals are required for the mode of the distribution to approximate the exact value. Similarly, determining the most probable location for the source is possible in both scenarios. The two-fold degeneracy of the sky position and related to the travel time of the signal to the detectors has been broken; relatively strong (high SNR) signals, specially for scenario 2, are needed for the source location to be constrained with accuracy.

Chapter 6 presents the experimental work carried out, by which the measurent of the shot-noise level of differently modulated and demodulated laser light was intended. Due to the poor outcome of this experiment and the lack of useful results the emphasis has been placed on a detailed description of the modulation apparatus, opto-electronic set up and the control system put together.

Chapter 7 looks to the future and briefly presents how to take this data analysis work forward.

Declaration

This thesis is my own composition except where indicated in the text. No part of this thesis has been submitted elsewhere for any other degree or qualification.

Acknowledgements

Completion of this work would have been impossible without the help and support of many people. First of all, I would like to thank the members of the Institute of Gravitational Research (IGR) for allowing me to join their group and making possible the completion of my PhD research in an enthusiastic and pleasant atmosphere. I feel privileged for the opportunity given and for the means facilitated by the IGR for the development of my research skills. I am grateful for the financial support received from the Science & Technology Facilities Council (STFC).

I am indebted, in particular, to my two supervisors, Dr. Ik Siong Heng and Prof. Kenneth A. Strain, for proposing interesting research subjects and helping me find ways around the obstacles that came across on the way. Thank you very much for being so patient and helpful during this time, and for revising my writing carefully and making valuable suggestions to improve its content and comprehension.

During the data analysis I ran into statistical problems for which the help of Dr. Martin Hendry was invaluable. His thorough approach and clear explanations led me securely through the derivation of some useful mathematical equations. Thank you Martin for your kind help.

Massimo Tinto provided me with thoughts that were vital in the correct understanding of some of his papers and their numerical implementation. Thank you Massimo for your always helpful and encouraging words.

I would like to thank Iain Sim for taking good care of my computer and putting at my disposal all the software necessary. Thank you Iain for your always quick and efficient help.

At the beginning of my research period experimental work was alien to me but Dr. Bryan Barr and Dr. Borja Sorazu, assisted in making my introduction to the field run more smoothly. Their experience and perseverance was invaluable for designing and putting together electronic circuits and optical components. Thank you for making the experimental side of my research much clearer and pleasant.

Many hours were spent in the lab building and testing electronic circuits, where Neil Robertson and Allan Latta were always around to help. Thank you for making those hours in the laboratory entertaining and for teaching me those scottish words that I haven't come across written anywhere yet! I would also like to thank Dr. Gavin Newton for sharing his knowledge of radio frequency with us and being patient in spite of the mess made in the laboratory. Also a big thank you to Alastair Grant for his help and for always sharing his knowledge and experience with us.

I have been very lucky in sharing room 465 with James Clark, Jennifer Toher, Fiona Speirits, Erin MacDonald and Colin Gill. Thank you all for your help and understanding. You have been really great officemates.

No matter how good the week had been, I always looked forward to the Friday gathering and the sometimes nonsensical but always soulful conversations until late. Thank you for the jokes, the thoughts and the support Asier, Duncan, Graham, Terry, Federico & Anna, Kepa & Lynne, Pablo & Rachel, Aitor & Lee. May we share many more unforgettable moments in the future.

Marianne, thank you for all that cheerful energy you radiate and the unconditional support during all this time, for you have been the one to see and suffer all the ups and downs. Your encouragement has been very important for me to complete this work.

Eta ez nituzke ahaztu nahi etxekoak: gurasoak, Prudencio Bastarrica eta Josepi Izagirre, ene bi anaiak, Aitor eta Iñaki, eta gure izeba

Begoña Izagirre. Eskerrak bihotz-bihotzetik gurasoei, gure onerako hartu dituzten nekeek ez izenik eta ez ordainik ez dutelako. Baita anaiei ere, emandako aholku eta indarrengatik (Arantzazuko egutegiko txisteak tarteko), eta izeba Begoñari urte askoan bere hegalpean babestu ninduelako.

Eta zuri Iñaki eta Amaia, betirako nere gogoan, han eta hemen, zoriontsu egin ninduzutelako. Betoz berriro barre algarak, musika goxoa eta oroitzapen garbiak, ulermenaren iturri. Eta iraun dezala horrek zutik urte askoan.

Agur eta ohore, ixilik beste belardi batzuetara joan diren horiei, honetan utzitakoaren esker onez.

Contents

1 Gravitational waves, sources and their detection **1**

1.1 Introduction 1
1.2 The theory of General Relativity 2
1.3 Gravitational radiation 2
1.3.1 Polarization of gravitational waves 4
1.3.2 Strength of gravitational waves 5
1.3.3 Frequencies of gravitational waves 7
1.4 Important gravitational radiation sources 8
1.4.1 Coalescing compact binaries 8
1.4.2 Burst signals 9
1.4.3 Continuous signals 10
1.4.4 Stochastic signals 11
1.5 Gravitational wave detectors 11
1.5.1 Worldwide network of gravitational wave detectors 13
1.5.2 Status Quo and future detectors 15
1.5.3 Scientific goals of second and third generation instruments 17
1.5.4 Multimessenger astronomy with future telescopes 20
1.6 Gravitational burst signals of galactic origin 21
1.6.1 Neutron stars and pulsars 21
1.6.2 Neutron stars as gravitational radiation sources 23
1.7 Oscillations of stars 24
1.7.1 Oscillations of black-holes 25
1.7.2 Oscillations of relativistic stars 26

2 Detectability of gravitational wave burst signals from galactic neutron stars 32
2.1 Introduction . . . 33
2.2 Neutron star population models . . . 33
2.2.1 Population 1: Disc-shaped NS population . . . 34
2.2.2 Population 2 & 3: Spherical NS populations . . . 35
2.3 Antenna patterns of laser interferometric gravitational wave detectors . . . 40
2.3.1 Strain and polarisation degree of the gravitational wave signal 44
2.3.2 Strain and antenna pattern functions . . . 45
2.4 Detectability study for the NS populations - location and orientation 54
2.4.1 Detector's location and orientation for signals from a particular sky direction . . . 54
2.4.2 Detector location and orientation to NS populations . . . 57
2.5 Detectability study for signals from NS populations - known detectors 58
2.5.1 Histograms of antenna patterns . . . 58
2.6 Detection probability for signals from NS populations . . . 78
2.6.1 Detection Probability for a single antenna . . . 78
2.6.2 Detection Probability for a network of antennae . . . 84
2.7 Review of chapter and conclusions . . . 94

3 Signal in the time and frequency domain 95
3.1 Introduction . . . 95
3.2 Signal in the time domain . . . 96
3.3 Signal in the frequency domain . . . 99
3.3.1 Continuous Time Fourier Transform (CTFT) . . . 99
3.3.2 Discrete Time Fourier Transform (DTFT) . . . 100
3.3.3 Discrete Fourier Transform (DFT) . . . 103
3.3.4 Relation between DTFT and DFT . . . 103
3.4 The z-transform . . . 107
3.4.1 Time-shifted signal . . . 108

4 Bayesian Data Analysis **111**
4.1 Introduction . . . 111
4.2 Bayesian Inference . . . 112
4.2.1 Model comparison . . . 113
4.2.2 Parameter estimation . . . 114
4.3 Noise and Signal . . . 115
4.3.1 Adding noise to the signal in the frequency-domain . . . 115
4.4 Calculation of the Signal to Noise Ratio (SNR) . . . 118
4.5 An illustrative example of the study method . . . 118
4.6 Calculation of the Likelihood Function . . . 122
4.6.1 Likelihood in the time domain . . . 122
4.6.2 Likelihood in the frequency domain . . . 123
4.7 Nested Sampling . . . 126
4.8 Nested Sampling procedure . . . 127
4.8.1 Terminating the iteration . . . 130
4.8.2 Generating a new object by random sampling . . . 130
4.8.3 Implementation of the nested sampling algorithm . . . 132
4.8.4 Posterior Sampling . . . 133

5 Model Comparison and Parameter estimation **135**
5.1 Data for analysis . . . 135
5.2 Priors . . . 139
5.3 Amplitude, frequency and damping time of the signal . . . 142
5.4 Scenarios and parameters considered . . . 144
5.5 Model comparison - evaluation of the odds ratio . . . 146
5.5.1 'Signal + noise' hypotheses . . . 148
5.5.2 'Only noise' hypothesis . . . 149
5.6 Detection and false-alarm rate threshold . . . 149
5.6.1 Scenario 1: f-mode . . . 150
5.6.2 Scenario 2: f- and p-modes . . . 152
5.7 Parameter estimation . . . 152
5.7.1 Scenario 1 - hypothesis 1K . . . 153
5.7.2 Scenario 1 - hypothesis 1G . . . 157

5.7.3 Scenario 1 - hypothesis 1U . . . 158
5.7.4 Scenario 2 - hypothesis 2K . . . 161
5.7.5 Scenario 2 - hypothesis 2U . . . 161
5.8 Discussion and Conclusions . . . 163
5.8.1 Scenario 1 . . . 163
5.8.2 Scenario 2 . . . 166

6 Shot-noise experiment **167**
6.1 The context and relevance of the experiment . . . 168
6.1.1 Standard quantum limit: shot-noise and radiation pressure noise . . . 169
6.1.2 Photon shot-noise . . . 170
6.2 Experiment . . . 170
6.2.1 General description of the experiment . . . 171
6.2.2 Mach-Zehnder interferometer (MZI) . . . 171
6.3 Modulation of Laser Light . . . 173
6.3.1 Gravitational waves and modulation of laser light . . . 173
6.3.2 Electro-optic modulation of laser beams . . . 174
6.4 Types of light modulation . . . 175
6.4.1 Amplitude Modulation . . . 175
6.4.2 Phase modulation . . . 176
6.4.3 Laser light electro-optical modulation . . . 178
6.4.4 Locking: the interferometer as a null instrument . . . 184
6.4.5 Measuring the shot-noise level . . . 193
6.4.6 Results . . . 198

7 Summary and Future work **200**

A Antenna Pattern study **203**
A.1 Probability density function of F_+ and $F_\times$ . . . 203
A.2 Probability density function of $\bar{F}$ . . . 205

B Polarisation degree λ study **208**
B.1 Unknown direction of angular momentum 208
B.2 Known direction of angular momentum 210

C Comparing Histograms: The mean value of a histogram **211**
C.1 Extracting information from histograms 213

D Calculation of antenna pattern functions **217**

E Chebyshev polynomials **226**

F Tables of Chebyshev coefficients **229**

G Discrete signals **235**

H Signal and noise in the frequency-domain **238**
H.1 Cartesian representation: Real and imaginary coefficients 239
H.2 Polar representation: Magnitude and phase 240
H.2.1 Absence of the signal: noise only acquired 240
H.2.2 Presence of the signal: signal + noise acquired 241

I MATLAB code - Nested Sampling Algorithm **246**
I.1 Matlab pseudo-code - working with logarithms 247
I.2 Matlab code used for hypothesis comparison and parameter estimation - working with logarithms 251

J Signal arrival order to detectors **281**

K Parameter Estimation Results **286**

L Schematics of the GEO600 photodetector **292**
L.1 Calculation of the inductance value for the RF resonant line within the GEO style PD version 292

Chapter 1

Gravitational waves, sources and their detection

1.1 Introduction

Serendipitous discoveries like the cosmic microwave background radiation (CMBR) and signals from pulsars were ground-breaking unexpected surprises that allowed the development of new branches of astronomy. The eagerly expected detection of gravitational radiation will also provide a new dimension for the understanding of the universe. When the second generation gravitational wave detectors start making detections, this new source of astrophysical information will throw light upon the mysteries of the universe on a daily basis. Detection and interpretation of gravitational waves will allow a deeper understanding of astronomical objects like neutron stars and black holes, together with the validation and refutation of various gravitational theories.

The theory of general relativity that postulated gravitational radiation is sound, for the existence of gravitational waves has already been confirmed indirectly. It is highly probable we are at the doorstep of a new and exciting science in which secrets of strong field gravity will be elucidated. The first detection of gravitational radiation seems imminent now and, when this occurs, an exciting path of discoveries will be laid ahead to continue interrogating nature.

1.2 The theory of General Relativity

It was 1905 when Albert Einstein published his revolutionary theory of *Special Relativity* (SR) in which he postulated that a) there is no absolute and well-defined state of rest or privileged reference frame, so that all uniform motion is relative, and b) light propagates in empty space with finite velocity c regardless the state of motion of the emitting body. Einstein introduced relativity of simultaneity abandoning the classical notion that time intervals between events are the same for all observers. Consequently, space and time lost their status as independent entities to be entwined as *spacetime* so that the only invariant quantity between two events is the fspacetime interval. This revolution of the concepts of time and space required the profound revision of other physical phenomena, gravity among them.

The *theory of General Relativity* (GR) was published by Albert Einstein in 1915; it provided a new and revolutionary geometrical interpretation of gravity that rivaled the Newtonian interpretation: the new theory embraced the axioms of special relativity, dispensing with the classical model of force fields acting instantaneously at a distance and replacing it with information about forces carried at the speed of light. Paraphrasing J. Wheeler, this is condensed in the often quoted *matter tells spacetime how to curve, and spacetime tells matter how to move*. For a mathematical description of gravity, Einstein derived the so-called field equations that relate the curvature of spacetime of a region to the matter and energy content within.

The theory of General Relativity has passed very stringent tests so far. It has been able to explain various physical phenomena, like the precession of the perihelion of Mercury, and predict new physics that have subsequently been proven right, like the deflection of light and the gravitational redshift. One important consequence of GR is the prediction of the existence of gravitational radiation.

1.3 Gravitational radiation

From the field equations Einstein derived that a moving mass is a source of gravitational radiation. The predicted intensity of the radiation was so small that its

detection was regarded close to impossible. Luckily, the inexorable advance of technology and the consideration of then unknown astronomical sources of strong gravitational radiation have allowed the possibility of detecting gravitational radiation to be reconsidered.

The Einstein field equations describe the curvature of spacetime in the presence of mass and energy. Far away from the source, in the weak-field regime, the deformation of the spacetime can be studied as a small distortion of the flat spacetime. In this regime, and from the linearized weak-field Einstein equations, a generic expression for the gravitational wave and its effect on free test-particles can be derived. For a detailed derivation of the gravitational wave function see (1; 2).

The analogy between electromagnetic and gravitational waves is tempting but not straight-forward: electromagnetic signals propagate through spacetime, but gravitational waves are the propagation of ripples of spacetime itself. Unlike electromagnetic signals gravitational waves interact very weakly with matter; on one hand, this makes their detection more difficult but, on the other, assures that the features of the physical mechanisms that generated the waves, and are imprinted on the radiation, will not be altered during their long journey through space before their detection.

Although indirect, the first evidence of the existence of gravitational radiation came from radio measurements of the binary pulsar PSR B1913+16 (3; 4), a binary formed of two neutron stars closely orbiting each other at relativistic speed. For this particular binary, radio pulses of one of the neutron stars can be seen from Earth, which allows tracking the evolution of their orbital period precisely. After eight years of careful measurements the actual orbital shrinkage was accurately established and compared to that which the general relativity predicted as a consequence of energy loss as gravitational wave reaction. The discrepancy between the measurement and the prediction was remarkably small ($< 0.5\%$) and although indirectly, proved the existence of gravitational radiation. This effect was first observed by R. Hulse and J. Taylor, for which they shared the Nobel prize in Physics in 1993. Since then, various binary pulsars have been investigated and the shrinkage of their orbits due to gravitational wave emission has been confirmed (5). The recent discovery of a binary neutron stars PSR

J0737-3039 where the pulsations of both members can be detected from Earth has permitted even more accurate observations (6).

1.3.1 Polarization of gravitational waves

Within the framework of general relativity gravitational waves are transverse waves that propagate with the speed of light. As in the electromagnetic signals, gravitational radiation has two independent polarization states; but the angle between the two states is $\pi/4$, rather than $\pi/2$. The passage of a wave distorts spacetime and produces changes in length in two orthogonal directions that oscillate with gravitational wave frequency. Fig. 1.1 shows the action of each polarization component on a circular ring of test masses. In accordance to the shape of the distortion produced by the wave its polarization states are called "*plus*" (+) and "*cross*" (×). The respective time function components of the wave are written as h_+ and $h_\times$, where h represents the *strain* or relative deformation (adimensional) of lengths caused by the gravitational wave. The orientation and degree of polarization depends on the relative orientation between the observer and the dynamics of the source. The measurement of the polarization of the gravitational wave can provide information about the orientation of the source.

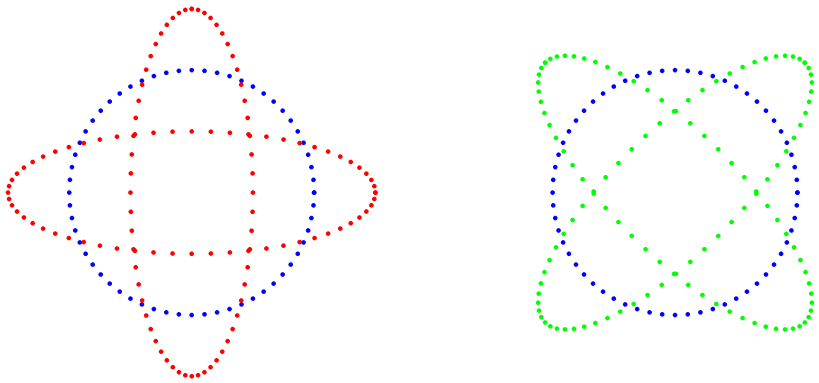

Figure 1.1: Diagram showing the two independent polarizations of a gravitational wave. A circular ring of test masses is located in the plane of the paper and the effect on it by a gravitational wave propagating perpendicularly to that plane considered. The deformation of the ring of test masses helps to visualize how the proper distances between the test particles change. *Left:* Effect of the plus '+' polarization. *Right:* Effect of the cross '×' polarization. The ring of particles will stretch and squeeze (the effect is extremely exaggerated in this figure) adopting an alternating circular-ellipsoidal-circular shape for each half wavelength of the passing gravitational wave.

1.3.2 Strength of gravitational waves

The Einstein field equations are too complicated to be solved analytically and to infer the amplitude of gravitational waves; these are often solved numerically with post-Newtonian approximations of various orders. The lowest order post-Newtonian approximation for the emitted radiation is the *quadrupole formula*, which depends on the density ρ and the velocity fields of the Newtonian system (7). The amplitude of the gravitational wave is, at its lowest order, the tensor:

$$h_{jk} = \frac{2}{r}\frac{d^2 Q_{jk}}{dt^2}, \tag{1.1}$$

where Q_{jk} is the second moment of the mass distribution, the spatial tensor

$$Q_{jk} = \int \rho \; x_j x_k \; d^3x. \tag{1.2}$$

The source that produces gravitational waves is the internal dynamical motion, but only the shape-changing portion of the system: a perfectly round star pulsating spherically would not produce any gravitational radiation, whereas a non-radial oscillation or spinning of a non-axymmetric object would generate gravitational radiation. A measure of the amount of shape-changing motions of a system is the kinetic energy of the non-spherical part $E^{\rm ns}_{\rm kin}$. Shape-changing dynamical motions provoke the amplitudes of the gravitational wave field h_+ and $h_\times$ to oscillate with amplitudes (8; 9):

$$h \sim \frac{G}{c^4}\frac{E^{\rm ns}_{\rm kin}}{r} \sim \; 10^{-20}\left(\frac{E^{\rm ns}_{\rm kin}}{M_s c^2}\right)\left(\frac{10 \text{ Mpc}}{r}\right) \tag{1.3}$$

where M_s is the mass of the sun, and 10 Mpc is the approximate distance scale for the local group of galaxies. Eq. 1.3 gives an indication of the small amplitudes of the gravitational field expected on Earth that need to be detected.

The strongest astrophysical sources are likely to have masses of order that of the sun or a few factors of ten larger. Similarly for the velocity where maximum velocities are a few factors of ten smaller than c. Combining both uncertainties the strongest amplitude expected is a few factors of ten up or down from 10^{-20}, very small indeed.

The absence of direct detection has allowed to establish upper limits on the strength of the gravitational wave signals expected. This has proved that the amplitude is smaller than the aforementioned fiducial figure of 10^{-20}. From the analysis of science data acquired by ground-based detectors, observational upper limits of the strength of gravitational waves have been now inferred for different type of sources: upper limit on the stochastic gravitational-wave background of cosmological origin (10), upper limits of PSR J1939+2134 (11), upper limits of 78 pulsars (12), beating the spin-down limit on gravitational wave emission (13), all-sky search for gravitational-wave bursts (14).

1.3.3 Frequencies of gravitational waves

Estimates of the duration and oscillation frequency of the gravitational waves are important in order to assess their detectability, for detectors do not have the same sensitivity across all the detection bandwidth. In some cases the frequency of the emission is dictated by the existing motion, such as the orbital movement of a binary or the spinning of a pulsar. Most generally, however, the frequency will be related to the internal oscillations of the system and therefore to its natural frequency f_0 (7).

$$f_0 = \sqrt{G\bar{\rho}/4\pi}, \tag{1.4}$$

where G is the gravitational constant and $\bar{\rho} = 3M/4\pi R^3$ is the mean density of the source. Although Eq. 1.4 is a Newtonian formula, it provides a remarkably good order-of-magnitude approximation to natural frequency values, even for highly relativistic sources such as black holes. For a neutron star of mass $1.4M_s$ and radius 10 km, the natural frequency is $f_0 = 1.9$ kHz. For a black hole of mass $10M_s$ and radius 2M $\equiv$ 30 km, $f_0 = 1$ kHz. And for a large black hole of mass $2.5 \times 10^6 M_s$, such as the one at the center of our galaxy, the frequency goes in inverse proportion down to the mass to $f_0 = 4$ mHz. In general, the characteristic frequency of a compact object of mass M and radius R is

$$f_0 = \frac{1}{4\pi}\left(\frac{3GM}{R^3}\right)^{1/2} \simeq 1\text{kHz}\left(\frac{10M_s}{M}\right). \tag{1.5}$$

Due to seismic disturbances ground based detectors will not able to detect signals of frequencies smaller than 10 Hz (second generation detectors). Third generation detectors' bandwidth will possibly be stretched in the lower end down to 1 Hz by reducing the gravity gradient noise using underground locations, and by reducing the seismic disturbances with special and active suspension systems (15). The future detector in space (LISA) will be able to detect gravitational waves in the range of 1 mHz to 100 mHz. The upper limit of this bandwidth is limited by the long arm distance between LISA's test masses and corresponds to approximately the reciprocal of the light travel time down its baseline.

1.4 Important gravitational radiation sources

Purposely generated man-made gravitational waves are too small to be detected; this is because huge masses accelerating rapidly are needed to distort the space-time and thus generate gravitational radiation of sufficient intensity. To get an estimate of the approximate amplitude of a man-made gravitational wave (16), imagine creating a wave generator with extreme properties: two masses of 1000 kg each at opposite ends of a beam 10m long, which rotates about an axis in the centre of the beam 10 times per second. The frequency of the waves will be 20 Hz, since the mass distribution of the system is periodic with a period of 0.05 s, only half the rotation period. The wavelength of the waves will therefore be $\sim 1.5 \times 10^7$ m, about the diameter of the earth. In order to detect gravitational waves, not near-zone Newtonian gravity, the detector must be at least one wavelength from the source. The amplitude is $\sim 5 \times 10^{-43}$ and it is far too small to contemplate detecting!

Astrophysical phenomena, including cataclysmic events, are the most promising sources to generate strong enough waves to be detected from Earth. An archetypical example includes core-collapse supernovae and coalescing binaries that inspiral inwards to finally merge at the end of their lifes. Depending on the type of source and its distance to Earth, the gravitational waves expected are various in strength, frequency, polarisation and duration.

Conventionally, the different gravitational signals expected from different sources are classified as *compact binary coalescence*, *burst*, *continuous* and *stochastic* signals. In the following sections, we concentrate on the signals detectable for ground-based detectors, with frequencies in the range of 1Hz to 10 kHz.

1.4.1 Coalescing compact binaries

Compact object binaries, formed by neutron stars and black holes orbiting each other, are a very promising source of gravitational radiation. These objects are the result of the evolution of massive star binaries that keep gravitationally bound after two supernovae explosions. The two objects orbit inspiraling into each other to end up merging into a unique compact black hole; the inward inspiraling reflects the energy loss due to the gravitational wave emission (see Section 1.3).

The frequency of the signal has been expected to be twice the rotation frequency of the source and proportional to the velocity of the objects in the case of binaries. This means that for most of the time the system will generate a low intensity and low frequency signal not detectable by gravitational detectors on Earth. Detectable predicted gravitational waves are only expected in the last period of the inspiral phase when the objects are close enough and their gravitational signals have a frequency within the detection bandwidth of ground-based detectors. The compactness of the objects avoids the distortion of the bodies until they are so close as to start the process of merging to fuse into a black hole and reach an equilibrium state.

The waveform of the inspiral phase is predicted accurately and allows inference of interesting astrophysical information like the masses of the binary and orbital parameters (17). The last stages of the black hole binaries are better understood than those involving neutron stars; it may be that the neutron star is disrupted by its companion when close enough. Measuring the gravitational radiation in the disruptive merging process would make possible to get precious information about the equations of state of neutron stars (18). Although oscillation modes of black holes have been studied for extensively, the waveforms expected from the merges and the subsequent ring-down and relaxation are quite uncertain.

1.4.2 Burst signals

A burst-type signal is a short signal in which the Doppler-shift produced by the rotation of the Earth can be neglected (19). Typically, they last for less than a second and their the frequency, polarization and duration is uncertain due to the random orientation and internal structure of the object. The expected burst signals are normally related to a sudden gravitational cataclysm like the core-collapse of massive stars, the sudden change of their internal structure, or binary coalescences – particularly the merger phase, which may be more amenable to analysis as an unmodeled burst than by using a matched template approach.

1.4.2.1 Gravitational collapse

An important source of gravitational burst signals is stellar gravitational collapse. This occurs at the end of the life of evolved stars that run out of fuel: the internal pressure that keeps the star in hydrostatic equilibrium vanishes and the star succumbs to its own gravity with catastrophic consequences. Sometimes the core of the star bounces back provoking an explosion known as supernovae (type II) and expels all the outer layers of the star to the interstellar medium. Depending on the mass and rotation degree of the progenitor different types of collapse are known and they can leave behind a neutron star or a black hole.

Long-duration γ-ray bursts (GRBs) (> 2 s) are thought to be powered by the core collapse of highly rotating massive stars, known as *collapsars*, to a black hole. The energy extracted from the disc of the black hole drives relativistic jets of high-energy photons that can be observed (20). Gravitational waves may be generated during the collapse itself and as a consequence of the oscillations of the compact object formed (ring-down).

Simulating gravitational core collapse is a very active area of research but there are still many uncertainties and as yet a fully relativistic 3D core collapse, including all the physics, cannot be simulated by computers. Waveforms expected from the collapse and posterior ringdown have been calculated (21; 22) but the amount of energy released in the form of gravitational waves is not well known. For a review of the astrophysics that can be learned from the gravitational waveforms emitted in the core collapse see (23).

Gamma Ray Bursts (GRBs) may be good allies in order to detect and analyse gravitational burst radiation generated by gravitational collapse. Given that the electromagnetic and gravitational signal travel at the same speed, the knowledge of the approximate time and the sky location of the GRB can greatly facilitate the search of the burst signal by the detectors.

1.4.3 Continuous signals

These are periodic signals with frequencies limited to narrow bandwidths and related to orbital rotation or spinning of compact objects like neutron stars and black holes. A rotating non-axisymmetric neutron star is believed to radiate

gravitational waves at two times its frequency of rotation. The strength of the signal emitted depends on the ellipticity of the neutron star, sustained by the solid crust of the neutron star or by accretion flow from a companion. When the sky location of the neutron star is known (thanks to its radio pulsations) the search for this type of signal is simplified, for the position of the source is mostly known and the frequency expected falls in a narrow range of the pulsating frequency. However, the rotation of the Earth and its motion around the solar system barycenter (7) makes the search of the signal more complicated and computationally very demanding.

1.4.4 Stochastic signals

It is believed that the universe has a random gravitational wave field produced by the superposition of the emission of miriad of background sources and also from fundamental processes as the Big Bang. This is basically background noise and it is characterised by its energy density per unit frequency, typically given as a fraction of the closure or critical cosmological density (7). Direct measurements of the amplitude of this background are of fundamental importance for understanding the evolution of the universe when it was younger than one minute. Using science data acquired during two years upper limits on the amplitude of the stochastic gravitational wave background have been limited and the energy density constrained (10).

The stochastic signal and the instrumental noise are similar and difficult to discern. The method for its detection consist in cross-correlating the signals acquired by two or more instruments (24).

1.5 Gravitational wave detectors

The weak nature of gravitational radiation makes the detection of gravitational waves difficult and the design of extremely sensitive detectors necessary. Filtering out the noise background requires sophisticated instruments and is itself a field that requires great expertise - signals of astrophysical origin need to be isolated.

There are mainly two classes of effective gravitational wave detectors: *laser interferometric detectors* and *resonant bar detectors*. Interferometric detectors search for the oscillations caused by the interaction of the gravitational wave with an electromagnetic light beam, whereas bar detectors measure the vibrations of a mass to which the gravitational wave transfers energy when passing (7).

J. Weber pioneered the construction of gravitational wave detectors in the 1960s by building the first resonant bar detector at the university of Maryland. This was a cylindrical bar of aluminium (two meter long and half a meter in diameter) working at room temperature, and to which piezoelectric transducers were attached to convert the vibrations into electrical signals. Weber reported detections but his claims were later discredited by the scientific community which was unable to reproduce his results (25; 26). His designs, however, were developed further to include cryogenic technology, new vibration isolators and transducers.

Various resonant bar detectors have been built and operated worldwide since then. Within the international collaboration group IGEC (27) there are the detectors ALLEGRO (USA), AURIGA (Italy), EXPLORER (CERN), NAUTILUS (Italy) and NIOBE (Perth, Australia). Unfortunately, due to funding restrictions, only EXPLORER and AURIGA continue acquiring data currently. The current generation of resonant-mass detectors exhibit sensitivity as small as $10^{-21}/\sqrt{\text{Hz}}$, in a narrow band tens of Hertz wide (28).

The archetypal gravitational wave beam detectors are ground-based large scale Michelson-type laser interferometric instruments comprised of two perpendicular arms having kilometer-scale lengths. Fabry-Pérot cavities may be used to increase the light travel time in the arms and to increase detection sensitivity. The detection principle is the measurement of the separation changes between freely suspended test masses at the extremes of the arms under the influence of a passing gravitational wave; this can be measured by precise interferometry. Sensitive measurements of the interferometer are possible thank to sophisticated electro-optical servo-loops that keep the instrument locked in a stable configuration. This way, minute light power variations caused by the passage of the wave can be sensed.

Laser interferometric detectors provide a better sensitivity than the resonant bars over a wider bandwidth. The approximate detection bandwidth of current

(first generation) ground-based laser interferometric detectors ranges from 40 Hz to 10000 Hz. Across this detection bandwidth the spectrum of the instrumental noise is not flat but shows three distinct regions. Seismic disturbances from the environment limit the sensitivity at low frequencies (< 40 Hz); in order to minimise the transmission of vibrations to the test masses, these are suspended with multi-staged structures. The thermal noise limits sensitivity at intermediate frequencies; this is related to the thermal vibrations of the test masses and the suspensions and is counteracted by careful choice of materials and fibers from which test masses are suspended. The shot-noise is the measurement limitation at high frequencies (> 200 Hz) where the quantum uncertainty of the light and its detection by photodetectors dominate. Across the detection band laser interferometric gravitational detectors are most sensitive around 150 Hz. A good introduction to the fundamentals of bar and laser interferometric detectors can be found in (29); a comprehensive review of developments of laser interferometer detectors and the technologies used for their control can be found in (30).

1.5.1 Worldwide network of gravitational wave detectors

A worldwide network of laser interferometric gravitational wave detectors has been established in the last twenty years. Laser interferometric gravitational wave detectors have a poor directional sensitivity: as linearly polarized quadrupolar instruments they measure only a projection of the wave impinging on the detector. A network of several instruments can reinforce the confidence of a detection and pinpoint the source's sky location by triangulation.

Current detectors, of different size and sensitivity, are spread across the five continents. The two major projects are called Laser Interferometric Gravitational Observatory (LIGO) (31) with 3 detectors located in the USA, and VIRGO (32) with one detector in Italy. Another two detectors of no lesser importance, GEO600 (33) in Germany and TAMA300 (34) in Japan, are smaller in size; they are not as sensitive as the LIGO and VIRGO detectors, but they have contributed decisively to the development of the technology incorporated currently in all the interferometers.

LIGO is a project led by Caltech/MIT with 3 detectors located in two sites: a 4-km (H1) and a 2-km (H2) instrument in Handford that share the same vacuum system, in Washington, and a 4-km (L1) instrument in Livingston, in Lousiana. GEO 600 is a German/British collaboration operating a 600 m instrument located close to Hanover, Germany. LIGO and GEO600 have collaborated together since 2001 under the LIGO Scientific Collaboration (LSC) (35) and have successfully exchanged technology, experience and data. Within the LSC, the GEO600 detector is also seen as a prototype where new components and technologies are developed and tested before taking them to the bigger interferometers.

VIRGO is a Italian/French enterprise operating a 3-km instrument developed by the VIRGO Collaboration (36) and located within the site of the European Gravitational Observatory (EGO) (37) in Cascina, Italy. Recently, VIRGO and LSC have signed an agreement to share data and analyse it jointly; many papers have been published already as a result of this agreement.

GEO600 has been operational since 2001 and has developed and tested many technologies that will soon be incorporated into the advanced LIGO and advanced VIRGO instruments like suspensions, mirror coatings and various interferometer configurations. Technology developed in GEO600 and considered now mature is being transferred to LIGO and VIRGO as a part of their planned upgrades, described in Section 1.5.2.

TAMA300 was the first gravitational wave interferometer to take data, and the collaboration has now proposed an ambitious second generation detector: the Large-scale Cryogenic Gravitational-Wave Telescope (LCGT) (38) is being planned in Japan. It consists of an underground detector of 3-km arms and will be the first to use cryogenic technology to reduce the effects of thermal noise. With good prospects, the project has been partially funded already.

All the aforementioned detectors are located in the North hemisphere, but there is also a small gravitational wave detector working in the South Hemisphere, in Western Australia. Plans for a bigger detector called the Australian Interferometric Gravitational Observatory (AIGO) (39; 40) are under way, a proposal of the Australian Consortium for Interferometric Gravitational Astronomy (ACIGA) (41).

The first generation of detectors (called initial) have progressively achieved and surpassed their design sensitivities making already possible a few years of data acquisition and analysis. Currently, the initial LIGO and VIRGO detectors are going through major upgrades towards their advance configuration (second generation). The advanced instruments will eventually replace the initial instruments with one ten times more sensitive. This means that the searchable volume of space will increase by three orders of magnitude.

1.5.2 Status Quo and future detectors

In 2007 the initial LIGO detectors finished a two year long data run (fifth science run S5) during which a full year of triple-coincidence data was collected at design sensitivity. Much of this run was also coincident with the data runs of GEO600 and VIRGO, forming the most sensitive worldwide network of gravitational-wave detectors to date (42). Analysis of S5 data have produced numerous publications in which, although no gravitational wave detection has been seen, upper limits on the emission of gravitational wave radiation and rates of various sources have been established: search of waves from compact binary coalescence (43), from known pulsars (44), periodic gravitational waves (45; 46).

After completion of S5, and as part of a staged upgrade toward the second generation instruments, the two 4-km LIGO detectors (L1 and H1) were taken offline to undergo a number of upgrades and increase the sensitivity by a factor of two (Enhanced LIGO). The main changes were the increase of light power, to be more sensitive at high frequencies, and the movement of the dark port detection system to a seismically isolated vacuum chamber (47). Also, the optics of the output table were completely changed and an output mode cleaner was incorporated for the first time. In case a close supernova went off during these upgrades the third LIGO detector (H2) was left in operation in conjunction with GEO600 in a program called *Astrowatch*. Both L1 and H1 are back online now as Enhanced LIGO and will collect science data for about a year, until completing the sixth science run (S6), working together with an slightly upgraded VIRGO and improved GEO (GEO-HF)(48).

The GEO-HF detector is currently going through alternate states of data acquisition and commissioning to incorporate the most advanced optical and interferometric techniques, including *squeezing*. This is an optical technique to reduce the phase noise below the standard quantum limit, which limits the sensitivity of the detector at high-frequencies, by injecting squeezed light of unbalanced quantum uncertainty of the two conjugate variables amplitude and phase, through the dark port. This way it is possible to reduce the shot-noise to lower values than the so-called Standard Quantum Limit (SQL) (49; 50; 51).

In 2011 all LIGO and VIRGO detectors will be taken offline for major upgrades (H2 detector will be stretched to have 4-km arms) that will take the four detectors to their advanced configuration.

1.5.2.1 Second generation (Advanced) detectors

Advanced LIGO and advanced VIRGO will be quantum-limited interferometers with a significant increase by sensitivity over initial detectors, and will start acquiring data in 2014. They will replace the initial instruments using the same premises and vacuum tanks but with major hardware changes. The new instruments will incorporate new components and technologies developed in the last 15 years: a more stable and powerful laser, bigger and heavier test masses with new test mass suspensions, new seismic isolation systems, and state of the art interferometer control system. The planned upgrades for advanced LIGO are described in (52). This modifications will permit to reduce the noise even further and stretch the detection bandwidth, from 40 Hz down to 10 Hz in its lower range. The installation of a signal recycling mirror at the sensing port will allow to tune the interferometer between wideband or narrowband operation (53). By changing the position and reflectivity of the signal-recycling mirror, the instrument can be tuned to have much lower shot noise in a specific narrow band, in exchange for higher combined light-pressure and shot-noise at other frequencies. The locus for noise amplitude minima for advanced LIGO in narrowband operation is shown in Fig.1 of (54). The advanced detectors will have a sensitivity 10 times better than the initial detectors and are expected to switch the science of gravitational radiation from discovery mode to regular astrophysical observation.

1.5.2.2 Third generation detectors

Second generation detectors are expected to start acquiring data after 2014. However, the design study for a ground-based detector is already under way as part of an ambitious plan to build a third generation detector called the *Einstein Telecope* (ET). The aim of this detector is to reduce the noise tenfold with respect to the second generation instruments and to increase the detection bandwidth lowering the seismic limitation from 10 Hz down to 1 Hz. Advanced detectors will be limited by the gravitational gradient noise in the lower part of the detection bandwidth, the thermal noise of the suspension and test masses in intermediate frequencies, and quantum noise for higher frequencies. New underground infrastructures with arms up to 10 km, cryogenic facilities to cool down the mirrors and the use of squeezed light will be necessary in order to lower the noise tenfold. Various topologies are being considered for the ET detector(55; 56).

ET is a project funded by the European commission and its design and feasibility studies are being carried out in conjunction by various European institutions (57) working together. The aim of this collaboration is to set the science goals of the instrument and to make decisions with respect to its future location, topology, technologies to incorporate data analysis needs (58).

Fig. 1.2 shows the noise curves for initial and advanced LIGO and VIRGO instruments, and the noise curve expected for ET.

1.5.3 Scientific goals of second and third generation instruments

It is believed that a few weeks of data of the advanced detectors will provide as much scientific insight as the initial detectors have done during the past 7 years. Given our current astrophysical understanding the detection of gravitational waves should become a near-certainty and regular astrophysical observations ought to commence (60).

The potential of the new detectors can be summarised in two fronts: more and better detections. More because the tenfold increase in sensitivity will bring a thousand-fold increase of space volume to explore; and better because it will allow for signals to be detected with a bigger signal to noise ratio. The benefit of

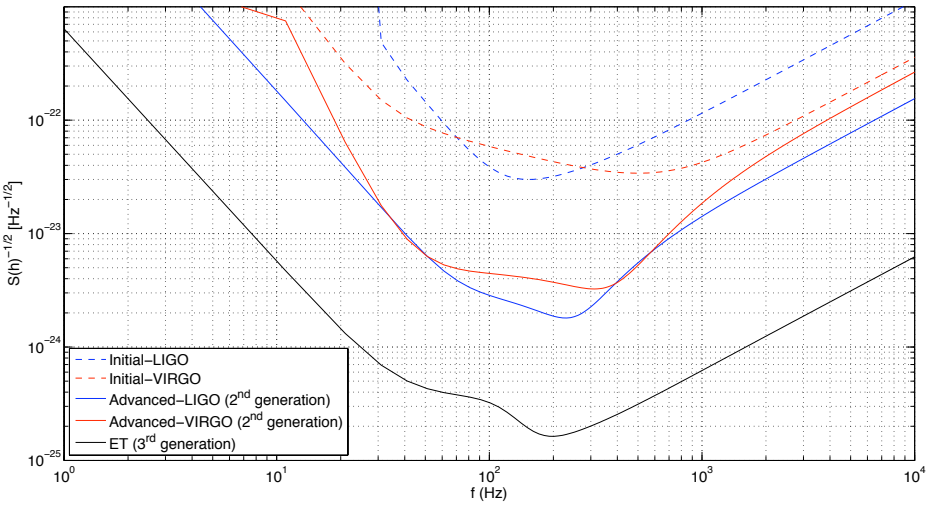

Figure 1.2: Sensitivity curves of ground-based (noise amplitude $\sqrt{S_h(f)}$) for initial, second and third generation instruments. Note the approximate tenfold increase in sensitivity from initial to advanced configuration and, in turn, from the advanced to the third generation instrument noise curve. Data taken from (7), except for advanced VIRGO (59).

a bigger scope of detection will come particularly from the better sensitivity in the mid-frequency region ($\approx$ 100 Hz). To learn about the astrophysical prospects within the range of advanced LIGO, see (54). For a review of the astrophysical potential of ET we refer the reader to the so-called vision document (58; 61).

To infer rates of detection of gravitational waves it is necessary to know the distribution of compact objects, the sources. Approximate abundance of neutron stars and black holes have been inferred from electromagnetic observations: signals from pulsars have permitted extrapolating the distribution of neutron stars for example. Although the case of black holes is more controversial, astronomers now recognize that there is an abundance of black holes in the universe. Observations across the electromagnetic spectrum have located black holes in X-ray binary systems in our galaxy, in the centers of star clusters and in the centers of galaxies (7).

In the following, a short summary of the major science potential of future detectors is presented (54). Considering archetypical values for neutron stars

of $1.4M_s$ and black holes of $10M_s$, inspiraling NS-NS binaries will be seen to a distance of 300 Mpc ($z \sim 0.1$), about 15 times further than the initial LIGO, and with a event rate 3000 times superior (about 10 events per year). NS-BH binaries will be visible to 650-1000 Mpc ($z \sim 0.2$) (about 13 events per year). Inspiraling BH-BH binaries will be seen to a cosmological distance of 2000 Mpc ($z \sim 0.5$) (about 500 per year) when for initial LIGO was up to 100 Mpc. All these figures are quite uncertain. Rates for inspiraling coalescences are also uncertain, see (53) for rates expected in the local universe ($z \sim 0$). Frequent detection of coalescing compact binaries with good SNRs will result not only in the inference of the masses of the components and their orbital parameters but also their distance. Provided the host galaxy can be identified an independent distance estimator will be available to astronomers.

Continuous signals from non-axisymmetrically deformed neutron stars will benefit from the combined effect of lowering the noise and widening the low frequency down from 10 Hz, for most of the continuous gravitational signals from deformed neutron stars (expected at twice the pulsar spin frequency) are in the 1 to 10 Hz region. The detection advantage provided by advanced detectors and ET are shown in (53). There is great uncertainty on the amplitudes expected from these sources but a lower sensitivity curve would allow constraining the maximum eccentricity of neutron stars even more and to learn about their structure.

Gravitational waves emitted by LMXBs (Sco X-1) would be marginally detectable for advanced detectors. The analysis of narrow sub-bands of strain data over long time durations could elucidate if it is the gravitational wave energy loss which avoids the neutron star to spin-up to the break-up limit. Assuming that there is some mechanism for the binary to lose angular momentum, as fast as it is accreting matter from the companion, the gravitational wave search would need to allow for the random evolution of the spin of the accreting body. A long enough integration of the signal acquired in narrowmode would make gravitational wave signals from LMXBs detectable (54).

1.5.4 Multimessenger astronomy with future telescopes

Much has been learned in experimental science by studying the same phenomena with different techniques and instruments. Gravitational waves are expected to complement the partial perspective of astronomical phenomena obtained in other disciplines. Electromagnetic and neutrino observations are complementary to gravitational wave astronomy.

There are celestial objects that will only be probed studying the gravitational radiation they emit. This is the case of coalescing periods of black holes or neutron stars, although perturbations of huge magnetic fields could emit electromagnetic radiation. Others, like coalescing binaries, core-collapse supernovae and magnetars are expected to be seen by gamma- and X-ray, visible light, infrared and radio waves.

Correlation in time and direction between observations that correspond to the same astrophysical event can greatly help in the search of gravitational waves, for laser interferometric detectors are very sensitive to the relative orientation of the source relative to the line of sight to Earth. For example, a core collapse supernova seen by optical telescopes would indicate an event of a few hours prior to the start of the optical observation, which would facilitate the search immensely. Detecting first the gravitational wave would be even better: if the signal was strong enough and seen by a network of interferometers, the location of the source could be inferred by triangulation thanks to the arrival time differences and optical telescopes could be pointed at the particular location to capture the glow of the supernovae. Similarly, GRBs detected by satellites would indicate the time of the cataclysm (core collapse or merger) plus the approximate location of the event in the sky. This, again, would ease considerably the search by reducing the parameter space need to be analysed.

The GRB and afterglow are an indirect indication of the engine but only by detection of their gravitational wave imprint will we have a direct probe of the internal physics. The predicted rate of NS binaries detected by the third generation detectors in combination of GRBs will provide redshift values for some of them that will provide an independent cosmological distance scale. GRBs in

conjunction of neutrino detections will provide precise time evolution of the cataclysm and will improve our understanding of their physics. For more information about the potential of combined observations and the multimessenger astronomy potential of the Einstein Telescope, see (61).

1.6 Gravitational burst signals of galactic origin

Sources likely to produce gravitational burst signals have been introduced in Section 1.4. Here we focus on those sources in our galaxy likely to generate gravitational burst signals detectable on ground-based laser interferometric gravitational waves.

Non-axisymetric core-collapse and the subsequent oscillations of the newly born compact object (neutron star or black hole) are a potential source of detectable signals. However, the expected rate of core-collapse supernovae in our galaxy, one every 30 years, is so low that the hopes to do science based on these events are quite dim. That is why here the focus is brought to events with higher rates and from galactic sources that could potentially be detected with instruments of second and third generation. Galactic neutron stars and mechanisms able to take them out of equilibirum, and make them oscillate while emitting exponentially damped ringdown gravitational waves of short duration, take protagonism here.

1.6.1 Neutron stars and pulsars

Even after 40 years of dedicated study, neutron stars are still mysterious objects. Their mass and diameter are quite well constrained but their internal structure is still rather uncertain. Detailed analysis of gravitational radiation from oscillatory neutron stars will increase the understanding of this exotic objects immensely.

As early as 1934, the existence of a new form of star, the neutron star, was predicted (62). Current belief is that neutron stars are the corpses of massive stars that underwent a sudden core-collapse after running out of fuel and being incapable of standing their own gravity. In case of more massive stars it is believed that the core-collapse forms a black hole instead. When the fuel runs out, the

sudden lack of internal pressure gives way to a fast gravitational collapse of the core that compresses up to nuclear densities. In the case of neutron stars, the enormous gravitational force crushes the electrons and nuclei of ordinary atoms to form matter consisting mostly of neutrons. Sometimes the compressed core bounces back resulting in expulsion of the outer layers of the star out in a visible supernova explosion and giving way to a supernova remnant visible for a few thousands of years.

The conservation of the magnetic field and angular momentum in the collapse leads to the creation of a compact object of extraordinary characteristics. Roughly the mass of our sun is compressed into an object of a few kilometers in diameter and density up to 10^{14} g cm^{-3}, which rotate rapidly and holds enormous magnetic fields of up to 10^{12} G. Although the internal structure of neutron stars is still a subject of much debate, the accepted simplified belief is that it has a liquid core surrounded by a solid crust, mostly comprised of neutron but possibly including other more exotic particles.

More than 30 years elapsed between the prediction of the neutron star and the serendipitous discovery of the first *pulsar* (i.e. pulsating radio star) in 1967 (63; 64). Shortly after their discovery, the connection of a rapidly rotating neutron star with a strong dipolar magnetic field acting as a energetic electric generator was established (65). The fact that a neutron star could rotate as rapidly as the period of the radio pulses established the final link between the *pulsar* and the neutron star. The radiation of a pulsar is powered by its rotation; particles are accelerated along the magnetic field lines to emit a beamed radiation that can be detected from Earth if the orientation of the pulsar is appropriate. This is when the rotating axis of the neutron star does not coincide with the magnetic dipole axis and the beamed radiation sweeps across the Earth.

Around 1900 pulsars have been found until now, most of them in the Galaxy and close the galactic plane. The majority of the pulsars are detectable only at radio wavelengths, but a few very young and short-period pulsars are also detectable at optical X-ray, and even γ-ray wavelengths. For a list of the known pulsars, see the ATNF catalogue (66; 67).

1.6.2 Neutron stars as gravitational radiation sources

Neutron stars, either in isolation or as members of binary systems, are expected to emit gravitational radiation through diverse mechanisms. Here the focus is brought to neutron stars in isolation likely to emit strong enough gravitational wave bursts. Various mechanisms have been proposed in relation with different known astrophysical phenomena.

1.6.2.1 Pulsar glitches

Overall, pulsars show a very regular rotation rate, but occasional time irregularities have been detected on a few young pulsars. These irregularities point to sudden structural changes of the neutron stars, which are a penetrating means of investigating their interior structure (67). Sudden structural changes present a strong link to the oscillation of neutron stars and the corresponding ringdown gravitational wave emission. Investigations on gravitational wave data analysis in the context of pulsar glitches have been carried out in (68).

A *glitch* is a sudden step on the rotation period of the neutron star that produces the pulsar time irregularity. These are rare events, observed predominantly in young pulsars. Vela and the Crab pulsars are the ones where most of the glitches have been seen and they are under continuous surveillance. In a typical glitch, a sudden rotational speed increase is followed by an exponential recovery that brings the slow down of the rotation to the values expected in the absence of the disruption. There are two main hypothesis to explain the glitch phenomena: a) the progressive reduction of the rotational speed diminishes the centrifugal force and the equilibrium ellipticity of the crust adjusts in a series of steps, and b) independent motion of the crust and the fluid interior and variable degree of coupling between them. The exponential recovery after a glitch is an indication that the pulsar does not rotate as a single body. The outer crust and the inner fluid rotate independently but the degree of coupling between them is not well understood yet. It may be that the external electromagnetic braking generates a differential rotation between the crust and the inner fluid. Depending the level of coupling between the two an erratic transfer of angular momentum from the fluid to the crust may be the cause of the glitch.

1.6.2.2 Magnetars: Soft gamma repeaters (SGR) and Anomalous X-ray pulsars (AXP)

Magnetars are slow rotating neutron stars (period of $\approx$ 8 s) with very strong magnetic fields ($\approx 10^{15}$ G). The current belief is that if after a type-II supernova collapse the hot newborn neutron star spins fast enough, it acquires an intense magnetic field, which is 1000 times stronger than a pulsar. The strong magnetic field brakes severely the spinning of the neutron star and the rotation period decreases very quickly. In its evolution the magnetic field moves through the solid crust of the magnetar, bending and stretching the crust. This process heats the interior of the star and occasionally breaks the crust in a powerful *starquake*. The accompanying release of magnetic energy creates a sudden burst of γ-rays, accounting for the fainter bursts that give SGR their name (69). The electromagnetic energy released on these flashes is extraordinary ($\approx 10^{46}$ erg s^{-1}) and is supported by changes on the magnetic field configuration of the neutron star. The repetition of the flashes, sometimes after a few years, is one of the features that differs them from Gamma ray bursts (GRB).

Only five SGRs have been detected so far, most of them in our galaxy and in isolation. SGRs cease emitting bright bursts after only about 10,000 years and probably only the youngest few have been detected.

The anomalous X-ray pulsars (AXP) are X-ray pulsars that present pulsations that fade in and out. In a similar fashion to SGRs the energy released is believed to come from the strong magnetic field. Magnetars are believed to go through stages where their magnetic field reconfigures and the neutron star oscillates emitting short-duration gravitational waves (70). Many millions of magnetars are believed to exist in our galaxy and in every other galaxy (69).

1.7 Oscillations of stars

Stars oscillate due to the movement of their internal matter. The vibrations of luminous stars can be studied by measuring the Doppler-shifts of known spectral lines (*asteroseismology*), from which information about the primary pulsation

modes can be obtained. The interior of the Sun has been studied this way (*helioseismology*) for many years now.

Compact objects (neutron stars and black holes) are also believed to oscillate after being taken out of their equilibrium configuration. But the oscillations of a black hole are not easy to visualize, for it does not possess any material to sustain such oscillations. These are oscillations of the spacetime metric, which is a dynamical entity itself, just like the fluid of a star. Oscillations caused by the motion of the fluid of a neutron star are easier to visualize. However, there are not the only type of oscillation to consider. There exists an additional family of oscillation modes, which are rather independent of the fluid and involve the spacetime of the star at equilibrium. In opposition to luminous stars, oscillations of compact objects are not stationary but dampened over a time period, which are represented by Quasi Normal Modes (QNMs). These modes play a prominent role in gravitational radiation emitted in a variety of astrophysical scenarios and will be seen by the new gravitational wave detectors (71). For a review of the oscillations expected from BHs and NSs, see (72).

The oscillation modes of a star can be divided into two general classes: *polar* (spheroidal) and *axial* (toroidal). The polar ones correspond to spheroidal deformations of the star, whereas the axial ones are associated with differential rotation. As far as the stellar fluid is concerned, polar pulsation modes exist for all conceivable stellar models, whereas the existence of axial modes rely upon nonzero rotation, magnetic field or shear modulus (73).

1.7.1 Oscillations of black-holes

The quasi-normal modes for various types of black holes have been calculated; these are quickly damped in a few milliseconds. The best known are for the Schwarzschild (74) and Kerr Black Holes (72). For other type of black holes they have not yet been calculated due to the complexity of the perturbation equations but the existence of infinite number of quasi-normal modes for black-holes has been demonstrated. Fig. 1.3 shows the frequency and damping values expected from the quasi normal oscillations of the simplest Schwarzschild black hole. Values

have been taken from (72; 75; 76) and are function of only the mass of the black hole.

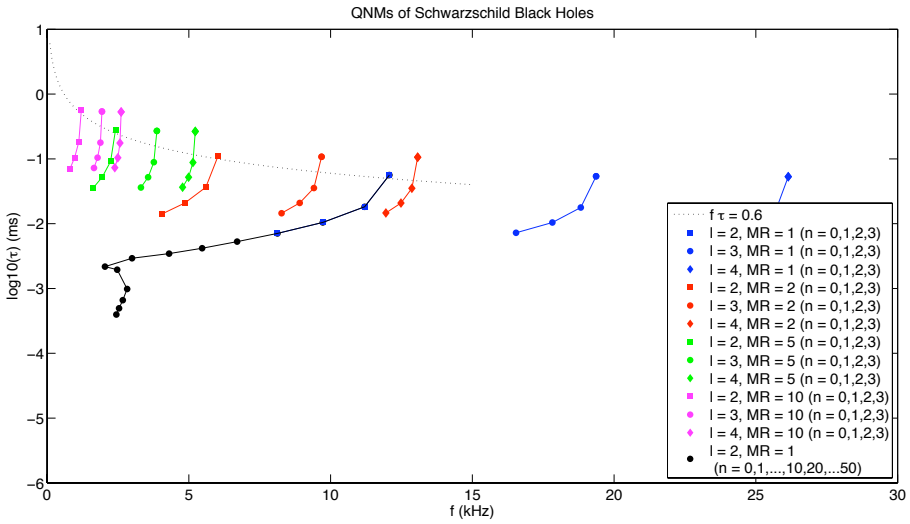

Figure 1.3: Frequency and damping times predicted for $l = 2$, (quadrupole), $l = 3$, $l = 4$ modes of quasinormal oscillations of Schwarzschild black holes of different masses (72). Damping times are very small (less than a msec) and have been plotted in logarithmic scale to show the range of values more clearly. The mass ratio (MR) shows the mass of the black hole in solar masses. The dotted line, given by the relation $f\tau = 0.6$ (75), with f in kHz and τ in ms, is a good approximation for the fundamental modes. The longest damping value τ of each mode is the fundamental $n = 0$, but $n = 1, 2$ and 3 are shown here too. For a black hole of one solar mass (MR $= 1$) more frequency modes are shown for the case of $l = 2$, taken from (76).

1.7.2 Oscillations of relativistic stars

Study of pulsating relativistic stars is important to understand the stability of compact objects and to know the gravitational radiation emitted by them. There are two main families of modes, namely *fluid*- and *spacetime*-modes. The fluid modes correspond to the analogue Newtonian modes but the spacetime or w-modes are unique to relativistic stars. In the following, the most important oscillation modes, for the case $l = 2$ (quadrupole) are described. Fig. 1.6 shows frequency and damping time values for neutron stars of different internal structure

(equation of state) from (75). The pulsation modes are named after Cowling's work in the 1940s (77).

1.7.2.1 Fluid modes

Unlike black holes, it is expected for neutron stars to have modes of oscillation associated to their internal fluid structure. These modes also exist in non-relativistic stars and they would continue forever if there was not a mechanism of dissipation in place. For neutron stars, one of the dissipation mechanisms will be the emission of gravitational radiation that carries energy away. The most important families of fluid modes for gravitational wave emission are the fundamental (f-mode), the pressure (p-mode) and the gravity (g-mode) (78):

- f-modes (fundamental). This is a stable mode which exists only for non-radial oscillations with frequency proportional to the mean density of the star. A typical neutron star has an f-mode of frequency in the range 1.5 – 3 kHz and damping time of less than a second, slowly damped in comparison to *non-fluid* modes, in the range of 0.1 – 0.5 s. f-mode frequencies and corresponding times for neutron stars have been computed and are tabulated in (75; 79). Values published by (79) and (75) are shown in Fig. 1.4, where frequency is plotted versus damping time.

- p-mode (pressure). These are radial or non-radial oscillations where the internal pressure is the restoring force. The oscillation frequency depends on the time for acoustic waves to cross the star. For a neutron star the oscillation frequencies are in the range 4 – 10 kHz (higher than for f-modes) and the damping times last longer, for a few seconds. Fig. 1.5 shows data from (75) where the damping time have been plotted versus oscillation frequency for p-modes.

- g-mode (gravity). This oscillation mode arises due to the gravity trying to smooth out material inhomogeneities. Buoyancy is the restoring force. For a typical neutron star the oscillations frequencies are lower than 100 Hz with very long damping times, up to years long.

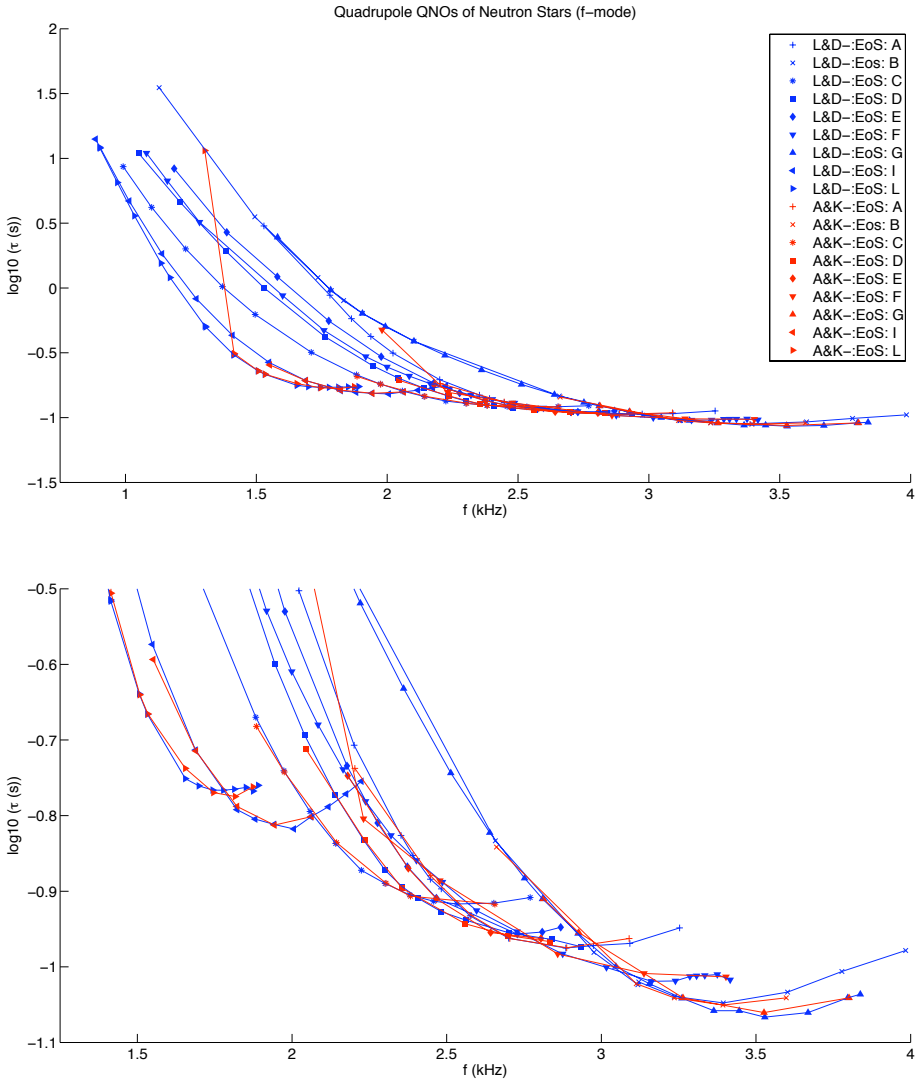

Figure 1.4: Frequency and damping time for f-modes (fundamental) of oscillating neutron stars, computed for various equations of state (EoS) by L&D (79) and A&K (75). The bottom plot is an inset of the upper plot and helps the visualization of closely packed data points in the range $-1 < \log_{10}\tau < -0.5$ s. Although the range of the frequency values is comparable with the oscillations of black holes (c.f. Fig. 1.3) the damping times are about 3 orders of magnitude bigger for neutron stars and have been plotted in seconds here. Only data points corresponding to EoSs common to both papers have been included here. Each data point corresponds to features that characterise the neutron star, like central density, radius and mass. For increasing central density values the oscillation frequency increase too but the damping time is shorter.

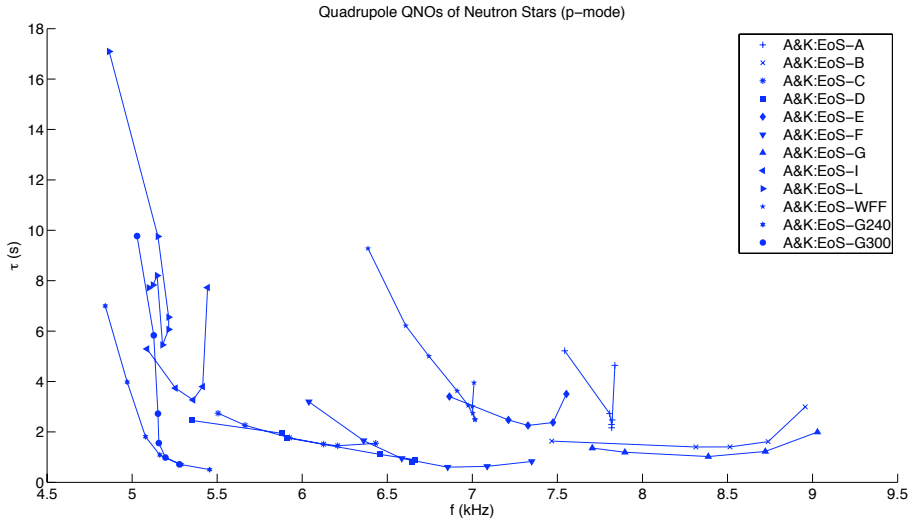

Figure 1.5: Frequency and damping times for p-modes (pressure) of neutron stars, computed for various equations of state (EoS) by A&K (75). The long damping times, in comparison to the f-modes (c.f. Fig. 1.4) and black holes (c.f. Fig. 1.3), make them easier to detect but the higher frequencies presents the disadvantage of shifting the detection region where the laser interferometric detector, limited by the shot-noise, is not the most sensitive.

1.7.2.2 Spacetime or w-modes

These modes do not have Newtonian counterparts for non-relativistic stars; they were first recognised by Kokkotas and Schutz (80). They are called w-modes for being related to the metric of the spacetime rather than to the fluid of the star. The energy is radiated quickly and therefore oscillations are damped more strongly than the fluid oscillations. There are three main families of spacetime modes: *curvature*, *trapped* and *interface*.

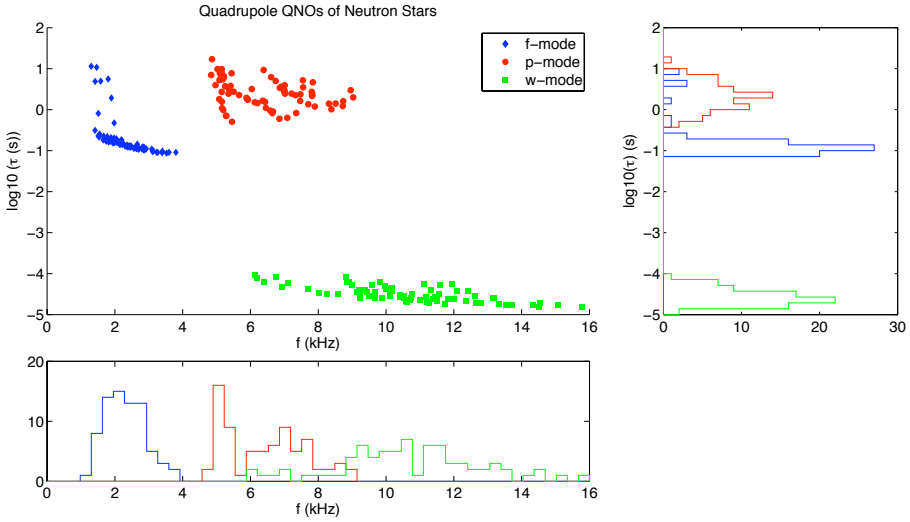

Figure 1.6: f-mode (fundamental), p-mode (pressure) and w-mode (spacetime) frequencies and damping times predicted for $l = 2$ (quadrupole) quasinormal oscillations of neutron stars for 12 different EoSs as published in (75). Note that all values corresponding to a particular mode tend to cluster in a particular region of the $f - \tau$ map. With laser-interferometric gravitational wave detectors with approximate bandwidths in the range of 10 to 10000 Hz we can foresee that the detection of w-modes is severely limited to the most compact neutron stars, which present the lower oscillation frequencies. From the comparison of this plot with Fig. 1.3 we can see that the f and τ values for neutron stars overlay with low-mass black hole's.

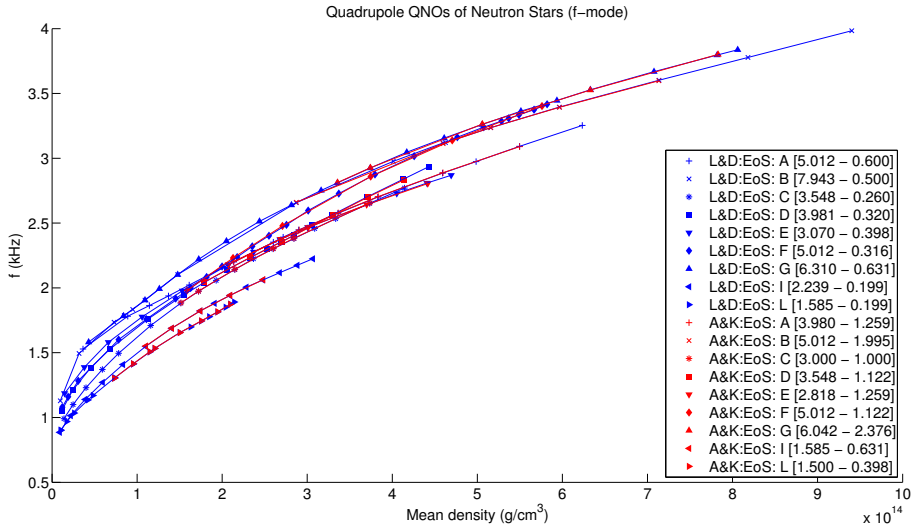

Figure 1.7: Relation between the mean density of the neutron star and the f-mode frequencies as given in (75; 79). Note the quasi-proportional relation between the mean density and the oscillation frequency. This can help constraining the mean density of the neutron star from the detection of gravitational waves produced by the ringing of the compact object. In the legend, between square brackets, the range of central density (in 10^{15}g cm^{-3}) of each EoS is reproduced.

Chapter 2

Detectability of gravitational wave burst signals from galactic neutron stars

For an individual ground-based detector, geographical location and azimuthal orientation of the detector do not matter when looking for burst signals from sources that are isotropically distributed in space. When any incoming direction is equally probable, there is no preferential location or orientation for a detector. This is not the case, however, for burst signals emitted by galactic neutron stars, due to their non-isotropic distribution with respect to the Earth and the detector. In this chapter three spatial models of the galactic populations of neutron stars are described and the detectability of possible burst signals emitted by these sources is assessed for the main ground-based detectors. Detectability is quantified by calculating a) the time and polarisation-averaged antenna pattern values and b) the probability the antenna power value is bigger than a particular threshold. Detectability of detectors working as single antennas or and for networks are studied. Throughout this work neutron stars have been considered as standard candle sources of gravitational wave burst-signals, so the gravitational wave amplitude at source is the same for all of them. This is why in this study, only their relative orientation with respect to the detector and the distance to Earth can affect their detectability.

2.1 Introduction

At the time of writing more approximately 1900 galactic pulsars have been discovered and studied (66). From their sky positions and spatial distribution the total number of galactic neutron stars may be extrapolated. After allowing for unknowns such as a) weak pulsars are seen out to shorter distances than the extent of the galaxy and b) the interstellar medium severely limits the propagation of the radio signals in some directions, an approximate picture of the spatial distribution of galactic neutron stars can be obtained. Despite the unknowns a statistically significant result has emerged from pulsar distribution study and it is believed there are between 10^5 and 10^6 active pulsars in the Galaxy (65; 81). Most pulsars are concentrated close to the galactic plane, within a 1 kpc thick layer and a distance of about 10 kpc from the centre. Measurement of their motions show that they have high velocities, presumably achieved at their violent kicks at birth, causing them to move away from the galactic plane at rates of about 200 km s^{-1}. As many neutron stars as pulsar must exist in the galaxy and the conservative number of 10^5 galactic neutron stars have been considered in the following sections.

2.2 Neutron star population models

In this section three different galactic neutron star (NS) population models are introduced. For each of the populations, the galactic locations of the sources can be sampled from their corresponding statistical spatial distributions, and the distance to the detector and their relative orientation at a particular time instant inferred. All the populations are defined on a orthogonal xyz frame centred on the Earth and where the galactic plane corresponds with the xy plane, and are shown in Fig. 2.1.

The main population considered has the shape of a disc centred in the galactic centre, which is compared with two spherical populations: one is also centred in the galactic centre, the other is centred in the Sun-Earth system. The latter is probably the least realistic of the three and have mainly been used as a reference in the comparisons, for it enhances the effect on the detectability of populations

that are not isotropically distributed around the Earth. The three populations are approximate, simplified models, for in reality we do not have enough observational information as to know the real spatial distribution of NS likely to emit gravitational radiation.

None of the NS populations considered in this work takes into account star density fluctuations across the Galaxy, like the Gould belt [1] or the galactic spiral arms with regions of a higher density of neutron stars.

2.2.1 Population 1: Disc-shaped NS population

This is probably the most realistic distribution considered and comprises 10^5 neutron stars spatially distributed in a disc-shaped galaxy. We will call this population *Disc-shaped* thereon. Based on previous galactic neutron star population models (82; 83) it is defined by the combination of two independent exponential probability distributions of the distance parameters r and z,

$$p(r)dr = \frac{1}{r_0} e^{-r/r_0} dr \quad \text{and} \quad p(z)dz = \frac{1}{2z_0} e^{-|z|/z_0} dz, \tag{2.1}$$

where r is the distance from a source to the galactic centre in the galactic plane, and z is the distance to the galactic plane. To specify a random direction constrained on the plane, a sample of the direction angle ϕ is drawn from the uniform distribution

$$p(\phi)d\phi = \frac{1}{2\pi}, \tag{2.2}$$

so that $x = r\cos\phi$ and $y = r\sin\phi$. This results in a distribution of sources symmetric to the galactic centre and to the galactic plane. The scale factors of the exponential distributions are $r_0 = 3.2$ kpc and $z_0 = 0.075$ kpc [2]. The figure,

[1] The Gould belt is described as a thin disc of radius 300 pc and of thickness 60 pc, tilted at 18° with respect to the galactic plane and centred at 100 pc from the Sun in the galactic anti-centre direction. The Gould belt is characterized by an overabundance of massive stars.

[2] An alternative model, proposed in (84) and (85), is to use a Gaussian probability density function in r,

$$p(r)dr = \frac{1}{\sqrt{2\pi r_0^2}} e^{-\frac{(r-r_c)^2}{2r_0^2}} dr, \quad p(z)dz = \frac{1}{2z_0} e^{-|z|/z_0} dz \tag{2.3}$$

adopted here, of 10^5 neutron stars in total in the Galaxy is rather conservative; it derives from the belief of there existing approximately 10^3 neutron stars exist within a distance of 3 kpc from the Earth. A reference distance of 8.5 kpc from the Sun-Earth to the galactic centre is assumed.

2.2.2 Population 2 & 3: Spherical NS populations

The two spherical distributions are defined statistically by the combination of independent distance and direction parameters. The distance r is, again, exponentially distributed

$$p(r)dr = \frac{1}{r_0} e^{-r/r_0} dr \tag{2.4}$$

and the 3D random direction is given by sampling the spherical angles (θ, ϕ)

$$p(\theta)d\theta = \sin\theta \quad \text{and} \quad p(\phi)d\phi = \frac{1}{2\pi}, \tag{2.5}$$

where θ is the latitudinal and ϕ is the azimuthal angle, so that $x = r\cos\theta\cos\phi$, $y = r\cos\theta\sin\phi$ and $z = r\sin\theta$ [1] The corresponding equatorial coordinates of declination and right ascension (δ,RA) can be thus readily obtained for each source of the population: the x-axis of the cartesian reference frame is defined in the direction from Earth toward the galactic centre, (θ, ϕ) are the same as the galactic coordinates (b, l), and one just needs to carry out the coordinate transformation $(b, l) \rightarrow$ (δ,RA) using spherical trigonometry (see, for example, (86)). Again, 10^5 sources have been considered for each population.

Although spatially identical, one of the two spherical distributions considered is centred on the galactic centre (called *Spherical-GC* thereon) and the other is centred on the Earth-Sun system (called *Spherical-ES* thereon). The latter is not the most realistic distribution but it has been included here for the benefit of the comparison of galactocentric distributions with a geocentric distribution. Fig. 2.1 and Fig. 2.2 show isometric and galactic plane edge-on views of the three NS populations. Note the Earth-Sun system is located at (0,0,0) and marked with a magenta dot.

[1] Randomized sky coordinates (θ, ϕ) can be obtained by using uniform deviates between 0 and 2π for ϕ and uniform deviates between -1 and $+1$ for $\sin\theta$.

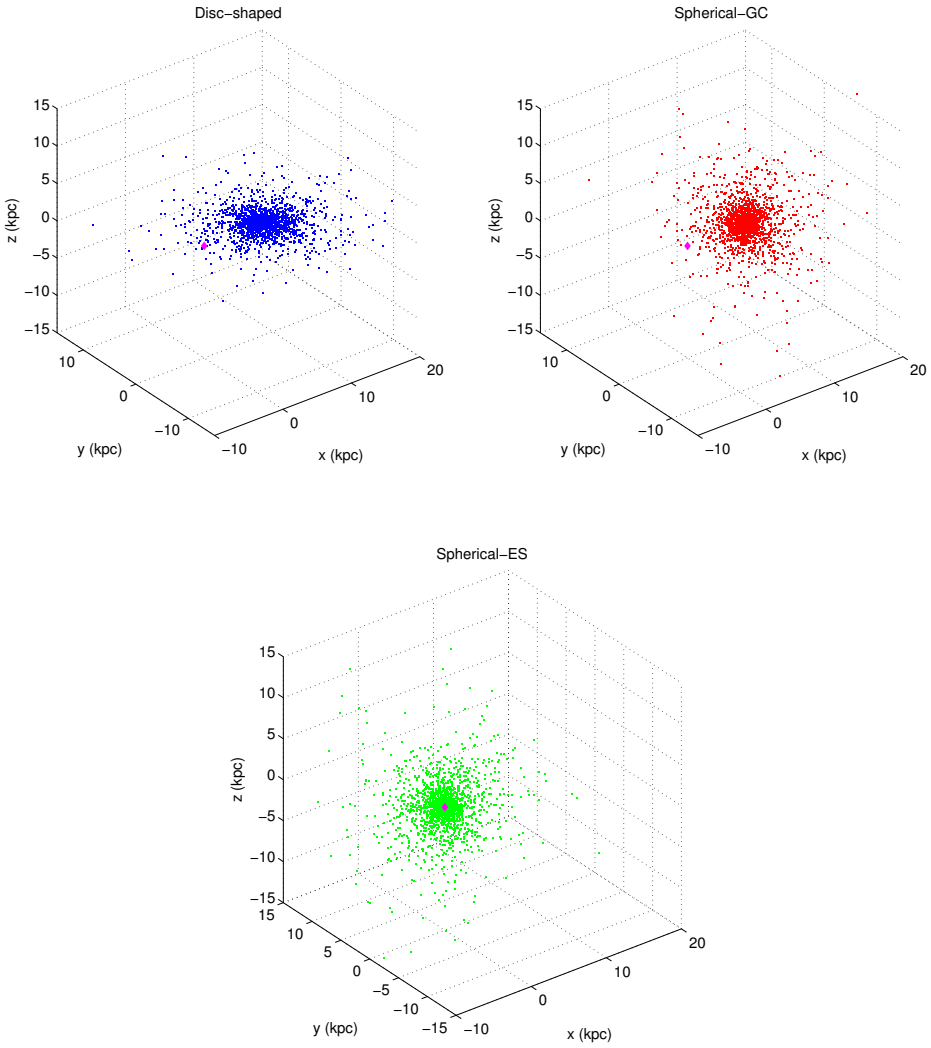

Figure 2.1: Isometric perspectives of the three modeled galactic NS populations. *Upper left*: Disc-shaped population. *Upper right*: Spherical distribution centred on the galactic centre. *Down*: Spherical distribution centred on the Sun-Earth. The magenta dot located at the centre (0,0,0) of the reference frame represents the location of the Earth-Sun. For an edge-on view of these three plots see Fig. 2.2. Note: To avoid cluttering this figure only 1 in 50 of the 10^5 neutron stars have been randomly chosen and plotted.

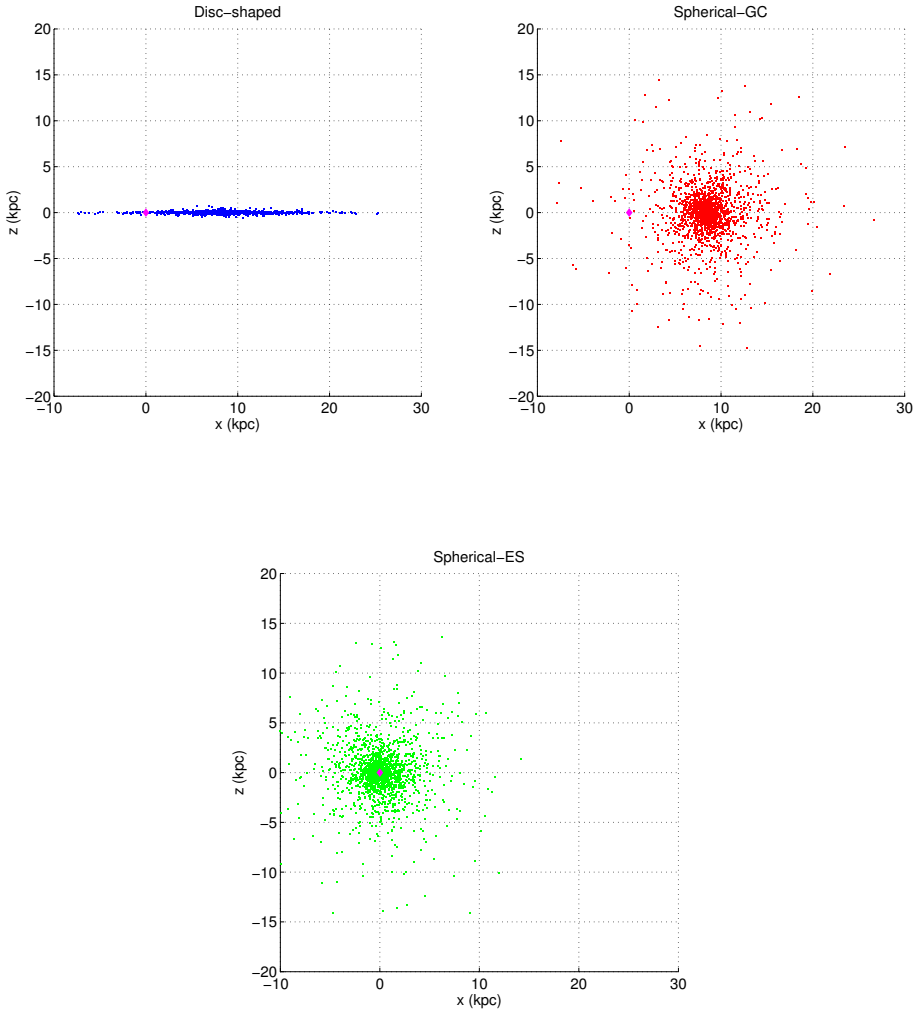

Figure 2.2: Edge-on views of the NS populations shown in Fig.2.1.

Fig. 2.3 shows the normalised histograms of r and z values for the three populations of 10^5 sources described. The plot on the right gives an idea of the thickness of the population. The spherical distributions enforce the position of sources to be further away from the galactic plane than the disc-shaped population (see Fig. 2.2), which encloses all the sources within a 3 kpc thick layer. The plots in this figure do not provide any information on where the populations are centred.

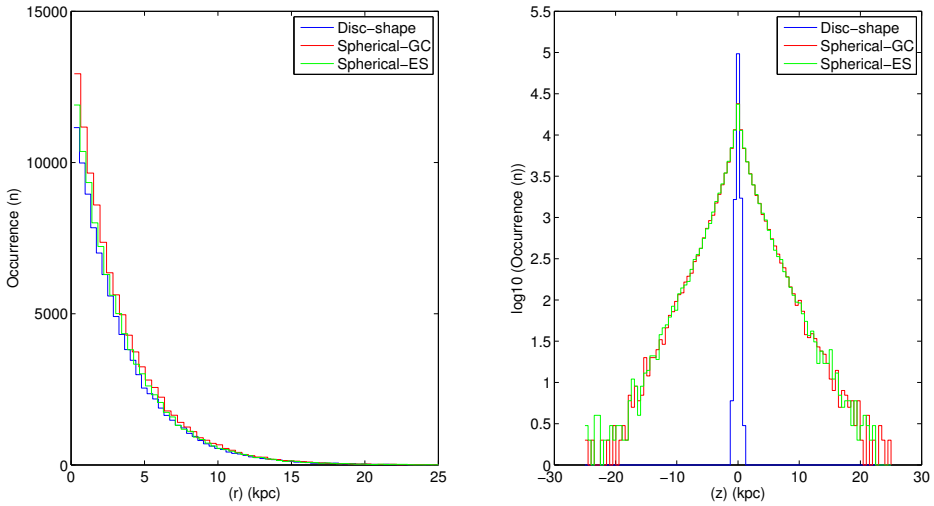

Figure 2.3: Histograms of r and z values of the 10^5 sources from the three NS populations considered and depicted in Fig. 2.1. *Left*: Each curve corresponds to an exponential distribution of r distance values. *Right*: Histogram of the distance z from the sources to the galactic plane.

Fig. 2.4 shows the distribution of distances to the sources from the Earth. For the two populations centred in the galactic centre the distribution peaks approximately at 8.5 kpc, where the density of source is highest; the population centred on the Earth peaks at $r = 0$, as expected. The distribution of the spherical population centred in the galactic centre is slightly narrower than the disc-shaped population due to the smaller scatter of the sources with respect to the galactic plane.

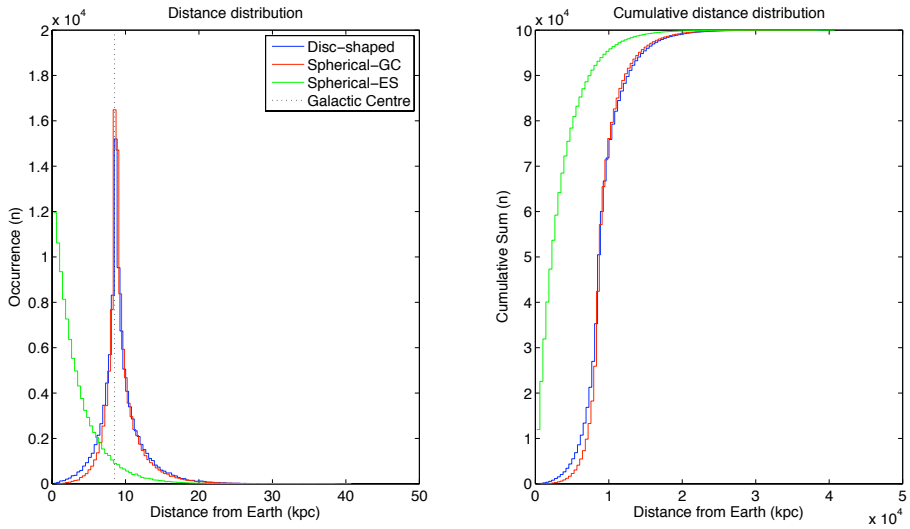

Figure 2.4: Histograms of the distances from Earth to the 10^5 neutron stars of the populations considered. *Left*: Distance distributions for the two populations centred in the galactic centre are similar and peak around their centres at 8.5 kpc (marked by a dotted vertical line). *Right*: Cumulative sum of the histograms given on the left.

Fig. 2.5 shows the distribution in declination and right ascension (δ,RA) of the sources of the three NS populations. As expected, the two populations centred in the galactic centre peak around the declination and right ascension of the galactic centre [δ_{GC} = -29° 00' 28" and RA_{GC} = 17h 45m 40s (J2000 epoch)] ≡ [-0.506, 4.649] rad. The spherical population centred on the Earth shows a uniform distribution in RA and $\sin\delta$, as expected for sources at random directions.

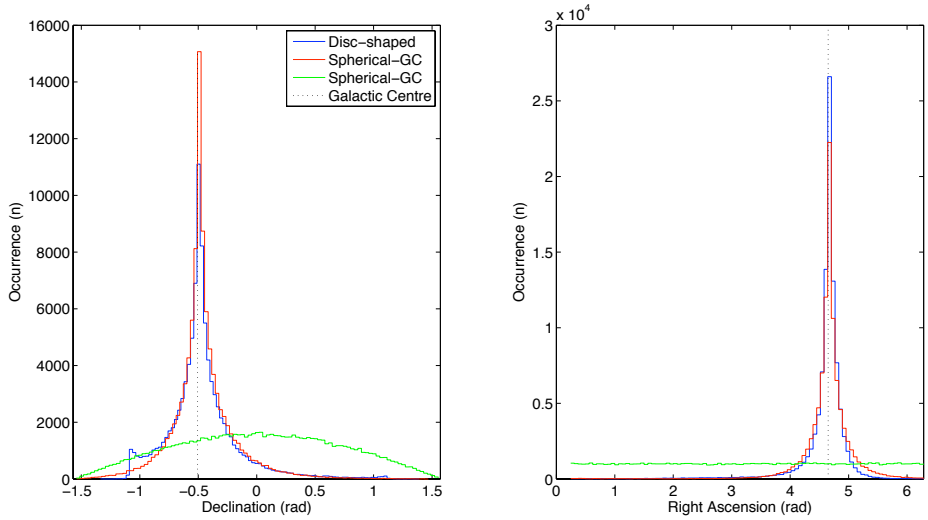

Figure 2.5: Distribution of the declination and right ascension (δ,RA) values for the 10^5 neutron stars of the populations considered. In a similar fashion to the distribution of distances (c.f. Fig. 2.4) both distributions centred at the galactic centre peak approximately at the declination and right ascension of the galactic centre (δ_{GC}, RA_{GC}), marked with dotted vertical lines.

2.3 Antenna patterns of laser interferometric gravitational wave detectors

The detection of gravitational burst signals is mainly conditioned by two factors: a) the orientation of the detector at the precise moment of the burst, and b) the distance to the emitting source. Table 2.1 lists the location/orientation/shape data of the detectors considered in this work, as published in (87; 88). The

detector named PERTH is fictional and it has been included for convenience to have at least one detector located in the southern geographical hemisphere; it has been located in Perth (Australia) and oriented as '×' with respect to the geographical compass directions. For a recent study of the possibilities of extending the LIGO network to Australia (89).

DETECTOR		**Location**		**Orientation**	**Shape**
No.	**Name**	**Lat.** (β)	**Long.** (γ)	(α)	(2Ω)
1	GEO600	52.3°	-9.8°	158.8°	94.3°
2	LIGO-H	46.5°	119.4°	261.8°	90°
3	LIGO-L	30.6°	90.8°	333.0°	90°
4	VIRGO	43.6°	-10.5°	206.5°	90°
5	TAMA300	35.7°	-139.5°	315.0°	90°
6	PERTH*	-31.9°	116.0°	0°	90°
East longitudes γ are negative here.					
α is measured ccw from the local meridian (N-S line) to the bisector of the arms.					
2Ω is the angle subtended between the arms of the detector.					
* A new detector is aimed to be built in the southern hemisphere, near Perth.					

Table 2.1: List of the geographical location, orientation and shape of the main laser gravitational wave detectors considered in this work. PERTH detector is fictitious and it has been added for the benefit of including at least one detector located in the southern hemisphere.

Typically, the directional sensitivity of a detector is represented by the *antenna pattern functions* F_+ and $F_\times$ ($-1 \leq [F_+, F_\times] \leq 1$), which indicate the factors of the amplitude of the gravitational wave polarisation components that will be seen by the detector. In general, for a source toward a direction given by the spherical coordinates (θ, ϕ) in the local reference frame of the detector [1], the antenna patterns can be calculated as:

[1] $\theta \in [0, \pi]$ is measured from the vertical of the plane of the detector and $\phi \in [0, 2\pi)$ from the first to second arm of the detector.

$$F_+(\theta,\phi,\psi) = \frac{1}{2}\sin 2\Omega\left[(1+\cos^2\theta)\cos 2\phi\cos 2\psi - \cos\theta\sin 2\phi\sin 2\psi\right] \quad (2.6a)$$

$$F_\times(\theta,\phi,\psi) = \frac{1}{2}\sin\Omega\left[(1+\cos^2\theta)\cos 2\phi\sin 2\psi + \cos\theta\sin 2\phi\cos 2\psi\right] \quad (2.6b)$$

where ψ is the polarisation angle, and 2Ω is the angle subtended by the arms of the detector ($2\Omega = \pi/2$ rad for L-shape detectors). Fig. 9.2–9.9 in (90) provide a good pictorial representation of the angles (θ,ϕ,ψ). For a detailed explanation of the antenna patterns and the derivation of their probability density functions see Appendix A.

To quantify the sensitivity in a particular direction it is convenient to define an averaged antenna pattern value $\bar{F}$, independent of the polarisation angle ψ:

$$\bar{F} = \sin(2\Omega)\sqrt{1/2(F_+^2 + F_\times^2)} \quad (2.7a)$$

$$= \frac{1}{2}\sin(2\Omega)\left[(1+\cos^2\theta)^2\cos^2(2\phi) + \cos^2\theta\sin^2(2\phi)\right]^{1/2}. \quad (2.7b)$$

Note that $\bar{F}$ weights equally both polarisation components ($+$ and $\times$) and thus represents the averaged antenna pattern function for the case of circularly polarised signals. Fig. 2.6 shows a sky-map sensitivity by plotting $\bar{F}$ values as function of the spherical angles (θ,ϕ) measured in the local frame of the detector. The detector has maximum sensitivity at directions normal to the plane of the detector ($\theta = 0,\pi$) and minimum sensitivity at directions edge-on to that plane ($\theta = \pi/2$), where the detector is blind at directions parallel and perpendicular to the bisector of the arms ($\phi = n\pi/4$ for odd n).

Under the assumption of equal probability for any incoming direction of the signal, $\bar{F}$ values in Fig. 2.6 can be histogrammed to infer their distribution. Note that the contour-plot of $\bar{F}$ is the result of calculating F_+ and $F_\times$ on a grid in which any cell corresponds to an equal spherical angle in the sky ($\cos\theta \sim \mathcal{U}[-1,1]$ and $\phi \sim \mathcal{U}[0,2\pi)$). The histogrammed values are shown in Fig. 2.7.

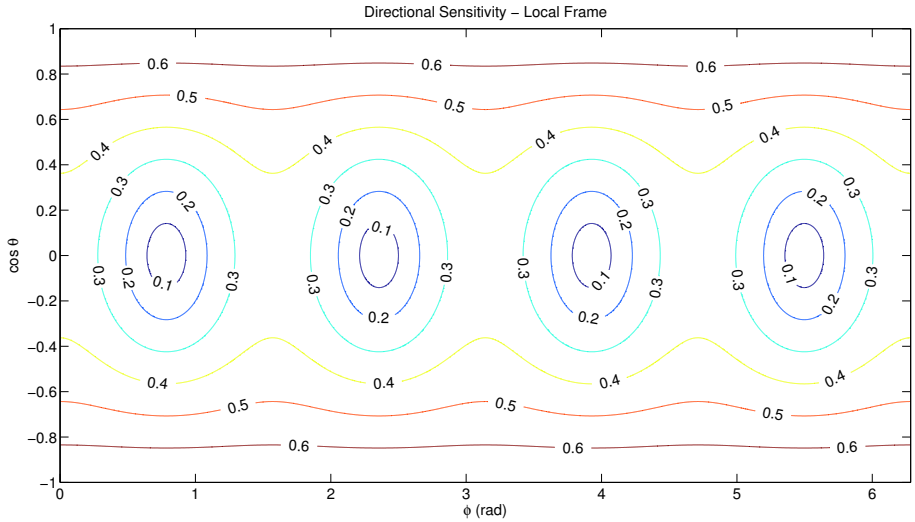

Figure 2.6: Directional sensitivity sky-map ($\bar{F}$ contour-levels) of an L-shaped detector, computed with Eq. 2.7. The directions are defined with the spherical angles (θ, ϕ) in the local frame of the detector.

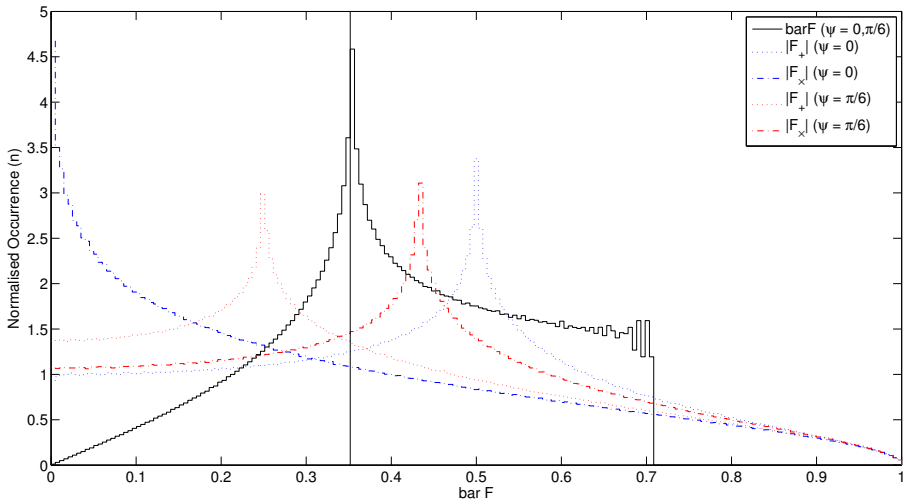

Figure 2.7: Normalised histogram of $\bar{F}$ values from the sky-map in Fig. 2.6 with the underlaying assumption that any direction for the source is equally probable. The values for $\bar{F}$ drop abruptly at $\sqrt{2}/2$ (the maximum value for an L-shaped detector); the most probable value is 0.352 (marked with a vertical line). In the background, histograms of $|F_+|$ and $|F_\times|$ values for two arbitrary polarisation angles ψ are shown, for comparison. $\bar{F}$, however, is independent of the polarisation angle ψ.

Given our belief that a gravitational burst from a neutron star can occur at any time, neither the location nor the orientation of the detectors matter when the spatial distribution of the sources is isotropic. In reality, however, the fact that most neutron stars are concentrated around the galactic centre and, for the case of the disc-shaped population, within a narrow strip parallel to the galactic plane makes the location/orientation of some detectors more suitable than others for detecting signals from these populations.

2.3.1 Strain and polarisation degree of the gravitational wave signal

The strain produced on the detector by the gravitational wave depends on the amplitude of the signal and the attenuation of the antenna pattern function at the time of the burst-signal. The strain generated can be expressed as a complex number in the form:

$$\frac{\delta l}{l_0} = -\sin 2\Omega \left[F_+ h_+ + F_\times h_\times \exp(i\delta)\right] \tag{2.8}$$

where δ reflects the phase difference between the + and $\times$ components and hence the degree of polarisation (i.e. linear, elliptical or circular). In general, for an elliptically polarised wave it is always possible to choose the orientation of the polarisation axes so that they coincide with the axes of the polarisation ellipse (91),

$$\delta = \pm\,\pi/2 \quad \text{and} \quad h_\times = \lambda h_+ \tag{2.9}$$

where λ is the *degree of elliptical polarisation* and takes values in the range [0,1]. Similarly to polarised electromagnetic signals the $\pm$ sign allows for right- or left-hand polarisation. Throughout this work, detectability for four degrees of polarisation of the gravitational burst-signals have been assessed:

- $\lambda = 1$ Circularly polarised (h_+ and $h_\times$ are equal).
- $\lambda = 0$ Linearly polarised ($h_+ > 0$ and $h_\times = 0$, or $h_+ = 0$ and $h_\times > 0$).
- $\lambda \sim \mathcal{U}[0,1]$ Random degree of polarization, sampled from uniformly distributed elliptical polarisation.

- $\lambda = f(\iota)$ Random degree of polarization, function of ι, the angle subtended between the angular momentum of the source (pointing anywhere with the same probability) and the line of sight from the detector, see (90):

$$\cos\iota \sim \mathcal{U}[-1,1], \quad \text{and} \quad \lambda = f(\iota) = \frac{2\cos\iota}{1+\cos^2\iota} \tag{2.10}$$

See Appendix B for more details and the probability distribution of λ, derived from the distribution of ι.

2.3.2 Strain and antenna pattern functions

The *antenna pattern* of a detector, η, is the relative displacement of the test masses compared to that achieved if the orientation and polarisation of the radiation were ideal (i.e. wave propagating perpendicularly to the plane of the detector and polarised parallel to its arms):

$$\eta = \frac{1}{h}\frac{\delta l}{l_0}, \tag{2.11}$$

and, hence, $\eta_{max} = 1$, when $\delta l/l_0 = h$.

2.3.2.1 Strain calculation on the local frame of the detector

The general expression of the strain induced by the wave can be derived for the local frame of the detector. An elegant derivation of this equation from first principles is given in (91):

$$\begin{aligned}
\frac{\delta l}{l_0} &= -\sin 2\Omega\,[F_+ h_+ + F_\times h_\times \exp(i\delta)] && \text{(2.12a)}\\
&= -\sin 2\Omega\,[A(\phi,\theta,\psi)h_+ + A(\phi,\theta,\psi+\pi/4)h_\times \exp(i\delta)] && \text{(2.12b)}\\
&= -\sin 2\Omega\,[(a_{11}a_{21} - a_{12}a_{22})h_+ + (a_{11}a_{22} + a_{12}a_{21})h_\times \exp(i\delta)] && \text{(2.12c)}
\end{aligned}$$

where a_{ij} are the elements of the rotation matrix $\mathbf{A}$ of Eulerian angles (θ,ϕ,ψ) between the wave-frame and the detector-frame. Here, again, the pair of spherical angles (θ,ϕ) point toward the direction of the source, and ψ is the polarisation

angle of the signal. Appendix D shows a detailed derivation of the rotation matrix **A**. Using Eq. 2.9, Eq. 2.12 can be written in a compact form as:

$$\eta = \frac{1}{h}\frac{\delta l}{l_0} = -\sin 2\Omega \left[A \pm i\lambda \bar{A}\right], \tag{2.13}$$

where A and $\bar{A}$ are functions valued at polarisation angles ψ shifted by $\pi/4$ rad. The antenna pattern η is by definition a complex number. $|\eta|/\sqrt{2}$ and $\bar{F}$ in Eq. 2.7 are equivalent for circularly polarised signals ($\lambda = 1$) and $\sin 2\Omega = 1$.

For linearly polarised signals (see Fig. 2.8) the contour lines for $\eta = F_+$ correspond well with contour lines for $\eta = F_\times$, in the sense that $F_\times(\theta, \phi, \psi) = F_+(\theta, \phi, \psi + \pi/4)$. The absolute value of the antenna pattern, $|\eta|$, is maximum for directions $\theta = 0, \pi$ and $\phi = \pi/4, 3\pi/4$, corresponding to a wave incident normal to the plane of the detector and with the same polarization as the detector (note that ϕ is here measured from the bisector of the two arms, see Appendix D). $|\eta|$ is null for any θ and $\phi = \pi/4, 3\pi/4$, which is when the vibration direction of the wave is in the bisector of the arms and its perpendicular direction.

For circularly polarised signals (see Fig. 2.9), again, the maximum values of $|\eta|$ are for directions normal to the plane of the detector at $\theta = 0, \pi$ and $\phi = 0, \pi/2$. Minimum sensitivity (blind spots) are at $\theta = \pi/2$ and $\phi = 0, \pi/2$. Elliptically polarised signals ($\lambda = 0.5$) have higher values of $|\eta|$ for $\theta = 0, \pi$ but are not uniform across ϕ either.

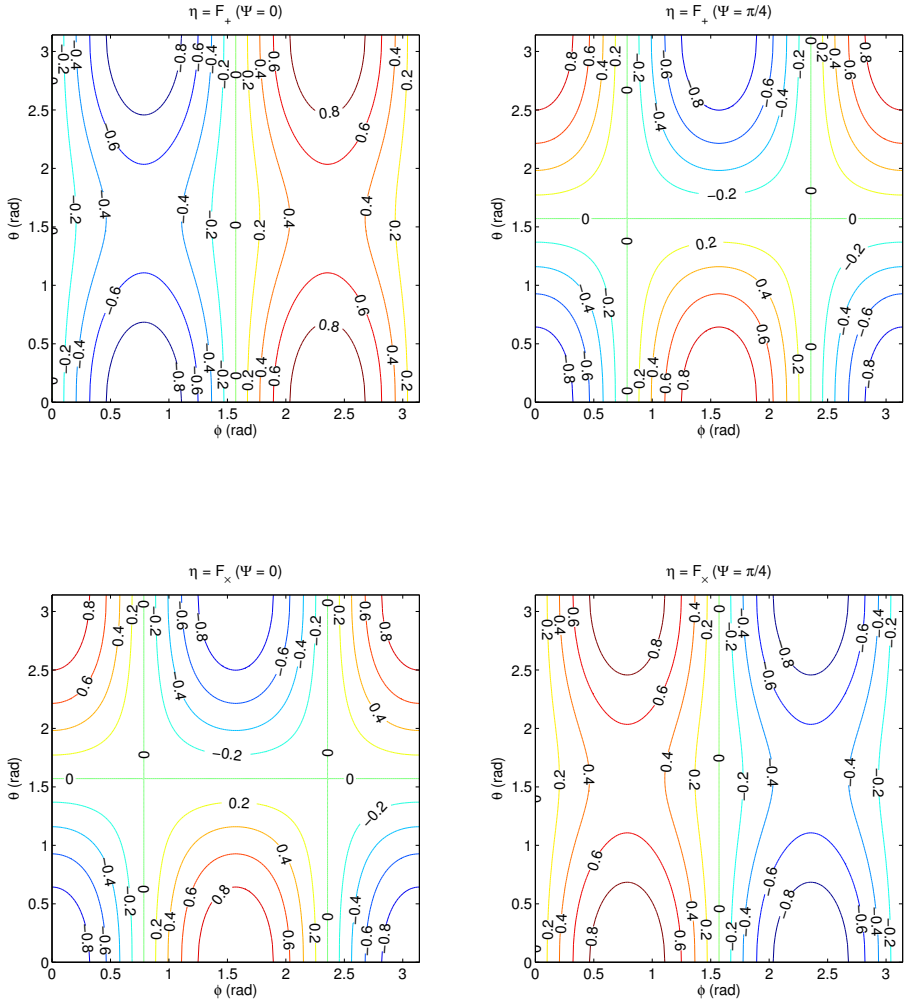

Figure 2.8: Contour map of the antenna pattern $\eta = F_+$, and alternative $\eta = F_\times$, for linearly polarised gravitational waves ($\lambda = 0$). F_+ and $F_\times$ for $\psi = 0$ and for $\psi = \pi/4$ are plotted side by side to show that they are equivalent. Note: The two subplots on the left differ in sign from Fig. 4 and Fig. 5 on (91), to compensate for the believed-to-be forgotten minus sign at deriving Eq. 2.15 from Eq. 2.14. (c.f. Eq. 2.12).

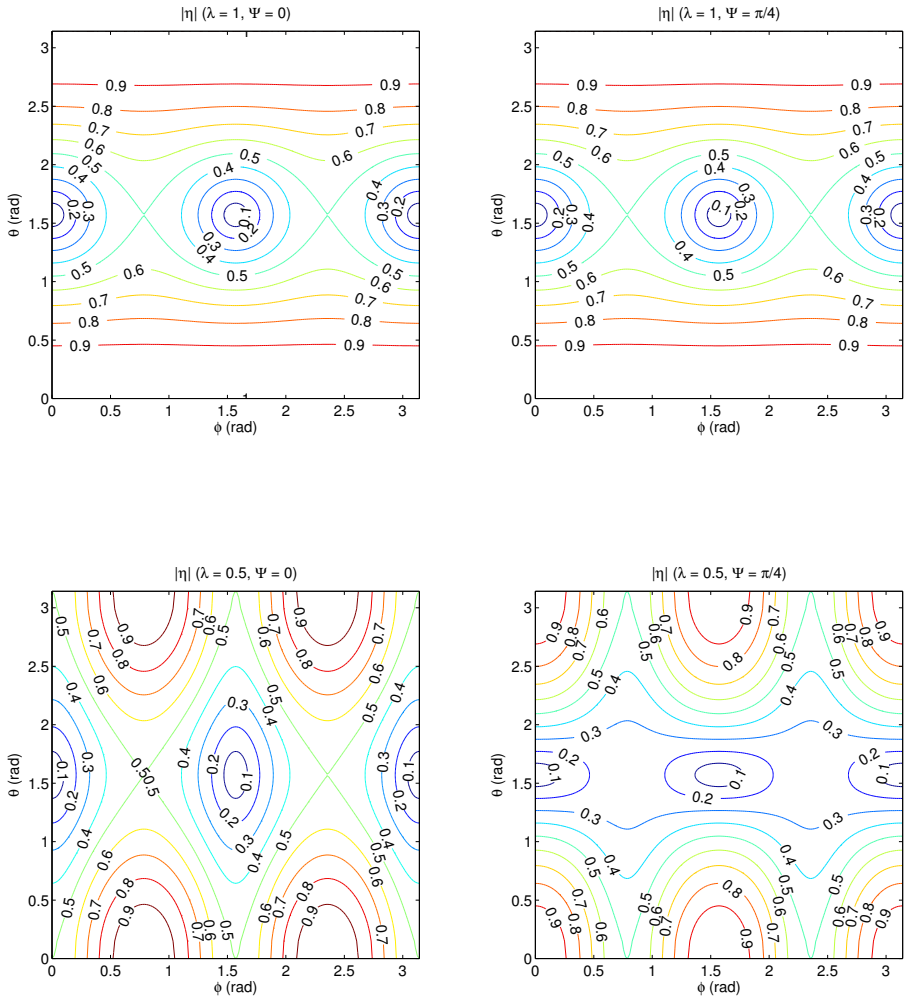

Figure 2.9: Contour map of the absolute value of the antenna pattern $|\eta|$ for non-linearly polarised gravitational waves. The two upper subplots show results for circularly polarised signals ($\lambda = 1$), whereas the lower subplots show elliptically polarised signals for an arbitrary value of $\lambda = 0.5$. As expected, the two upper subplots are the same, for the polarisation angle does not matter when considering circularly polarised signals. Note: The two upper subplots correspond well with Fig.6 on (91).

2.3.2.2 Strain calculation on a generic detector frame

The calculation of the antenna patterns for a detector of generic location/orientation to a source with sky-position given in equatorial coordinates (δ,RA) is not straight forward with the Eqs. 2.12; Schutz and Tinto (91) devised a systematic way of computing the antenna pattern η for generic cases:

$$\frac{\delta l}{l_0} = -\sin 2\Omega \left[F_+ h_+ + F_\times h_\times \exp(i\delta)\right] \tag{2.14a}$$

$$= -\sin 2\Omega \left[C([\alpha,\beta,\gamma],[\phi,\theta,\psi])h_+ + C([\alpha,\beta,\gamma],[\phi,\theta,\psi+\pi/4])h_\times \exp(i\delta)\right] \tag{2.14b}$$

$$= -\sin 2\Omega \left[(c_{11}c_{21} - c_{12}c_{22})h_+ + (c_{11}c_{22} + c_{12}c_{21})h_\times \exp(i\delta)\right] \tag{2.14c}$$

where c_{ij} are elements of the matrix $\mathbf{C}$ that combines two successive Eulerian rotations $\mathbf{A}$ and $\mathbf{B}$ of the reference frame where the signal is originally defined. For a detailed derivation of the generic expression in Eq. 2.14 see (91).

The first rotation matrix $\mathbf{A}(\theta,\phi,\psi)$ transforms the signal amplitude to an intermediate reference frame rotating fixed to the Earth (θ,ϕ and ψ are not the same angles as in Section 2.3.2.1); and the second rotation matrix $\mathbf{B}(\alpha,\beta,\gamma)$ transforms the intermediate coordinates into the detector's frame. The combined matrix $\mathbf{C} = \mathbf{BA}$ is a 3×3 matrix that allows for any generic transformation from the wave frame to the detector frame. In the following we define the Eulerian angles involved in rotations $\mathbf{A}$ and $\mathbf{B}$:

- α Angle between the bisector of arms and local meridian (N-S line).
- β Latitude of detector's location.
- γ Longitude of detector's location.
- θ 'Co-declination' of the source direction: $\theta = \pi/2 + \delta$, so that $\theta \in [0,\pi]$.
- ϕ Hour-angle of the source from Greenwich, GHA = GLST - RA (GLST is the local sidereal time at Greenwich and RA is the right ascension of the source).
- ψ Polarisation angle (see Fig.9.9 on (90)).

- 2Ω Angle subtended between arms.

For more information about the rotation matrices **A** and **B** and explanatory figures depicting the frame rotations see Appendix D. Similarly to Eq. 2.12, Eq. 2.14 can be written in a compact form using Eq. 2.9 to obtain the generic expression of the antenna pattern:

$$\eta = \frac{1}{h}\frac{\delta l}{l_0} = -\sin 2\Omega \left[C \pm i\lambda \bar{C}\right] \equiv \eta_{DN} \tag{2.15}$$

where, again, C and $\bar{C}$ are functions valued at polarisation angles ψ shifted by $\pi/4$ rad. The addition of the subindex DN (for *Distance No*) is to differentiate the standard antenna pattern from the antenna pattern in which the distance to the source will be included η_{DY} (*Distance Yes*).

Due to the complex-valued nature of η it is convenient to define the *antenna power* $X = |\eta|^2$,

$$X = \sin^2 2\Omega \left[C^2 + \lambda^2 \bar{C}^2\right], \tag{2.16}$$

and the averaged antenna power (rms value) $\langle X\rangle^{1/2}$. Considering the periodicity properties of C and $\bar{C}$ the rms of Eq. 2.16 can be expressed as:

$$\langle X\rangle^{1/2} = (1+\lambda^2)^{1/2}\langle C^2\rangle^{1/2}. \tag{2.17}$$

And this, computed over a large number of trials for multiple source positions, burst-times and polarisation angles, provides a measure to the detectability of a particular detector.

So far, only the location and orientation of the detector at the time of the burst have been considered. However, and especially under the assumption of all sources being standard candles of gravitational radiation, the additional consideration of the distance from the source to the detector is important, because the strain seen by the detector is inversely proportional to the distance to the source. See Fig. 2.4 for the distance distribution of the populations of NS described. To account for the distance to the source, a distance factor referenced in the fiducial distance D_0 has been added to the computation of the antenna pattern:

$$\eta_{DY} = \frac{D_0}{D}\eta_{DN} = -\sin 2\Omega \frac{D_0}{D}\left[C \pm i\lambda \bar{C}\right]. \tag{2.18}$$

We can readily see that for a source located at the galactic centre: $D = D_0 \rightarrow \eta_{DN} = \eta_{DY}$. Since the antenna pattern is modulated by the distance factor D_0/D, there are instances, especially for the population centred on the Earth, where $\eta_{DY} > 1$ [1]. This is the reason why the histograms of the antenna pattern values presented in the following sections have been calculated and compared in the range $|\eta| \in [0, 1]$.

2.3.2.3 Directional sensitivity sky-maps

Directional sensitivity of an antenna in its local frame is shown as a contour-map of $\bar{F}$ values in Fig. 2.6 with the underlying assumption of considering circularly polarised signals (see Eq. 2.7). A more generic polarisation-degree dependent antenna pattern can be defined as:

$$|\eta|_\lambda = \sin 2\Omega \sqrt{(C^2 + \lambda^2 \bar{C}^2)/2}. \tag{2.19}$$

Fig. 2.10 depicts the directional sensitivity map $\bar{F} = |\eta|_{\lambda=1}$ for the detectors VIRGO and PERTH. Each detector presents maximum sensitivity for a particular declination, which depends on the latitude of the detector, and a particular sidereal time, which depends on the detector's longitude.

Fig. 2.11 show the time-averaged absolute values of the antenna factor $\bar{F} = |\eta|_{\lambda=1}$ and reflects how well a detector can see sources at a particular declination.

[1] Being faithful to the theoretical definition of the antenna power, η, this is counter-intuitive but can help understanding the effect of including the distance to each of the sources in the population.

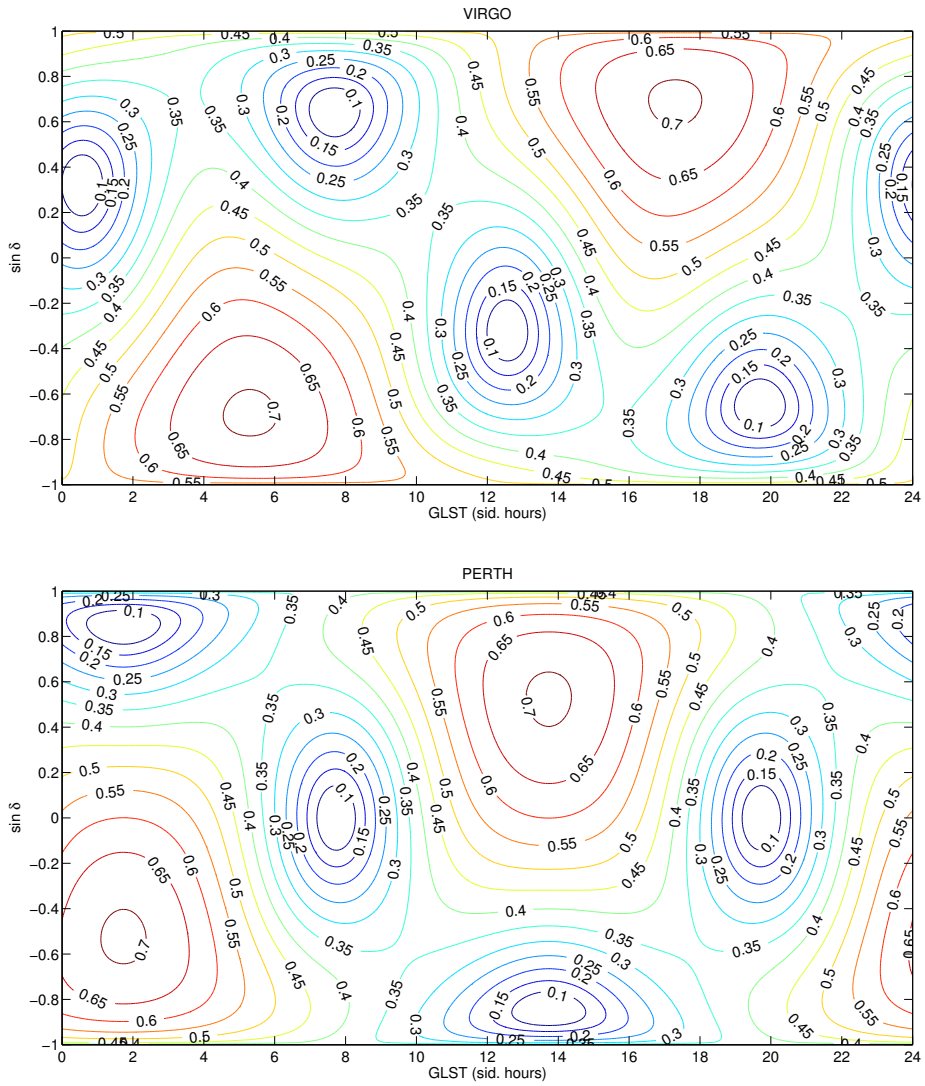

Figure 2.10: Sensitivity sky-maps for detectors VIRGO and PERTH depicted by the contour levels of $\bar{F} = |\eta|_{\lambda=1}$ computed with Eq. 2.19 (c.f. (88)). Note that the directional sensitivity is the same for two sources at symmetric locations with respect to the celestial equator, at 12 sidereal hours apart. The time-averaged values or the generic sensitivity to a particular declination can be obtained by averaging horizontally the values of these contour-maps, see Fig. 2.11.

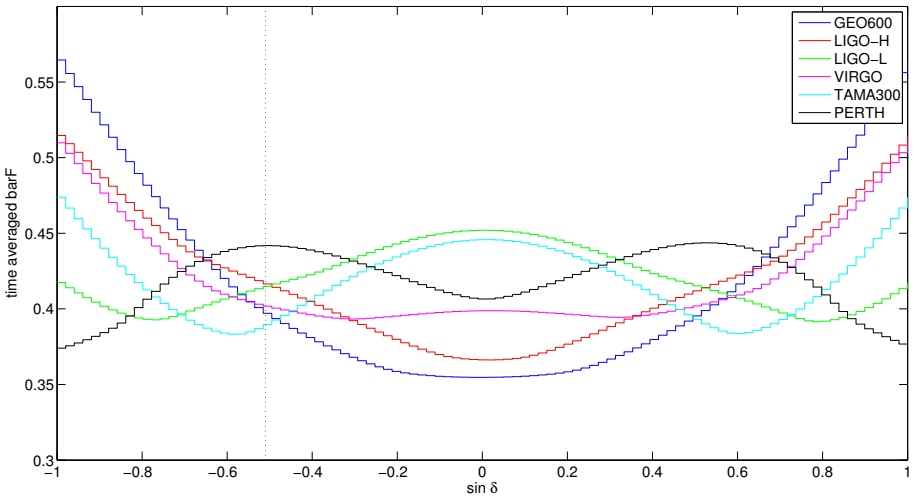

Figure 2.11: Time-averaged antenna pattern values $\langle|\eta|_{\lambda=1}\rangle$ for the detectors listed in Table 2.1. The vertical dotted line marks the declination for the Galactic Centre, which approximately coincides with one of the maxima of the curve for the PERTH detector (c.f. Fig. 2 in (88)).

2.4 Detectability study for the NS populations - location and orientation

The study of the detectability of burst gravitational wave signals from galactic NS sources has been divided in two sections. This first section is a study of the best geographical location and orientation for a L-shaped Michelson type laser interferometric gravitational wave. The detectability of burst signals of various polarization degrees, incoming from a particular sky direction have been studied first, and from neutron stars of the populations described in Section 2.2 later. Effect of the location (geographical latitude) and orientation (azimuthal angle with respect to the compass directions) have been studied by computing time- and polarization angle averaged antenna power values.

2.4.1 Detector's location and orientation for signals from a particular sky direction

Two particular sky directions are studied in this section: toward the Virgo cluster and toward the Galactic centre. The time-averaged antenna pattern values can be obtained by considering sources at random hour-angle values sampling from $(\phi - \gamma) \sim \mathcal{U}[0, 2\pi)$. The random polarization angles are obtained by sampling from $\psi \sim \mathcal{U}[0, 2\pi)$. Fig. 2.12 and Fig. 2.13 show the rms antenna power values $\langle X \rangle^{1/2}$ as a function of the location (geographical latitude β) and orientation (azimuthal rotation α, measured ccw from the local meridian) of a ground-based L-shape detector observing at the direction of the Virgo cluster ($\theta = \pi/2 + \delta \approx 102°$) and at the Galactic centre ($\theta \approx 61°$). The plots are the averaged results of 10^4 samples for each (β, α) cell considered on a $180° \times 180°$ grid map.

Fig. 2.12 corresponds to the Virgo direction and matches Fig. 8 in (91). Each subplot represents results for signals of a different polarisation degree λ. The contour-levels are symmetric to the equator ($\beta = 0$): two detectors with the same orientation α at opposite latitudes β and -β, present symmetrical positions with respect to a fixed sky-direction at two instants 12 sidereal hours apart. Regardless of the polarisation degree of the signal, a latitude change has a bigger effect than the orientation change, and for the higher latitudes ($|\beta| > 45°$) the orientation

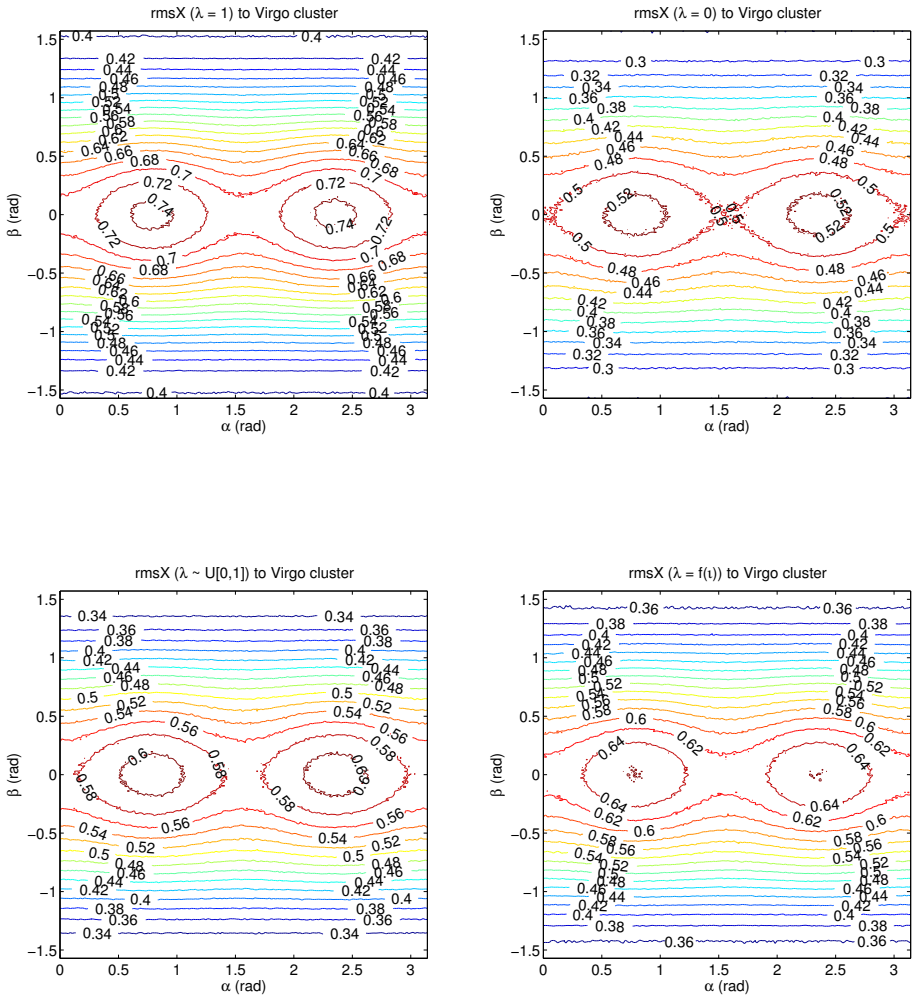

Figure 2.12: Side by side comparison of the rms antenna power $\langle X \rangle^{1/2}$ for signals of different degrees of polarisation λ coming from the Virgo cluster.

does not matter. The maximum detectability, given by the highest rms antenna power, is for a detector located in the equator and oriented at $\alpha = \pi/4, 3\pi/4$ – this is when the arms of the detector are aligned with the N-S and E-W compass directions (geographical '+'). As expected from Eq. 2.17 the smallest values of $\langle X \rangle^{1/2}$ are for linearly polarised signals ($\lambda = 0$), and the biggest for circularly polarised signals ($\lambda = 1$).

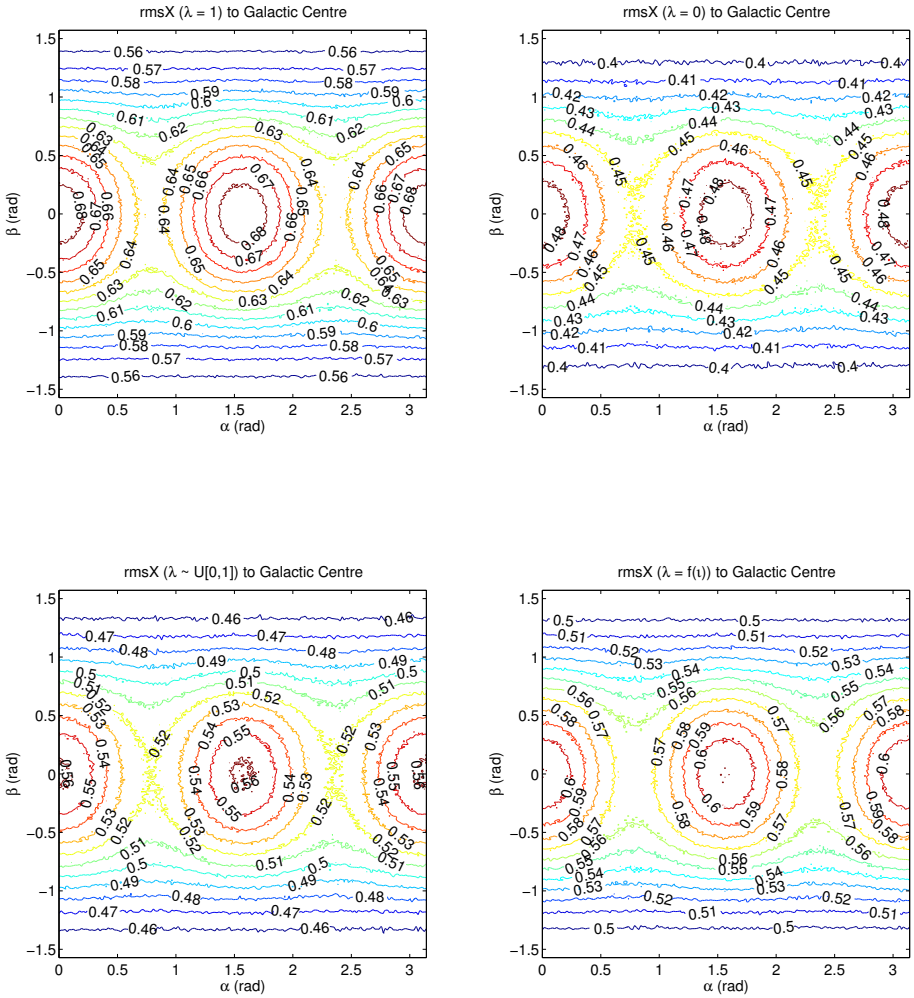

Figure 2.13: Same as Fig. 2.12 but for signals incoming from the Galactic centre.

The maximum sensitivity toward the galactic centre, depicted in Fig. 2.13, is

again for detectors located in the equator. There is, however, a notable and interesting difference with respect to the results for the signals coming from the Virgo cluster (c.f. Fig. 2.12): the ideal azimuthal orientations are for $\alpha = 0, \pi/2$ (geographical '$\times$'), and the orientation of the detector does not affect the detectability for locations at higher values of latitude ($|\beta| > 60°$). Also, the maximum differences between the antenna power values in the equator and the poles are smaller (less contrast in the contour map): a reduction of 18% for the galactic centre versus a reduction of 46% for the Virgo cluster. This shows that the latitude and orientation changes are not so drastic for the detection of sources towards the galactic centre as for toward the Virgo cluster.

2.4.2 Detector location and orientation to NS populations

The computation of time- and polarisation-averaged antenna power values $\langle X \rangle^{1/2}$ for sources scattered non-isotropically around the detector, as is the case for the *Disc-shaped* and *Spherical-GC* NS populations defined in section 2.2, is more complicated and computationally more intense than just looking at a particular direction, as it was done in Section 2.4.1.

For these populations, to average results in time, random hour-angle values for the sources cannot be sampled from a uniform distribution – this is because at each particular instant sources are clustered preferentially in certain sky region: the hour-angle of each source was computed at short intervals of time for a whole rotation of the Earth (24 sidereal hours).

Each calculation of the antenna pattern η was carried out for a particular source, time instant, polarisation angle and polarisation degree. As before, a random polarisation angle was drawn for each source by sampling from $\psi \sim \mathcal{U}[0, 2\pi)$. For each particular instant and for a source i of a particular population, $\theta_i = \pi/2 + \delta_i$, and the hour-angle from Greenwich is $\mathrm{GHA}_i = \mathrm{GLST} - \mathrm{RA}_i = \phi_i$.

For accurate time-averaged results, the consideration of the smallest time interval possible is desired; also, a statistically significant number of sources and a finely meshed (α, β) grid map. However, and given constraints in the computation power, the results shown in the following correspond to a scaled-down simulation

for time intervals of 60 minutes, populations of 10^4 sources and a grid map of $(\alpha \times \beta) = 3^\circ \times 3^\circ$.

Fig. 2.14 and Fig. 2.15 depict the contour-plots of the time and polarisation rms averaged antenna power values $\langle X \rangle^{1/2}$ for the two galactocentric populations considered. In both cases the pattern is similar to when the incoming direction of the signal is fixed to the galactic centre (c.f. Fig. 2.13). The tendency of orientation losing importance for higher latitude values remains. The contour levels are not completely symmetric with respect to the equator – slightly shifted toward northern geographical latitudes. Here, again, the maximum values of $\langle X \rangle^{1/2}$ are for detectors located close to the equator and azimuthal orientation of $\alpha = 0, \pi/2$, the '$\times$' geograhical locations. The reduction between the equator and the poles is of about 10% for the two galactocentric populations, showing less contrast than the contour map for the case of fixed direction to the galactic centre. This is expected, because a cluster of sources will 'smear out' the results producing a contour map with less contrast than for a unique direction.

2.5 Detectability study for signals from NS populations - known detectors

The detectability of each detector listed in Table 2.1 to signals from galactic neutron stars has been measured in two different ways by: a) studying histogrammed values of antenna pattern values $|\eta|$ ($|\eta|_{DN}$ and $|\eta|_{DY}$ have also been compared), and by b) approximating detection probability by computing the fraction of trials where the rms value of the antenna power $X^{1/2}$ is bigger than a particular threshold $X_*^{1/2}$.

2.5.1 Histograms of antenna patterns

The appropriateness of a detector to see signals from a particular population can be assessed by histogramming all the antenna pattern values $|\eta|$ corresponding to all the sources of that population. For a quantitative comparison of histograms the mean of the values histogrammed $\bar{x}$ have been used (i.e. the first moment of the probability distribution), for the visual comparison of many overlaying

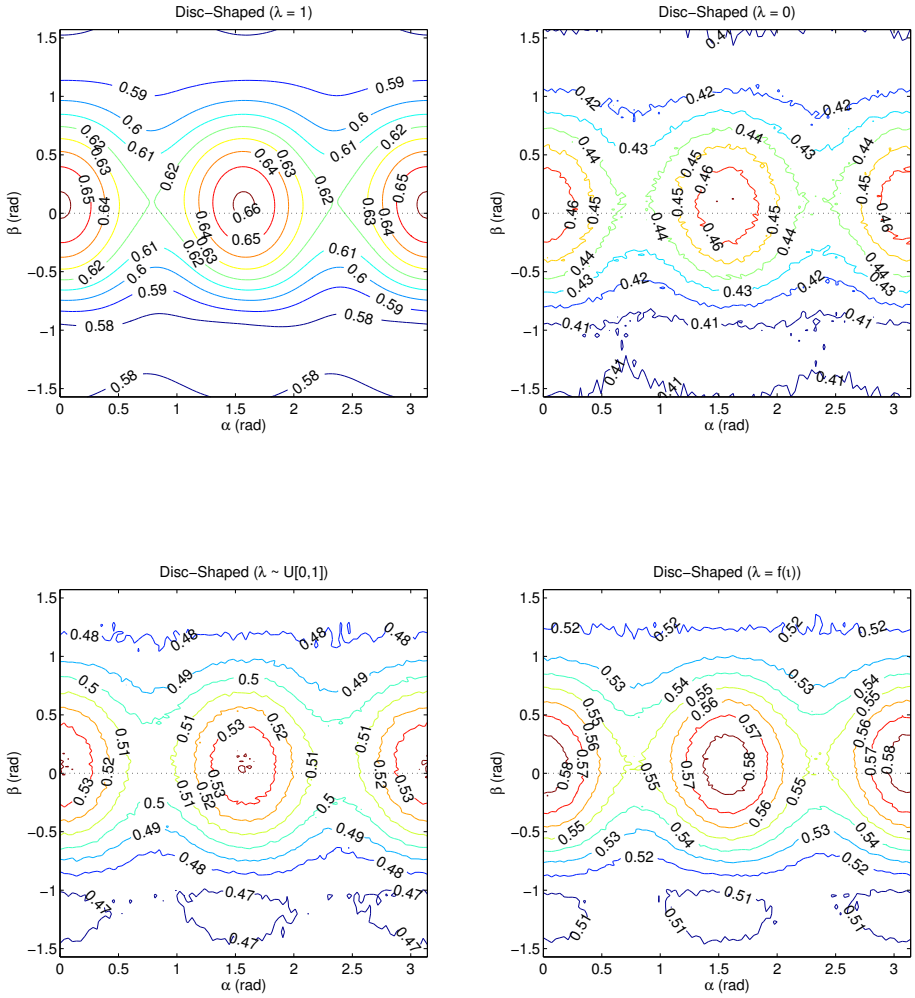

Figure 2.14: The rms antenna power $\langle X \rangle^{1/2}$ contour plots showing the effect of the location (latitude β) and orientation (α) of an L-shaped detector observing the Disc-shaped population of neutron stars. Each subplot represents values for signals of a degree of polarisation λ.

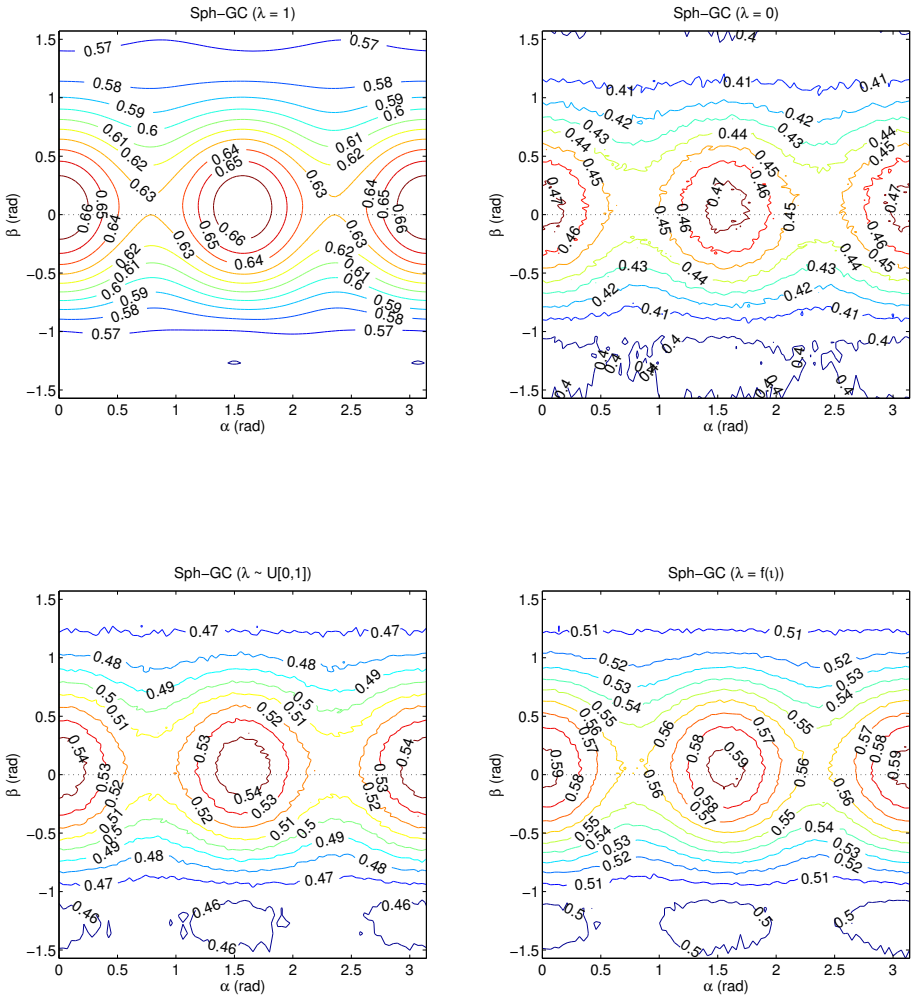

Figure 2.15: Same as Fig. 2.14 but for the galactocentric spherical population of neutron stars.

histograms is not practical. The computation of the mean is readily done by multiplying the number of occurrences in each bin with the value of the bin itself. Thus, two histograms with the same number of elements have the same area under the curve but generally not the shape and mean values. In general, for a group of N histogrammed values $\{x\}$ the mean value $\bar{x}$ can be computed as follows:

$$\bar{x} = \frac{1}{N}\sum_{i=1}^{m} n_i x_i = \frac{1}{N}\sum_{k=1}^{N} x_k, \tag{2.20}$$

where m is the number of bins, and n_i and x_i are the number of occurrences in and the value for the i^{th} bin, respectively. All the $\bar{x}$ values, corresponding to all the possible histograms, fall within the range $[x_1, x_m]$: $\bar{x}$ is lowest when all the values lay in the first bin ($\bar{x} = x_1$) and highest when all the values lay in the last bin ($\bar{x} = x_m$). For more details on the calculation of $\bar{x}$ and the range of values taken, see Appendix C.

The histograms of the antenna pattern values $|\eta|$ have been composed by computing and binning all their values (10^5 for each population) in the range [0,1]: we focus on this range even though a) the maximum value of $|\eta|_{DN}$ is never bigger than $\sqrt{2}/2$ (see Fig. 2.7) and b) $|\eta|_{DY}$ may be bigger than 1 a few instances).

Fig. 2.16 depicts the sources of each population considered, overlaid on a sensitivity sky-map (see Eq. 2.7 and Fig. 2.10), for VIRGO (located in the northern geographical hemisphere) and PERTH (located in the southern geographical hemisphere) at two instants 12 sidereal hours apart: t_1 = GLST = 19h30m and t_2 = GLST = 07h30m. Note the abscissas have been labelled differently for the two representations, for they both take values in the range $[0, 2\pi)$ rad $\equiv [0, 24)$ hour but GLST is valid to the directional sensitivity map in the background and GHA (Greenwich Hour Angle) is valid for the scattered sources. From the comparison of the two plots it is readily seen that, for example, PERTH is better located to detect signals coming from the galactic centre at instant t_1 than at instant t_2, and also that PERTH is better located than VIRGO at instant t_1.

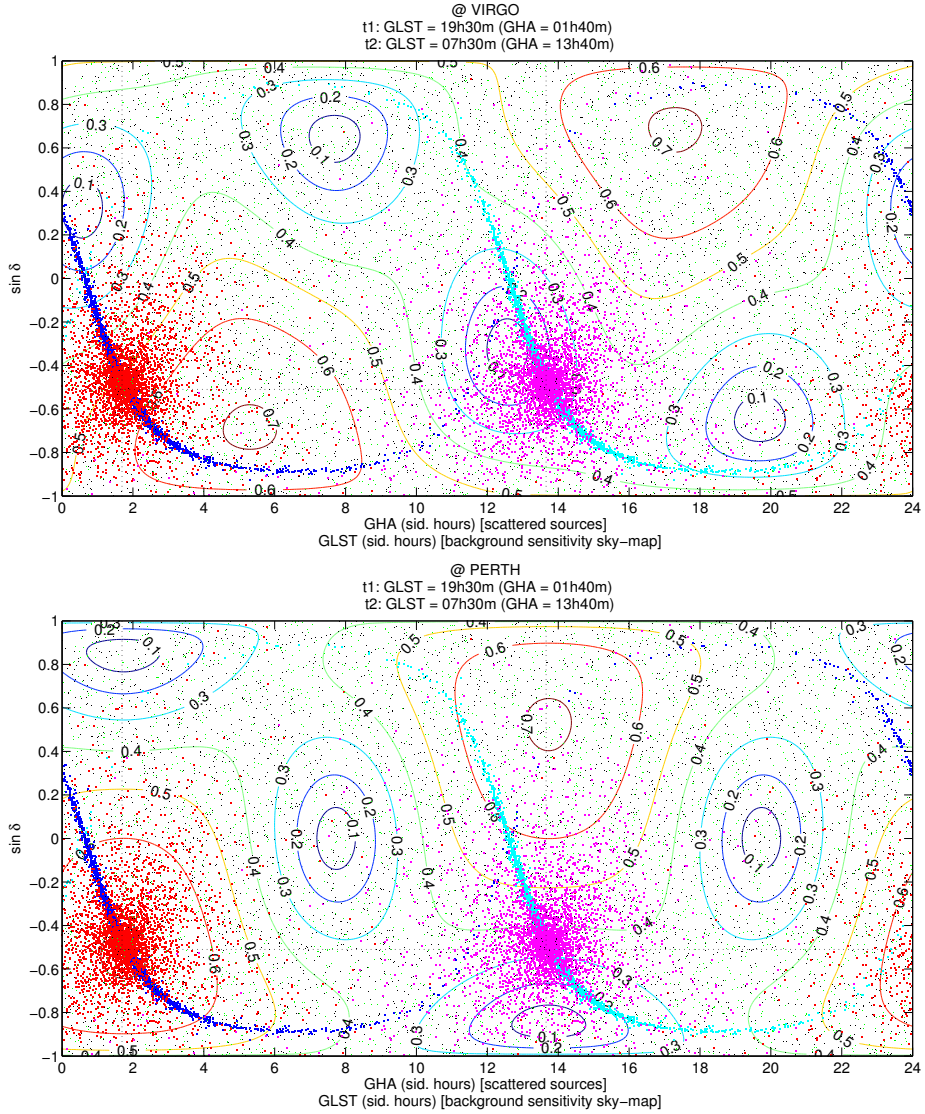

Figure 2.16: Disc-shaped (blue dots) and spherical-GC (magenta dots) populations of neutron stars overlaid on the directional sensitivity sky-map of VIRGO (*upper plot*) and PERTH (*lower plot*) detectors at two time instants 12 sidereal hours apart: GLST = 19h30m and 07h30m. The green dots, scattered isotropically all over the directional sensitivity sky-map in the background correspond to the Spherical-SE population centred on Earth. The dotted lines mark the location/time of the galactic centre (δ = -0.51, RA = 17h45m40s $\equiv$ 4.649 rad) at the particular instants studied.

Fig. 2.17 and Fig. 2.18 depict histograms of $log_{10}(|\eta|)$ values for the 10^5 sources of each population emitting with random polarisation angles at the two instants considered in Fig. 2.16 (only histograms for $\lambda = 0$ and $\lambda = f(\iota)$ are shown). This exercise has been done for each population and polarisation degree considered, taking the distance factor into account ($|\eta|_{DY}$ with Eq. 2.18) and not taking it ($|\eta|_{DN}$ with Eq. 2.15).

The same information is shown more in detail in Fig. 2.19 and Fig. 2.20, by means of normalised histograms of $|\eta|$ values restricted to the range [0,1], where most of the values fall. From the comparison of these histograms, it is noticeable, again, that PERTH is more suitably located than VIRGO for both instants. Note that the histograms corresponding to the population centred on the Earth (*Spherical-SE*) 'do not evolve in time', as expected from a population distributed isotropically around the detector – any instant is equally suited to detect the signals from the population.

Table 2.2 lists the $\bar{x}$ values (mean values) of the histograms calculated corresponding to the two instants studied and shown in Fig. 2.19 and Fig. 2.20. By comparing the tabulated values it is observed that: a) for the spherical-SE population the mean values hardly differ between the two instants (a sign that the histogram does not evolve); b) PERTH has higher mean values than VIRGO for any polarisation degree at both instants (as highlighted by Fig. 2.16); c) there is a marked reduction of the mean value from t_1 to t_2 for the spherical-GC population; d) the mean value $\bar{x}$ is smaller when the distance factor is considered, especially for the spherical population centred in the Earth.

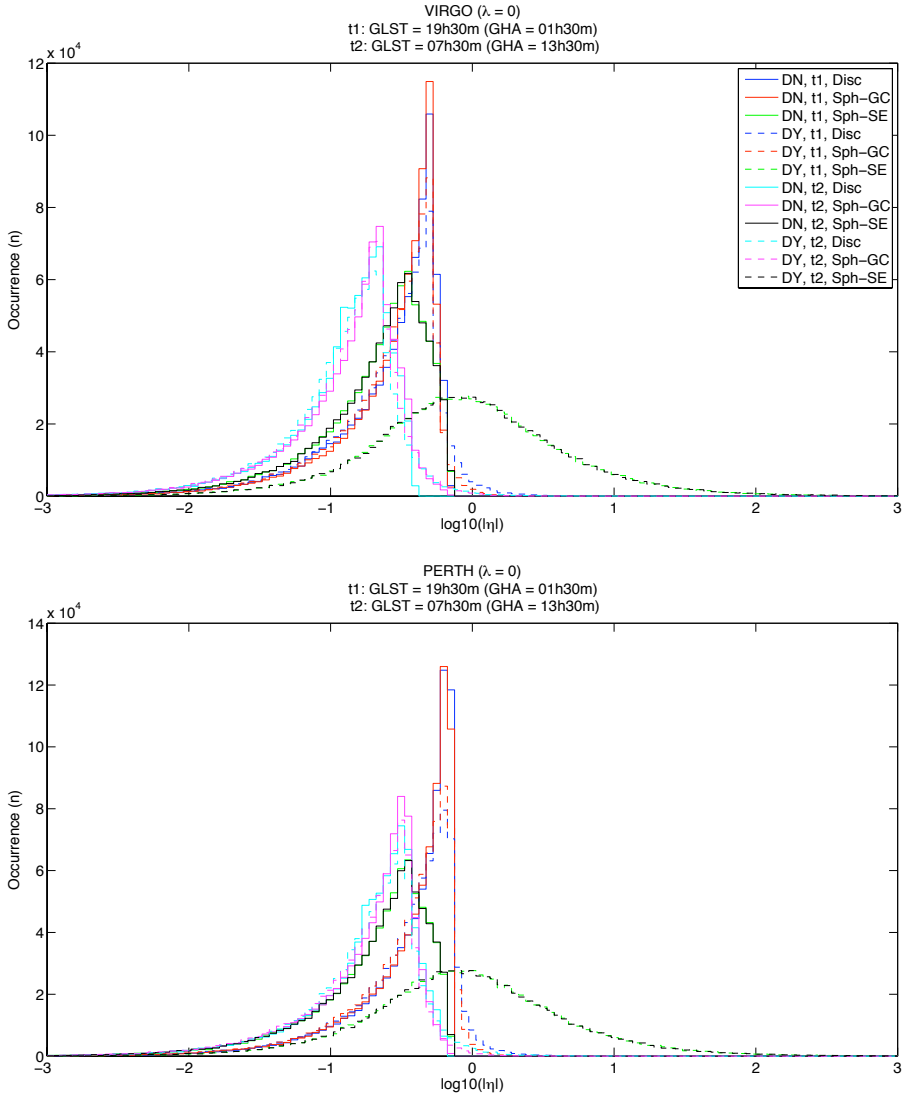

Figure 2.17: Histograms of the logarithms of the antenna pattern values $|\eta|_{DN}$ and $|\eta|_{DY}$ at two instants 12 sidereal hours apart. Results are plotted for linearly polarised signals ($\lambda = 0$) from the three populations considered as detected by VIRGO and PERTH.

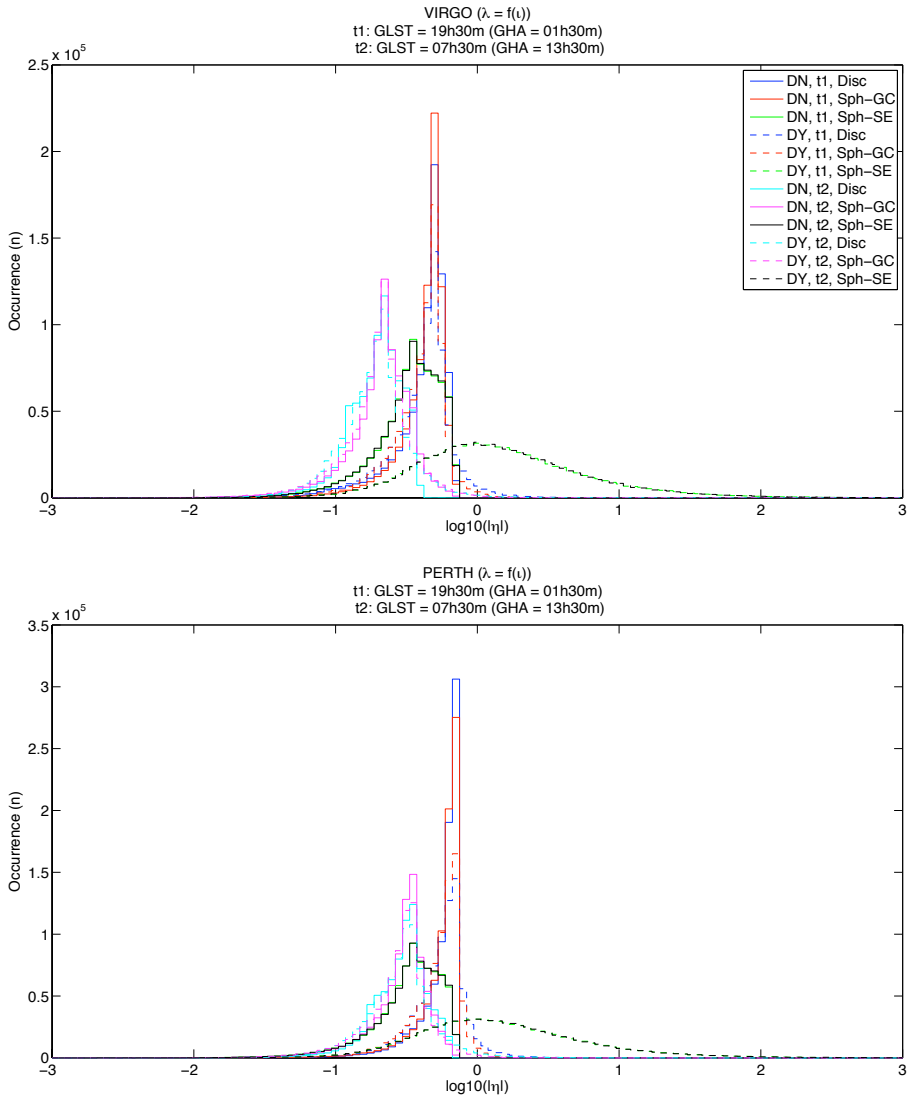

Figure 2.18: Same as Fig. 2.17 but for elliptically polarised signals ($\lambda = f(\iota)$).

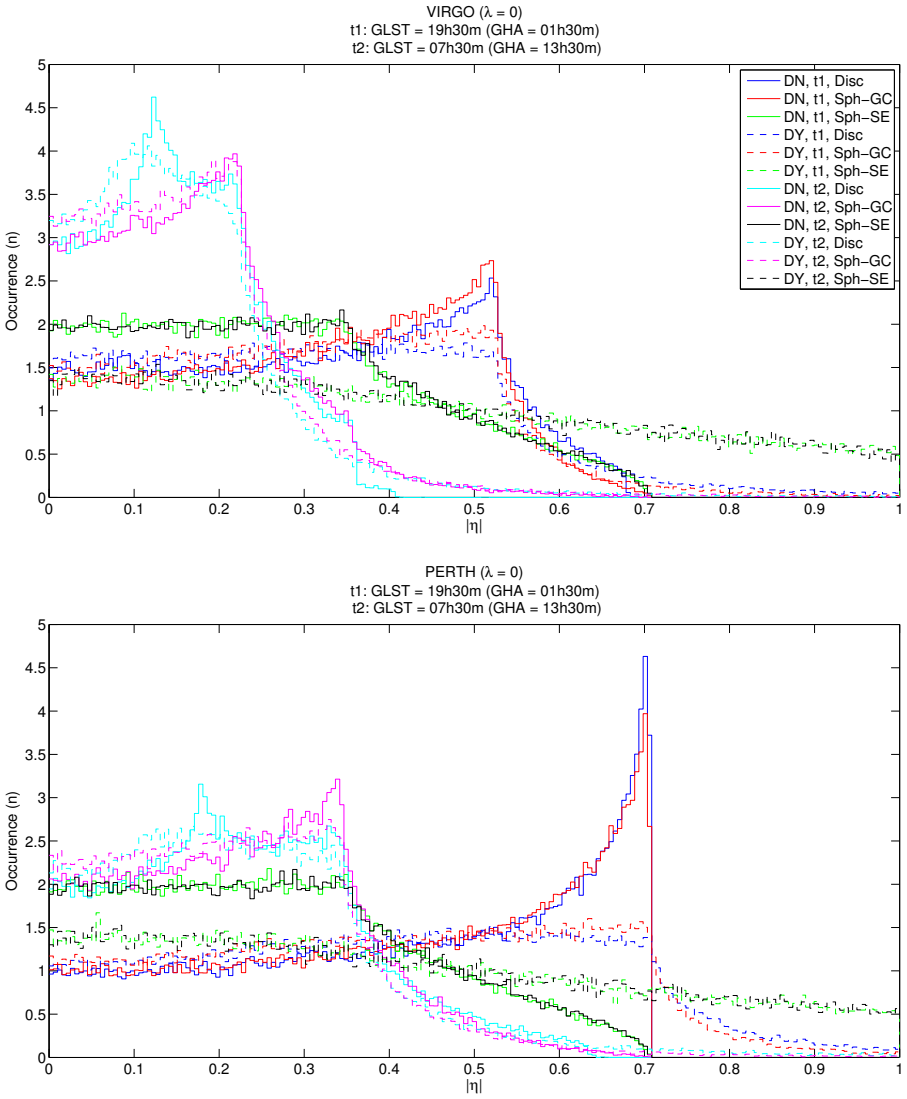

Figure 2.19: Normalised histograms of the antenna pattern values $|\eta|_{DN}$ and $|\eta|_{DY}$ at two instants 12 sidereal hours apart. Results are plotted for linearly polarised signals ($\lambda = 0$) from the three populations considered as detected by VIRGO and PERTH. Visual inspection quickly shows the difference in the distribution of antenna pattern values between the instants t_1 and t_2 for the galactocentric populations.

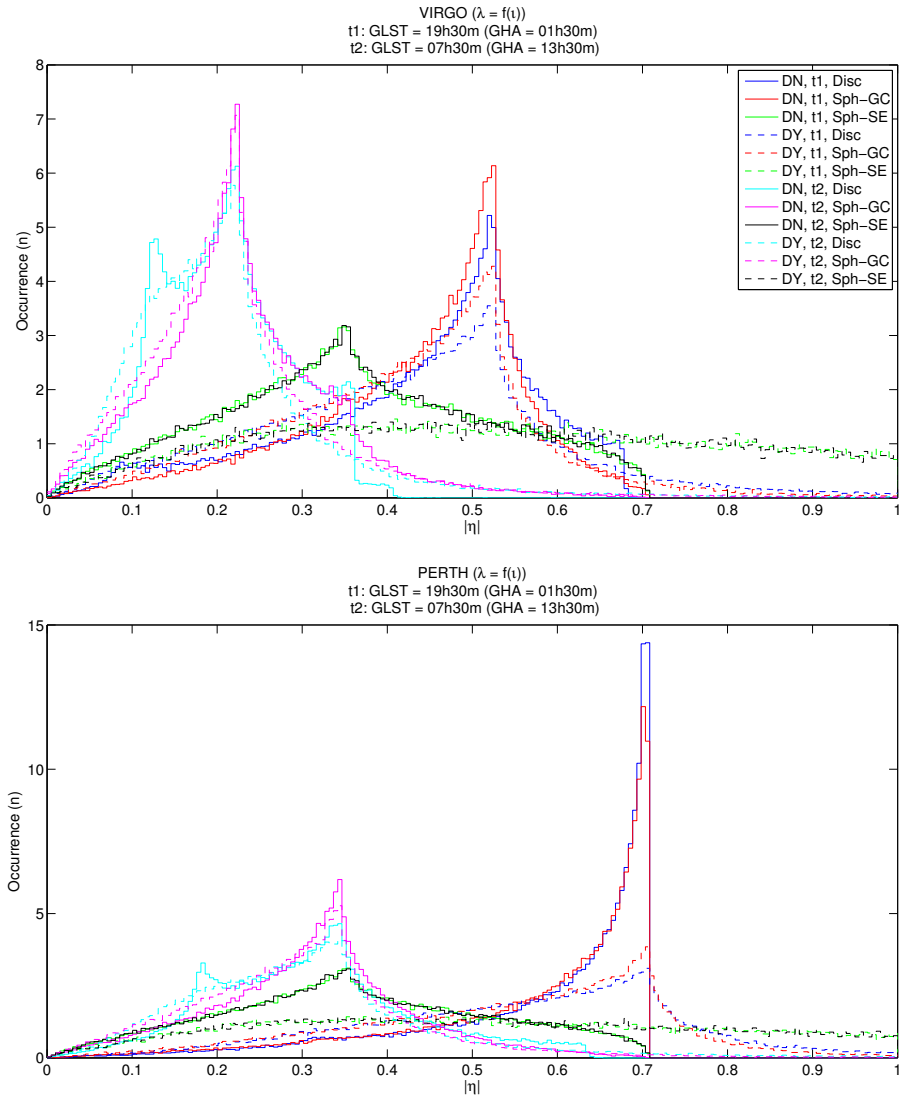

Figure 2.20: Same as Fig. 2.19 but for elliptically polarised signals ($\lambda = f(\iota)$).

$\bar{x}$ values of $\lvert\eta\rvert$ histograms for instants 12 sidereal hours apart							
POPULATION		**Disc-shaped**		**Spherical-GC**		**Spherical-SE**	
DETECTOR	**Polarisation**	t_1	t_2	t_1	t_2	t_1	t_2
VIRGO							
DN	$\lambda = 1$	0.5004	0.2365	0.5007	0.2617	0.4164	0.4174
DY		0.4647	0.2382	0.4744	0.2496	0.2008	0.2022
DN	$\lambda = 0$	0.3174	0.1497	0.3184	0.1658	0.2638	0.2648
DY		0.3058	0.1532	0.3060	0.1601	0.2242	0.2241
DN	$\lambda \sim \mathcal{U}[0,1]$	0.3920	0.1853	0.3929	0.2053	0.3268	0.3273
DY		0.3744	0.1888	0.3761	0.1975	0.2235	0.2251
DN	$\lambda = f(\iota)$	0.4325	0.2041	0.4329	0.2258	0.3602	0.3613
DY		0.4085	0.2070	0.4131	0.2167	0.2159	0.2163
PERTH							
DN	$\lambda = 1$	0.6648	0.3587	0.6555	0.3580	0.4171	0.4178
DY		0.5934	0.3407	0.6109	0.3406	0.1994	0.1997
DN	$\lambda = 0$	0.4215	0.2281	0.4173	0.2276	0.2643	0.2658
DY		0.3968	0.2236	0.3975	0.2190	0.2229	0.2231
DN	$\lambda \sim \mathcal{U}[0,1]$	0.5216	0.2816	0.5147	0.2805	0.3270	0.3275
DY		0.4857	0.2737	0.4879	0.2695	0.2238	0.2244
DN	$\lambda = f(\iota)$	0.5758	0.3095	0.5675	0.3094	0.3610	0.3614
DY		0.5284	0.2983	0.5347	0.2962	0.2142	0.2150

Table 2.2: $\bar{x}$ values corresponding to the two instants 12 sidereal hours apart at VIRGO and PERTH as shown in Fig. 2.20.

Rather than analysing only two instants, the study of the time- and polarisation-averaged histograms (over a whole rotation of the Earth) is more significant. Fig. 2.21 and Fig. 2.22 show time- and polarisation-averaged antenna pattern values $\langle|\eta|\rangle$ for each detector and population. Again, only two polarisation degrees are shown, but Table 2.3 shows the $\bar{x}$ values of all the histograms calculated. The last curve shown in each of the subplots corresponds to any detector looking at the spherical-SE population. The histograms are the result of averaging the antenna power values calculated for 10^5 sources, with random polarisation angles, every 1 minute.

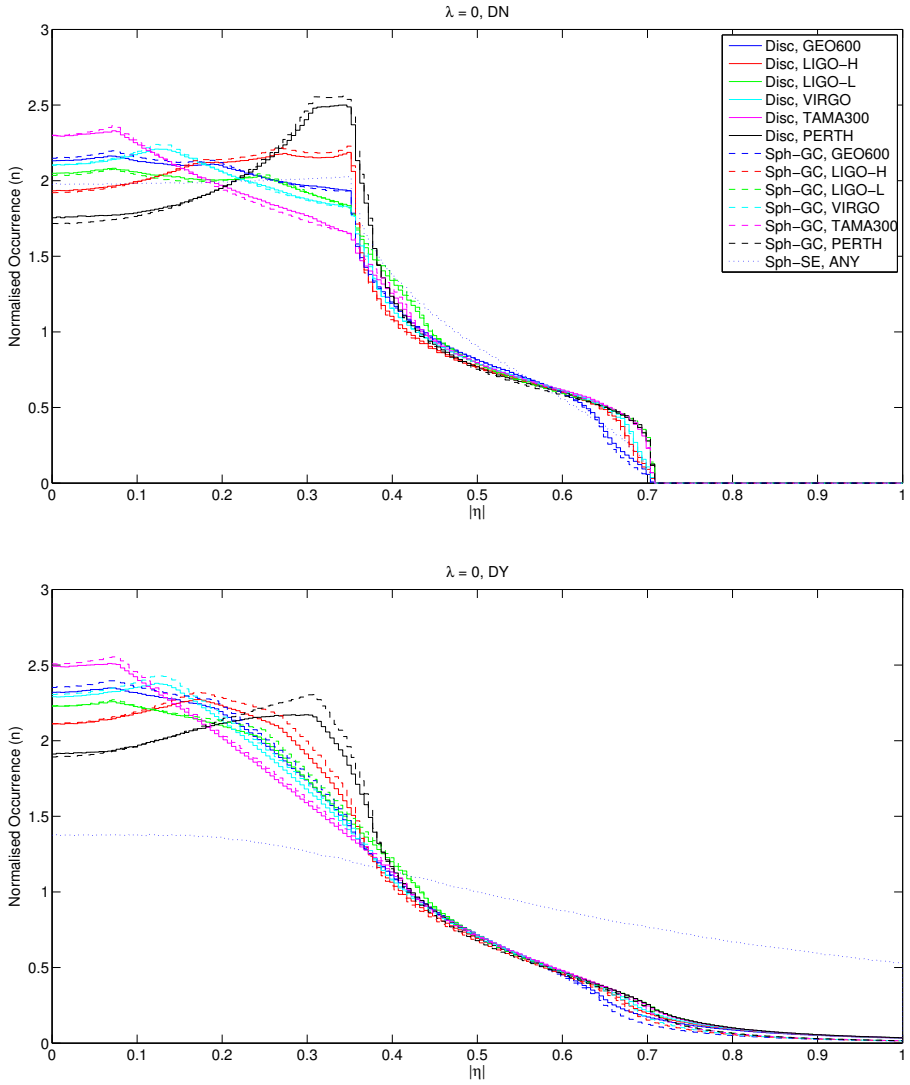

Figure 2.21: Comparison of time- and polarisation(angle)-averaged histograms for $|\eta|$ for linearly polarised ($\lambda = 0$) signals. Visual observation quickly shows the advantage of the PERTH detector (particularly in the range $0.2 < |\eta| < 0.4$) in comparison to the rest of the detectors.

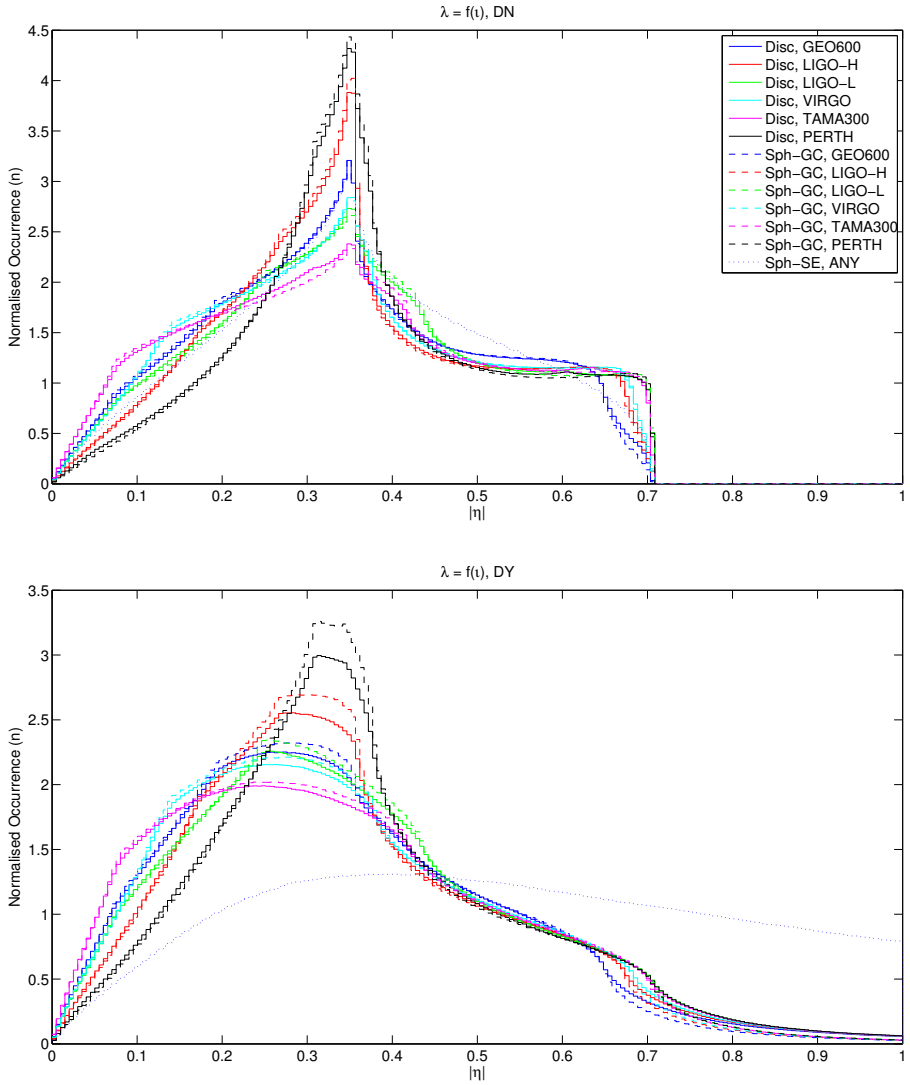

Figure 2.22: Same as Fig. 2.21 but for elliptically polarised signals ($\lambda = f(\iota)$).

$\bar{x}$ values for time-averaged $\lvert\eta\rvert$ histograms							
		Disc-shaped		Sph-GC		Sph-SE	
DET	**Pol.**	**DN**	**DY**	**DN**	**DY**	**DN**	**DY**
GEO600	$\lambda = 1$	0.3994	0.3773	0.3961	0.3758	0.4157	0.2014
LIGO-H		0.4102	0.3870	0.4085	0.3874	0.4169	0.2010
LIGO-L		0.4146	0.3912	0.4157	0.3936	0.4170	0.2010
VIRGO		0.4047	0.3816	0.4032	0.3820	0.4169	0.2011
TAMA300		0.4023	0.3794	0.4023	0.3806	0.4169	0.2011
PERTH		0.4299	0.4057	0.4310	0.4086	0.4170	0.2009
GEO600	$\lambda = 0$	0.2534	0.2476	0.2513	0.2417	0.2637	0.2244
LIGO-H		0.2603	0.2540	0.2592	0.2492	0.2645	0.2242
LIGO-L		0.2630	0.2567	0.2638	0.2534	0.2646	0.2242
VIRGO		0.2567	0.2506	0.2558	0.2458	0.2645	0.2242
TAMA300		0.2552	0.2492	0.2552	0.2451	0.2645	0.2241
PERTH		0.2727	0.2660	0.2734	0.2629	0.2646	0.2241
GEO600	$\lambda \sim \mathcal{U}[0,1]$	0.3132	0.3033	0.3106	0.2978	0.3259	0.2252
LIGO-H		0.3217	0.3112	0.3203	0.3071	0.3269	0.2249
LIGO-L		0.3251	0.3146	0.3260	0.3122	0.3269	0.2249
VIRGO		0.3173	0.3070	0.3161	0.3029	0.3269	0.2249
TAMA300		0.3155	0.3053	0.3154	0.3019	0.3269	0.2248
PERTH		0.3371	0.3261	0.3379	0.3239	0.3270	0.2247
GEO600	$\lambda = f(\iota)$	0.3455	0.3315	0.3426	0.3273	0.3595	0.2169
LIGO-H		0.3548	0.3401	0.3533	0.3374	0.3606	0.2165
LIGO-L		0.3586	0.3438	0.3596	0.3430	0.3607	0.2165
VIRGO		0.3500	0.3355	0.3487	0.3328	0.3606	0.2166
TAMA300		0.3480	0.3336	0.3479	0.3317	0.3606	0.2165
PERTH		0.3718	0.3564	0.3728	0.3559	0.3607	0.2164

Table 2.3: $\bar{x}$ values for time- and polarisation-averaged histograms of $\langle|\eta|_\lambda\rangle$ values.

By careful analysis of the histograms and the corresponding *mu* values detectors have been sorted out by their importance for detectability of signals from galactic neutron stars. In the following, the most important points are summarised:

- $\bar{x}$ values for the spherical-SE population are similar for all detectors. This reinforces the point made previously on that for this population the time-averaged histograms are the same for any detector and they do not 'evolve in time'.

- For both the galactocentric populations and regardless the polarisation degree λ, the most suitably located/oriented detector is PERTH and the worst is GEO600. Order from best to worse is PERTH, LIGO-L, LIGO-H, VIRGO, TAMA, GEO600.

- The fact that GEO600 is not a perfect L-shaped antenna (see Table 2.1) biases slightly the comparison between detectors. This bias is most noticeable on $\bar{x}$ values for the spherical-SE population: as expected, from the corresponding non-evolving histograms in time all the detectors show the same $\bar{x}$ value within a small tolerance, save GEO600, which has a slightly higher value due to its slight V-shape.

- For any population and polarisation degree there is a slight difference of $\bar{x}$ values when the distance factor is taken into consideration and when it is not. With the distance factor included the $\bar{x}$ value is slightly smaller, and for the case of the spherical population centred on the Earth it reduces to half. The main reason for this is that only antenna pattern values in the range [0,1] are histogramed and thus the contribution of a small percentage of the population is neglected.

- When the distance factor is not included, the $\bar{x}$ values of the histograms for elliptically polarised signals are intermediate between those obtained for circularly and linearly polarised signals.

Histograms and their corresponding $\bar{x}$ values evolve throughout the sidereal day differently depending the detector's location and orientation, the population considered, and the polarization degree of the signals taken into account. Fig. 2.23 portray the evolution of the $\bar{x}$ value for VIRGO and PERTH, during one rotation of the Earth. The times for which the $\bar{x}$ value is highest show the spells for which the detector is best oriented to a particular population; these have been marked by vertical lines.

Fig. 2.24 shows the evolution of the $\bar{x}$ values for all the detectors and populations considered; for the sake of briefness, only one polarisation degree ($\lambda = f(\iota)$) is shown. It is observable that each detector presents a spell in which it is more suitably oriented to the two galactocentric populations. The times and peaks values of the $\bar{x}$-value curves are listed in Table 2.4 and Table 2.5. In the following, the most important points concluded from the figures and the tables are listed:

- As expected, evolution of the $\bar{x}$ values corresponding to the spherical population centred on the Sun-Earth are flat and show the uniform exposure of a detector to the sources during the rotation of the Earth.
- The curves for the two elliptically polarised signals ($\lambda \sim \mathcal{U}[0,1]$ and $\lambda = f(\iota)$) are flanked by the circular (highest) and linear polarisation (lowest) curves.
- Overall, given any population and polarisation degree, the $\bar{x}$ values are smaller when the distance factor is included; this is especially noticeable in the much lower DC level for the spherical population centred on Earth.
- The time differences between the peaks of the $\bar{x}$ value-curves match the longitude differences between detectors well, with an uncertainty of always less than 20 and typically less than 5 min. This indicates that the maximum sensitivity of a detector to the galactocentric populations is around the time when the galactic centre crosses the meridian in the location of the detector.

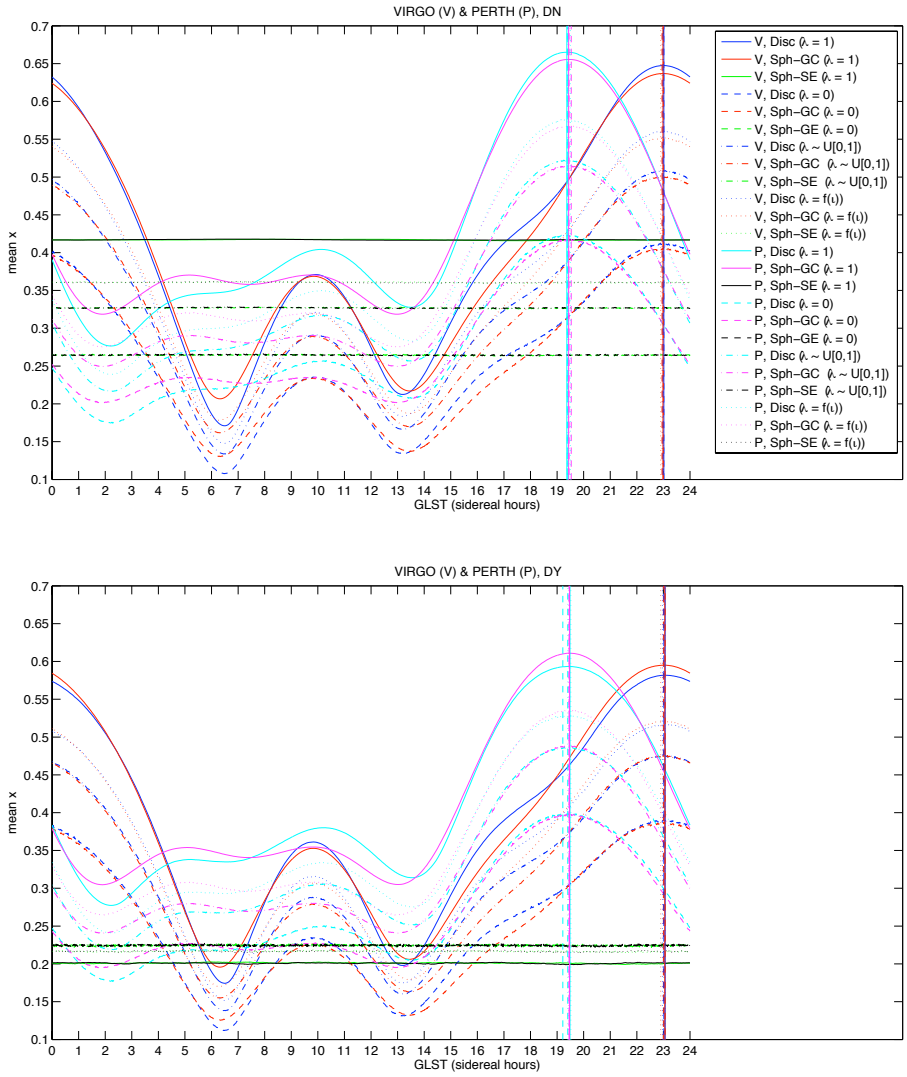

Figure 2.23: Evolution of the $\bar{x}$ values during one rotation of the Earth (24 sidereal hours) for VIRGO and PERTH.

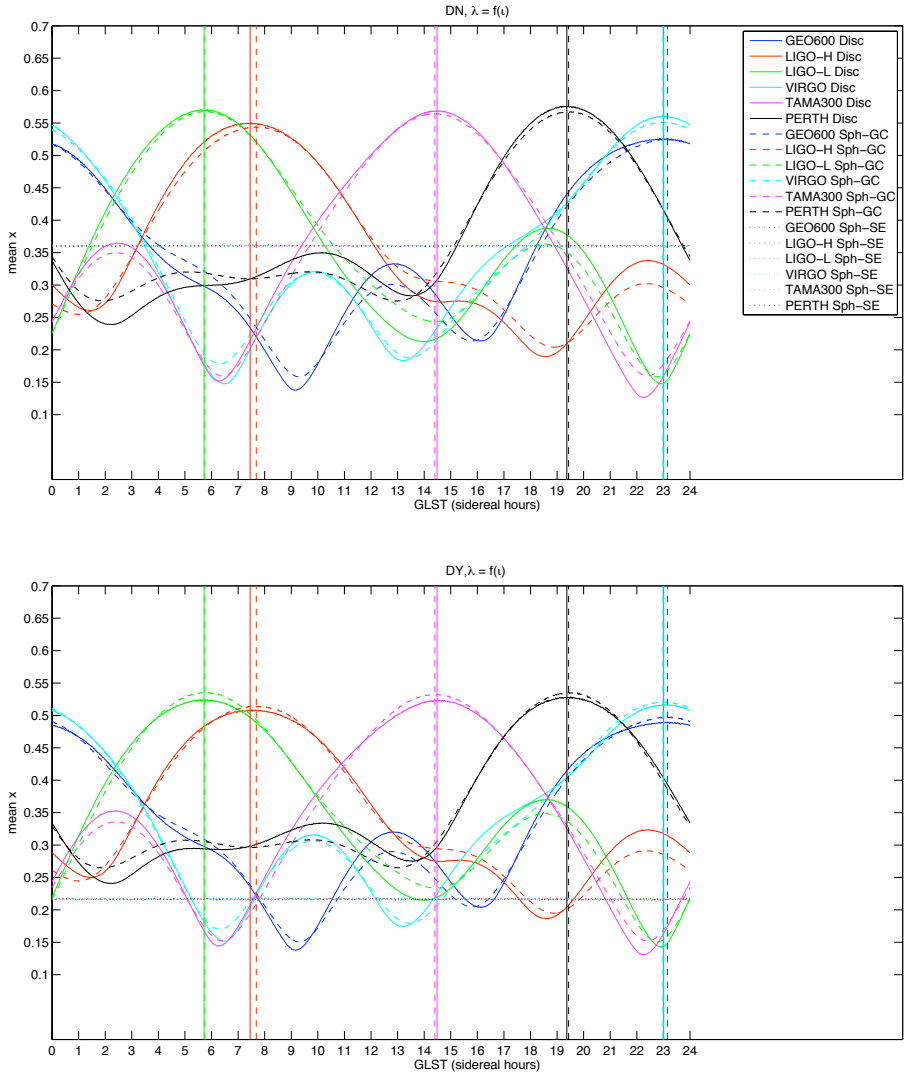

Figure 2.24: Evolution of $\bar{x}$-values along a sidereal day for the three populations and all the detectors; in this figure elliptically polarised signals ($\lambda = f(\iota)$) are considered.

Peak values and times for evolution curves of $\bar{x}$ values - I				
POPULATION		**Disc-shaped**	**Spherical-IG**	**Spherical-SE**
DETECTOR	**Polarisation**	**Peak GLST ($\bar{x}$ value)**		**Flat ($\bar{x}$ value)**
GEO600				
DN	$\lambda = 1$	23:00:00 (0.6070)	23:09:00 (0.6062)	(0.4165)
DY		23:09:00 (0.5533)	23:10:00 (0.5691)	(0.2030)
DN	$\lambda = 0$	22:49:00 (0.3867)	23:05:00 (0.3862)	(0.2658)
DY		23:06:00 (0.3683)	23:05:00 (0.3693)	(0.2268)
DN	$\lambda \sim \mathcal{U}[0,1]$	22:58:00 (0.4769)	23:05:00 (0.4762)	(0.3273)
DY		23:14:00 (0.4495)	23:10:00 (0.4538)	(0.2276)
DN	$\lambda = f(\iota)$	23:09:00 (0.5260)	23:08:00 (0.5248)	(0.3611)
DY		23:09:00 (0.4896)	23:10:00 (0.4976)	(0.2192)
LIGO-H				
DN	$\lambda = 1$	07:27:00 (0.6350)	07:41:00 (0.6284)	(0.4178)
DY		07:37:00 (0.5728)	07:42:00 (0.5879)	(0.2028)
DN	$\lambda = 0$	07:40:00 (0.4044)	07:37:00 (0.3996)	(0.2662)
DY		07:31:00 (0.3834)	07:37:00 (0.3817)	(0.2267)
DN	$\lambda \sim \mathcal{U}[0,1]$	07:16:00 (0.4994)	07:45:00 (0.4937)	(0.3286)
DY		07:34:00 (0.4683)	07:58:00 (0.4695)	(0.2275)
DN	$\lambda = f(\iota)$	07:30:00 (0.5503)	07:40:00 (0.5441)	(0.3620)
DY		07:31:00 (0.5085)	07:40:00 (0.5150)	(0.2187)
LIGO-L				
DN	$\lambda = 1$	05:43:00 (0.6585)	05:45:00 (0.6561)	(0.4177)
DY		05:44:00 (0.5895)	05:48:00 (0.6112)	(0.2031)
DN	$\lambda = 0$	05:26:00 (0.4198)	05:41:00 (0.4178)	(0.2664)
DY		05:26:00 (0.3965)	05:43:00 (0.3980)	(0.2268)
DN	$\lambda \sim \mathcal{U}[0,1]]$	05:37:00 (0.5176)	05:46:00 (0.5153)	(0.3284)
DY		05:37:00 (0.4826)	05:57:00 (0.4887)	(0.2270)
DN	$\lambda = f(\iota)$	05:51:00 (0.5708)	05:43:00 (0.5682)	(0.3620)
DY		05:51:00 (0.5245)	05:43:00 (0.5357)	(0.2187)

Table 2.4: Part I: Peak values and times of the $\bar{x}$ value evolution curves for detectors GEO600, LIGO-L and LIGO-H. Note that the values corresponding to the spherical neutron star population centred in the Sun-Earth are flat; for these the DC level is listed.

Peak values and times for evolution curves of $\bar{x}$ values - II				
POPULATION		**Disc-shaped**	**Spherical-IG**	**Spherical-SE**
DETECTOR	**Polarisation**	**Peak**		**Flat**
		GLST ($\bar{x}$ value)		**($\bar{x}$ value)**
VIRGO				
DN	$\lambda = 1$	23:01:00 (0.6475)	22:59:00 (0.6369)	(0.4177)
DY		23:04:00 (0.5818)	23:03:00 (0.5951)	(0.2026)
DN	$\lambda = 0$	23:01:00 (0.4124)	23:00:00 (0.4059)	(0.2665)
DY		23:01:00 (0.3908)	23:00:00 (0.3872)	(0.2266)
DN	$\lambda \sim \mathcal{U}[0,1]$	23:00:00 (0.5087)	22:54:00 (0.5005)	(0.3282)
DY		22:58:00 (0.4756)	22:54:00 (0.4756)	(0.2274)
DN	$\lambda = f(\iota)$	22:59:00 (0.5604)	22:57:00 (0.5517)	(0.3620)
DY		23:01:00 (0.5170)	23:04:00 (0.5212)	(0.2187)
TAMA300				
DN	$\lambda = 1$	14:29:00 (0.6569)	14:24:00 (0.6521)	(0.4176)
DY		14:30:00 (0.5887)	14:25:00 (0.6080)	(0.2024)
DN	$\lambda = 0$	14:30:00 (0.4180)	14:21:00 (0.4157)	(0.2662)
DY		14:44:00 (0.3953)	14:21:00 (0.3963)	(0.2267)
DN	$\lambda \sim \mathcal{U}[0,1]$	14:36:00 (0.5159)	14:29:00 (0.5123)	(0.3282)
DY		14:38:00 (0.4818)	14:29:00 (0.4862)	(0.2272)
DN	$\lambda = f(\iota)$	14:35:00 (0.5689)	14:32:00 (0.5646)	(0.3619)
DY		14:26:00 (0.5235)	14:32:00 (0.5328)	(0.2188)
PERTH				
DN	$\lambda = 1$	19:22:00 (0.6650)	19:26:00 (0.6555)	(0.4179)
DY		19:29:00 (0.5935)	19:28:00 (0.6109)	(0.2021)
DN	$\lambda = 0$	19:24:00 (0.4232)	19:32:00 (0.4175)	(0.2663)
DY		19:13:00 (0.3992)	19:27:00 (0.3977)	(0.2264)
DN	$\lambda \sim \mathcal{U}[0,1]$	19:23:00 (0.5225)	19:27:00 (0.5151)	(0.3284)
DY		19:24:00 (0.4867)	19:27:00 (0.4890)	(0.2271)
DN	$\lambda = f(\iota)$	19:30:00 (0.5758)	19:26:00 (0.5679)	(0.3622)
DY		19:31:00 (0.5288)	19:26:00 (0.5356)	(0.2186)

Table 2.5: Part II: Peak values and times of the $\bar{x}$ value evolution curves for detectors VIRGO, TAMA300 and PERTH.

2.6 Detection probability for signals from NS populations

In section 2.4 and section 2.5 time- and polarisation-averaged antenna pattern and power values were used to assess the goodness of the location and orientation of a particular detector. In this section, we proceed to quantify the detectability as a probability by calculating the statistics of successful random trials.

An interesting and flexible way of assessing the detectability as a probability is to compute the fraction of trials (sources) that result on antenna power values $X^{1/2}$ over an arbitrary threshold $X_*^{1/2}$ (92). For the lowest threshold possible ($X_*^{1/2} = 0$), all the trials fall over and the detection probability is thus one, whereas there is not one trial over the highest possible threshold ($X_*^{1/2} = 1$) and the detection probability is zero. For infinite number of trials, the fraction would correspond to the exact detection probability, but for a finite number of trials, the procedure provides an approximate result of the detection probability with a computable maximum uncertainty.

2.6.1 Detection Probability for a single antenna

Fig. 2.25 to Fig. 2.27 show the detection probability curves of VIRGO and PERTH for the two instants depicted in Fig. 2.16. Each figure shows the detection probability curves of the two detectors for a different neutron star population, emitting with random polarisation angle and the polarisation degrees considered so far, when the distance factor is considered and when it is not. From the comparison of their detection probability curves it is obvious that both detectors are better located/oriented at instant t_1 than at instant t_2. The curves were obtained by calculating the antenna power values $X^{1/2}$ (Eq. 2.16) for each of the 10^5 sources and computing the fraction of them resulting over 100 threshold values uniformly distributed in the range [0,1]. Again, note in Fig. 2.27 that the detection probability curve corresponding to the spherical geocentric population is the same for the two time instants (does not evolve in time). The detection probability curves for the elliptically polarised signals are flanked by the curves corresponding to circular and linearly polarised signals.

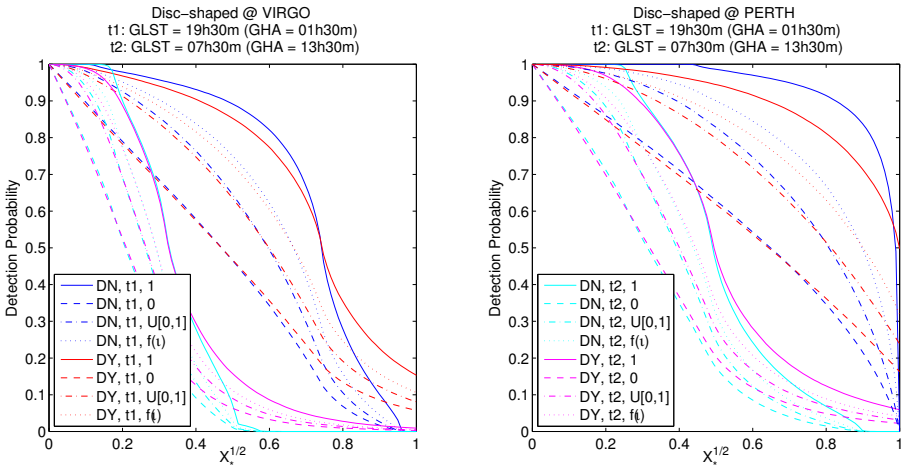

Figure 2.25: Detection probability curves for the disc-shaped NS population at the two instants depicted in Fig. 2.16 for VIRGO and PERTH detectors.

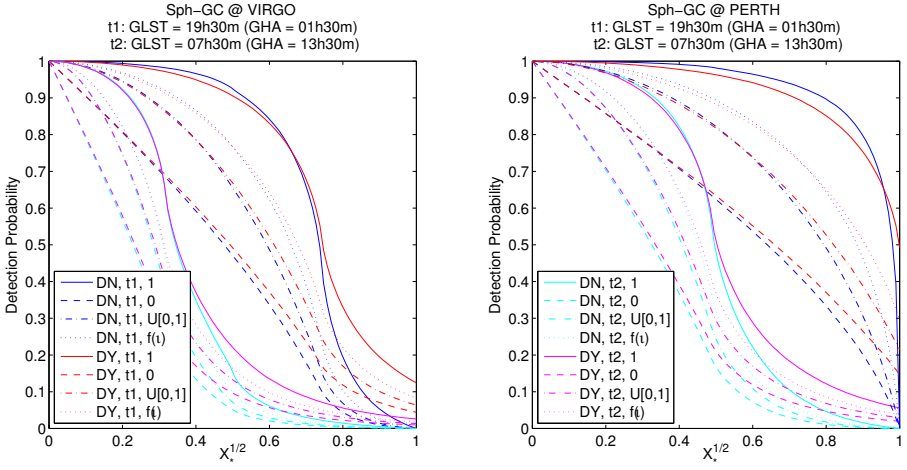

Figure 2.26: Same as Fig. 2.25 but for the galactocentric spherical NS population.

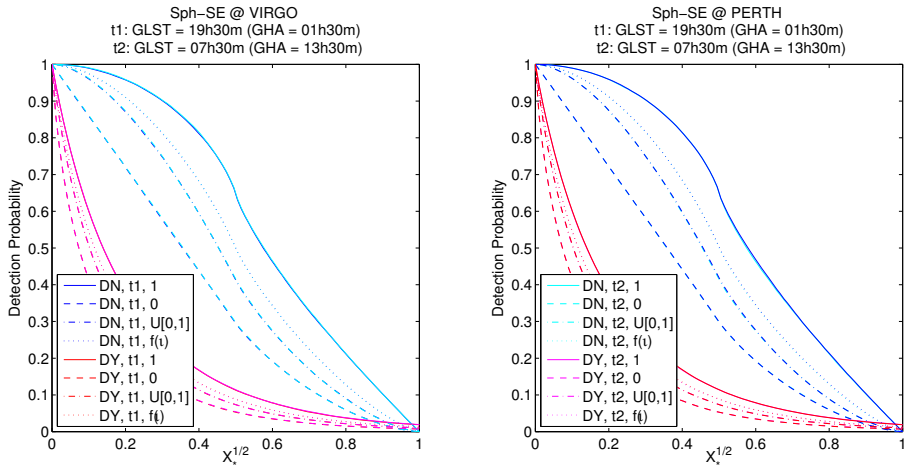

Figure 2.27: Same as Fig. 2.25 for the geocentric spherical NS population. As expected, both instants analysed result in the same detection probability curve, highlighting the fact that there is not preferential time or orientation for this NS population.

To average over one rotation of the Earth, detection probability curves have been computed at intervals of 5 minutes and results averaged. For the two galactocentric populations shown in Fig. 2.28 and Fig. 2.29, the detection probability curves indicate that some detectors are better located and oriented than others: PERTH outperforms the rest and that TAMA300 is the worst. This supports the opinion that a detector located in the southern geographical hemisphere presents a better detectability to galactocentric populations. As expected, and generalising results on Fig. 2.27, Fig. 2.30 shows that the time-averaged detection probability curve is equal for any detector looking at the spherical population centred on Earth.

All the detection probability curves shown in the three abovementioned figures have been characterised by a linear square fit of Chebyshev polynomials in the range $0 \leq X_*^{1/2} \leq 0.5$. The coefficients of the fit are shown in Appendix E to facilitate comparisons.

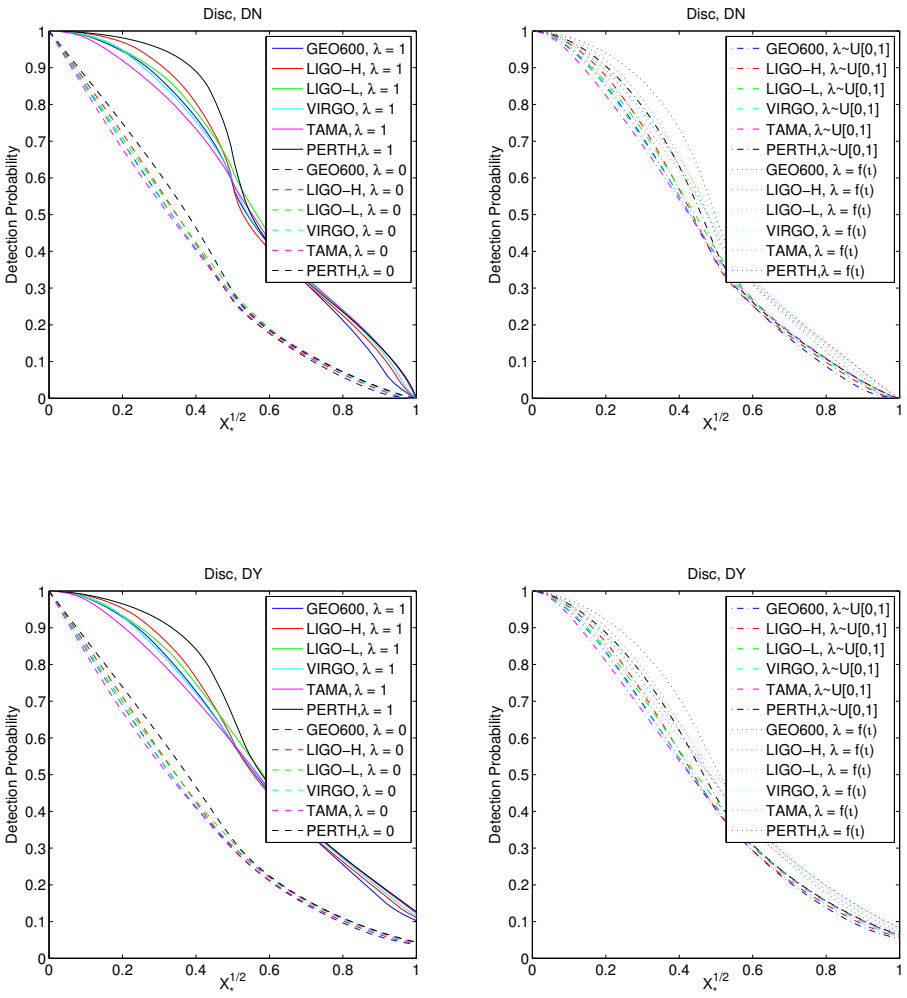

Figure 2.28: Time-averaged detection probability curves of all the detectors, for disc-shaped NS population.

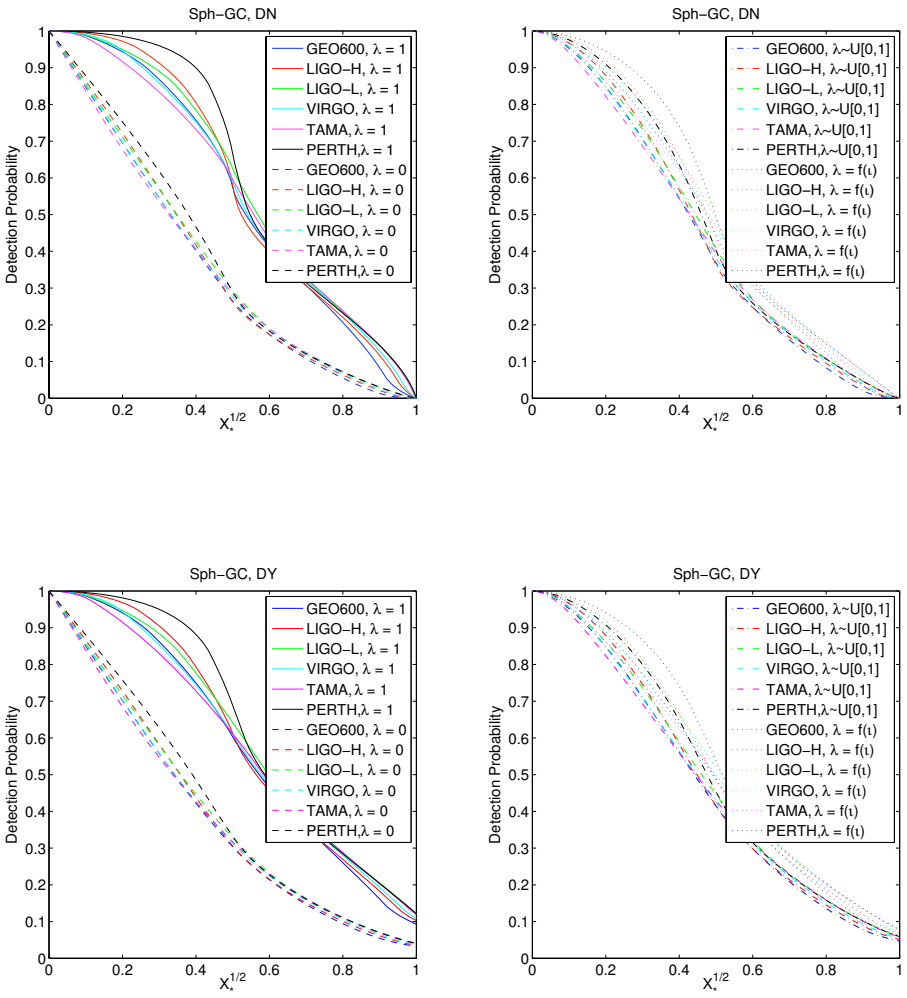

Figure 2.29: Time-averaged detection probability curves of all the detectors, for the galactocentric spherical NS population.

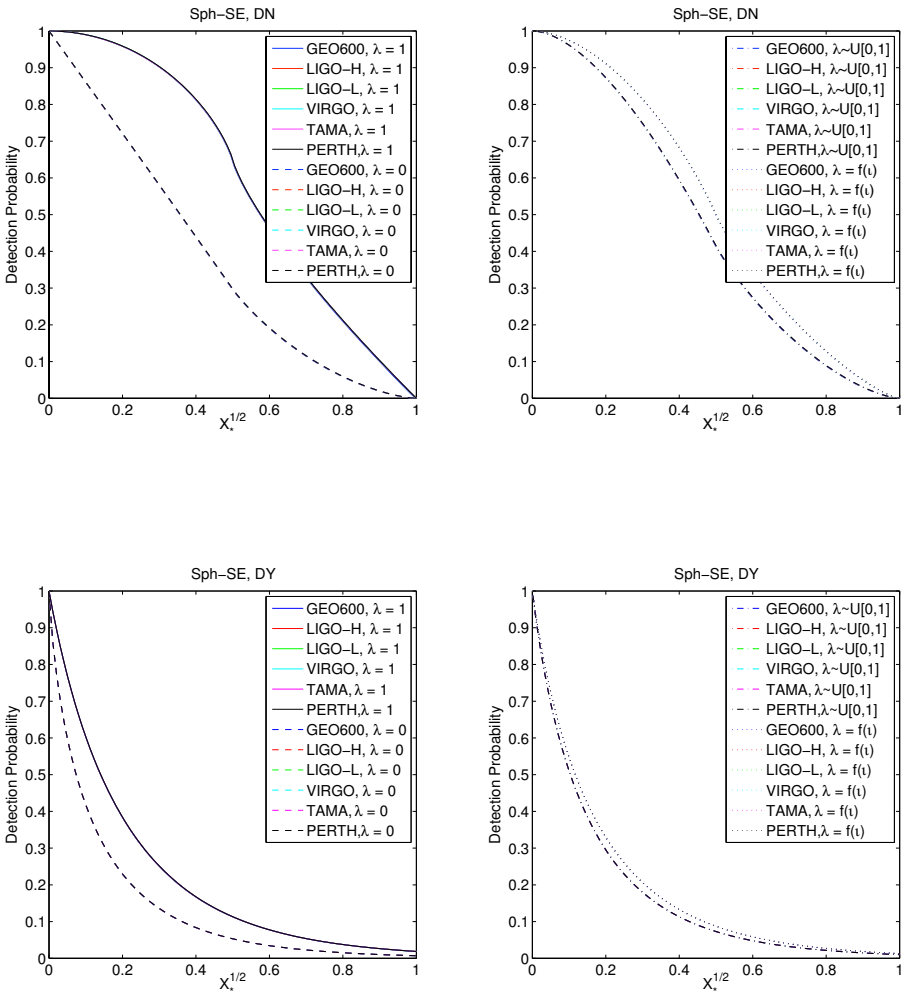

Figure 2.30: Time-averaged detection probability curves of all the detectors, for the geocentric spherical NS population.

2.6.2 Detection Probability for a network of antennae

Gravitational wave detectors are often part of a network of detectors, for the joint analysis of data jointly increases detectability greatly. Correlation analysis between data sets acquired by detectors at different location/orientation can enhance greatly the outcomes of the data analysis process. For example, the source sky-direction may be located by triangulation, due to the arrival-time differences and the modulation of the signal due to the unique antenna patterns of each detector. It may be that the burst-signal is well seen (i.e. with a high enough SNR) by one detector but is poorly detected by another, due to a less ideal orientation of the second detector at that particular instant. The detection probability of the network is approximated, again, by computing the fraction of trials for which their antenna power values $X^{1/2}$ are bigger than a set up threshold $X_*^{1/2}$.

2.6.2.1 Detection probability: network of two antennae

Detection probability curves have been computed for all the combinations of pairs of detectors, populations, and polarization degrees considered. Fig. 2.31 and Fig. 2.32 show one example, for the VIRGO-PERTH detector pair, with signals of different polarisation degree and distance factor. The contour lines in these figures represent the probabilities (i.e. ratios) of the rms antenna power values independently be bigger than a chosen threshold. The calculation of ratios is computationally very demanding and it has been carried out only for networks of two detectors. For networks of more than two detectors, shown in the following sections, only the ratios for thresholds of rms antenna power values resulting simultaneously over a chosen threshold have been computed.

The results do not differ much between the two galactocentric populations. Non-concentric contour levels show a favourable condition of detection for PERTH over VIRGO, especially for low threshold values ($X_*^{1/2} < 0.5$): the probability of detecting a source with $(X_{P*}^{1/2}, X_{V*}^{1/2}) = (0.4,0.2)$ is bigger than for detecting (0.2,0.4). This asymmetry smooths out for higher values of $X_*^{1/2}$. The concentric contour lines show that all detectors are in equal footing to detect the geocentric spherical population.

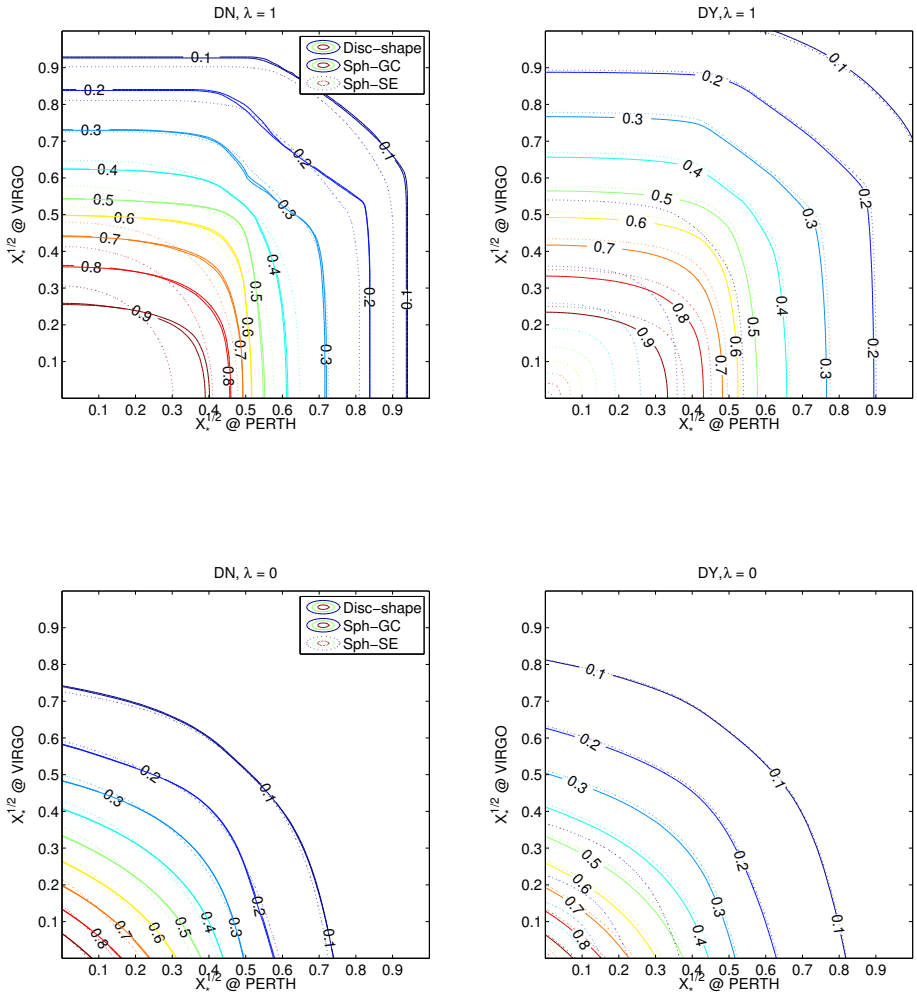

Figure 2.31: Coincident VIRGO – PERTH detection probability surfaces for the three source populations, for circular and linearly polarised signals.

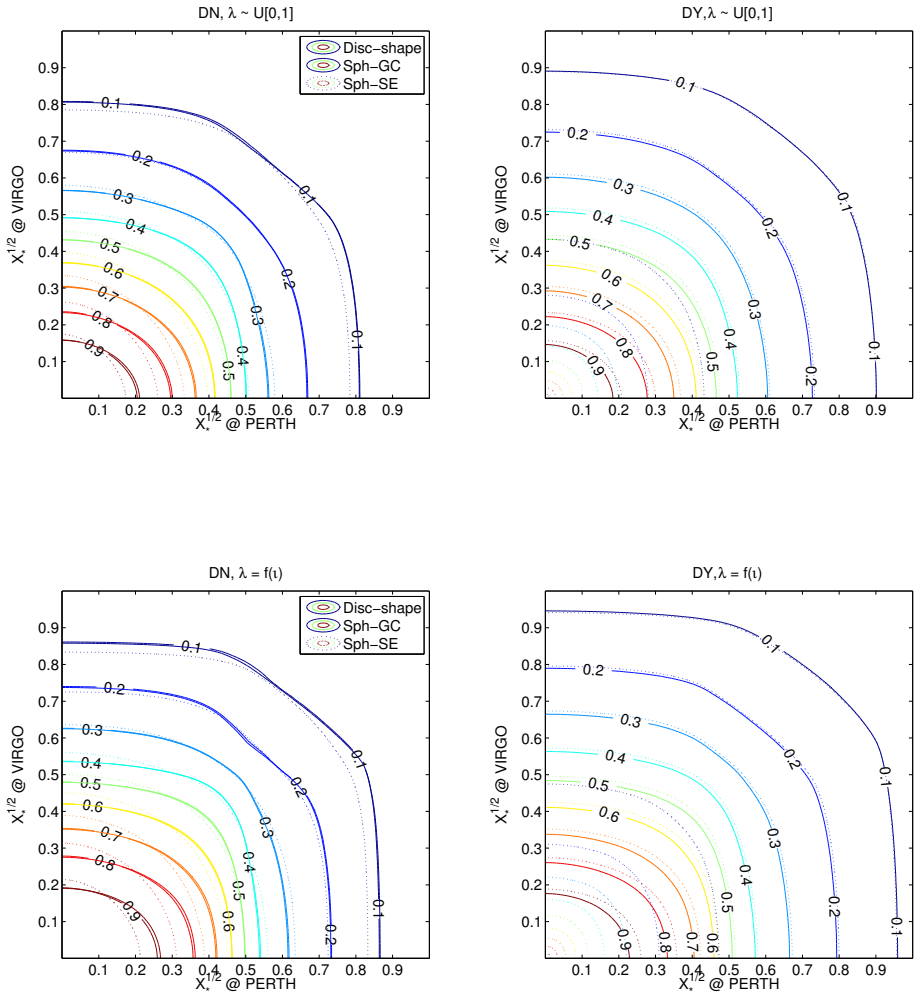

Figure 2.32: Coincident VIRGO – PERTH detection probability surfaces for the three source populations, for elliptically polarised signals.

In this section contour lines (2D) have been used to represent results of a network of two detectors. However, when a network comprises more than two detectors the representation of the probability is more difficult. A way of simplifying the representation is by representing with a curve (1D) the number of times for which the antenna power value is over a threshold, simultaneously at all the detectors in the network. This study has been done in Section 2.6.2.2.

2.6.2.2 Detection probability: networks of more than two antennae

In this section, the time-averaged detection probability curves for networks of two, three, four, five and six detectors are shown. The statistics for when all the detectors in the network present antenna power values over a particular threshold simultaneously have been computed.

Fig. 2.33 to Fig. 2.37 show the detection probability curves for networks with an increasing number of detectors. For networks of more than two detectors results are shown for a limited number of combinations to avoid cluttering the plots: only the case of polarisation degree $\lambda = f(\iota)$ is shown for two of the NS populations. The legends make reference to the detectors with the numbers assigned in Table 2.1. The coefficients of the Chebyshev polynomials that fit the curves are presented in Appendix E.

In Fig. 2.33 the detection probability curves for pairs of detectors comprising VIRGO or PERTH are shown and compared against the detection probabilities of all the antennae working individually. Obviously, any combination of a pair of detectors has a lower coincidence detection probability than detectors working individually. For the disc-shaped population, Det 2-6 (LIGO-H & PERTH) are the best located/oriented and Det 5-4 (TAMA & VIRGO) are the worst. Det 1-4 (GEO & VIRGO) show remarkably higher values of detection probability for thresholds values bigger than 0.5.

For networks of three antennae in Fig. 2.34 the trio Det 1-4-6 (GEO600 & VIRGO & PERTH) prove to be a network with remarkably high detection probability values for threshold values bigger than 0.5. For networks of four antennae in Fig. 2.35 there is no clear network outperforming the rest of combinations. Something similar happens for networks of five antennae in Fig. 2.36.

Fig. 2.37 compares the progressively decreasing detecting probability curves, by each time including an extra detector in the network. The probability for all the six detectors to show an antenna pattern value higher than 0.5 simultaneously is negligible, especially when the distance factor is not considered.

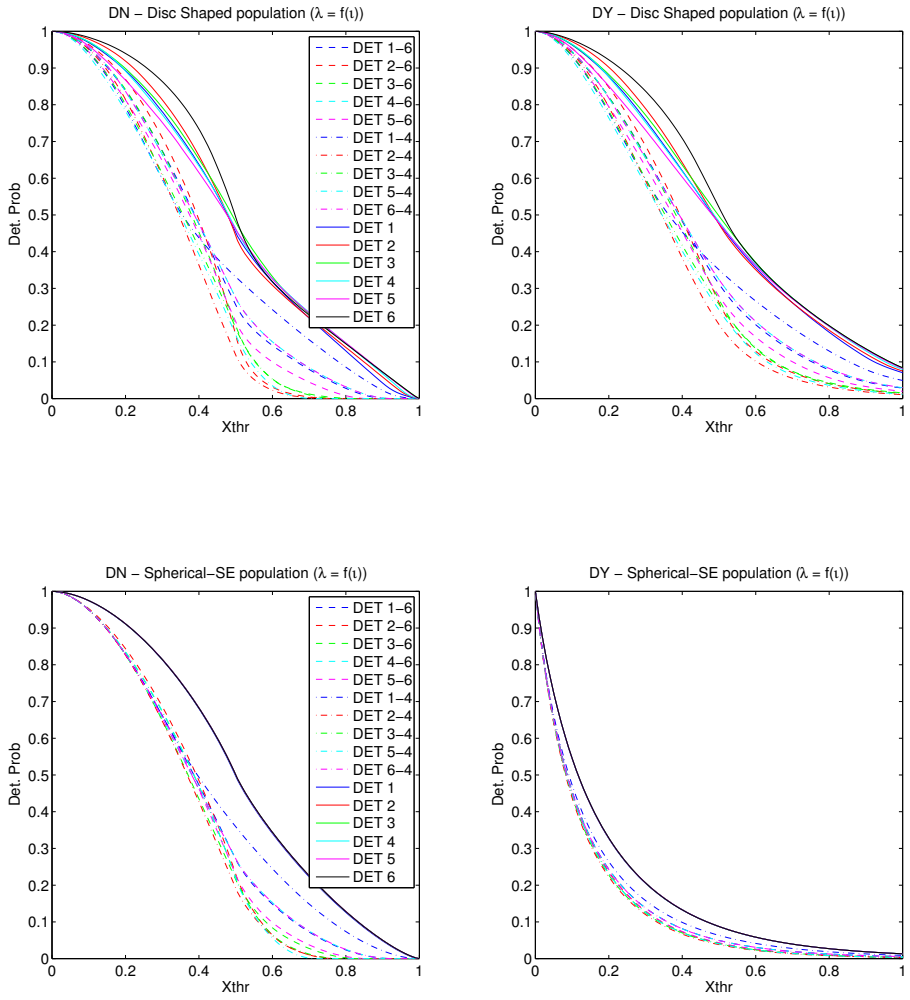

Figure 2.33: Time-averaged detection probability curves for antennae working individually and in pairs, for the disc-shaped and spherical-SE populations, and signals polarised with $\lambda = f(\iota)$.

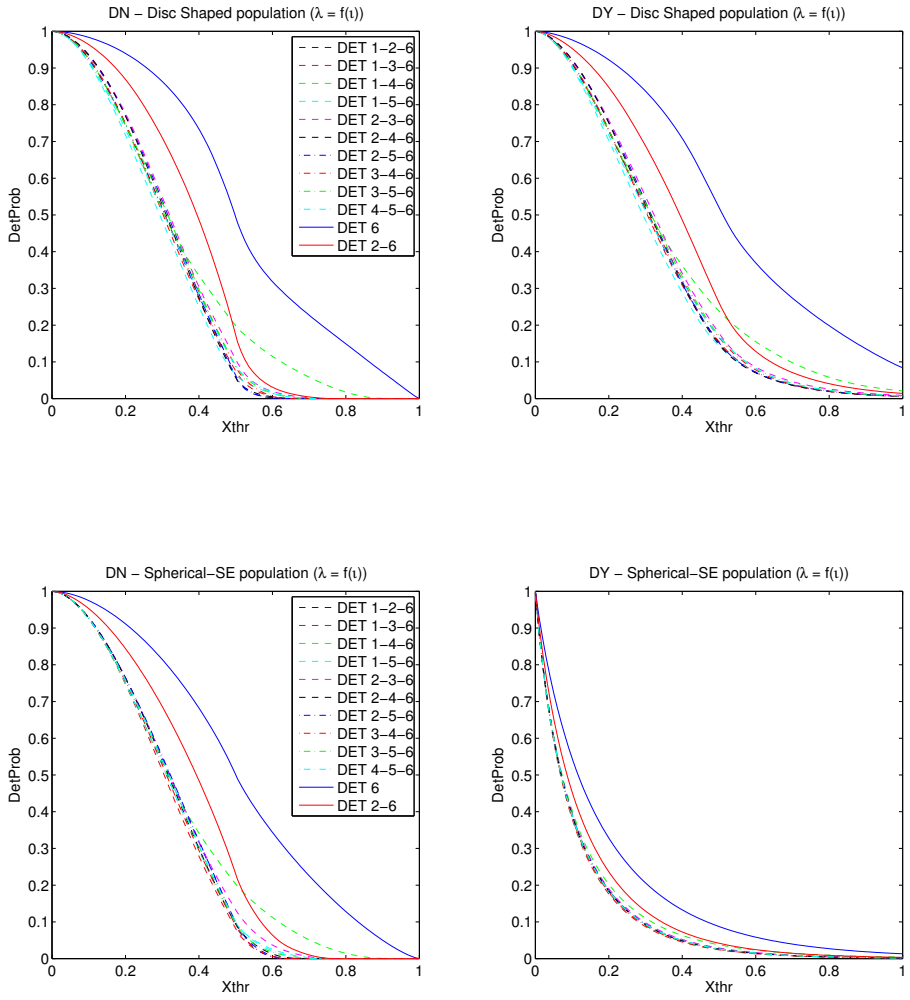

Figure 2.34: Time-averaged detection probability curves for antennae working individually and in threes, for the disc-shaped and spherical-SE populations, and signals polarised with $\lambda = f(\iota)$.

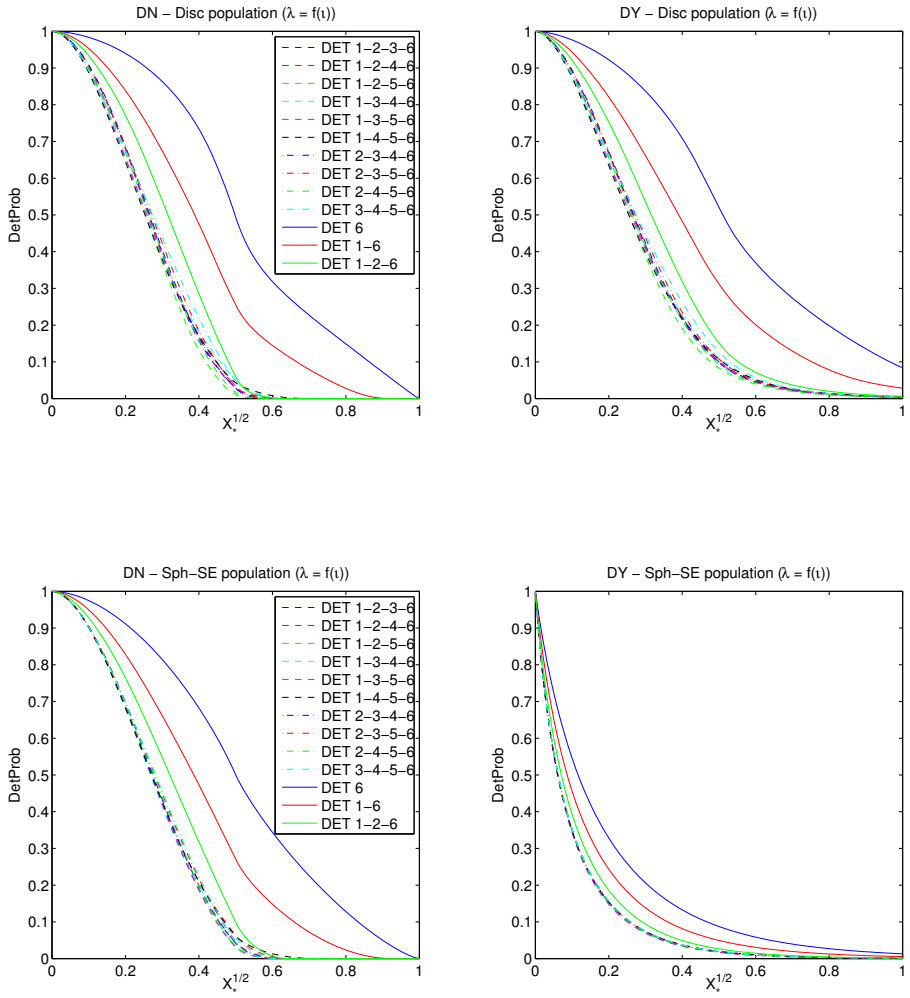

Figure 2.35: Time-averaged detection probability curves for antennae working individually and in fours, for the disc-shaped and spherical-SE populations, and signals polarised with $\lambda = f(\iota)$.

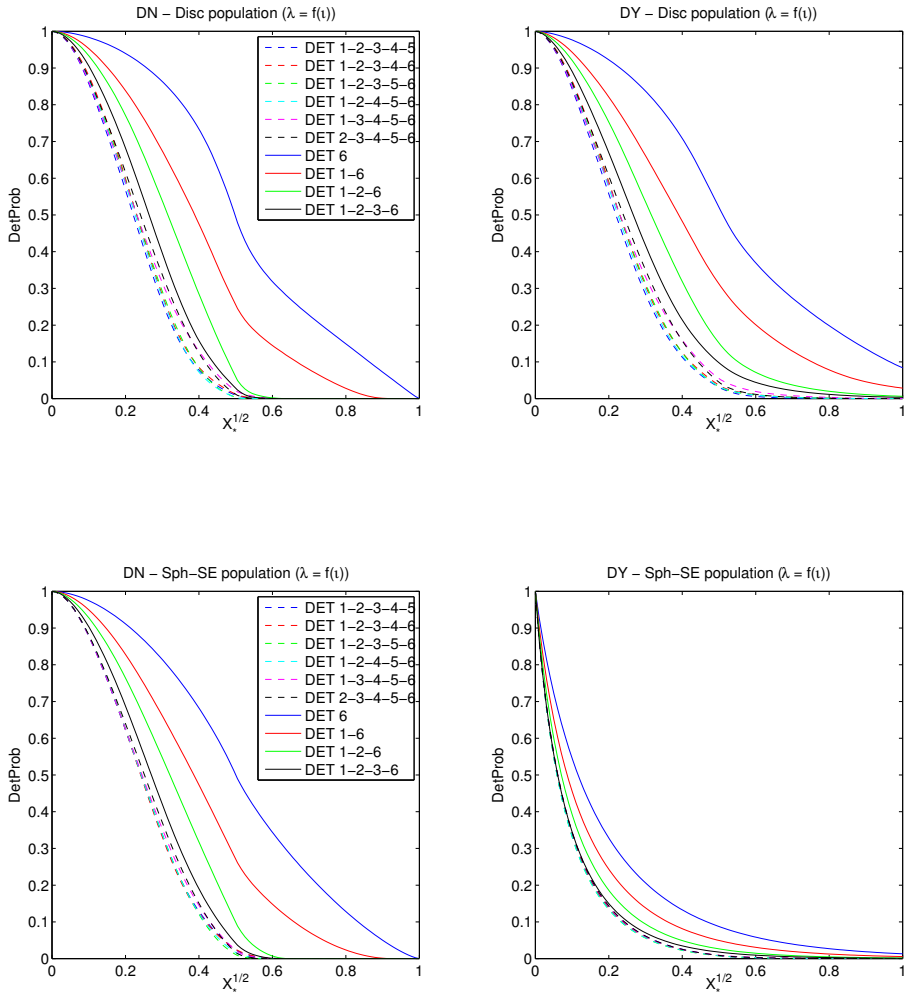

Figure 2.36: Time-averaged detection probability curves for antennae working individually and in fives, for the disc-shaped and spherical-SE populations, and signals polarised with $\lambda = f(\iota)$.

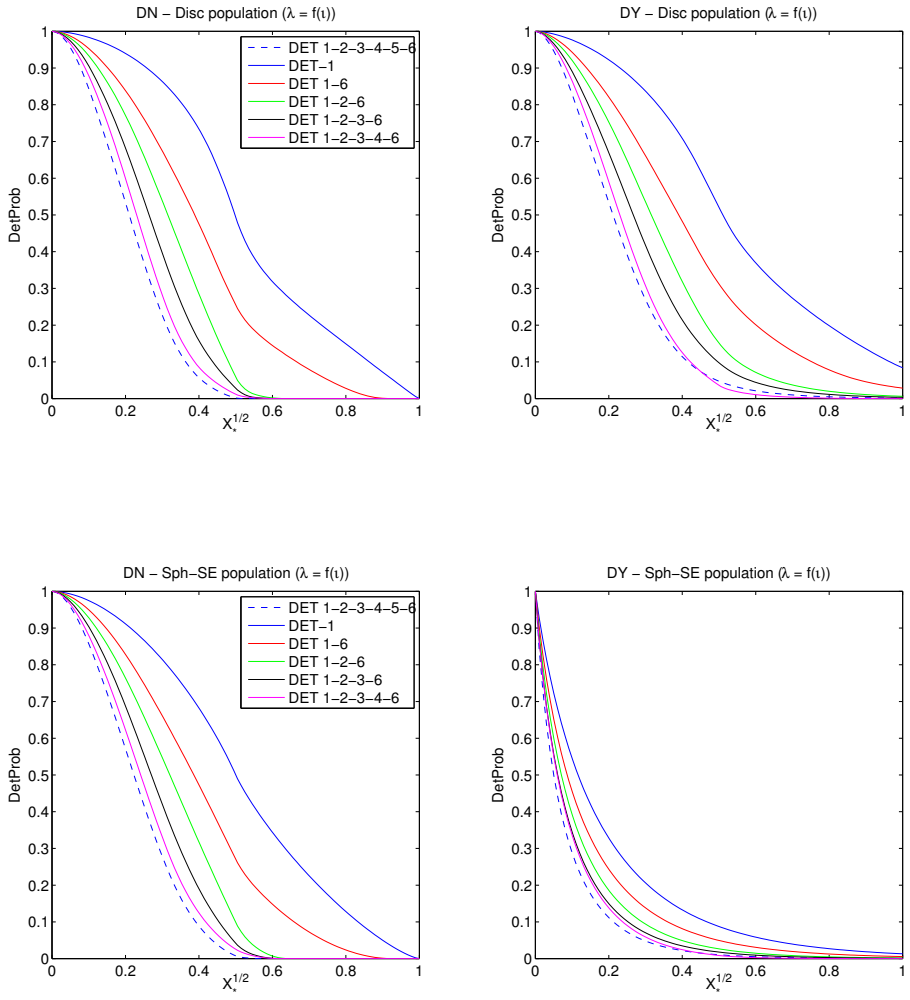

Figure 2.37: Detection probability curves for antennae working individually and in networks of two, three, four, five and six antennae, for disc-shaped and spherical-SE populations, and signals polarised with $\lambda = f(\iota)$.

2.7 Review of chapter and conclusions

Three galactic neutron star populations were presented in section 2.2: two are galactocentric, one disc-shaped and another spherical; the third is spherical geocentric. Distributions of the distances to sources from Earth, their declination and right ascension were inferred for these populations.

In Section 2.3, following (91), a systematic procedure to calculate antenna pattern and power values and the concept of distance factor is introduced; this modulates the antenna pattern values depending on the proximity of the source to the Earth. This leads to the time- and polarisation-averaged antenna patterns and to the directional sensitivity maps for a detector, first in its own local frame and then in a more generic frame. A list of the studied detectors is provided: all are well-known apart from a hypothetical one in the future located in the south hemisphere to enrich the analysis.

In Section 2.4 the detectability of signals from galactic neutron stars was studied as a function of the location and orientation of the detector, assuming signals of various polarisation degrees. The analysis concentrated first on two particular sky-directions (galactic centre and Virgo cluster) and was extended subsequently for the case of the NS populations defined previously. A preference for the location of the detector on the equator and azimuthal '$\times$' orientation was concluded for the galactocentric populations. Intuitively, this can be understood by considering that it is a detector located in the equator the one that sweeps the biggest area in the celestial sphere by the effect of the Earth's rotation.

Histograms in Section 2.5 of time- and polarisation-averaged antenna pattern values have been used to compare the detectability of well-known gravitational wave detectors to burst gravitational waves from neutron stars of the populations modeled. The sidereal times when the detectors are most sensitive to galactocentric NS populations are calculated. In Section 2.6 detection probabilities were calculated by inferring the fraction of trials for which the antenna power is over a particular threshold. Results are presented for detectors working as single antennae or as part of a network, where more or less suitable combinations of detectors are identified. Coefficients of Chebyshev polynomials to fit the detection probability curves are given in the Appendix F.

Chapter 3

Signal in the time and frequency domain

3.1 Introduction

In this chapter a burst gravitational signal is modeled as an exponentially damped sinusoid, the way chosen to model a gravitational wave ringdown signal emitted by a neutron star suddenly taken out of equilibrium (see Section 1.4.2). The emission of gravitational radiation is thought to be an important damping mechanism but of uncertain duration. Furious boiling of a recently born neutron star after core collapse or the sudden change in the structure of the neutron star (sometimes reflected as glitching in the radio signal emitted), may be two examples of the burst signal modeled here.

The ringdown signal is characterised by the amplitude, oscillation frequency, damping time and polarization (degree and orientation) of the gravitational signal. Its detection depends on the strength of the signal projected onto the detector that results from the relative orientation between the source and the detector.

This chapter presents various time to frequency transformations that are subsequently applied onto our particular signal in question, the exponentially damped sinusoid or ringdown signal. It is introductory material summarising common data analysis techniques (see (93)) and applied to our signal in question. In Section 3.2 the discrete time version of the signal is derived by a conversion from

continuous to discrete time notation - time goes to sample index and the frequency goes to radians per sample. In Section 3.3 the ringdown signal is modeled in the frequency domain by using the discrete Fourier transforms. Useful relations betweem the Discrete Fourier Transform (DFT) and the Discrete Time Fourier Transform (DTFT) are presented, showing the possibility of computing the Fourier coefficients of a finite discrete signal using the analytical form that provides the Fourier coefficients of the corresponding infinite signal. This allows a quick computation of the Fourier coefficients for the frequency points desired, mostly concentrated in narrow bandwidths in the case of our signal. The relation between the DFT and DTFT with the more generic z-transform is shown in Section 3.4. This is interesting with regards to the way of obtaining the Fourier coefficients of a time-shifted version of the signal.

3.2 Signal in the time domain

A gravitational wave signal detected by a laser interferometric gravitational antenna is generally represented as a weighted combination of its two polarisation components ('+' and '×') (91). The continuous adimensional strain inflicted on the detector by the wave can be written as:

$$h(t) = \frac{\delta l(t)}{l_0} = -\sin(2\Omega)[F_+ h_+(t) + F_\times \exp(i\delta) h_\times(t)], \tag{3.1}$$

where, again, 2Ω is the angle subtended between the arms of the interferometer. The *antenna pattern functions* F_+ and $F_\times$ take values in the range [-1,1] depending on the relative orientation, between the direction in which the wave propagates and the detector, and the orientation of the polarisation axes with respect to the arms of the detector. Appendix D describes a systematic way of calculating F_+ and $F_\times$, both when the location of the source is given in the detector's reference frame, and more generally, when the equatorial coordinates of the source and time of the event are known.

An elliptically polarised gravitational wave can be described mathematically in a similar fashion to an electromagnetic wave by the combination of the two polarisation components. It is always possible to choose the orientation of the

polarisation axes ψ to coincide with the axes of the polarisation ellipse, see (91), so that:

$$\delta = \pm\,\pi/2, \quad h_\times = \lambda h_+ \tag{3.2}$$

where λ is a real number in the interval [0,1] called the *degree of elliptical polarisation*. For a ringdown signal let us consider each of the polarisation components, individually, as sine-exponentials:

$$h_+ = h_{0+}\, e^{-t/\tau} \sin(\Omega_0 t) \tag{3.3a}$$

$$h_\times = h_{0\times}\, e^{-t/\tau} \sin(\Omega_0 t) \tag{3.3b}$$

where τ is the damping time and Ω_0 is the oscillation frequency. Assuming the detection of the signal by a L-shaped interferometer ($2\Omega = \pi/2$) and considering $h_{0+} = h_0$ and $h_{0\times} = \lambda h_0$, Eq. 3.1 can be written as:

$$h(t) = h_0\, e^{-t/\tau}[F_+ \sin(\Omega_0 t) + \lambda F_\times \cos(\Omega_0 t)]. \tag{3.4}$$

This is the representation of a continuous signal. In practice, detector data is sampled and recorded discretely in time and as a consequence, the analysis of the data recorded by the gravitational wave detector is generally carried out in discrete time.

Let us now introduce our signal model in Eq. 3.4 with a slightly different notation more convenient to handle the discrete signals resulting from the sampling process of their continuous counterparts. Instead of the continuous time variable (t), the sample number $[n]$ may be used to represent discrete time values. The sampling process can be written mathematically as:

$$h[n] = h(t)|_{t=nT}, \quad \text{for} \quad n = 0, 1, 2, ... \tag{3.5}$$

where T is the *sampling interval* or the time between two consecutive samples. The *sampling frequency* is the inverse of the sampling interval, $f_s = 1/T$, and $\Omega_s =$

$2\pi f_s$ is known as the *sampling angular frequency*. Using the discrete notation Eq. 3.4 converts as:

$$h[n] = h_0 e^{-a\cdot[n]}[F_+ \sin(w_0 \cdot [n]) + \lambda F_\times \cos(w_0 \cdot [n])] \cdot \mu[n], \tag{3.6}$$

where $[n] = -\infty, ..., -1, 0, 1, ..., \infty$ are the discrete sample numbers and $\mu[n]$ is the unitary step at $n = 0$, so that only positive values of $[n]$ are considered. $w_0 = 2\pi\Omega_0/\Omega_s = \Omega_0 T$ is the discretised oscillation frequency (in rad sample^{-1}) and $a = 2\pi/(\Omega_s \tau)$ is the discretised damping time (in samples^{-1}). For a detailed derivation of the discretised expression of the signal see appendix G. Simplifying the notation, Eq. 3.6 can be written as:

$$h_{SC}[n] = e^{-an}[C_S \sin(w_0 n) + C_C \cos(w_0 n)] \tag{3.7}$$

where $C_S = h_0 F_+$, $C_C = \lambda h_0 F_\times$. Fig. 3.1 shows an example of a discretised signal as a combination of a sine and a cosine-exponential given by Eq. 3.7.

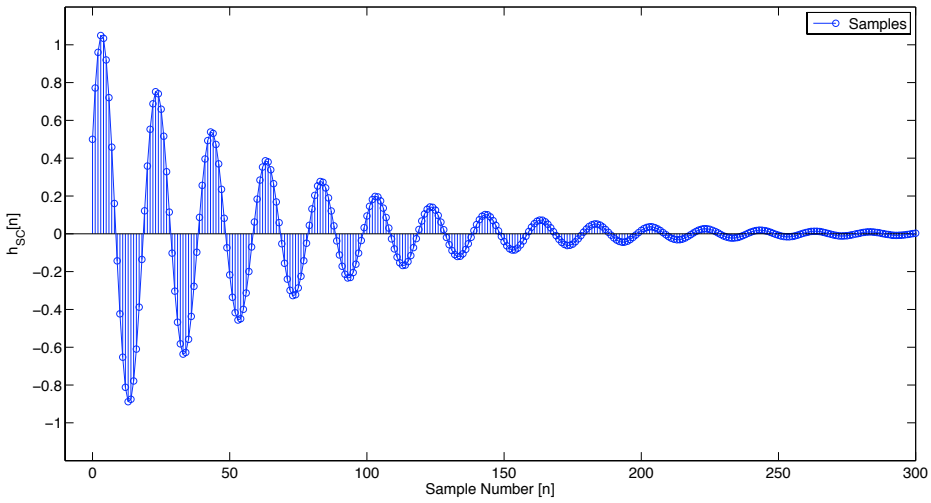

Figure 3.1: Discrete version of an exponentially damped sinusoid (Eq. 3.7) of arbitrary parameter values $C_S = 1$ and $C_C = 0.5$, $\Omega_s/\Omega_0 = 20$ samples per cycle ($w_0 = 2\pi\Omega_0/\Omega_s = \pi/10 = 0.3142$ rad/sample) and inverse damping time of $a = 2\pi/(\Omega_s\tau) = 1/60$ samples^{-1}.

3.3 Signal in the frequency domain

Throughout this work the frequency representation of discrete exponentially damped sinusoidal signals have been used repeteadly. These can be readily obtained through a Fourier transform of the time-domain representation. There are various types of Fourier transforms depending on whether the signal is continuous or discrete, and whether the frequency representation is periodic or not. For the frequency analysis of discrete signals the Discrete Fourier Transform (DFT) and its fast algorithm called Fast Fourier Transform (FFT) are convenient and often used.

In the following, the Continuous Time Fourier Transform (CTFT), the discrete time Fourier transform (DTFT) and its relation to the Discrete Fourier Transform (DFT) are presented. This is to explain the computational advantage provided by the close form DTFT with respect to the DFT. For more details and the conventions used in the following pages, see (93).

In the following sections different Fourier transforms are presented for a ring-down signal presented in Fig. 3.1 of arbitrary parameter values $C_S = 1$ and $C_C = 0.5$ (elliptical polarisation of $\lambda = 0.5$), $\Omega_s/\Omega_0 = 20$ samples per cycle ($w_0 = 2\pi\Omega_0/\Omega_s = \pi/10 = 0.3142$ rad/sample) and inverse damping time of $a = 2\pi/(\Omega_s\tau) = 1/60$ samples^{-1}.

3.3.1 Continuous Time Fourier Transform (CTFT)

Generally, continuous signals in the time-domain can be transformed into the frequency-domain with the CTFT. The result is a continuous spectrum of infinite bandwidth of real frequency values ($-\infty < \Omega < \infty$). The inverse transformation, called the *Fourier Integral*, allows the recovery of the original signal as a sum of infinitesimally small complex exponential terms of the form $1/(2\pi)e^{j\Omega}d\Omega$. The continuous Fourier transform $X_a(j\Omega)$ and its inverse $x_a(t)$ can be written as:

$$\mathscr{F}_{CTFT}\{x_a(t)\} = X_a(j\Omega) = \int_{-\infty}^{\infty} x_a(t)e^{-j\Omega t}\,dt \tag{3.8a}$$

$$\mathscr{F}^{-1}_{CTFT}\{X_a(j\Omega)\} = x_a(t) = \frac{1}{2\pi}\int_{-\infty}^{\infty} X_a(j\Omega)e^{j\Omega t}d\Omega. \tag{3.8b}$$

The CTFT of exponentially damped sine and cosine functions are:

$$x_S(t) = e^{-bt}\sin(\Omega_0 t) \Longleftrightarrow X_S(j\Omega) = \frac{\Omega_0}{[b^2 + \Omega_0^2 + \Omega^2] + j\,2b\Omega} \tag{3.9a}$$

$$x_C(t) = e^{-bt}\cos(\Omega_0 t) \Longleftrightarrow X_C(j\Omega) = \frac{j\,\Omega}{[b^2 + \Omega_0^2 + \Omega^2] + j\,2b\Omega} \tag{3.9b}$$

where $b = 1/\tau$ is the inverse of the damping time and Ω_0 is the angular oscillation frequency. The Fourier transform is commutative and linear and the CTFT of the combination of two continuous exponential sinusoids defined in Eq. 3.4 can be written as:

$$h_{SC}(t) = C_S x_S(t) + C_C x_C(t) \Longleftrightarrow H_{SC}(j\Omega) = C_S X_S(j\Omega) + C_C X_C(j\Omega) \tag{3.10a}$$

$$= \frac{C_S\Omega_0 + j\,C_C\Omega}{[b^2 + \Omega_0^2 + \Omega^2] + j\,2b\Omega}. \tag{3.10b}$$

The spectrum of the signal defined continuously in Eq. 3.10 is a complex function of real valued frequencies Ω and can be represented equivalently by the pairs of *Real* $\Re\{H_{SC}(j\Omega)\}$ and *Imaginary* $\Im\{H_{SC}(j\Omega)\}$ coefficients, or *Magnitude* $|H_{SC}(j\Omega)|$ and *Phase* $\Theta(j\Omega)$ components. Fig. 3.2 shows the two pairs of variables that represent the CTFT of Eq. 3.4 as per Eq. 3.10.

3.3.2 Discrete Time Fourier Transform (DTFT)

The DTFT of a discrete-time sequence $x[n]$ is the representation of the signal in terms of the complex exponentials e^{-jwn}, where w is the real frequency variable. If the DTFT exists, it is unique and the original sequence can be recovered by applying the inverse of the original transformation.

$$\mathscr{F}_{DTFT}\{x[n]\} = X(e^{jw}) = \sum_{n=-\infty}^{\infty} x[n]\,e^{-jwn} \tag{3.11a}$$

$$\mathscr{F}^{-1}_{DTFT}\{X(e^{jw})\} = x[n] = \frac{1}{2\pi}\int_{-\pi}^{\pi} X(e^{jw})\,e^{jwn}dw. \tag{3.11b}$$

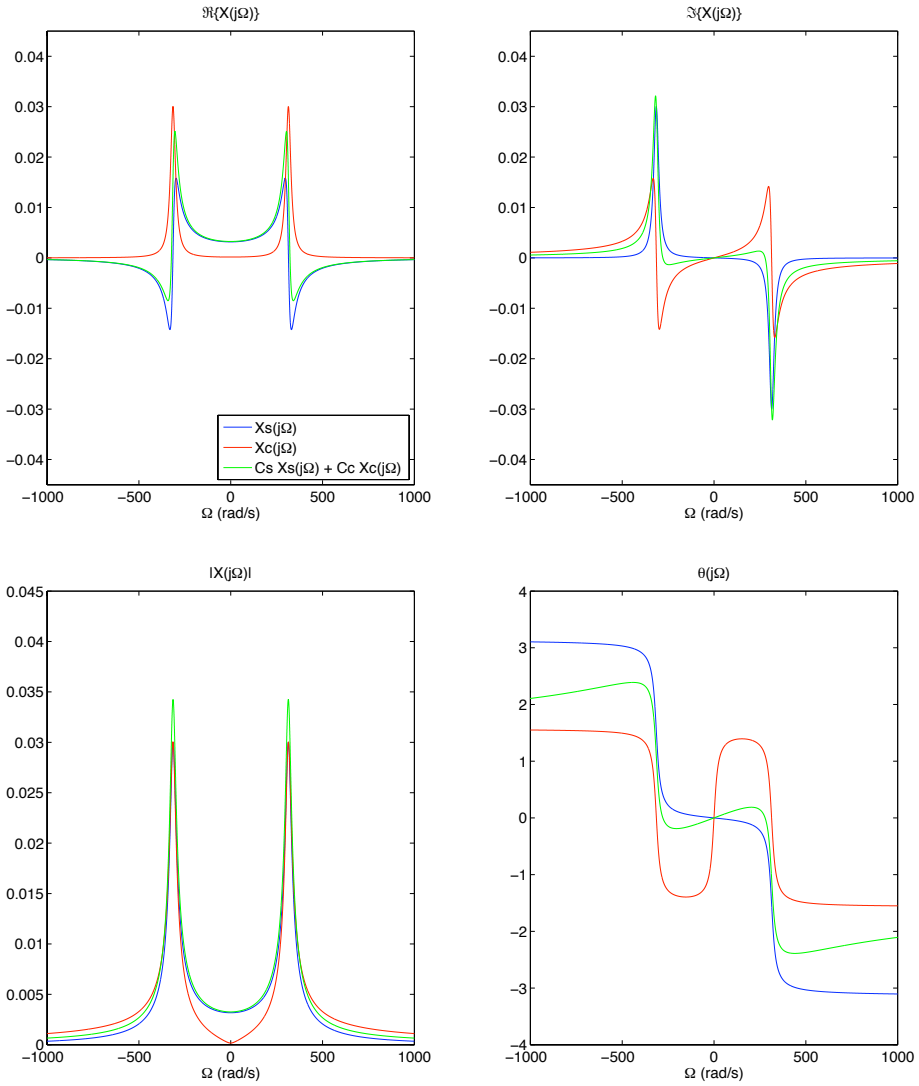

Figure 3.2: Continuous Time Fourier Transform (CTFT) of an exponentially dampened sinusoidal signal (see Fig. 3.1) given by Eq. 3.10. The spectrum is non-periodic and defined continuously in the range $[-\infty,\infty]$. The upper two subplots show the real and imaginary coefficients and the lower two subplots show the equivalent pair, magnitude and phase. The two peaks are located at the positive and negative oscillation frequency Ω_0.

The result of the DTFT is a complex function $X(e^{jw})$ (periodic in 2π) that can be written in rectangular form as a combination of *real* and *imaginary* coefficient functions:

$$X(e^{jw}) = X_{re}(e^{jw}) + j\, X_{im}(e^{jw}), \quad \text{where} \quad \begin{cases} X_{re}(e^{jw}) = \Re[X(e^{jw})] \\ X_{im}(e^{jw}) = \Im[X(e^{jw})], \end{cases} \tag{3.12}$$

or alternatively, as a combination of *magnitude* and *phase* functions:

$$X(e^{jw}) = |X_{re}(e^{jw})|e^{j\theta(w)}, \quad \text{where} \quad \begin{cases} |X(e^{jw})| = [X_{re}^2(e^{jw}) + X_{im}^2(e^{jw})]^{-1/2} \\ \theta(w) = \tan^{-1}\{X_{im}(e^{jw})/X_{re}(e^{jw})\}. \end{cases} \tag{3.13}$$

For a real discrete sequence $x[n]$, $X_{re}(e^{jw})$ and $|X(e^{jw})|$ are even functions, whereas $X_{im}(e^{jw})$ and $\theta(w)$ are odd functions. For most practical discrete-time sequences, the DTFT is a convergent geometric series, which may be summarised as a simple closed-form. The DTFT of exponentially damped sinusoidal signals of infinite duration, defined for positive values of $[n]$, can be expressed in closed form as follows:

$$x_S[n] = e^{-an}\sin(w_0 n)\,\mu[n] \Longleftrightarrow X_S(e^{jw}) = \frac{w_0}{[a^2 + w_0^2 + w^2] + j2aw} \tag{3.14a}$$

$$x_C[n] = e^{-an}\cos(w_0 n)\,\mu[n] \Longleftrightarrow X_C(e^{jw}) = \frac{a + jw_0}{[a^2 + w_0^2 - w^2] + j2aw} \tag{3.14b}$$

Again, due to the commutative and linearity properties of the Fourier transforms, Eqs. 3.14 can be combined and the corresponding DTFT expression of the discrete signal in Eq. 3.7 can be written as:

$$h_{SC}[n] = C_S x_S[n] + C_C x_C[n] \Longleftrightarrow H_{SC}(e^{jw}) = C_S X_S(e^{jw}) + C_C X_C(e^{jw}) \tag{3.15a}$$

$$= \frac{C_S w_0 + C_C a + j\, C_C w_0}{[w_0^2 + a^2 - w^2] + j\, 2aw}. \tag{3.15b}$$

Fig. 3.3 shows the real and imaginary coefficients and the equivalent magnitude and phase pair representation of the expression in Eq. 3.15. The DTFT is periodic

in 2π and it is customary to present its spectrum on a normalised frequency axis $w/\pi \in [0, 2]$. Showing only half of the period $w/\pi \in [0, 1]$ is enough to characterise the signal because the real coefficients and magnitude values are even functions, whereas the imaginary coefficients and phase values are odd functions.

3.3.3 Discrete Fourier Transform (DFT)

The DFT provides a transformation from the discrete time-domain to the discrete frequency-domain. The DFT of a discrete signal $x[n]$ of length N is defined as:

$$\mathscr{F}_{DFT}\{x[n]\} = X[k] = \sum_{n=0}^{N-1} x[n]\, e^{-j2\pi kn/N}, \quad 0 \leq k \leq N-1 \tag{3.16a}$$

$$\mathscr{F}^{-1}_{DFT}\{X[k]\} = x[n] = \frac{1}{N} X[k]\, e^{j2\pi kn/N}, \quad n = 0, ..., N-1. \tag{3.16b}$$

The transform results in the mapping of the N time-points to the same number of frequency-points. It can be efficiently computed with the Fast Fourier Transform algorithm (FFT).

3.3.4 Relation between DTFT and DFT

The N-point DFT $X[k]$ of a discrete signal $x[n]$ is simply the DTFT $X(e^{jw})$ evaluated at N uniformly spaced frequency points $w_k = 2\pi k/N$, for $0 \leq k \leq N-1$. This is an interesting relation, for when the closed form of the DTFT exists and is known, it allows the computation of the results of a N-point DFT just by evaluating the analytical function of the DTFT at the desired frequency points with:

$$X[k] = X(e^{jw})|_{w=2\pi k/N}, \quad \text{for} \quad 0 \leq k \leq N-1. \tag{3.17}$$

The frequency resolution of the DFT depends on the number of points N to be transformed, $f_{res} = f_s/N$. An increase in the frequency resolution can be gained at the expense of processing a bigger number of points, zero-padding if required, but thin turn increases the computation time. If the closed-form of the DTFT is

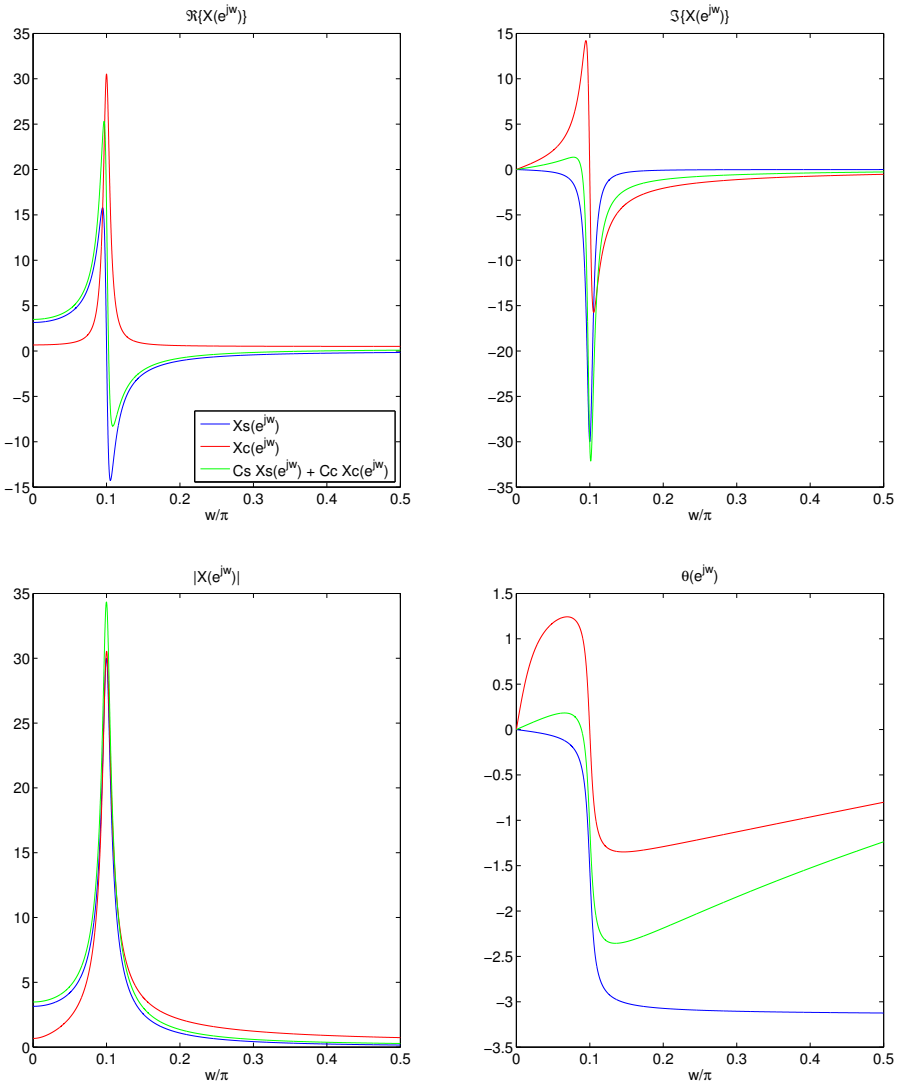

Figure 3.3: Discrete Time Fourier Transform (DTFT) of an exponentially dampened sinusoidal signal (see Fig. 3.1) plotted using the expression in Eq. 3.15. The spectrum is periodic in 2π and continuous but only the relevant quarter of the period is shown here, for clarity.

known, it is straight-forward and faster to materialise a discrete Fourier transform and calculate as many frequency points as desired.

Fig. 3.4 shows the comparison of the real and imaginary coefficients of the DTFT, the curve given by the closed form in Eq. 3.15, corresponding to a signal of infinite length, with a DFT of $N = 1000$ point DFT of the discrete signal of length 15τ given by Eq. 3.7.

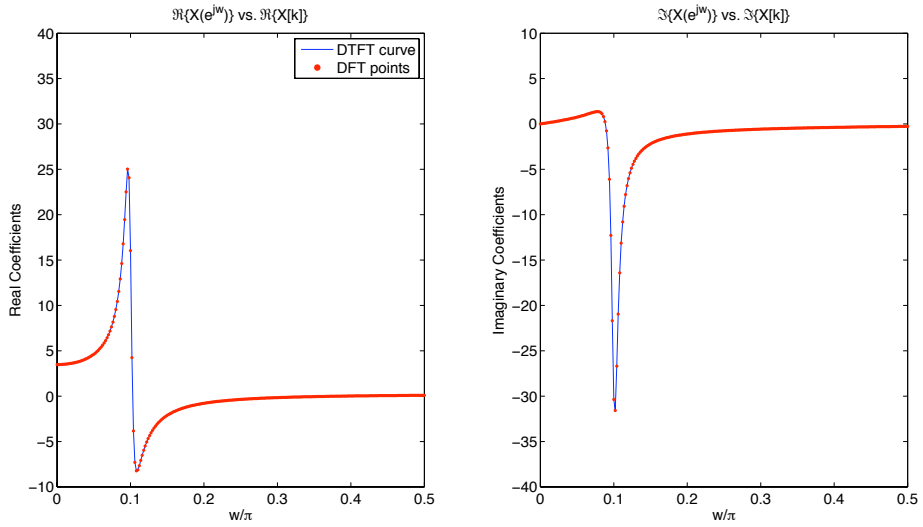

Figure 3.4: Comparison of the DTFT curve with the $N = 1000$ point DFT. Note that the DFT points lay exactly on the DTFT curve, showing that the computation of values at the desired frequency points using the closed form of the DTFT (see Eq. 3.15), is equivalent to do a DFT of a finite discrete signal (see Eq. 3.16a). Only a quarter of the period 2π is shown here, for clarity.

In the case of damped signals, the DTFT of a discrete signal of finite length that captures the non-zero region does not differ significantly from the DTFT of the corresponding signal of infinite length. This is convenient, for once the signal decays, it does not add more power to the spectrum and the closed-form representation for the infinite series (see Eq. 3.15) is valid for the DTF of a finite and truncated discrete signal that captures the relevant part of the signal. In Fig. 3.5 the case of an exponentially damped sinusoid is shown and it is observed that the DTFT of a finite signal of length 5τ is already quite a good approximation to the closed-form corresponding to the infinite sequence.

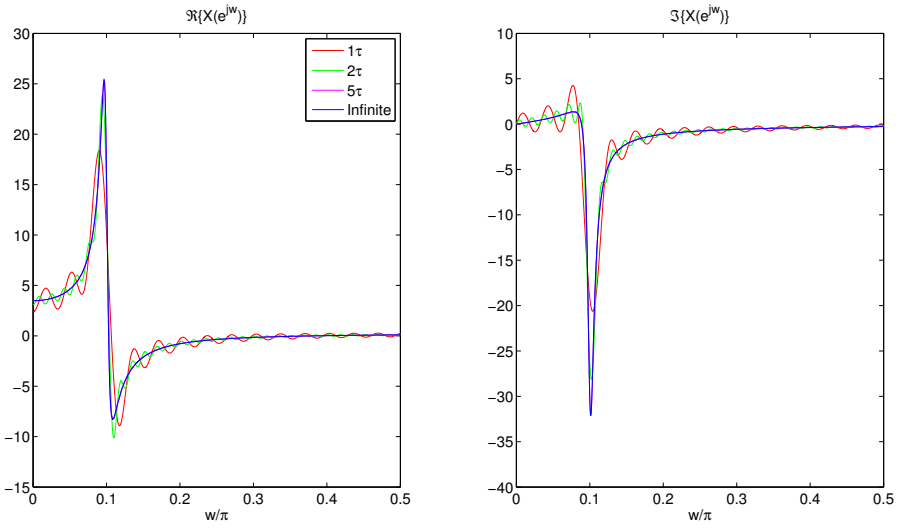

Figure 3.5: Real and imaginary curves of the DTFT of the signal in Fig. 3.1. The result of the closed form (Eq. 3.15) corresponding to the signal of infinite length is compared with its truncated (finite duration) versions of τ, 2τ and 5τ. The DTFT for the truncated signals has been obtained by adding a finite number of exponential terms (Eq. 3.11a). Note that for signals longer than 5τ the result of the addition of complex terms is very similar to the closed form, underpinning the decision using the later to calculate the DFT of damping signals longer than 10τ.

3.4 The z-transform

The relation between the z-transform and the discrete time Fourier transform is presented: the z-transform and its properties provide convenient tools to calculate the Fourier transform of a discrete shifted signal, once the transform of its non-shifted version is known.

The generalisation of the Fourier transform of discrete signals leads to the z-transform, a function of the complex variable $z = re^{jw}$. For real valued sequences $x[n]$, the z-transform is a rational function of the complex variable z and is defined as follows:

$$\mathscr{Z}\{x[n]\} = G(z) = \sum_{n=-\infty}^{\infty} x[n]z^{-n} = \sum_{n=-\infty}^{\infty} x[n]r^{-n}e^{-jwn}. \tag{3.18}$$

For the case of $r = 1$ ($|z| = 1$) the z-transform $G(z)$ reduces to the DTFT expression, when this exists. For most of the discrete functions the sum of terms in z can be expressed in closed analytical form:

$$G(z) = \frac{p_0 + p_1 z^{-1} + ... + p_{M-1}z^{-(M-1)} + p_M z^{-M}}{d_0 + d_1 z^{-1} + ... + d_{N-1}z^{-(N-1)} + d_N z^{-N}}. \tag{3.19}$$

The z-transforms of the discrete damped sinusoidal functions in Eqs. 3.14 are:

$$x_S[n] = r^n \sin(w_0 n)\mu[n] \Longleftrightarrow X_S(z) = \frac{r \sin w_0 z^{-1}}{1 - 2r\cos w_0 z^{-1} + r^2 z^{-2}}, \quad |z| > |r| \tag{3.20a}$$

$$x_C[n] = r^n \cos(w_0 n)\mu[n] \Longleftrightarrow X_C(z) = \frac{1 - r\cos w_0 z^{-1}}{1 - 2r\cos w_0 z^{-1} + r^2 z^{-2}}, \quad |z| > |r| \tag{3.20b}$$

where $r = e^{-a} = e^{-2\pi/(\Omega_s \tau)} = e^{-1/(f_s \tau)}$ and, again, $\mu[n]$ limits the time-domain to positive values of n, for a causal signal. The region of convergence $|z| > |r|$ assures that there is a unique relation between the z-transform and the discrete-time sequence. For a detailed derivation of these formulae, see (93). If the z-transform can be written in closed form as a rational function, the values corresponding to the desired discrete frequency points can be readily computed in Matlab (94) using the *freqz* command. In Table 3.1, we highlight two important properties of

	Time domain **Discrete signals**	**Frequency domain** **z-transform**
Linearity	$\alpha\ g[n] + \beta\ h[n]$	$\alpha\ G(z) + \beta\ H(z)$
Time-shift (n_0 points)	$g[n - n_0]$	$z^{-n_0}G(z)$

Table 3.1: Two useful properties of the z-transform.

the z-transform that ease the calculation of the frequency transforms of signals shifted discretely in time later.

Due to the *linearity* property the z-transform of the exponentially damped signal $h_{SC}[n]$ in Eq. 3.15 can be written as a combination of the Eqs. 3.20 to obtain:

$$H_{SC}(z) = C_S X_S(z) + C_C X_C(z) = \frac{1 - r(C_S \sin w_0 - C_C \cos w_0)z^{-1}}{1 - 2r \cos w_0 z^{-1} + r^2 z^{-2}} \tag{3.21}$$

where, again, $C_S = h_0 F_+$ and $C_C = \lambda h_0 F_\times$ are the amplitudes of the sine and cosine exponentials, respectively, and w_0 is the angular frequency of the oscillation in rad sample^{-1}.

3.4.1 Time-shifted signal

Mathematically, the discrete time-shifted version of the modeled signal in Eq. 3.7 can be written in the form:

$$\begin{aligned} h_{SCsh}[n] &= h_{SC}[n - n_0] \\ &= e^{-a\,[n-n_0]}[C_S \sin(w_0[n - n_0]) + C_C \cos(w_0[n - n_0])], \end{aligned} \tag{3.22}$$

where n_0 is the number (integer) of samples the signal has been shifted. Fig. 3.6 depicts the same signal as in Fig. 3.1 shifted by $n_0 = 10$ samples to the right. Note that for a data stretch of finite duration. The time-shift involves zero-padding n_0 samples from the left and truncating n_0 samples from the right. However, if a long enough stretch of data is considered, this is not a problem for exponentially damped signals, for no relevant data is lost from the right hand side.

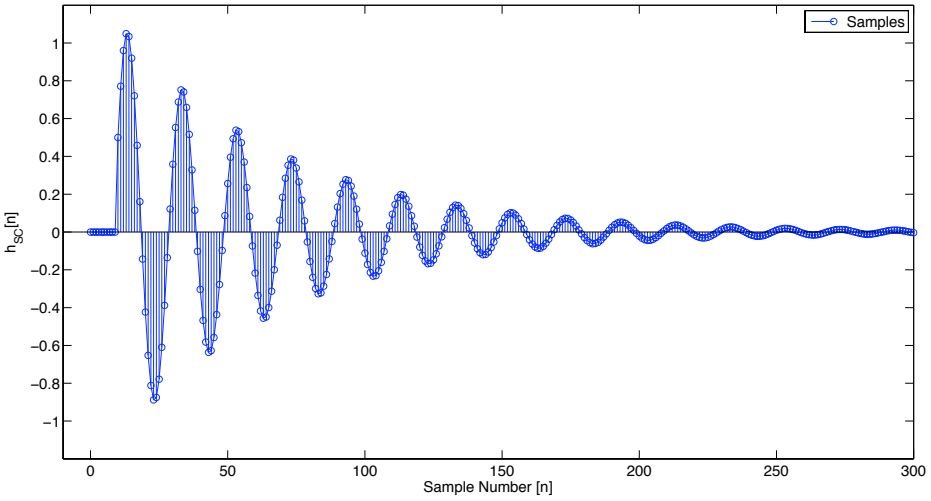

Figure 3.6: Signal in Fig. 3.1 shifted $n_0 = 10$ samples to the right.

Once the z-transform $\mathscr{Z}(x[n])$ of a function is known, the z-transform of its time-shifted version $\mathscr{Z}(x[n-n_0])$ can be readily calculated using the properties summarised in Table 3.1. Following these rules, the z-transform of a time-shifted exponentially damped sinusoid can be written as:

$$\begin{aligned} x_{Ssh}[n] &= x_S[n-n_0] \\ &= r^{n-n_0}\sin(w_0[n-n_0]) \Longleftrightarrow X_{Ssh}(z) = \frac{r\sin w_0 z^{-(n_0+1)}}{1-2r\cos w_0 z^{-1}+r^2z^{-2}} \end{aligned} \tag{3.23a}$$

$$\begin{aligned} x_{Csh}[n] &= x_C[n-n_0] \\ &= r^{n-n_0}\cos(w_0[n-n_0]) \Longleftrightarrow X_{Csh}(z) = \frac{z^{-n_0}-r\cos w_0 z^{-(n_0+1)}}{1-2r\cos w_0 z^{-1}+r^2z^{-2}}, \end{aligned} \tag{3.23b}$$

where the subindex S_{sh} and C_{sh} stand for sine and cosine shifted signals, respectively. Making use of the linearity property we can write the z-transform of Eq. 3.7 as:

$$X_{SCsh}(z) = \frac{z^{-n_0}+r[C_S\sin w_0 + C_C\cos w_0]z^{-(n_0+1)}}{1-2r\cos w_0 z^{-1}+r^2z^{-2}}. \tag{3.24}$$

Fig. 3.7 compares the DTFT spectra of exponentially damped signals time-shifted a different number of samples to the right.

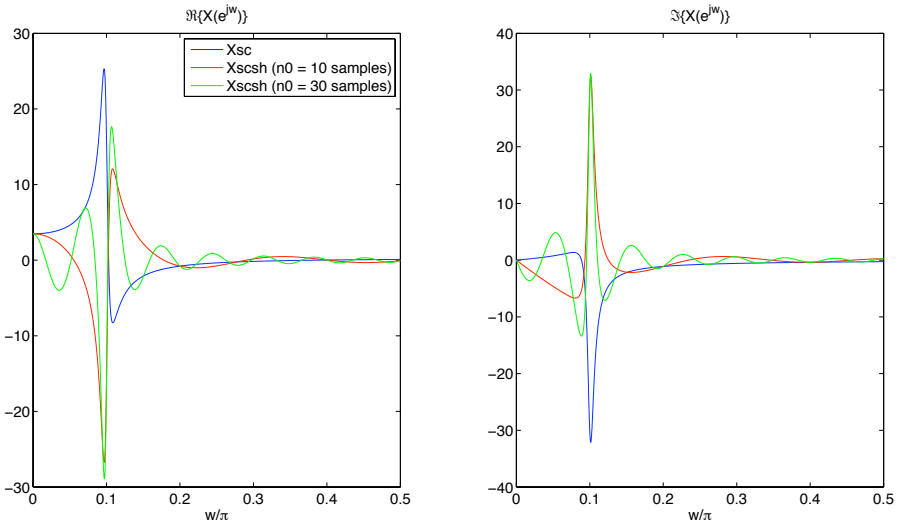

Figure 3.7: Real and imaginary coefficients of the DTFT spectra of the signal shown in Fig. 3.1 shifted a different number of samples to the right. The spectra have been calculated with the expression in Eq. 3.24.

Chapter 4

Bayesian Data Analysis

4.1 Introduction

Historically, the quantification of the probability has been exemplified by the *frequentist approach*, where the repetition of an experiment multiple times can be done, or at least conceived, and conclusions extracted. The probability assigned to each of the possible outcomes is stipulated as their rate of realisation. Rolling a dice and calculating the probability of getting any particular side up is a clear example: after millions of trials the overall number of positive outcomes would be expected to be very close to 'one out of six'.

Bayesian probability, in stark opposition to the frequentist probability, provides a more natural approach to the quantification of probability. One of the merits of the Bayesian probability is that its calculation allows the inclusion of factors (related information known before analysing the data) that may alter the balance of probability towards full certainty or full uncertainty.

The Bayesian computation of probability combines the information provided by the data obtained in the experiment with any prior beliefs or assumptions about the hypothesis being considered. The information given by the data is the *Likelihood* and measures the possibility of getting those and no other data. It is interpreted as the level of fitness between our hypothesis, generally symbolised as a mathematical function, and the data. The priors are lighter or stronger beliefs before the acquisition of the data that will shape our final belief.

Bayesian inference has been applied for the data analysis in diverse fields, particularly where the characterization of weak signals masked by noise is required. Astronomy and particle physics are fields where Bayesian data analysis has been applied successfully: image reconstruction (95), model selection in Cosmology (96), analysis of Cosmic Microwave Background data (97), Extrasolar planet detection (98), etc.

The astronomical branch of gravitational wave detection have made ample use of Bayesian inference too, in order to analyse the data obtained by a network of detectors and carry out model comparison and parameter estimation. Different type of expected gravitational wave signals have been analysed. In the following some references relevant to the work presented in this thesis are mentioned: Bayesian approach to the detection problem in gravitational wave astronomy (99), gravitational waves from in-spirals by a network of detectors (100; 101; 102), white-dwarfs on LISA data (103), estimation of pulsar parameters from gravitational wave data (104), robust Bayesian detection of unmodelled bursts (15; 105), Bayesian inference with nested sampling algorithm (106).

4.2 Bayesian Inference

In Bayesian inference the likelihood of each of a set of competing hypotheses $\{H_i\}$ can be computed in light of the observed data and any previous information prior to the acquisition of the data – the prior information specifies the hypotheses being considered and their relation with the data. The Bayesian notation $p(H_i|\mathbf{D}, I)$ expresses the probability of a hypothesis H_i, given the data $\mathbf{D}$ and the prior information I, where the arguments must be understood as propositions. Two basic rules build the principles of Bayesian probability calculation: The *sum rule*,

$$p(H_i|I) + p(\bar{H}_i|I) = 1, \tag{4.1}$$

where $\bar{H}_i$ signifies the proposition that is true if one of the alternatives to H_i is true; and the *product rule*,

$$p(H_i, \mathbf{D}|I) = p(H_i|I)p(\mathbf{D}|H_i, I) = p(\mathbf{D}|I)p(H_i|\mathbf{D}, I), \tag{4.2}$$

which splits the combined probability of two propositions in two alternative ways. Reordering Eq. 4.2 we arrive at the *Bayes theorem*, the most important equation to compute probabilities within Bayesian inference,

$$p(H_i|\mathbf{D}, I) = \frac{p(H_i|I)p(\mathbf{D}|H_i, I)}{p(\mathbf{D}|I)}. \tag{4.3}$$

The Bayes theorem describes a learning process in which the probability of each hypothesis considered is shaped in light of new data acquired. $p(H_i|I)$ is the *prior probability* of the hypothesis H_i before considering the data. After considering the data the probability of that hypothesis, $p(H_i|\mathbf{D}, I)$, is called *posterior probability*. $p(\mathbf{D}|H_i, I)$ measures the ability of hypothesis H_i to explain the data acquired and is called the *likelihood*, and $p(\mathbf{D}|I)$ is the evidence or global likelihood for the set of hypotheses. The sum of the posterior probabilities of all the hypotheses considered must equal to one $\sum_i p(H_i|\mathbf{D}, I) = 1$. That is why:

$$p(\mathbf{D}|I) = \sum_i p(H_i|I)p(\mathbf{D}|H_i, I). \tag{4.4}$$

4.2.1 Model comparison

In an effort to understand an experimental result, there may be interest in comparing various parameterized models put forward in order to explain the outcome of the experiment. The models may differ in shape and in number of parameters. The selection of the most appropriate model to explain the data can be done by means of a model comparison exercise. It is common to compare two models, M_i and M_j, by calculating their odds ratio, the ratio of their posterior probabilites:

$$O_{ij} = \frac{p(M_i|\mathbf{D})}{p(M_j|\mathbf{D})} = \frac{p(M_i|I)}{p(M_j|I)} \frac{p(\mathbf{D}|M_i, I)}{p(\mathbf{D}|M_j, I)} = \frac{p(M_i|I)}{p(M_j|I)} B_{ij}, \tag{4.5}$$

where the first factor is the prior odds ratio (consideration of any belief that favours one model to the other before considering the data). B_{ij} is called the *Bayes factor* and compares the likelihoods of the models trying to explain the data. If we set the prior odds ratio to unity, reflecting no prior preference for either model, the odds ratio reduces simply to be the ratio of marginal likelihoods of the two models.

Note that in the context of models described by a set of parameters the likelihood of a model M_i can be expressed as:

$$p(\mathbf{D}|M_i, I) = p(\mathbf{\Theta}|I)p(\mathbf{D}|M_i, \mathbf{\Theta}, I) \tag{4.6}$$

Bayesian inference presents a built-in property by which models 'more complicated than necessary' are penalized with respect to the 'simplest': the *Ockham's razor*. An intuitive understanding of the mechanism by which this penalization occurs can be obtained from the following example, taken from (107). Denote by M_n a model for which $\mathbf{\Theta} = \{\theta_1, ..., \theta_n\}$ is n-dimensional, ranging over a parameter space Ω_n. Now introduce a new model M_{n+1} by adding a new parameter θ_{n+1} and going to a new parameter space Ω_{n+1}, in such a way that $\theta_{n+1} = 0$ represents the old model M_n.

On the subspace Ω_n the likelihood is unchanged by this change of model: $p(\mathbf{D}|\theta, M_{n+1}, I) = p(\mathbf{D}|\theta, M_n, I)$. But the prior probability $p(\theta|M_{n+1})$ must now be spread over a larger parameter space than before and will, in general, assign a lower probability, $[p(\mathbf{D}|M_{n+1}, I)]$, to a neighbourhood Ω' of a point in Ω_n than did the old model, $[p(\mathbf{D}|M_n, I)]$.

For a reasonably informative experiment, we expect that the likelihood will be rather strongly concentrated in small subregions $\Omega'_n \in \Omega_n$ and $\Omega'_{n+1} \in \Omega_{n+1}$. Therefore, if with M_{n+1} the maximum-likelihood point occurs at or near $\theta_{n+1} = 0$, Ω'_{n+1} will be assigned less prior probability than is Ω'_n with model M_n, and we have $p(D|M_n, I) > p(D|M_{n+1}, I)$; the likelihood ratio generated by the data will favour M_n over M_{n+1}. This is Ockham phenomenon. A quantitative detailed example of the Ockham's razor follows in (107). Another illustrative quantitative example can be found in (108) for two different models that assume delta-function likelihood functions.

4.2.2 Parameter estimation

By a model, a hypothesis that some particular physics governs the system is understood here. This physics leads to a set of parameters describing the phenomena, for example some fit coefficients, that could take different values within the context of the model. Are the values of the parameters consistent with the data?

The likelihood is the integrated probability that the data arose from different sets of parameter values within the model. This is multiplied by the probability that those parameters are correct in the context of the model, integrated over all possible values of the parameters. When a particular model M is assumed to be true, the hypothesis space $\{H_i\}$ corresponds with the parameter space $\{\theta_i\}$ of the model. The global likelihood of the model $\mathcal{L}(M, \mathbf{D})$, given the data $\mathbf{D}$, can be computed with the continuous version of Eq. 4.4.

$$p(\mathbf{D}|M) = \int ... \int d\theta \; p(\mathbf{\Theta}|M) \; p(\mathbf{D}|\mathbf{\Theta}, M) = \mathcal{L}(M, \mathbf{D}) \tag{4.7}$$

where $p(\mathbf{\Theta}|M)$ encloses any prior beliefs about the parameters and $p(\mathbf{D}|\mathbf{\Theta}, M)$ is the likelihood for a particular curve of the model, shaped by that point in the parameter space.

4.3 Noise and Signal

The measurement of a gravitational wave signal by a detector can never be ideal: even in the absence of a signal the measurement will result in a noisy output due to unpredicted displacements, or apparent displacements, of the test masses. This is the instrumental noise and is caused mainly by seismic and thermal disturbances and quantum effects of the instrument. Throughout this work instrumental noise is assumed to be stationary and Gaussian, of zero mean. The validity of the assumption of the noise to be stationary is stronger for short burst signals, for neither sudden nor progressive changes on the instrument are expected during the short duration of these signals.

4.3.1 Adding noise to the signal in the frequency-domain

Realistic data for analysis and testing of algorithms was obtained by adding the signal and the simulated instrumental synthetic noise together. Creation of synthetic noise in the time-domain, of known spectral power matching the sensitivity curve of the detector is not a trivial task. This can be done, however, by means of an iterative algorithm, first proposed in (109) and later improved in (110), where the spectrum of the noise desired is defined as a transfer function.

The improved algorithm has now been included into the LTPDA Matlab Toolbox, oriented to LISA data analysis, see (111).

Throughout this work the synthetic noise has been directly generated in the frequency domain by sampling two variables, the magnitude $|n[k]|$ and the phase $\theta[k]$, for each frequency bin $[k]$. A random phase value is obtained by sampling from a uniform distribution, whereas the random magnitude is obtained by sampling from a Rayleigh distribution[1]. Mathematically, this can be written as:

$$|n[k]| \sim \text{Rayleigh}(n[k]; n_{rms}[k]) \tag{4.8a}$$

$$\theta[k] \sim \mathcal{U}[0, 2\pi), \tag{4.8b}$$

where the average noise magnitude $n_{rms}[k]$ for each frequency bin $[k]$ corresponding to a N-point DFT can be computed if the power spectral density value $S_n[k]$ of that bin is known (see (112)) as follows:

$$S_n[k] = \frac{2\,|n_{rms}[k]|^2}{f_s\,S_2} \quad k = 0, ..., N. \tag{4.9}$$

f_s is the sampling frequency and $S_2 = \sum_{j=0}^{N-1} w_j^2$ is the window sum to account for the number of points N of the DFT and any gain or attenuation imposed on the signal by a window. In our case, for a rectangular window covering the whole length of N points (i.e. no window at all), $S_2 = N$. The important bit is that knowing the power spectral density of the noise $S_n[k]$, the average or expected magnitude of the noise $|n_{rms}[k]|$ for each frequency bin can be computed with Eq. 4.9 .

For independent and uncorrelated gaussian noise, the amplitude of an arbitrary frequency bin $|n[k]|$ follows a Rayleigh probability distribution, see Appendix H. By definition, the uncertainty of a Rayleigh distribution is the mode value itself; hence, the random noise magnitude for a particular frequency bin

[1]Interferometer noise can be thought of being a result of a filter operating on an input consisting of uncorrelated Gaussian noise (the power spectrum of the input has completely independent samples with random phases). The phase shifts at each bin are determined by the transfer function of the filter; but since the phase of the input noise is random from bin to bin, even if the phase shift due to the filter is highly correlated from bin to bin, the phase outputs are still random and uncorrelated.

$|n[k]|$ can be readily obtained by drawing a sample from a Rayleigh distribution of uncertainty proportional to the average magnitude of the noise: $\sigma = \sqrt{2/\pi}\,|n_{rms}[k]|$ (see Eqs. 4.8).

Once we have the magnitude and phase of the noise in each frequency bin, it is easy to convert the complex vector sampled $\tilde{n}[k] = |n[k]|\angle\theta[k]$ to its alternative cartesian representation $(n_{\Re}[k], n_{\Im}[k])$ by:

$$n_{\Re}[k] = |n[k]| \cos\theta[k] \tag{4.10a}$$

$$n_{\Im}[k] = |n[k]| \sin\theta[k]. \tag{4.10b}$$

The realistic detector data can be simulated by adding the real and imaginary coefficients of the signal and the noise. Fig. 4.1 is a graphical representation of the sampling of the random noise vector and its vectorial addition to the signal.

$$s_{\Re}[k] = h_{\Re}[k] + n_{\Re}[k] \tag{4.11a}$$

$$s_{\Im}[k] = h_{\Im}[k] + n_{\Im}[k] \tag{4.11b}$$

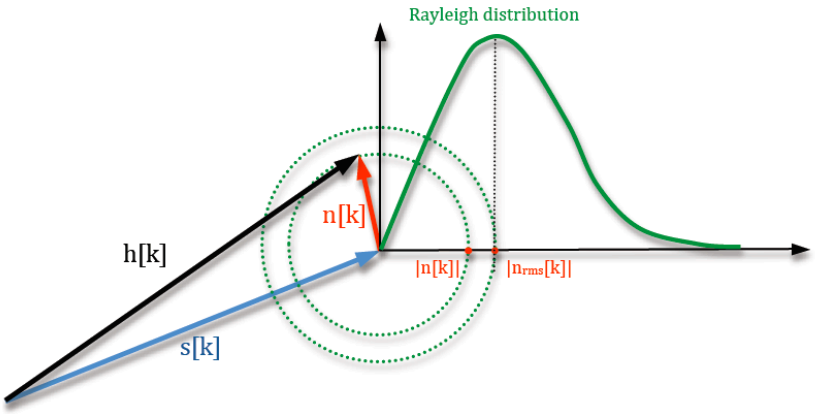

Figure 4.1: Graphical description of the generation of the complex noise vector $\tilde{n}[k]$ by sampling magnitude $|n[k]|$ from a Rayleigh distribution and the phase $\theta[k]$ from a uniform distribution, see Eq. 4.8. The average magnitude of the noise $|n_{rms}[k]|$ is the uncertainty parameter of the Rayleigh distribution.

4.4 Calculation of the Signal to Noise Ratio (SNR)

The signal to noise ratio (SNR) quantifies the relative size of the signal with respect to the instrumental noise it is embedded in. For a continuous signal expressed in the frequency domain the signal to noise ratio ρ can be calculated as:

$$\rho^2 = 2 \int_0^\infty \frac{|h(f)|^2}{S_h(f)}\, df. \tag{4.12}$$

This is the largest SNR achievable with a linear filter applied to the output of the detector. Eq. 4.12 arises naturally in the context of *matched filtering theorem*, see (30). The equivalent of Eq. 4.12 for discrete signals that has been used in this work:

$$\rho^2 = 2 \sum_{k=k_{min}}^{k_{max}} \frac{|h[k]|^2}{S_h[k]}, \tag{4.13}$$

where the range of frequencies within the bins $[k_{min}, k_{max}]$ is the bandwidth where the majority of the power of the signal is concentrated.

4.5 An illustrative example of the study method

In the following, a realistic example of a gravitational wave signal detected at the instant GLST = 0h by a network of second generation ground-based laser interferometric detectors is presented. The signal corresponds to an oscillating neutron star located in the galactic centre, which presents two clear oscillation modes: the f-mode (fundamental) and the p-mode (pressure).

The amount of energy channeled into each oscillation mode is not certain, and in turn, neither is the amplitude of the gravitational wave incoming from the oscillating compact object. Here, and for the sake of the illustration, an arbitrary value of the gravitational wave energy has been considered for the f-mode (enough as to obtain a significant SNR in the noisiest of the detectors considered). The amplitude corresponding to the f-mode is calculated as per the equation published in (75). Quite arbitrarily, and given the uncertainty of

the energy channeled to the p-mode, its amplitude was taken to be a fifth of the amplitude corresponding to the f-mode. Polarization degree λ and polarisation angle ψ are considered independent and again arbitrary values from within their logical ranges have been assigned to them. All the values of the parameters are listed in Table 4.1. Fig. 4.3 and Fig. 4.5 show the spectra of the signals as detected by the second generation detectors considered.

Parameters of the exponentially damped sinusoids				
Description		**Units**	f**-mode**	p**-mode**
Energy	E^{gw}	$M_s c^2$	7×10^{-6}	-
Amplitude	h_0	-	1.543×10^{-21}	$3.086\times^{-22}$
Frequency	f_0	Hz	3090	7838
Damping Time	τ	sec	0.109	4.64
Number of cycles	$n \approx \sqrt{f\tau}$	-	336	36368
Polarization degree	λ	-	0.7	0.3
Polarization angle	ψ	-	1.2	2.3
Declination	δ	rad	$-28°$ 56' (-0.505 rad)	
Right Ascension	RA	rad	17h56m (4.64 rad)	
Distance	d	kpc	8.5	
@ GLST = 0h	SNR $[F_+, F_\times]$		SNR $[F_+, F_\times]$	
Detector	f-mode		p-mode	
Adv-LIGO-H	10.13 [-0.330,0.282]		17.9 [0.423,0.101]	
Adv-LIGO-L	7.52 [-0.285,0.026]		8.45 [0.188,0.216]	
Adv-VIRGO	4.30 [-0.930,0.188]		5.02 [0.699,0.641]	
PERTH-ET	89.1 [-0.346,-0.455]		65.7 [-0.164,0.547]	

Table 4.1: Parameter values for burst-gravitational waves modeled as exponentially damped sinusoids. The values of frequency and damping time are taken from (75) where expected values for f- and p-modes of oscillating neutron stars for different equations of estate are listed. The source location is the galactic centre and the polarisation parameters, λ and ψ values, have been chosen randomly.

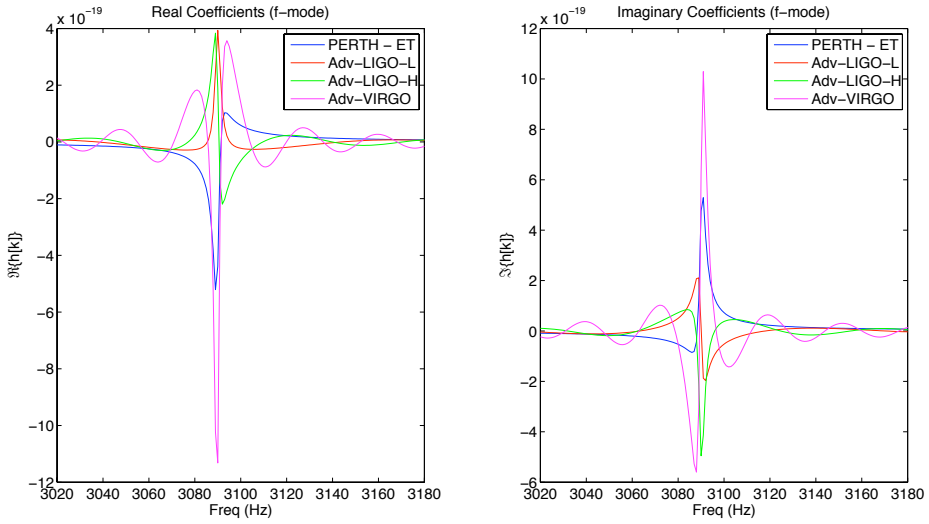

Figure 4.2: Spectrum of the exponentially damped sinusoidal gravitational wave signal expected from the f-mode oscillation of a neutron star as seen by four ground-based detectors at instant GMST = 0h. Parameter values are listed in Table 2.1.

.

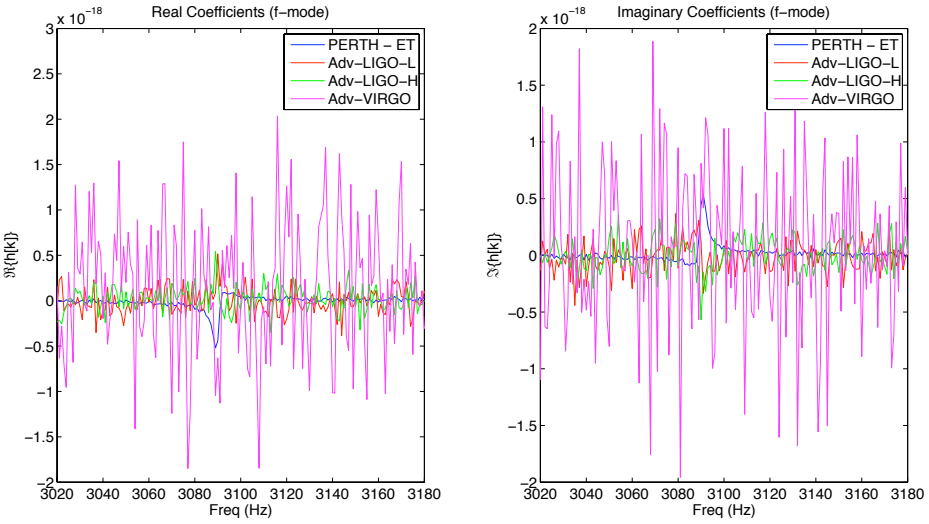

Figure 4.3: Same as Fig. 4.2 after considering the noise of each detector.

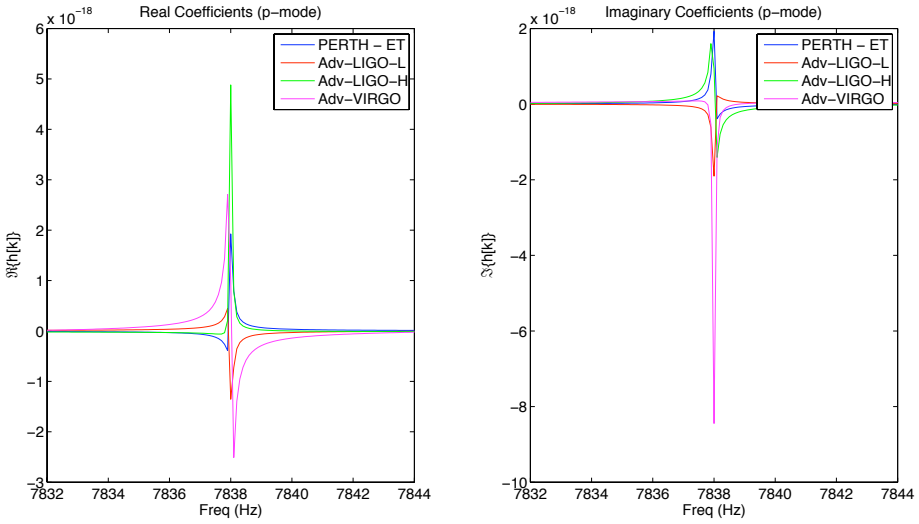

Figure 4.4: Spectrum of the exponentially damped sinusoidal gravitational wave signal expected from the p-mode oscillation of a neutron star as seen by four ground-based detectors at instant GMST = 0h. Parameter values are listed in Table 2.1.

.

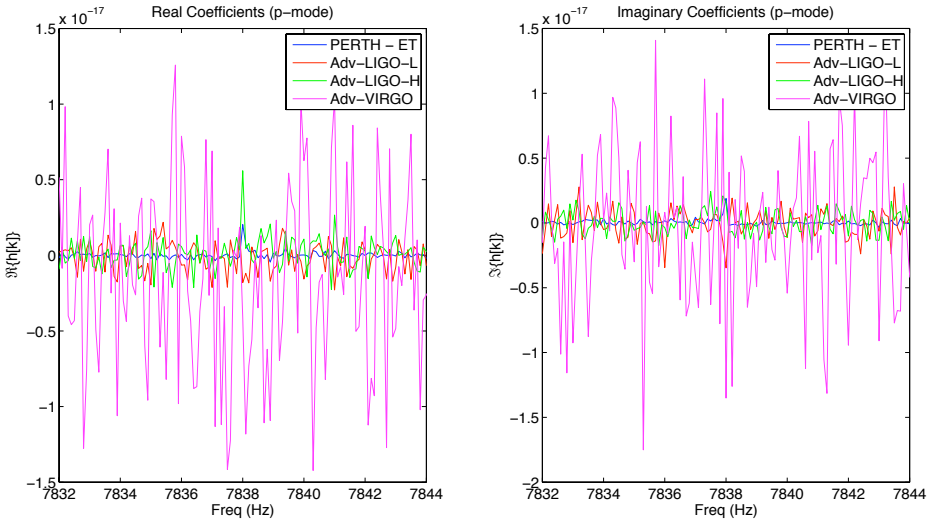

Figure 4.5: Same as Fig. 4.2 after considering the noise of each detector.

4.6 Calculation of the Likelihood Function

The concept of likelihood has been introduced in section 4.2. Here, the likelihood function and its computation will be considered. In the process of contrasting the data acquired against a model, the likelihood quantifies the probability of the data to be explained by that particular model assumed to be true. The calculation of likelihood is possible due to the knowledge of the average level of the instrumental noise, and it may be carried out either in the time or in the frequency domain, for both domains provide equivalent representations of the signal. In the following, the two equivalent formulae to compute the likelihood in both domains are shown. A more detailed derivation of these formulae is included in Appendix H.

4.6.1 Likelihood in the time domain

The discrepancy between the acquired data-set $\{s[n]\}$ and the signal model $\{h[n]\}$ are the errors $\{e[n]\}$. For each datum measured we have:

$$e[n] = s[n] - h[n], \quad n = 1, ..., N. \tag{4.14}$$

Under the consideration that the error made on each datum is gaussian of zero mean and stationary, so that $e[n] \sim \mathcal{N}(0, \sigma[n])$, the probability of observing one particular datum is:

$$p(e[n]|\sigma[n], I) = \frac{1}{\sigma[n]\sqrt{2\pi}} \exp\left[-\frac{(s[n] - h[n])^2}{2\sigma[n]^2}\right], \tag{4.15}$$

where I represents any background information or knowledge prior to the acquisition of the data. If all the sample errors are independent and identically distributed, that is $p(e[n], e[n+1]|\cdot) = p(e[n]|\cdot)\, p(e[n+1]|\cdot)$, the joint probability for the set of error values $\{e[n]\}$ is the result of the multiplication of all the individual probabilities:

$$p(\{e[n]\}|\{\sigma[n]\}, I) = \prod_{n=1}^{N} p(e[n]|\sigma[n], I). \tag{4.16}$$

In general, each sample will have its own particular standard deviation $\sigma[n]$. The joint probability of acquiring a particular set of values $\{s[n]\}$, given that the signal model $h[n] = M([n]; \{\theta\})$ is true, is equal to the probability of getting the set of errors $\{e[n]\}$. This is known as the global likelihood $\mathcal{L}$ of the model M:

$$\mathcal{L}(M) = p(\{s[n]\}|M, \{\sigma[n]\}, I) = p(\{e[n]\}|\{\sigma[n]\}, I), \tag{4.17}$$

and can be written as:

$$\mathcal{L} = \prod_{n=1}^{N} \frac{1}{\sigma[n]\sqrt{2\pi}} \exp\left[-\frac{(s[n] - h[n])^2}{2\sigma[n]^2}\right]. \tag{4.18}$$

To keep numerical values under control, it is often convenient to work with the logarithm of the likelihood instead:

$$\log \mathcal{L} = -N/2 \ \log(2\pi) - N \log(\sigma[n]) - \sum_{n=1}^{N} \frac{(s[n] - h[n])^2}{2\sigma[n]^2}. \tag{4.19}$$

4.6.2 Likelihood in the frequency domain

In the frequency domain, a complex number (complex vector) characterises each harmonic of the spectrum and may be represented as a pair of real and imaginary coefficients (*cartesian*) or as a pair of magnitude and phase (*polar*). Thus, the probability of obtaining a particular complex value in a frequency bin can be represented by a bivariate probability density function. The calculation of the likelihood function in the frequency domain either with the cartesian or polar representation is discussed more in detail in Appendix H. Again, and assuming that the only discrepancy between the spectrum of the acquired data and the modeled signal is due to the instrumental noise, we can write:

$$\tilde{n}[k] = \tilde{s}[k] - \tilde{h}[k] \begin{cases} n_{\Re}[k] = s_{\Re}[k] - h_{\Re}[k] \\ n_{\Im}[k] = s_{\Im}[k] - h_{\Im}[k] \end{cases} \qquad k = 0, ..., K-1, \tag{4.20}$$

where $\square_{\Re}[k] = \Re\{\square[k]\}$ and $\square_{\Im}[k] = \Im\{\square[k]\}$ are the real and imaginary coefficients of the complex value $\tilde{\square}$ representing the harmonic corresponding to the kth frequency bin. $\square$ represents any of $\tilde{s}, \tilde{h}$ or $\tilde{n}$.

If the noise in the time domain is gaussian with zero mean and uncorrelated, the real and imaginary coefficients of a frequency bin of its discrete Fourier transform are gaussian with zero mean and uncorrelated too; also, the uncertainty of the distribution is equal for the real and imaginary coefficients (i.e. $\sigma_{\Re}[k] = \sigma_{\Im}[k] = \sigma[k]$). The joint probability of $n_{\Re}[k]$ and $n_{\Im}[k]$ is then a bivariate normal probability distribution function of zero mean $\mu = [0, 0]$ and covariance $\Sigma = [0, \sigma^2[k]; 0, \sigma^2[k]]$, so that:

$$p(\tilde{n}[k]|\sigma[k], I) = p(n_{\Re}[k], n_{\Im}[k]|\sigma[k], I) \tag{4.21a}$$

$$= \frac{1}{2\pi\sigma^2[k]} \exp\left[-\frac{(s_{\Re}[k] - h_{\Re}[k])^2 + (s_{\Im}[k] - h_{\Im}[k])^2}{2\sigma[k]^2}\right]. \tag{4.21b}$$

If all the errors are independent and identically distributed, that is $p(\tilde{n}[k], \tilde{n}[k+1]|\cdot) = p(\tilde{n}[k]|\cdot)\, p(\tilde{n}[k+1]|\cdot)$, the probability for the set of error values $\{\tilde{n}[k]\}$ can be written as the multiplication of all the individual probabilities:

$$p(\{\tilde{n}[k]\}|\{\sigma[k]\}, I) = \prod_{k=1}^{K} p(\tilde{n}[k]|\sigma[k], I). \tag{4.22}$$

Given that the model $\{\tilde{h}[k]\} = M([n]; \{\theta\})$ is true, the joint probability of acquiring the set of values $\{\tilde{s}[k]\}$ is equal to the probability of obtaining the set of errors $\{\tilde{n}[k]\}$. This is the likelihood of the model:

$$\mathcal{L} = \prod_{k=1}^{K} \frac{1}{2\pi\sigma^2[k]} \exp\left[-\frac{(s_{\Re}[k] - h_{\Re}[k])^2 + (s_{\Im}[k] - h_{\Im}[k])^2}{2\sigma[k]^2}\right]. \tag{4.23}$$

Again, to keep numerical values under control the likelihood may be expressed in logarithmic form as:

$$\log\mathcal{L} = -K\log(2\pi) - \sum_{k=1}^{K} 2\log(\sigma[k]) + \frac{(s_{\Re}[k] - h_{\Re}[k])^2 + (s_{\Im}[k] - h_{\Im}[k])^2}{2\sigma[k]^2}. \tag{4.24}$$

Equivalently, the likelihood may be computed using the magnitude and phase (*polar* representation) of the complex numbers $\tilde{n}[k]$, $\tilde{s}[k]$ and $\tilde{h}[k]$, where:

$$\tilde{n}[k] \equiv N[k]\angle\theta_{\tilde{n}}[k]$$
$$\tilde{s}[k] \equiv S[k]\angle\theta_{\tilde{s}}[k]$$
$$\tilde{h}[k] \equiv H[k]\angle\theta_{\tilde{h}}[k].$$

To simplify the notation, the phase difference between the acquired data and the modeled signal is defined as $\alpha[k] = |\theta_{\tilde{s}}[k] - \theta_{\tilde{h}}[k]|$. In analogous form to Eq. 4.21 the cosine rule in the triangle formed by the vectors $\tilde{n}, \tilde{h}$, and $\tilde{s}$ the joint probability of getting noise of magnitude and phase $N[k]\angle\theta_{\tilde{n}}[k]$ in the kth bin can be written as:

$$p(N[k], \alpha[k]|H[k], \sigma[k]) = \frac{H[k]}{2\pi\sigma[k]^2} \exp\left[-\frac{H[k]^2 + S[k]^2 - 2H[k]S[k]\cos(\alpha[k])}{2\sigma[k]^2}\right]. \tag{4.25}$$

The joint probability of acquiring the set of values measured $\{\tilde{S}[k]\}$, given that the model $\{\tilde{H}[k]\} = M\{\theta\}; [n])$ is true, is equal to the probability of the set of errors. This is the likelihood of the model:

$$\mathcal{L} = \prod_{k=1}^{K} p(N[k], \alpha[k]|H[k], \sigma[k]) \tag{4.26a}$$
$$= \prod_{k=1}^{K} \frac{H[k]}{2\pi\sigma[k]^2} \exp\left[-\frac{H[k]^2 + S[k]^2 - 2H[k]S[k]\cos(\alpha[k])}{2\sigma[k]^2}\right] \tag{4.26b}$$
$$= (2\pi)^{-K} \exp\left[-\sum_{k=1}^{K} 2\log(\sigma[k]) - \log(H[k]) + \frac{H[k]^2 + S[k]^2 - 2H[k]S[k]\cos(\alpha[k])}{2\sigma[k]^2}\right]. \tag{4.26c}$$

And taking logarithms this is:

$$\log\mathcal{L} = (2\pi)^{-K} - \sum_{k=1}^{K} 2\log(\sigma[k]) - \log(H[k]) + \frac{H[k]^2 + S[k]^2 - 2H[k]S[k]\cos(\alpha[k])}{2\sigma[k]^2} \tag{4.27}$$

4.7 Nested Sampling

Nested sampling is a relatively new Monte Carlo method by Skilling (113) intended for general Bayesian computation. It reverses the usual approach of Monte Carlo Markov Chain (MCMC) methods, by directly targeting the value of the *evidence* rather than the posterior probability distribution. Samples from the posterior distribution are an optional by-product of the computation. The nestled sampling algorithm and its implementation are covered in (114).

In this work the nested sampling method was preferred over the MCMC methods. This was a personal decision and I do not pretend to claim any overall extra advantages for one or the other. The decision taken was mainly due to the nested sampling being a more systematic and clear algorithm to implement for me. I tried MCMC approaches but the difficulty to ascertain the convergence of the algorithm and deciding on the convenience of the number of chains to use was a reason to opt for the nested sampling algorithm, which I implemented in Matlab.

Eq. 4.2 can be written in a slightly different form where the hypothesis under consideration is a particular model with the set of parameters $\mathbf{\Theta}$. Then, the joint probability of the set of parameters and the data acquired $\mathbf{D}$ can be written in two ways following the product rule (see (114)):

$$\text{Joint} \equiv \text{Prior} \times \text{Likelihood} = \text{Evidence} \times \text{Posterior} \tag{4.28a}$$

$$p(\mathbf{\Theta}, \mathbf{D}|I) = p(\mathbf{\Theta}|I)p(\mathbf{D}|\mathbf{\Theta}, I) = p(\mathbf{D}|I)p(\mathbf{\Theta}|\mathbf{D}, I) \tag{4.28b}$$

$$= \mathcal{L}(\mathbf{\Theta})\pi(\mathbf{\Theta}) = ZP(\mathbf{\Theta}), \tag{4.28c}$$

where the likelihood is $\mathcal{L}(\mathbf{\Theta}) = p(\mathbf{D}|\mathbf{\Theta}, I)$, the prior is $\pi(\mathbf{\Theta}) = p(\mathbf{\Theta}|I)$, the evidence is $Z = p(\mathbf{D}|I)$, and the posterior is $P(\mathbf{\Theta}) = p(\mathbf{\Theta}|\mathbf{D}, I)$. Due to the normalization requirement of probability density functions, $\int P(\mathbf{\Theta})d\mathbf{\Theta} = 1$, the evidence Z can be separated from the shape $P(\mathbf{\Theta})$ to be written as:

$$Z = \int \mathcal{L}(\mathbf{\Theta})\pi(\mathbf{\Theta})d\mathbf{\Theta} = \int \mathcal{L}\, dX \tag{4.29}$$

where $dX = \pi(\mathbf{\Theta})d\mathbf{\Theta}$ is the element of probability mass associated with the prior density $\pi(\mathbf{\Theta})$. As a function of the scalar value of the evidence Z the distribution

of the posterior mass is:

$$dP = p(\mathbf{\Theta})d(\mathbf{\Theta}) = Z^{-1}\mathcal{L}(\mathbf{\Theta})\pi(\mathbf{\Theta})d\mathbf{\Theta}. \tag{4.30}$$

The evidence Z measures the goodness of the model to interpret the data and it is the crux for model comparison through the *Bayes factor*. However, its calculation by rastering over all dimensions of $\mathbf{\Theta}$ becomes rapidly impractical for models with many dimensions.

The nested sampling provides an efficient way of calculating the integral for Z in Eq. 4.29, using the prior mass X directly, as a sum of $\mathcal{L}\ dX$ elements following an iterative process that sweeps over the parameter space. To see how it works, let us define the fraction of prior mass with likelihood greater than λ:

$$X(\lambda) = \int_{\mathcal{L}(\mathbf{\Theta})>\lambda} \pi(\mathbf{\Theta})d(\mathbf{\Theta}). \tag{4.31}$$

As the bordering likelihood λ increases, the enclosed prior mass X decreases from $X(0) = 1$ to $X(\infty) = 0$. Inverting the function as $(\mathcal{L}(X(\lambda)) \equiv \lambda)$, the evidence becomes a one-dimensional integral over the unit range:

$$Z = \int_0^1 \mathcal{L}(X)\ dX, \tag{4.32}$$

where $\mathcal{L}(X)$ is a strictly decreasing function.

4.8 Nested Sampling procedure

The nested sampling technique uses a group of n objects (points in the parameter space) uniformly sampled with respect to the prior $\pi(\mathbf{\Theta})$ and subject to an evolving hard constraint $\mathcal{L}(\mathbf{\Theta}) > \mathcal{L}^*$. The objects keep moving toward regions of higher likelihood through an iterative process and finding the regions of the parameter space that contribute significantly to the evidence integral in Eq. 4.29.

In terms of X, the objects are uniformly sampled subject to the constraint $X < X^*$ (where X^* corresponds to $\mathcal{L}^*$). At each iteration, the object with the lowest value of likelihood is replaced with a new object of higher likelihood. This is usually done by selecting an object randomly and evolving it through a Markov

Chain to obtain another object with a higher likelihood. The algorithm keeps iterating inwards in X, upwards in $\mathcal{L}$, to locate the tiny region where most of the joint distribution is to be found.

On entry of a new iteration, there are n objects restricted to the prior mass $X < X^*$. The object with the lowest likelihood, which corresponds to the largest X, is the largest of n numbers uniformly distributed in $(0, X^*)$. Note that this likelihood value will not correspond exactly with the prior mass X assigned to it but it is a approximation when enough objects are involved in the process. There is an uncertainty on the value of the largest X chosen, and the shrinkage $t = X/X^*$ is distributed as:

$$p(t) = n\ t^{n-1}. \tag{4.33}$$

Iterations continue by taking the object with the lowest likelihood $(X, \mathcal{L})$ as the new limit $(X^*, \mathcal{L}^*)$. Throughout the iterative process only one set of shrinkage factor values $\mathbf{t}$ will be correct: that one corresponding to the randomly selected values $\mathbf{\Theta}$. The uncertainty on the shrinkage factors induces an uncertainty on the computed evicence Z, which can be calculated (see (113)).

The contribution to the evidence at iteration k is the area $\mathcal{L}_k w_k$ where the simplest width is $w_k = X_{k-1} - X_k$, which keeps accumulating as:

$$Z_k = Z_{k-1} + \mathcal{L}_k(X_{k-1} - X_k). \tag{4.34}$$

During the iterative process $\mathcal{L}_k w_k$ starts rising, with the likelihood $\mathcal{L}_k$ increasing faster than the widths w_k decrease: the important regions of the parameter space are being found. Eventually, $\mathcal{L}$ flattens off and the decreasing width dominates the increasing likelihood, so the contributions pass across a maximum and start to fall away. Fig. 4.6 and Fig. 4.7 show graphically the evolution of the nested sampling algorithm in a two dimensional parameter space and with $n = 3$ objects. The evidence Z is the area under the green curve, which is approximated by adding the areas of the rectangles with height $\mathcal{L}_k$ and width w_k given by the approximate prior mass difference assigned through the iterative prior shrinking process.

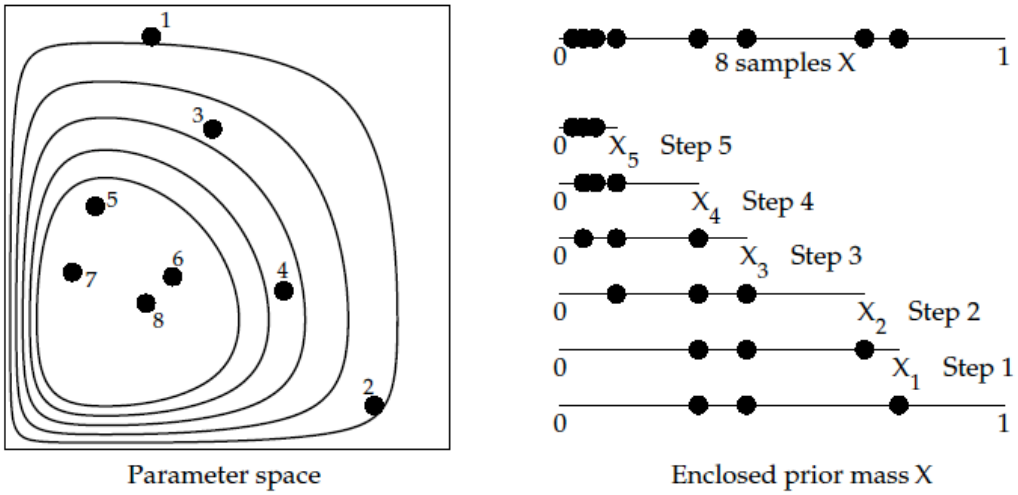

Figure 4.6: Likelihood contours shrink by factors of $e^{-1/n}$ in area and are roughly followed by succesive objects 1,2,3,4,5. Reproduced from (115).

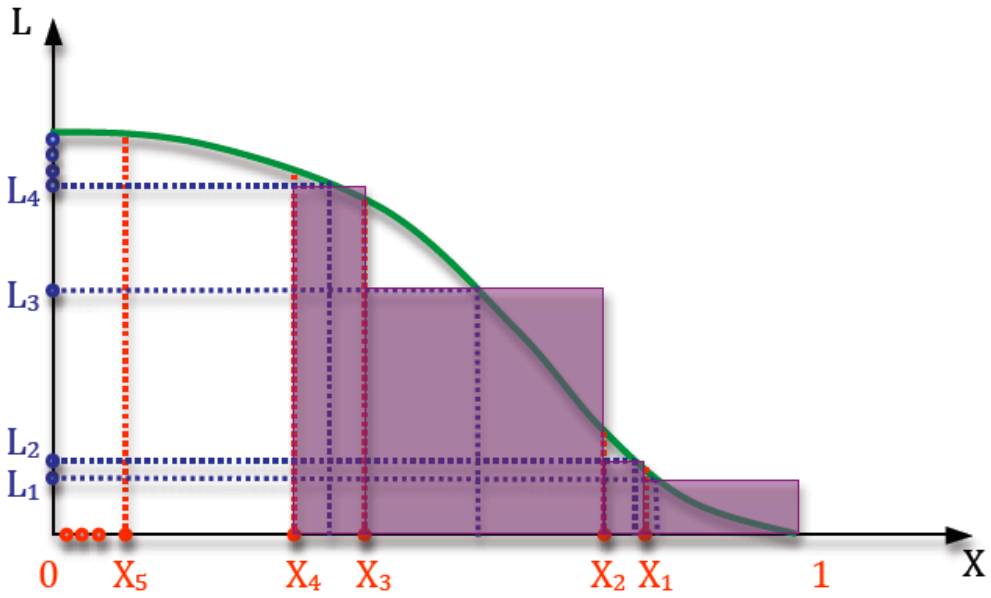

Figure 4.7: Evolution of the nested sampling algorithm for a bivariate probability distribution function with 3 objects shown in Fig. 4.6. Nested likelihood contours enclose succesively shrinking prior mass regions and evidence Z is approximated by adding areas of the rectangles. Increasing the number of objects used in the iterative process the approximation of the evidence (area under the green curve) is more accurate.

4.8.1 Terminating the iteration

The algorithm needs to run until most of the evidence Z has been found. The simplest is to stop the algorithm after a pre-set number of iterations, but this does not assure the regions of parameter space with the biggest contributions to Z will be found. A better way of terminating the iteration is to check that the maximum possible contribution to the evidence (given by the object with the highest likelihood value) is already smaller than a tiny pre-set fraction f of the accumulated evidence. When this is fullfilled it means that the contributions to Z are tailing off and the sum is nearly complete. At iteration k, the check for termination can be written as:

$$max(\mathcal{L}_1, ..., \mathcal{L}_N)X_k < fZ_k \tag{4.35}$$

where $\mathcal{L}_i$ are the likelihoods of the current N points in the parameter space. The iterations should be continued for long enough as to practically accumulate all the evidence. After the last iteration all the objects should be concentrated in a small region in the parameter space and their contribution to evidence should be minimal.

4.8.2 Generating a new object by random sampling

At every iteration of the nested sampling algorithm the object with the lowest likelihood needs to be replaced by a new one, generated from the prior and subject to the hard constrainst $\mathcal{L} > \mathcal{L}^*$. The domain of the prior obeying the constraint shrinks geometrically and, generally, it is not expected to find an object in this small domain easily.

With complicated models, particularly those with multiple parameters, it is rare that the samples from the distribution can be obtained directly. Various clever strategies have been devised to allow drawing representative samples from a target distribution. The *Markov chain Monte Carlo* (MCMC) is one of them and makes possible to sample iteratively from distributions that converge to the desired target probability distribution.

In the process of obtaining a new object, guidance provided by previous iterates and the active objects may be used: one of the current objects can be

randomly chosen and evolved through a Markov chain to get a new object that complies with the constrain and it is far enough from the starting point as to lose memory of the starting point. A Metropolis-Hastings Markov chain has been used in this work to evolve a known object to another to replace the one with the lowest likelihood.

4.8.2.1 Markov chain

A Markov chain refers to a series of values $\{\boldsymbol{\Theta}\}$ obtained sequentially that satisfy the *Markov property*: $\boldsymbol{\Theta}_{t+1}$ is dependent only on its nearest past value $\boldsymbol{\Theta}_t$. An adequate transition probability density function q (called "kernel") maps two consecutive values $q(\boldsymbol{\Theta}_{t+1}|\boldsymbol{\Theta}_t)$, where the kernel is considered to be time homogeneous (not changing with t).

The convergence of a chain is guaranteed if it is irreducible and aperiodic (116). It is irreducible if under the transition rule q considered there exists a non-zero probability of visiting any particular state – from all starting points, the Markov chain must eventually be able to jump to all states in the target distribution with positive probability. Aperiodicity implies that the samples of the chain do not show a repetitive pattern – the chain does not oscillate between different states in a regular periodic movement.

Many clever methods have been devised to sample from a target distribution by constructing Markov chains. In the following, the *Metropolis-Hastings* algorithm is presented, an extensively applied algorithm that has been used in this work.

4.8.2.2 Metropolis-Hastings algorithm

The Markov chain extends itself by carefully accepting only some of the proposed candidates. The *Metropolis-Hastings* algorithm defines explicitly the acceptance/rejection rules for the Markov chain in a two-stage iterative process: 1) value Y is proposed for $\boldsymbol{\Theta}_{t+1}$ from a proposal distribution $q(Y|\boldsymbol{\Theta}_t)$ easy to evaluate; 2) the decision whether to accept or not the candidate Y as the next

value of the chain $\mathbf{\Theta}_{t+1}$ is taken on the basis of the ratio given by the *Metropolis ratio*:

$$r = \frac{\pi(Y)}{\pi(\mathbf{\Theta}_t)} \frac{q(\mathbf{\Theta}_t|Y)}{q(Y|\mathbf{\Theta}_t)}. \tag{4.36}$$

The denominator assess the probability of a forward jump $\mathbf{\Theta}_t \rightarrow Y$ whereas the numerator is the probability of the reverse path $Y \rightarrow \mathbf{\Theta}_t$. If the proposal distribution q is symmetric, so that $q(\mathbf{\Theta}_t|Y) = q(Y|\mathbf{\Theta}_t)$, then the second factor in Eq. 4.36 is equal to one and it can be dropped. If $r \geq 1$ the value proposed is accepted and incorporated to the chain $\mathbf{\Theta}_{t+1} = Y$. If $r < 1$ the proposed value is accepted with probability r: draw a value from an uniform distribution $u \sim \mathcal{U}[0, 1]$ and set $\mathbf{\Theta}_{t+1} = Y$ only if $r \geq u$; if $r < u$ the proposed value is not accepted and $\mathbf{\Theta}_{t+1} = \mathbf{\Theta}_t$ (the chain remains in the same point). Mathematically, this is summarised with the *acceptance probability* $\alpha(\mathbf{\Theta}_t, Y)$, which is given by:

$$\alpha(\mathbf{\Theta}_t, Y) = \min(1, r) = \min\left(1, \frac{\pi(Y)}{\pi(\mathbf{\Theta}_t)} \frac{q(\mathbf{\Theta}_t|Y)}{q(Y|\mathbf{\Theta}_t)}\right). \tag{4.37}$$

For a step by step explanation of the implementation of this algorithm and various examples see (117). A proof that following this acceptance rule the stationary distribution of the Markov chain is the desired target distribution is provided there.

4.8.3 Implementation of the nested sampling algorithm

Steps for the implementation of the algorithm are rather well defined. However, and depending on the problem at hand, the user has a choice on the ways the new object to replace the one with the lowest likelihood will be proposed. The crux is to have enough objects, and to evolve them adequately to sweep all the parameter space so that all the important regions are considered. One possible way to find a candidate to replace the object with the lowest likelihood is to evolve an object through a Markov chain in order to obtain an appropriate candidate. For an example of its implementation see (114); complementarily a pseudo-code is presented here in the Appendix in I.

In this work the implementations of the nested sampling used between $n = 100$ and $n = 300$ objects. Mostly, the number of objects used depended on the number of variables involved. Using as many objects as possible was aimed to improve accuracy but the long computation times for multidimensional parameter spaces constrained their number. At each iteration a randomly selected object was evolved through a Markov chain in order to get a candidate for the replacement. The transition kernel q consisted on a multivariate normal distribution centred on the selected object and with a covariance equal to a scaled-down covariance matrix of all the current objects. The fact that the uncertainty of the proposal distribution reduces with each iterate – adaptive as the shrinking proceeds – makes possible to look for a candidate in the region where all the active points are and in a direction that takes into account the correlations between variables. The sampling from the multivariate normal distribution can be written as:

$$\mathbf{\Theta}_{t+1} \sim \mathcal{N}(\mathbf{\Theta}_t, \mathbf{\Sigma}) \tag{4.38}$$

where the elements of the covariance matrix $\mathbf{\Sigma}$ are:

$$\Sigma_{ij} = c\,\frac{1}{n}\sum_{i,j=1}^{n}(\theta_i - \bar{\theta_i})(\theta_j - \bar{\theta_j}) \tag{4.39}$$

and $c < 1$, for the scaled-down covariance matrix considered. The Markov chain can have as many links m as desired and the last point is set as the new live point to replace the one with the lowest likelihood. In our case, and following parameters used in (118), $c = 0.1$ and $m = 20$ were adopted. These are quite arbitrary values with which the algorithm performed well. Each state is accepted with the probability shown in Eq. 4.37 when complying the likelihood constraint $\mathcal{L}(\mathbf{\Theta}_{t+1}) < \mathcal{L}_*$. If at the end of the m trials no candidate has yet fullfilled the requirements, the chain is started from another object and evolved again until finding an adequate candidate.

4.8.4 Posterior Sampling

In the previous sections it has been shown how the nested sampling algorithm is focused on calculating the evidence. In the process, a list of objects (points in the

multidimensional parameter space) are recorded, the one with the lowest likelihood value at each iteration of the algorithm. Since these points have succesively higher likelihood values obtained by sweeping the parameter space, they are a representation of the posterior distribution density. It is possible to compute the contribution of each of the samples to the accumulated evidence Z by:

$$p_k = \frac{\mathcal{L}_k w_k}{Z} = \frac{\mathcal{L}_k \; e^{-k/N}}{Z}. \tag{4.40}$$

Posterior samples may be generated in proportion to their contribution to Z during the nested sampling process: those samples that contributed tiny amounts to the total evidence, and extracted during the process from non-relevant regions of the parameter space (small likelihood), generate few posterior samples. On the other hand, those more contributory samples taken from regions where the likelihood is concentrated, generate more posterior samples.

For example, considering a perfect sweep of the parameter space, if a particular sample $\mathbf{\Theta}_i$ contributed to Z three times as much as $\mathbf{\Theta}_j$ did $[p(\mathbf{\Theta}_i) = 3p(\mathbf{\Theta}_j)]$, it means that when sampling from the posterior distribution, it is three times more likely to get $\mathbf{\Theta}_i$ than $\mathbf{\Theta}_j$. With this in mind, samples from the posterior distribution can be obtained with ease, for example, with *starcaise sampling* (114). Similarly, any statistics $Q(\mathbf{\Theta})$ of the posterior distribution can be computed from the samples.

The number of posterior distribution samples is limited by the number of iterations done by the algorithm, and this is directly related to the number of objects used in the simulation. In order to get enough samples for a fair representation of the posterior distribution it may be necessary to run the algorithm with more objects, causing the algorithm to progress more slowly but sweeping the parameter space more exhaustively and calculating Z more precisely too.

Chapter 5

Model Comparison and Parameter estimation

This chapter presents the Bayesian analysis followed in order to extract information from data suspected of containing a burst-type gravitational wave. This is intended as a follow-up analysis to be carried out once the preliminary pipeline has flagged a gravitational wave signal candidate; for example, from the analysis of a spectrogram in which a sudden increase of the power of the signal has been observed.

Generally, the gravitational wave signal will be weak at detection and, most probably, concealed within the instrumental noise. Quantifying the likelihood of the presence of a signal is important and justifies the *model comparison* exercise: typically, the probability of collected data to be purely instrumental noise is compared against the probability of the data to contain a signal of a particular model. Once the presence of the signal is ascertained the model that 'makes best justice' to the data is chosen and the most likely value of its parameters estimated. Then, the parameter values and their uncertainties need to be translated into physical language to obtain significant astrophysical information.

5.1 Data for analysis

Detector data analysed throughout this work has been obtained by injecting signals into synthetic instrumental noise in the frequency domain, as explained in

Section 4.3. In general, the length of data to process depends on the number of detectors in the network and the number of frequency points included in the calculation of the likelihood, which, in turn, depend on the bandwidth and frequency resolution considered. In this chapter, the detector network comprising the three advanced instruments (Adv-LIGO-L, Adv-LIGO-H and Adv-VIRGO) was considered and the projections of a signal from the galactic centre at the particular instant of GLST = 0h were studied.

Adopting the subindex i to consider each of the oscillation modes ($i = 1$ for f-mode and $i = 2$ for p-mode), the generic expression of the Fourier transform of an exponentially damped sinusoid gravitational wave signal projected onto one particular detector j can be written using Eq. 3.24 as follows:

$$\tilde{h}^{(j)}(f;\boldsymbol{\Theta}) = \sum_{i} \tilde{h}_i^{(j)}(f;[h_{0i}, f_{0i}, \tau_i, \lambda_i, \psi_i], \delta, \mathrm{RA}) \tag{5.1a}$$

$$= \sum_{i=1}^{I} \frac{z^{-n_{0j}} + r_i[C_{Sij}\sin w_{0i} + C_{Cij}\cos w_{0i}]z^{-(n_{0j}+1)}}{1 - 2r_i\cos w_{0i} z^{-1} + r_i^2 z^{-2}}, \tag{5.1b}$$

where $z = e^{jw}$ and $w[k] = 2\pi f[k]/f_s$. Here, there is an underlying assumption that all the detectors of the network have the same frequency resolution. In the following, the parameters in Eq. 5.1 are explained more in detail:

- n_{0j} is the number of shifted samples for each detector j. The data acquired by the detector of the network first receiving the signal is modeled as a non-shifted signal, $n_{01} = 0$ (this is the only non zero-padded stretch of data). The rest of the detectors within the network present a definite time-shift Δt, which can be translated into a positive integer number ($n_0 = round(f_s \Delta t)$) corresponding the number of samples elapsed since the signal was detected in the first detector. The procedure followed to calculate time differences between detectors is covered in Appendix J.

- $w_{0i} = 2\pi f_{0i}/f_s$ is the oscillation frequency of each mode i in units of rad sample^{-1}. Fiducial oscillation frequency values for w_{01} (f-mode) and w_{02} (p-mode) of neutron stars used in this work have been taken from (75) and are shown in Table 5.1.

- $r_i = e^{-2\pi/(f_s \tau_i)}$ is the damping time for each of the modes i in units of sample^{-1}.

- $C_{Sij} = h_{0i} F_{+ij}$ and $C_{Cij} = h_{0i} \lambda_i F_{\times ij}$ are the amplitudes of the sine and cosine components, respectively, for each mode i on detector j. The antenna patterns F_{+ij} and $F_{\times ij}$ are functions of the relative orientation of the source and the detector j at the time of the burst and with the polarisation angle of each mode ψ_i. The procedure to calculate the antenna pattern values, function of the instantaneous location/orientation of the detector, is covered in Appendix D. λ_i is the polarisation degree for mode i depending on the orientation of the source in space ι (see Appendix B).

It is straight-forward to calculate the real and imaginary coefficients of the Fourier transform of the exponentially damped sinusoidal signal with Eq. 5.1, the generic DTFT expression. There exists advantages of using this analytical expression:

- The complex value for any particular frequency bin $[k]$ is readily computed, there is no need to calculate the DFT of the whole data stretch. Thus, it is easy to focus on any bandwidth of interest with the desired frequency resolution by simply computing the analytic expression for those frequency values.

- If required, after a variable change $z \rightarrow z^*$ it is possible to calculate the DFT at non-uniformly spaced frequency points. This is known as the Warped Discrete Fourier Transform (WDFT) and is a convenient tool for analysing signals where most of the power is concentrated in one or several narrow bandwidths (several oscillation modes, for example) and the frequency bands between those regions, containing most of the power, are not important. The reader is referred to (93; 119; 120) for more information about the WDFT. Note: in this work the calculation of the likelihood was limited to uniformly spaced frequency points within appropriate bandwidths.

Eq. 5.1, in combination with Eq. 4.24, allows the calculation of the logarithm of the likelihood for stretches of data of several detectors that may include one

or more oscillation modes. The total likelihood of the data $\mathbf{D}$ acquired by all the detectors in the network can be then written as:

$$p(\mathbf{D}|M,I) = \mathcal{L}(M,\mathbf{D}) = \prod_{j=1}^{J} \mathcal{L}^{(j)}. \tag{5.2}$$

In this work, the amount of data used to compute the likelihood is constrained to those frequency points within the bandwidths where most of the energy of the signal has seen to be concentrated in the spectrogram. Fig. 5.1 shows the real and imaginary coefficients of an arbitrary exponentially damped signal, where the borders of the bandwidths limiting the frequency points, included in the computation of the likelihood, are marked with dashed vertical lines. The regions outwith those delimited by the vertical lines hardly contain any signal energy and are omitted from the computation of the likelihood.

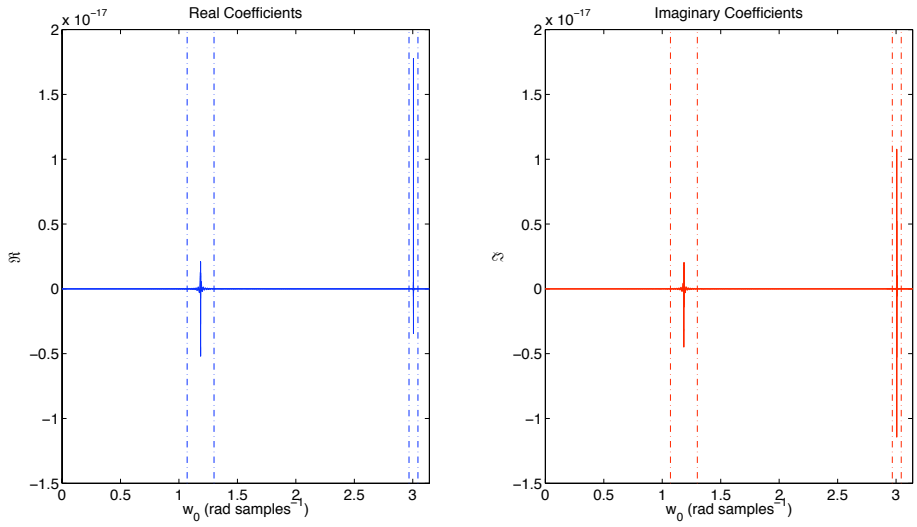

Figure 5.1: Real and imaginary coefficients of an exponentially damped sinusoidal signal of two oscillation modes. The vertical lines show the bandwidths enclosing the frequency points used in the calculation. The lack of features outwith the two bands justifies the motivation to compute the likelihood using only the frequency points within the bandwidths. For a detailed representation of the spectrum corresponding to the f-mode, see Fig. 4.5.

The f-mode oscillation is short, with an approximate duration of a tenth of a

second, whereas the p-mode oscillation is larger and it can last for a few seconds. Consequently, the relevant frequency band that captures the power of the signal is wider for the f-mode than for the p-mode. Throughout this work bandwidths of $\Delta f_f/2 = 300$ Hz and $\Delta f_p/2 = 100$ Hz around the most energetic frequency bin have been adopted, with a frequency resolution of $f_{res} = 0.05$ Hz. Thus, the frequency points at which real and imaginary coefficients are computed fall in the range $w_f = 2\pi/f_s[f_0 - \Delta f_f, f_0 + \Delta f_f]$ and $w_p = 2\pi/f_s[f_0 - \Delta f_p, f_0 + \Delta f_p]$ in increments of $\Delta w = 2\pi f_{res}/f_s$. This means that, in general, when both oscillations are included, Eq. 5.1 needs to be computed at $\Delta f_f/f_{res} + \Delta f_p/f_{res} = 600/0.05 + 200/0.05 = 12000 + 4000 = 16000$ frequency points per each detector and likelihood evaluation.

5.2 Priors

Bayesian methods combine the data acquired and any previous information to infer posterior probabilities. It is important to establish what is known and the degree of certainty of the hypotheses considered, the values of the parameters of the model in our case, for there are instances when something is known about one or more parameters of the model. In the Bayesian inference this is called prior information and it reflects the knowledge previous to analysing the data. This information can be incorporated into the Bayesian inference process so that our final beliefs are shaped in light of the prior information and the acquired data. In the following, the priors of all the parameters of the models considered are presented.

- Amplitude h_0: The amplitude of the gravitational wave is related to the size of the oscillation of the compact star. Unfortunately, the energy channeled into the oscillation modes is not well known, due to the varied mechanisms expected to make the neutron star ring. In this work, a minimum and a maximum energy emitted as gravitational radiation were assumed and their corresponding amplitude values calculated (see Section 5.3). The amplitude is a *scale parameter*: it is mapped to the range of energies encompassing a few orders of magnitude with Eq. 5.12. The state of ignorance within the

range of amplitude values may be represented by Jeffrey's prior, a uniform probability distribution in a logarithmic scale (see (117)):

$$\pi(h_0|I) = \begin{cases} \frac{1}{h_0 \log(h_{0max}/h_{0min})}, & \text{if} \quad h_{0min} < h_0 < h_{0max} \\ 0, & \text{otherwise.} \end{cases} \tag{5.3}$$

This prior probability is not defined for the case of $h_0 = 0$ but this was not a problem, for a minimum non-zero energy/amplitude has always been considered. The wide range of energy values E^{gw} from 0.001×10^{-6} to 100×10^{-6} $M_s c^2$ has been adopted.

- Frequency f_0: The search is limited to a range of frequencies around the most energetic pixel in the spectrogram. A prior distribution biased towards the central frequency value may be justifiable; however, complete ignorance within a reasonable range around that value has been preferred, reflected by a uniform or flat prior of the form:

$$\pi(f_0|I) = \begin{cases} \frac{1}{(f_{0max} - f_{0min})}, & \text{if} \quad f_{0min} < f_0 < f_{0max} \\ 0, & \text{otherwise.} \end{cases} \tag{5.4}$$

- Damping time τ: The search is limited to the range of time around the duration of the signal indicated by the spectrogram. Again, a prior distribution biased to that particular value could be used but complete ignorance has been assumed within a reasonable range of values by means of a uniform prior:

$$\pi(\tau|I) = \begin{cases} \frac{1}{(\tau_{max} - \tau_{min})}, & \text{if} \quad \tau_{min} < \tau < \tau_{max} \\ 0, & \text{otherwise.} \end{cases} \tag{5.5}$$

- Polarisation degree λ: In general, from the spectrogram of gravitational wave data only, nothing will be known about the polarisation degree. Unless orientation of the neutron star is known, complete ignorance is assumed

and the search is open to any degree of ellipticity from linear polarisation $\lambda_{min} = 0$ to circular polarisation $\lambda_{max} = 1$:

$$\pi(\lambda|I) = \begin{cases} \frac{1}{(\lambda_{max}-\lambda_{min})} = 1, & \text{if} \quad \lambda_{min} < \lambda_0 < \lambda_{max} \\ 0, & \text{otherwise.} \end{cases} \tag{5.6}$$

When the location of the source is known, it may be that from electromagnetic observations of the nebula around the neutron star the orientation of its angular momentum vector ι is known with some uncertainty; from here, in turn, the distribution of λ may be inferred (see Appendix J) and the prior could be then approximately written as a Gaussian distribution:

$$\pi(\lambda|I) = \mathcal{N}(\mu_\lambda, \sigma_\lambda) = \frac{1}{\sigma_\lambda\sqrt{2\pi}} \exp\left[-\frac{(\mu_\lambda - \lambda)^2}{2\sigma_\lambda^2}\right], \tag{5.7}$$

where μ_λ and σ_λ are deduced from fitting $\pi(\lambda)$ obtained from $p(\iota)$.

- Polarisation angle ψ: In general, considering the spectrogram of gravitational wave data only, nothing will be known about the polarisation angle. Thus, complete ignorance is assumed and the search is open to any polarisation angle. Since the antenna pattern functions $(F_+, F_\times)$ are the same for any two polarisation angles π rad apart, the search is carried out in the range of values limited between $\psi_{min} = 0$ and $\psi_{max} = \pi$. This is given by the uniform prior:

$$\pi(\psi|I) = \begin{cases} \frac{1}{(\psi_{max}-\psi_{min})} = \frac{1}{\pi}, & \text{if} \quad \psi_{min} < \psi < \psi_{max} \\ 0, & \text{otherwise.} \end{cases} \tag{5.8}$$

Here, again, from electromagnetic observations it may be possible to constrain the polarisation angle with a Gaussian distribution centred in the real value of the form:

$$\pi(\psi|I) = \mathcal{N}(\mu_\psi, \sigma_\psi) = \frac{1}{\sigma_\psi\sqrt{2\pi}} \exp\left[-\frac{(\mu_\psi - \psi)^2}{2\sigma_\psi^2}\right], \tag{5.9}$$

where σ_ψ is set to include the real value of ψ within a range of $\pm 5^\circ$ (± 0.087 rad) of the mean value with probability higher than 95%.

- Declination (δ) and Right Ascension (RA): For a source of unknown location any direction is taken as equally probable – isotropically distributed. If the surface of a sphere was meshed for each cell to have the same solid angle, the source would have the same probability of being in any cell. For equatorial coordinates with the ranges $\delta \in [-\pi/2, \pi/2]$ and RA $\in [0, 2\pi]$, the total ignorance about the sky-location can be defined by the following two independent uniform distributions:

$$\pi(\sin\delta|I) = \frac{1}{(\sin\delta_{max} - \sin\delta_{min})} = \frac{1}{2} \quad \text{and} \quad \pi(RA|I) = \frac{1}{2\pi}. \tag{5.10}$$

  A random sky location can be defined by selecting (δ,RA) from two uniform distributions: $\sin\delta \sim \mathcal{U}$[-1,1] and RA $\sim \mathcal{U}[0, 2\pi]$.

Table 5.1 shows the exact parameter values of the injected signals and the range of the parameter space searched. The amplitude of the signal is a function of the energy released as gravitational radiation by the oscillations of the neutron star. The frequency and damping time values are fiducial and have been taken from tabulated values (75) corresponding to the f- and p-modes of neutron star oscillations.

Table 5.2 shows the arrival order and the time differences, in milliseconds and number of samples, to the detectors chosen and the antenna pattern functions for each mode and detector.

5.3 Amplitude, frequency and damping time of the signal

The amplitude of the gravitational burst signal reaching the detector depends on the energy emitted by the source and the distance to it. Rough estimates of gravitational-wave amplitudes far away from the pulsating star can be obtained with the standard relation for the energy flux (121):

$$F = \frac{c^3}{16\pi G}|\dot{h}| = \frac{1}{4\pi r^2}\frac{dE}{dt}, \tag{5.11}$$

PARAMETER VALUES					
Description	**Par.**	**Units**	**min.**	**max.**	**Exact**
(Energy)	E^{gw}	$M_s c^2$	0.001×10^{-6}	$1 \times 100 \times 10^{-6}$	several*
Amplitude	h_{0f}	-	1.79×10^{-23}	5.67×10^{-21}	several**
Osc. frequency	f_{0f}	Hz	3070	3110	3090
Damping time	τ_f	sec	0.01	1	0.109
Pol. degree	λ_f	-	0	1	0.4
Pol. angle	ψ_f	rad	0	π	1.2
Amplitude	h_{0p}	-	3.58×10^{-24}	1.13×10^{-21}	several***
Osc. frequency	f_{0p}	Hz	7818	7858	7838
Damping time	τ_p	sec	0.1	10	4.64
Pol. degree	λ_p	-	0	1	0.7
Pol. angle	ψ_p	rad	0	π	2.4
Declination	δ	rad	$-\pi/2$	$\pi/2$	-0.5063
Right Ascension	RA	rad	0	2π	4.6498

* function of the energy and distance to the source $d = 8.5$ kpc (see Eq. 5.12).

** exact values and SNR can be seen on tables summarising results in Appendix K.

*** taken to be a fifth of the amplitud of the f-mode.

Table 5.1: Exact values of the waveforms injected and limits of the searched parameter space for f- and p-modes.

ARRIVAL ORDER AND TIME DIFFERENCES							
Name	**Arrival**			f**-mode**		p**-mode**	
	Pos.	**Time (ms)**	**Samples***	F_+	$F_\times$	F_+	$F_\times$
Adv-LIGO-H	1	0	0	-0.330	0.282	0.423	0.101
Adv-LIGO-L	2	6.8	111	-0.285	0.026	0.188	0.216
Adv-VIRGO	3	21.5	352	-0.930	0.188	0.699	0.641

Signal incoming from the galactic centre at GLST = 0h.

Polarisation angles for each mode shown in Table 5.1.

* Assuming sampling frequency $f_s = 16384$ Hz.

Table 5.2: Arrival order, time differences, and antenna patterns for f- and p-modes described in Table 5.1 of the detectors.

which, in combination with i) $dE/dt = E/2\tau$, ii) the assumption that the signal is monochromatic, iii) knowledge that the effective amplitude achievable after matched filtering scales as the square root of the number of observed cycles, $h_{\rm eff} = h_0\sqrt{n} = h_0\sqrt{f_0\tau}$, provide an estimate of:

$$h_{\rm eff} \approx 1.294 \times 10^{-20} \left(\frac{E}{10^{-6}M_s c^2}\right)^{1/2} \left(\frac{2\ \text{kHz}}{f_0}\right)^{1/2} \times \left(\frac{8.5\ \text{kpc}}{d}\right) \tag{5.12}$$

for the f-mode. For the case of a supernova, it is quite conservative to assume an energy release of $10^{-6}M_s c^2$ in the form of gravitational radiation (121). For the fiducial values of $f_0 = 2$ kHz, $\tau = 0.1$ s and $d = 8.5$ kpc, $h_0 = 9.15 \times 10^{-22}$.

In the absence of a similar expression to Eq. 5.12 for the calculation of the amplitude of the p-mode, this has been considered in this work, quite arbitrarily, as a fifth of the f-modes' amplitude.

5.4 Scenarios and parameters considered

Several hypotheses grouped in two realistic scenarios have been considered in this chapter; they represent different states of knowledge/ignorance, summarised in Table 5.3. Each of the hypotheses considered makes different assumptions with respect to the shape of the signal, its polarisation and the location of the source.

Two scenarios have been considered depending on whether only one oscillation mode (f), or two oscillation modes (f and p), are known/suspected. We assume this information can be inferred from the spectrogram that picked up the burst candidate in the first instance. Different degrees of knowledge (or ignorance) about the signal depend on whether, from electromagnetic observations a) the location of the source is known and b) something about the orientation of the neutron star in space is known.

It may be that the candidate source is a catalogued pulsar of precisely known sky-location and that the antenna pattern functions F_+ and $F_\times$ at a particular instant of time are better defined, although not completely, with the polarisation angle ψ generally unknown. Knowledge of the location of the source reduces in two dimensions the parameter space to be studied in two dimensions. For

those sources with known locations, X-ray images of the nebula region around the pulsar may be available, from which the orientation of the angular momentum vector could be estimated (122; 123). If the approximate direction of the angular momentum is known, a credibility interval for the polarisation degree λ and the polarisation angle ψ values may be inferred. This information can then be incorporated into the model selection and parameter estimation by constraining the priors of λ and ψ to a narrower range.

In the following, the scenarios and hypothesis considered in this work are listed:

- SCENARIO 1 - One oscillation mode is detected: f-mode.
  - H_{10}: NOISE: The data acquired is only instrumental noise. No model is involved in this hypothesis.
  - $H_{1\mathrm{K}}$: SIGNAL + NOISE: The data acquired contains the signal plus instrumental noise. The sky location of the source is known but nothing about its orientation. The model has 5 unknown parameters of independent uniform priors: $[h_0, f_0, \tau, \lambda, \psi]$.
  - $H_{1\mathrm{U}}$: SIGNAL + NOISE: The data acquired is the signal plus instrumental noise. Neither the source's sky-location nor anything about its orientation are known. The model has 7 unknown parameters of independent uniform priors: $([h_0, f_0, \tau, \lambda, \psi], [\delta,\mathrm{RA}])$.
  - $H_{1\mathrm{G}}$: SIGNAL + NOISE: The data acquired is the signal plus instrumental noise. The source's sky-location and the direction of the angular momentum are known with some uncertainty. There are 5 unknown parameters, from which three have uniform priors (h_0, f_0, τ), and the other two are related to the polarisation of the signal (λ, ψ), function of a Gaussian distribution of ι.
- SCENARIO 2 - Two oscillations modes are detected: f- and p-modes.
  - H_{20}: NOISE: The data acquired is only instrumental noise. No model is involved in this hypothesis.

- $H_{2\mathrm{K}}$: SIGNAL + NOISE: The data acquired contains the signal plus instrumental noise. The source's sky-location of the source is known but nothing about its orientation. The model considers two oscillation modes with $2{\times}5 = 10$ unknown parameters of independent priors: $[h_{0i}, f_{0i}, \tau_i, \lambda_i, \psi_i]$, for $i = 1(f - mode) and i = 2(p - mode)$.
- $H_{2\mathrm{U}}$: SIGNAL + NOISE: The data acquired contains the signal plus instrumental noise. Neither the source's sky- location nor anything about its spatial orientation are known. The model considers two oscillations with $2{\times}5 + 2 = 12$ unknown parameters of independent uniform priors: $[h_{0i}, f_{0i}, \tau_i, \lambda_i, \psi_i]$ for $i = 1, 2$ and [δ,RA].

All the hypotheses of each scenario use the same number of frequency points to evaluate the likelihood of the model. Cross-scenario hypothesis comparison is not carried out, due to the different number of frequency points used for hypothesis considering one or two oscillation modes.

5.5 Model comparison - evaluation of the odds ratio

The odds ratio is a convenient way of comparing two hypotheses: it measures for which one of them is the data more favourable. Here, as explained before, each hypothesis corresponds to a model. Typically, one hypothesis considers the data acquired to be a combination of signal plus noise, whilst the other considers the data to be only instrumental noise. The odds ratio can be written:

$$O_{S,N} = \frac{p(H_S|\mathbf{D}, I)}{p(H_N|\mathbf{D}, I)} = \frac{p(H_S|I)}{p(H_N|I} \frac{p(\mathbf{D}|H_S, I)}{p(\mathbf{D}|H_N, I)} = \frac{p(H_S|I)}{p(H_N|I)} B_{S,N}. \tag{5.13}$$

where $\mathbf{D}$ is the data acquired by the detectors. H_S can be any hypothesis of scenario 1 ($H_{1\mathrm{K}}, H_{1\mathrm{U}}$, or $H_{1\mathrm{G}}$) and H_N is H_{10}. Similarly, for scenario 2 H_S could be any of $H_{2\mathrm{K}}$ or $H_{2\mathrm{U}}$ and H_N is H_{20}. Before analysing the data it is common to consider that the two hypotheses are equally probable, $p(H_S|I) = p(H_N|I)$; then the odds ratio $O_{S,N}$ reduces to the Bayes factor $B_{S,N}$. This way, and without any

Scenarios and hypotheses considered											
Hyp.	**Sc.**	**S-N**	**Mode**	**Parameters**							
				h_0	f_0	τ	λ	ψ	δ	RA	ι
H_{10}	1	N	f	n/a	n/a	n/a	n/a	n/a	n/a	n/a	n/a
H_{1K}	1	S+N	f	u	u	u	u	u	k	k	n/a
H_{1U}	1	S+N	f	u	u	u	u	u	u	u	n/a
H_{1G}	1	S+N	f	u	u	u	$\sim$k	$\sim$k	k	k	$\sim$k
H_{20}	2	N	f	n/a	n/a	n/a	n/a	n/a	n/a	n/a	n/a
			p	n/a	n/a	n/a	n/a	n/a	-	-	-
H_{2K}	2	S+N	f	u	u	u	u	u	k	k	n/a
			p	u	u	u	u	u	-	-	-
H_{2U}	2	S+N	f	u	u	u	u	u	u	u	n/a
			p	u	u	u	u	u	-	-	-

k $\equiv$ known, $\sim$k $\equiv$ quasi-known (Gaussian prior).

u $\equiv$ unknown (Uniform prior).

n/a $\equiv$ not applicable.

Table 5.3: The two scenarios and their hypotheses considered.

previous bias, we let the data speak by calculating the ratio of the likelihoods of two models. In logarithmic notation the Bayes factor is:

$$\log B_{S,N} = \log(p(\mathbf{D}|H_S, I)) - \log(p(\mathbf{D}|H_N, I)). \tag{5.14}$$

5.5.1 'Signal + noise' hypotheses

For those hypotheses that consider the acquired data as a combination of signal plus noise, the computation of the marginal likelihood (likelihood of the model trying to interpret the data) requires integrating over the prior domain of all the parameters of the model:

$$p(\mathbf{D}|H_S, I) = \int_{\mathbf{\Theta}} d\mathbf{\Theta}\ p(\mathbf{\Theta}|H_S)\ p(\mathbf{D}|H_S, \mathbf{\Theta}, I), \tag{5.15}$$

where the combined prior of the parameters (a point in the parameter space) is the multiplication of each individual prior, as defined in section 5.2,

$$p(\mathbf{\Theta}|H_S) = \prod_i p(h_{0i}|I)\ p(f_{0i}|I)\ p(\tau_i|I)\ p(\lambda_i|I)\ p(\psi_i|I), \tag{5.16}$$

and the logarithm of the likelihood of a particular set of parameter values is:

$$\log \mathcal{L}(\mathbf{D}, H_S) = \log(p(\mathbf{D}|H_S, \mathbf{\Theta}, I)) = \tag{5.17a}$$

$$= \sum_{j=1}^{J} \left[-K \log(2\pi) - \sum_{k=1}^{K} 2 \log(\sigma^{(j)}[k]) + \frac{(s_{\Re}^{(j)}[k] - h_{\Re}^{(j)}[k])^2 + (s_{\Im}^{(j)}[k] - h_{\Im}^{(j)}[k])^2}{2\sigma^{(j)}[k]^2} \right], \tag{5.17b}$$

where $\mathbf{D} \equiv \{\tilde{s}^{(j)}\}$ is the combination of the Fourier coefficients of the data acquired in the detectors of the network. In turn, $[s_{\Re}^{(j)}, s_{\Im}^{(j)}]$ and $[h_{\Re}^{(j)}, h_{\Im}^{(j)}]$ are the Fourier coefficients of the data acquired and of the signal modeled $\tilde{h}^{(j)}(f; \mathbf{\Theta})$ in Eq. 5.1, for a detector j.

The integration for the calculation of the marginal likelihood in Eq. 5.15 using brute force over a close parameter space grid is computationally very demanding and thus impractical. In this work, all the marginal likelihood calculations for model comparison and parameter estimation have been carried out using the nested sampling algorithm presented in section 4.7.

5.5.2 'Only noise' hypothesis

For the hypothesis H_N, which assummes that the acquired data is only instrumental noise, there are no parameters to integrate over, because the instrumental noise profile is known. There is no signal expected, ($h^{(j)}_{\Re}[k] = h^{(j)}_{\Im}[k] = 0$), and the expression in Eq. 5.17 reduces to:

$$\log(p(\mathbf{D}|H_N, I)) = \sum_{j=1}^{J} \left[-K\log(2\pi) - \sum_{k=1}^{K} 2\log(\sigma^{(j)}[k]) + \frac{s^{(j)}_{\Re}[k]^2 + s^{(j)}_{\Im}[k]^2}{2\sigma^{(j)}[k]^2} \right]. \tag{5.18}$$

For the noise only case, evaluating the marginal likelihood with Eq. 5.18 is straight-forward, for it does not require integration over parameter values.

5.6 Detection and false-alarm rate threshold

The minimum strength of the signal necessary to claim a detection has been investigated first. The odds ratio between the hypotheses of H_S and H_N (see Eq. 5.13) can be used to discern whether a stretch of data is more likely to be only noise or otherwise contains a particular modeled signal. By considering equal priors for both hypotheses a threshold value of the Bayes factor can be established, above which the presence of the signal can be claimed.

The false alarm rate indicates the probability of claiming the presence of the signal when in reality only noise is present. The probability that this happens can be inferred from the computation of $\log B_{S,N}$ for multiple noise realisations where purposedly the signal has not been added. Due to the variability of different noise realisations and to the randomness of the nested sampling algorithm, the resulting $\log B_{S,N}$ values show a distribution and the lower and upper limits enclosing $(1-\alpha)$ of the probability mass can be inferred. Taking the upper limit of this range as a threshold value is the same as saying that a stretch of data resulting in a Bayes factor higher than this threshold contains the signal with a probability bigger than $(1-\alpha)$. In other words, there is a probability α to claim a detection when there is only noise present.

5.6.1 Scenario 1: f-mode

Fig. 5.2 shows the distribution of the resulting Bayes factor values from 100 different noise realisations for each of the hypotheses considered, where the logarithm of the Bayes factors $\log B_{1\mathrm{K},10}$, $\log B_{1\mathrm{U},10}$ and $\log B_{1\mathrm{G},10}$ have been calculated and histogrammed. As expected, the fact that $\log B_{S,N} \ll 0$ for all the trials indicates that the data containing only noise always favours the hypothesis H_{10} better than any of the 'signal + noise' hypotheses ($H_{1\mathrm{K}}$, $H_{1\mathrm{U}}$ or $H_{1\mathrm{G}}$). The comparison of the histograms highlights the effect of Occam's razor, which penalises the more complicated models ($H_{1\mathrm{U}}$ has two extra parameters due to the unknown location of the source) and results in overall lower values of $\log B_{1\mathrm{U},10}$ over $\log B_{1\mathrm{K},10}$.

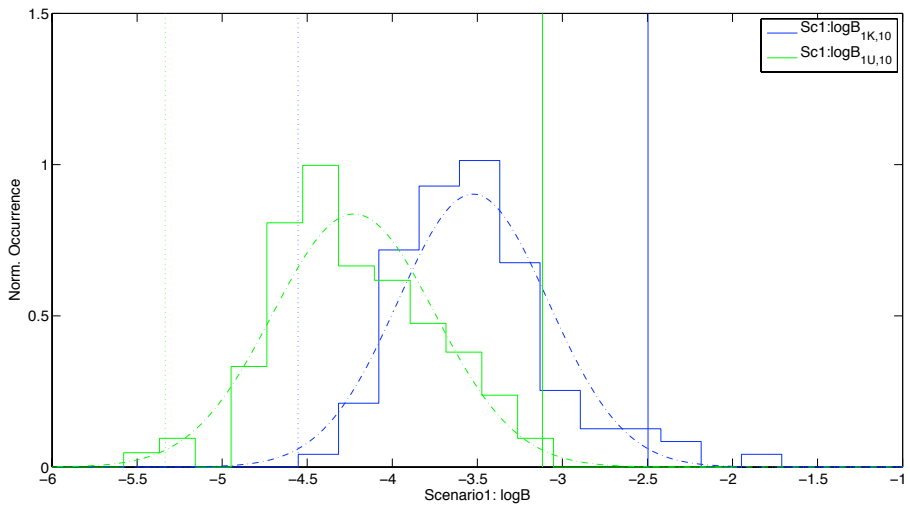

Figure 5.2: Normalised distribution of $\log B_{S,N}$ factors recovered from running the algorithm 100 times for different noise realisations. The spread of the distribution arises from the combination of different noise realisations and the random nature of the nested sampling algorithm. The dashed curves correspond to the Gaussian distributions fitted: the vertical lines enclose 98% of the probability mass of the fitted distribution, delimiting the 1% false alarm rate of $\log B_{S,N}$ thresholds at -2.496 and -3.117.

Fig. 5.3 shows Bayes factors when the stretch of data acquired contains instrumental noise plus signals of increasing strength, generated by increasing the amount of energy channeled to the f-mode oscillation. For each of the SNR

values considered the average value of five trials has been computed to reduce the bias introduced by the uncertainty of their distribution. Values of $\log B_{S,N}$ factor increase rapidly for increasing values of SNR, showing that it is a sensitive indicator of the presence of the signal. For low values of SNR the factor favours the 'only noise' hypothesis, but as the strength of the signal increases, there is a point at which the factor crosses the $\log_{S,N} = 0$ threshold, indicating that for any signal of bigger strength the existence of the modeled signal is favoured. As expected, for the same value of SNR, the Bayes factor is smaller for the more complicated models.

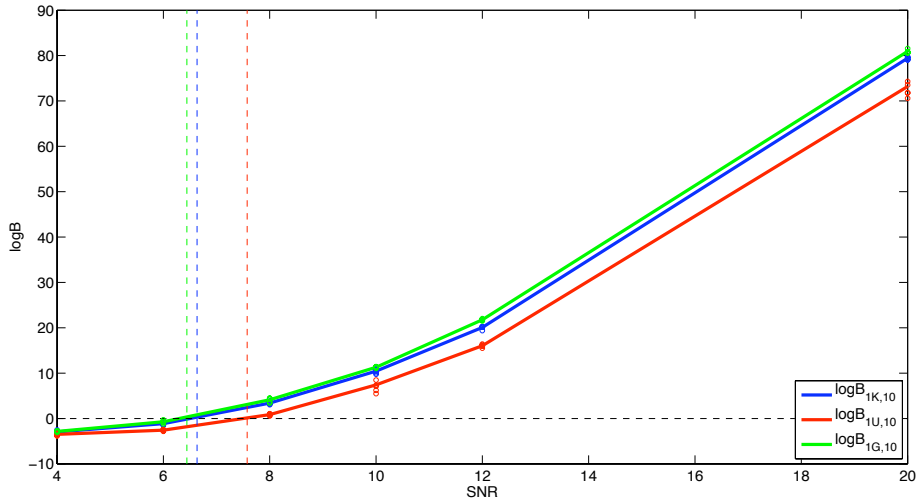

Figure 5.3: The recovered $\log B_{S,N}$ (dots) and their mean (joined with continuous lines) values for progressively stronger signals. The Bayes factor grows quickly for increasing SNR values showing that it is a sensitive indicator of the presence of a signal. The horizontal dashed line at $\log B_{S,N} = 0$ marks the borderline between the regions where noise or signal are more likely. The vertical dashed lines correspond with the intersections of the curves with the horizontal line and mark the strengths of the signal where this border is located: at approximate SNR values of 6.44, 6.63 and 7.57. As reflected in Fig. 5.2 for the same SNR value the model with more parameters presents a lower value of $\log B_{S,N}$, as expected.

5.6.2 Scenario 2: f- and p-modes

The resulting $\log B_{S,N}$ values from 100 different noise realisations when the signal is not present have been computed and histogrammed for the hypotheses in scenario 2. The resulting values present a Gaussian-like distribution shown in Fig. 5.4.

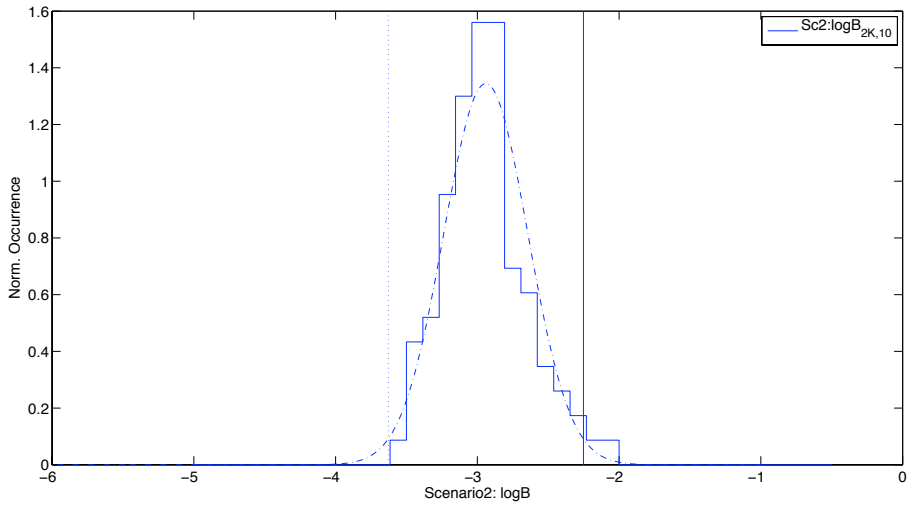

Figure 5.4: Normalised distribution of $\log B_{S,N}$ factors recovered from running the algorithm 100 times for different noise realisations. The uncertainty on the $\log B$ arises from the combination of different noise realisations and the random nature of the nested sampling algorithm. The dashed curve corresponds to the Gaussian fit and the vertical dotted lines enclose 98% of the probability, delimiting the 1% false alarm rate of $\log B_{S,N}$ thresholds at -2.251.

5.7 Parameter estimation

The results of the parameter estimation exercise with increasing signal strength is presented in this section. For each of the hypotheses under the two scenarios considered, the most probable parameter values and the limits of the 95% credibility intervals have been inferred from their posterior probability distributions.

The procedure followed consisted of injecting a signal of known characteristics into the detector noise and then recover the values of the parameters that

characterise the injected signal, based on different degrees of knowledge represented by the hypotheses. To emulate a realistic situation, the data for analysis was created by projecting a signal of known characteristics and incoming from a known sky location (galactic centre) to all the detectors of the network at an arbitrarily chosen time instant (GLST = 0h). The projection of the signal onto each detector was injected (added) to a noise realisation in accordance with the noise level expected of each detector, as explained in Section 4.3.

The posterior probability distributions for the parameters of each of the models considered were computed for signals of increasing strength, several times for each SNR value. Samples of the posterior probability are generated from the samples recorded in the course of the nested sampling to compute the evidence, as explained in section 4.8.4. Values obtained from the resampling have been histogrammed and the statistics of their distribution obtained. For the parameter estimation, the same noise realisation was used for all the trials; this was done so that the progressive evolution of the statistics of the recovered parameter values could be observed as the strength of the signal increased.

5.7.1 Scenario 1 - hypothesis 1K

The sky-position of the source is known and only the shape of the signal injected has to be determined (see summary in Table 5.3). Fig. 5.5 shows the posterior probability density, resulting from averaging 5 runs of the nested sampling algorithm with the same noise realisation, of the parameters defining the shape of the waveform. As expected, the dispersion of the probability of each parameter tends to narrow and shift toward the exact value as the SNR increases. In this respect, all the parameters behave well, aside from the posterior probability distribution of the polarisation degree λ, which constrains around the exact value only for high SNR ~ 20 values.

In the following, as an example the progress of the nested sampling algorithm for the calculation of the marginal likelihood of the hypothesis $H_{1\mathrm{K}}$ is presented. The algorithm has been run five times with the same number of objects for the case of a relatively strong signal (SNR = 12) embedded into instrumental noise (same noise realisation for all the runs). Fig. 5.6 depicts the successive points of

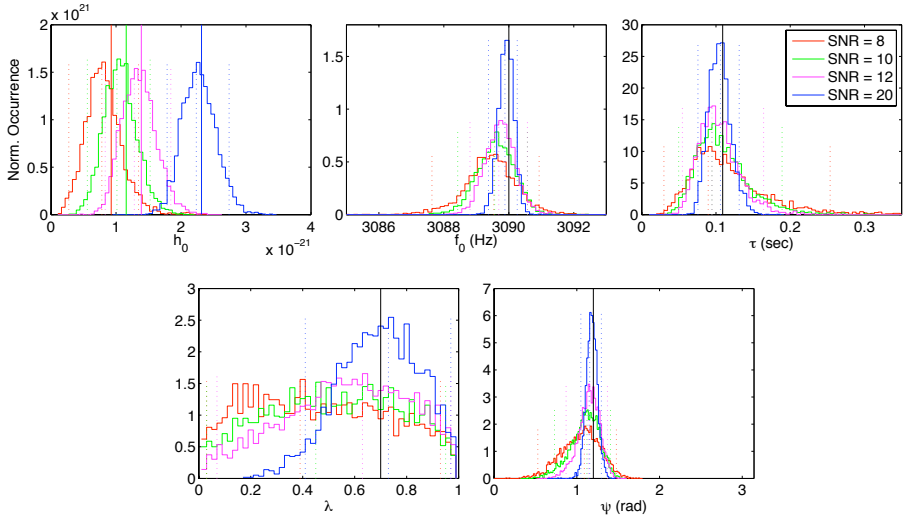

Figure 5.5: Posterior probability distributions and parameter estimation of the 5 parameters of the model for hypothesis $H_{1\mathrm{K}}$. The exact values of the parameters for the signal injected are marked with a vertical continuous line and tabulated in Table 5.1. The modes and 95% credibility intervals for each parameter are listed in the Appendix K, Table K.1.

the parameter space visited during the computation of the evidence; these are the points of the parameter space that contributed to the accumulation of the evidence and correspond to those with the lowest likelihood discarded, one per iteration. Note that for all runs the algorithm finished after approximately 2800 iterations: it was stopped when the contribution to the evidence was smaller than e^{-5} times its current value.

Fig. 5.7 gives another perspective of the evolution of the algorithm. On the left hand side, the relation between the likelihood and the prior mass $\mathcal{L}(X)$ is shown. This figure is the realistic counterpart of Fig. 4.7, included here for illustrative purposes, with the logarithmic x-axis to reflect the geometrical reduction of X and the sudden increase of likelihood for a small fraction of the prior probability mass. The right hand side depicts the fraction of the final evidence accumulated in each iteration.

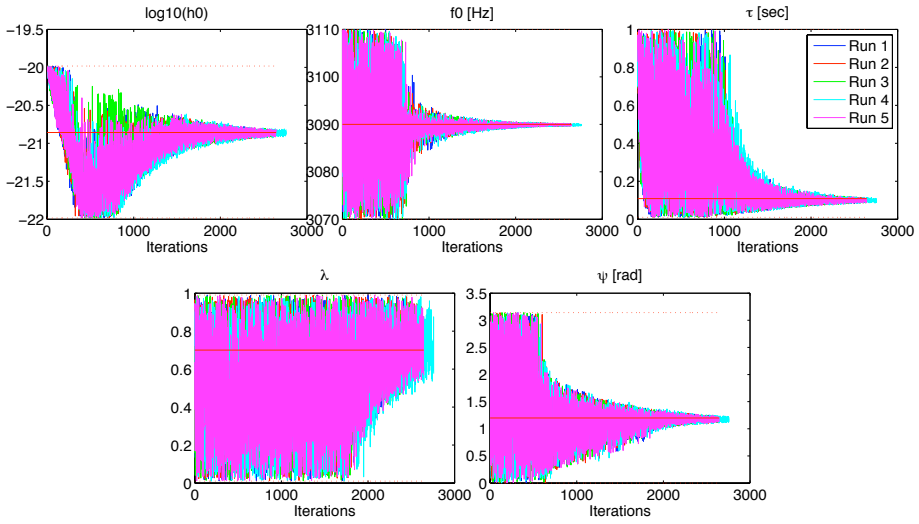

Figure 5.6: Evolution of the samples with nested sampling algorithm, for the case of a signal of SNR = 12. Each subplot shows the evolution of each parameter for five runs using the same noise realisation and number of objects. The horizontal continuous line marks the position of the exact value injected, whereas the dotted lines delimit the borders of the parameter space searched.

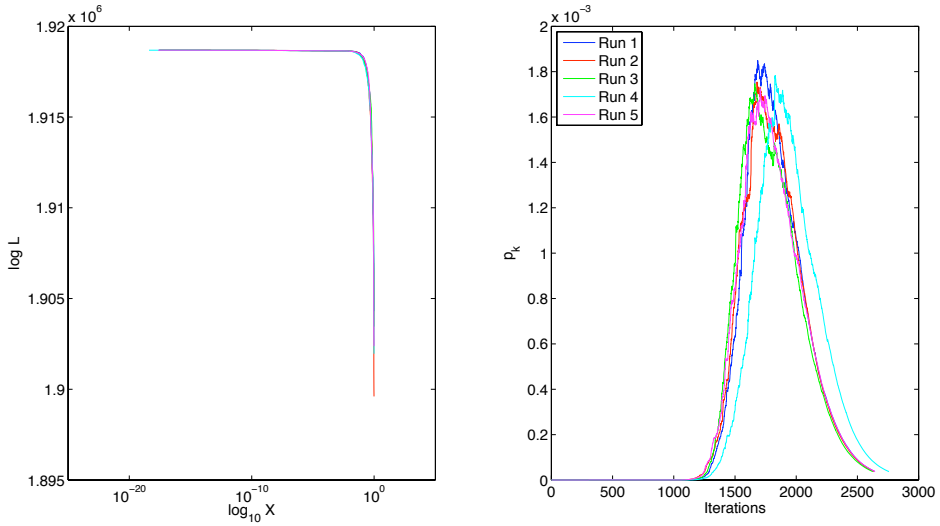

Figure 5.7: Progress of the nested sampling corresponding to the evolution of the algorithm for 5 runs depicted in Fig. 5.6. The plot on the left shows the evolution of the likelihood in function of the prior mass X (read from right to left, from 1 to 0). The plot on the right shows the evolution of the contributory fraction of the evidence p_k (see Eq. 4.40) at each iteration. For any of the runs, the first 1000 iterations, approximately, were used to locate the contributory region of the parameter space and in the next 1500 iterations most of the evidence was found. The slightly different evolution curves show the randomness of the algorithm (only of the algorithm, for the same noise realisation has been used for all), caused by the random position of the objects at onset and their random evolution to areas of higher likelihood.

5.7.2 Scenario 1 - hypothesis 1G

The sky-position of the source is assumed to be known and again, as for hypothesis $H_{1\mathrm{K}}$, only the shape of the waveform had to be determined. There is some prior information regarding the polarisation degree and polarisation angle (see summary Table 5.3): Gaussian distributions centred on the exact value and enclosing 95% of the probability mass within a region of $\pm$ 5° have been adopted both for ι (λ is derived from there, see Appendix J) and for ψ. Thus, the priors considered are $\pi(\lambda) = \mathcal{N}(\mu_\lambda, \sigma_\lambda) = \mathcal{N}(0.689, 0.098)$ and $\pi(\psi) = \mathcal{N}(\mu_\psi, \sigma_\psi) = \mathcal{N}(1.2, 0.043)$. Fig. 5.8 shows the posterior probability densities of the parameters. Again, as for hypothesis $H_{1\mathrm{K}}$, the increasing strengths of the signal move the mode of the distribution toward the exact value while its uncertainty decreases. As expected, the uncertainty of λ and ψ are considerably smaller than for the hypothesis $H_{1\mathrm{K}}$ (c.f. Fig. 5.5).

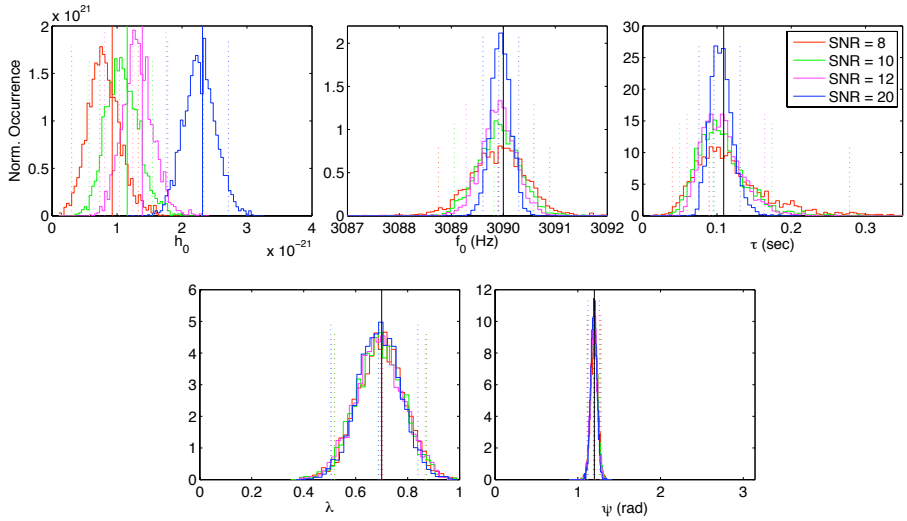

Figure 5.8: Posterior probability distributions and parameter estimation of the 5 parameters of the model for hypothesis $H_{1\mathrm{G}}$. The exact values of the parameters for the signal injected are marked with a vertical continuous line and tabulated in Table 5.1. The modes and 95% credibility intervals for each parameter are listed in the Appendix K, Table K.2.

5.7.3 Scenario 1 - hypothesis 1U

In this hypothesis the location of the source is not known and hence the parameter space has two extra dimensions to search for. In an effort to locate the sky-location of the source, working with declination values in the range $\delta \in [-\pi/2, \pi/2]$ has been avoided by applying a change of variables, $S = \pi/2 - \delta$, that shift the range of declination values to $S \in [\pi, 0]$ to the positive axis. The reason behind this change of variable is that the scale factor of the proposal distribution to generate the new object candidates during the nested sampling algorithm (see Section 4.8.3) is based on the covariance matrix of the active objects; and it may happen that these objects form a cluster of positive and negative declination values, thus biasing the standard deviation of the proposal distribution toward zero, which is not desired. On the other hand, the values of the right ascension have been used as such, but wrapped as a phase value so to be always defined in the range RA $\in [0, 2\pi]$.

Fig. 5.9 shows how the mode of the posterior distribution of each parameter shifts towards the exact value and the uncertainty is decreased as the strength of the signal increases. Again, it is observed that even for quite high SNR values the polarisation degree λ is not well defined and its probability distribution is rather ill-behaved. This is most probably related to the uncertainty of the source's sky-location. Fig. 5.10 and Fig. 5.11 show the posterior probability distributions of the two variables defining the sky-location of the source. These figures show that the two-fold degeneracy caused by the 'time of flight' has been broken. This is due to the fact that the detectors sample different superpositions of the two polarization components, and therefore the expression for the likelihood is able to break the two-fold degeneracy.

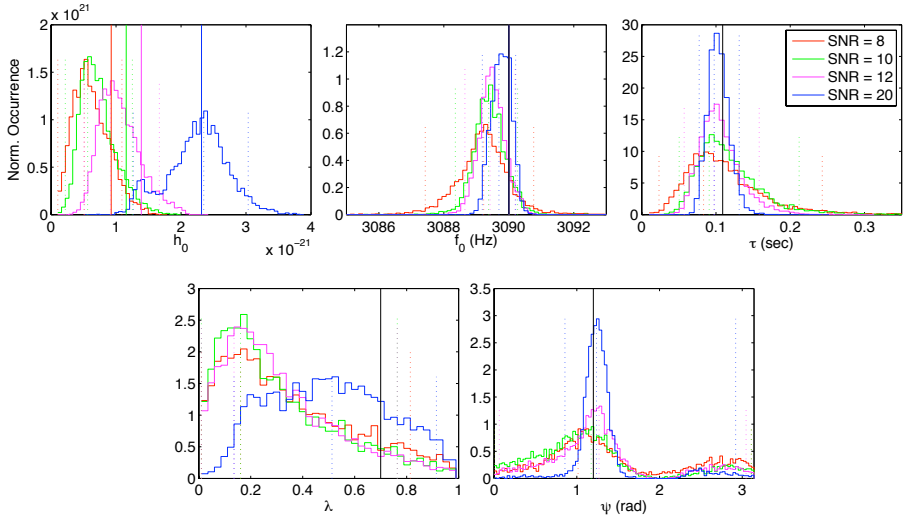

Figure 5.9: Posterior probability distributions and parameter estimation of the 5 parameters of the model for hypothesis $H_{1\mathrm{U}}$. The exact values of the parameters for the signal injected are marked with a vertical continuous line and tabulated in Table 5.1. The modes and 95% credibility intervals for each parameter are listed in the Appendix K, Table K.3.

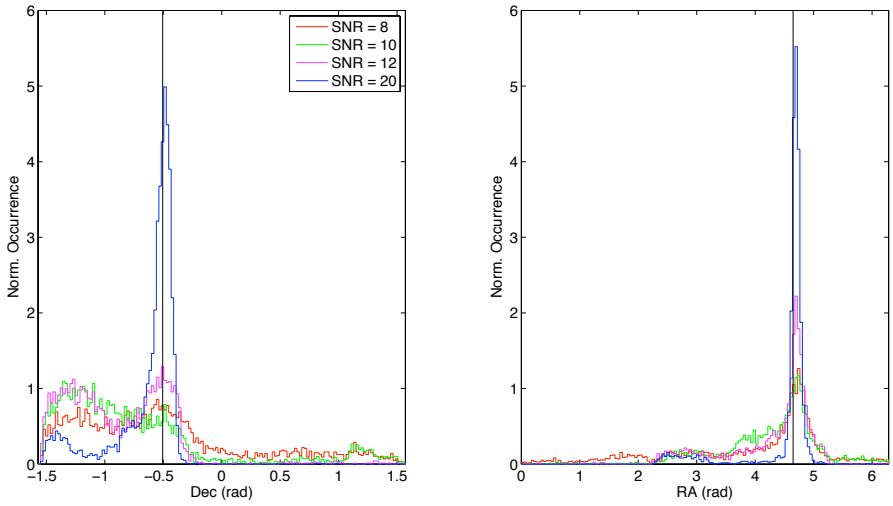

Figure 5.10: Posterior probability densities of the two parameters defining the source's sky-location. The exact value injected for each parameter is marked with a vertical continuous line.

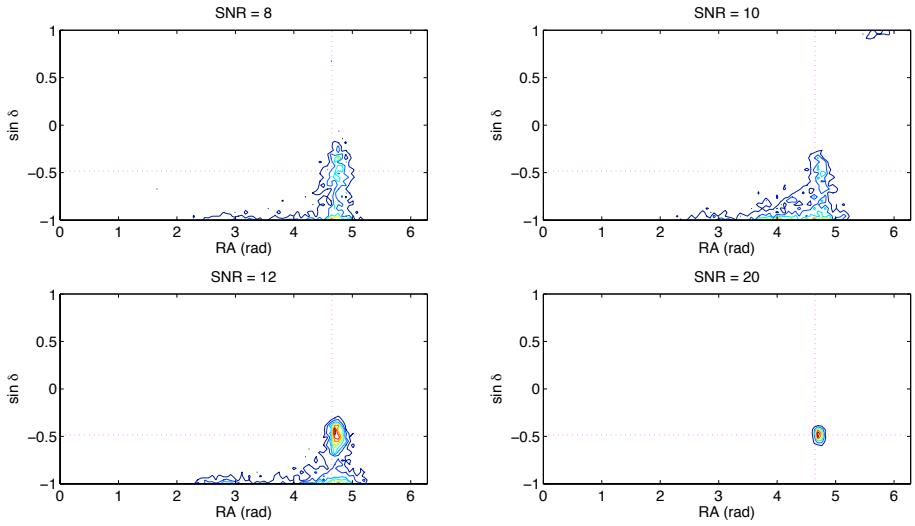

Figure 5.11: Posterior probability densities, as 2D histograms, of the two parameters defining the source's sky-location, for signals of various strength.

5.7.4 Scenario 2 - hypothesis 2K

In this hypothesis the sky-position of the source is known but nothing much about the burst gravitational wave that contains two oscillation modes shown in spectrogram (see summary Table 5.3). In the following the results of the estimation of the parameter values that define the signal are shown. Fig. 5.12 and Fig. 5.13 show the posterior probability densities (averaged for 5 runs of the algorithm) of the 10 parameters that define the signal related to the f and p oscillation modes.

Signals stronger than in scenario 1 were necessary in scenario 2 to get significant information out of the parameter estimation exercise: for SNR = 10 the parameters for the f-mode are better constrained for $H_{1\mathrm{K}}$ than for $H_{2\mathrm{K}}$. The added uncertainty of the second oscillation (p-mode) requires a stronger signal to constraint the values related to the first (f-mode).

5.7.5 Scenario 2 - hypothesis 2U

In this hypothesis the location of the source is not known and hence the parameter space has two extra dimensions. Again, a change of variable has been applied to the declination value for the reasons explained in Section 5.7.3. Fig. 5.14 and Fig. 5.15 show the posterior probability density (results of 5 runs of the algorithm averaged) of the parameters defining the signal combining the f and p oscillation modes, respectively, related to the hypothesis $H_{2\mathrm{K}}$. Fig. 5.16 shows the posterior probability distribution of the two parameters of the location of the source and Fig. 5.17 their representation as a 2D histogram.

Again, the necessity of signals of high SNR is shown to be able to constrain the values of the signal, especially for the p mode. Parameters like the damping time τ_p and polarisation angle ψ_p do not get contrained around the exact value for small values of SNR.

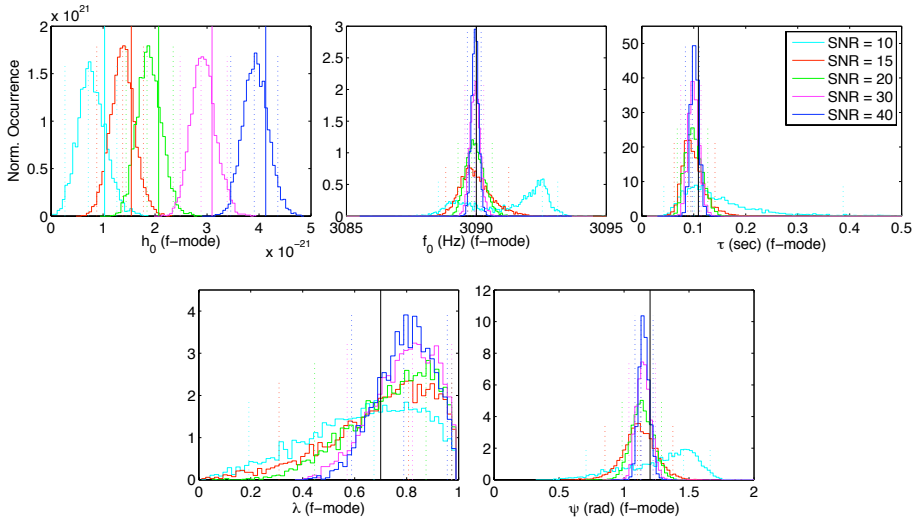

Figure 5.12: Posterior probability distributions and parameter estimation of the 5 parameters for the f-mode of the model for hypothesis H_{2K}. The exact values of the parameters for the signal injected are marked with a vertical continuous line and tabulated in Table 5.1. The modes and 95% credibility intervals for each parameter are listed in the Appendix K, Table K.4.

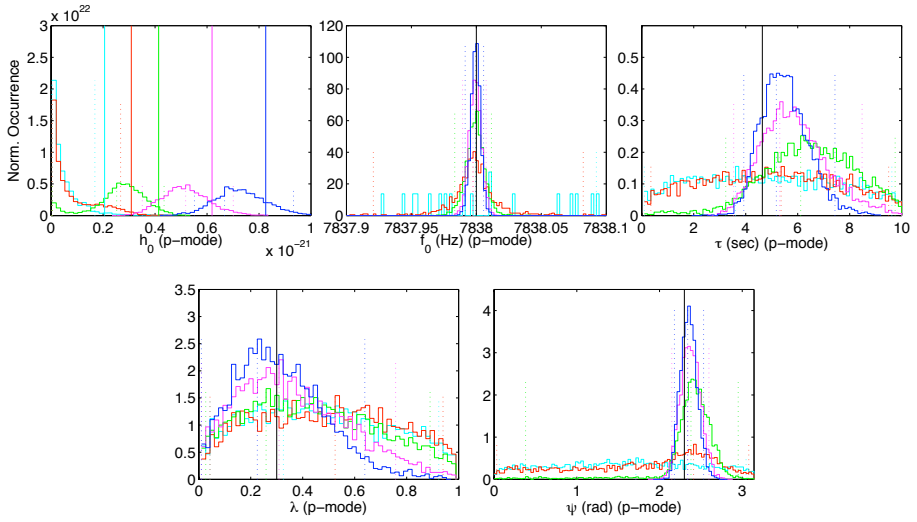

Figure 5.13: Posterior probability distributions and parameter estimation of the 5 parameters for the p-mode of the model for hypothesis H_{2K}. The exact values of the parameters for the signal injected are marked with a vertical continuous line and tabulated in Table 5.1. The modes and 95% credibility intervals for each parameter are listed in the Appendix K, Table K.4.

5.8 Discussion and Conclusions

5.8.1 Scenario 1

Overall, for all the hypotheses of scenario 1 the posterior probabilities of the signal parameters are well defined. As expected, the uncertainty of the probability distributions of the signal parameters narrow down and their mode shifts toward the exact value for signals of increasing strength.

It is fortunate that the oscillation frequency of the signal can be estimated with great accuracy. As expected, the estimation is more precise when the location and the approximate orientation of the source are known. The discrepancy between the mode and the exact value is always smaller than 0.02% for any of the three hypotheses considered in scenario 1. This is encouraging keeping in mind the need to differentiate precisely the values of the oscillation frequencies in order to discern equations of state in mind.

The polarisation degree λ_f is the only parameter that requires a considerable signal strength to constrain its distribution significantly around the exact value. Estimation of the polarisation degree is poorest when the location of the source is not known, for which not even with the highest SNR analysed the distribution shows a preference for the exact value. The correlation between the amplitude parameter h_0 and the degree of polarisation λ is suspect for the inability of constraining the latter. Equally, the estimation of the amplitude of the signal is better when the location of the source is known than when it is not known.

It is significant that for the hypothesis H_{1G} (see Fig. 5.8), for which the location of the source is known and the orientation of the neutron star ι is known with an uncertainty of $\pm 5^\circ$ (and thus $\sigma_\lambda \approx 0.1$, see Appendix K), that the 95% credibility interval ($\approx 2\sigma$ for a normal distribution) results in a posterior probability distribution of $\sigma_\lambda \approx 0.0875$ that hardly varies with increasing signal strength. This shows that even when the rest of the parameters are well known, there is always a considerable uncertainty on the polarisation degree λ. For the polarisation angle ψ, where the exact value is assumed to be known with an uncertainty $\pm 5^\circ$ ($\sigma_\psi = 0.043$), the uncertainty of its posterior probability distribution is approximately $\sigma_\psi = 0.0375$ rad: a slight narrowing of the uncertainty is observed

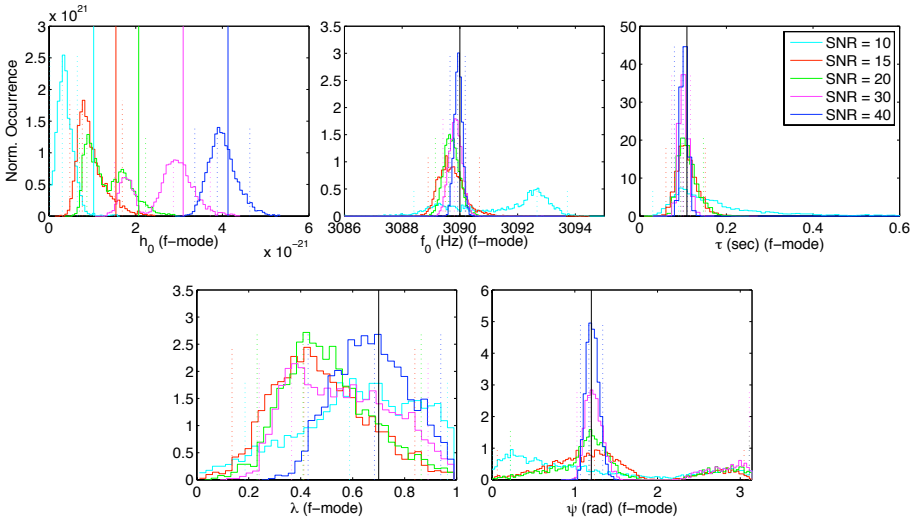

Figure 5.14: Posterior probability distributions and parameter estimation of the 5 parameters for the f-mode of the model for hypothesis $H_{2\mathrm{U}}$. The exact values of the parameters for the signal injected are marked with a vertical continuous line and tabulated in Table 5.1. The modes and 95% credibility intervals for each parameter are listed in the Appendix K, Table K.5.

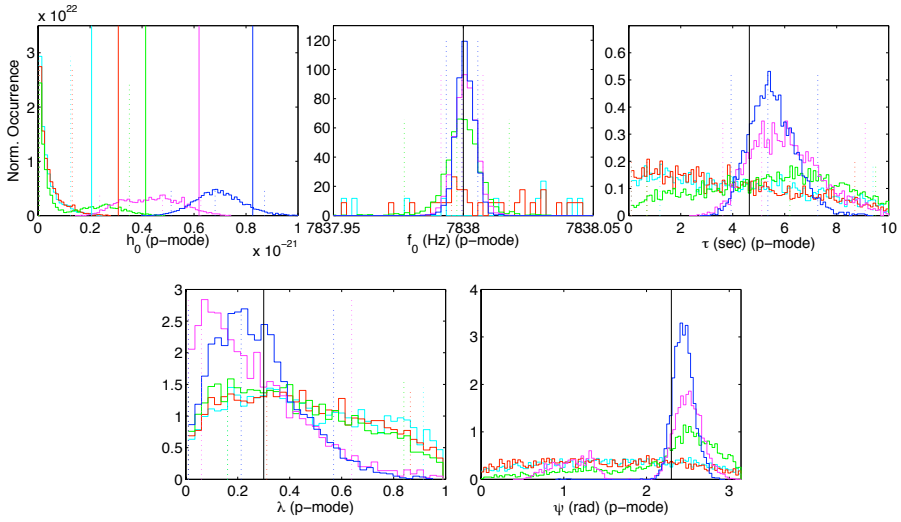

Figure 5.15: Posterior probability distributions and parameter estimation of the 5 parameters for the p-mode of the model for hypothesis $H_{2\mathrm{U}}$. The exact values of the parameters for the signal injected are marked with a vertical continuous line and tabulated in Table 5.1. The modes and 95% credibility intervals for each parameter are listed in the Appendix K, Table K.5.

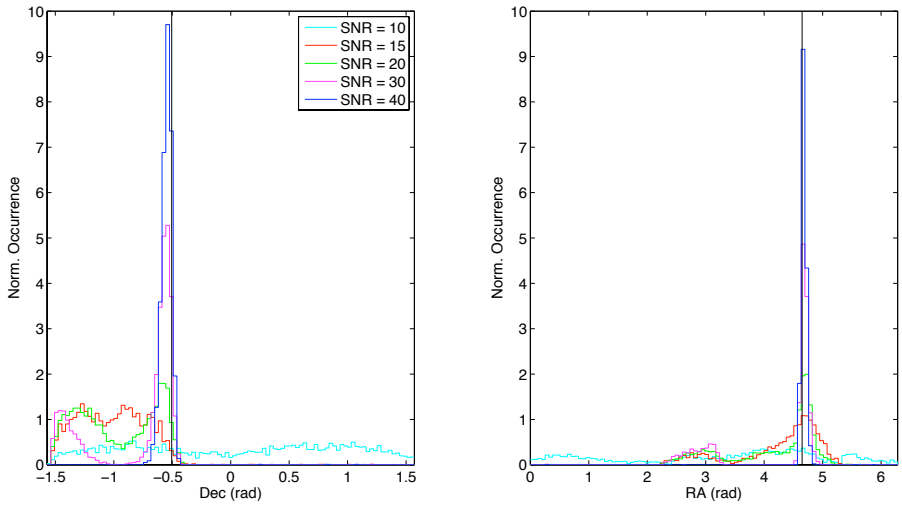

Figure 5.16: Estimation of the 5 parameters of the f-mode hypothesis. The exact value injected for each parameter is marked with a vertical continuous line.

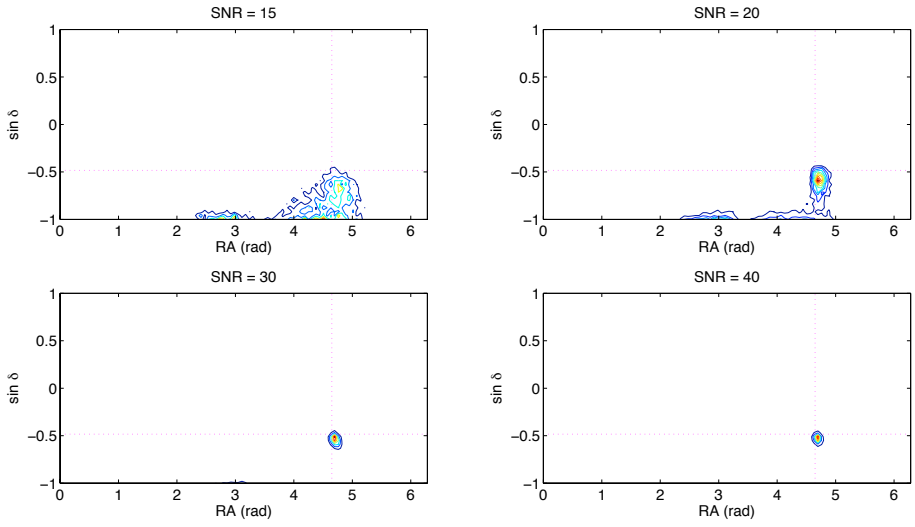

Figure 5.17: Estimation of the 5 parameters of the p-mode hypothesis. The exact value injected for each parameter is marked with a vertical continuous line.

for the strongest signal but it is otherwise similar to the uncertainty assigned for the prior $\pi(\psi) = \mathcal{N}(\mu_\psi, \sigma_\psi)$.

Pinpointing the location of the source is possible but its position is clearly constrained only for relatively high SNR values. Something interesting and positive is that the two-fold degeneracy of the source location and related to the 'flight-time' is easily broken: once other unknown parameters (apart from the two source location parameters) are included in the computation, the probability of source location is constrained to only one patch in the sky. The combination of sine and cosine components modulated by the antenna patterns at the arrival of the signal to different detectors, make possible to infer the position of the source uniquely. Some accuracy may be lost for using a rounded number of samples instead of dealing with the time shift value itself with the required decimals.

5.8.2 Scenario 2

Generally speaking, a stronger signal is necessary to constrain the values of the hypotheses in scenario 2 than in scenario 1, particularly to constrain the parameters that define the p-mode oscillation. The values of damping time τ_p and polarisation angle ψ_p only start showing some preferential values for high SNR values. Fortunately, for the hypotheses of scenario 2, as for scenario 1, the value of the oscillation frequency is estimated with great accuracy. The discrepancy between the mode and the exact value is always smaller than 0.02% for the two hypotheses considered in scenario 2. Pinpointing the source requires a stronger signal in scenario 2 than in scenario 1. Here, again, the degeneracy of the source location is easily broken. This shows that the uncertainty of location is higher for scenario 2 than for scenario 1. Again, this is for the extra uncertainty that a second oscillation mode includes, even having a lower amplitude – five times lower than the main oscillation mode.

Chapter 6

Shot-noise experiment

This chapter presents the experimental work carried out by myself with the help of colleagues at the Department of Physics and Astronomy in the University of Glasgow. It consisted in building a small Mach-Zehnder interferometer in order to measure the shot-noise level for modulated laser-light at the port of destructive interference. It is known that the shot-noise level varies depending the modulation type and demodulation scheme, and the aim of the experiment was to quantify it.

This chapter contains a detailed description of the interferometer built, the control system to keep it stable and the electro-optical set up used to achieve laser-light modulated in various ways. The results of the measurements carried out are presented at the end of this chapter; these are, unfortunately, not significant due to the difficulties confronted at the exercise of reducing the electrical noise to a level lower than that of the shot-noise at the time of taking measurements. Here I have tried to describe faithfully the work carried out and the difficulties faced, for the benefit of anyone interested on repeating and extending this experiment successfully.

6.1 The context and relevance of the experiment

A direct consequence of propagating gravitational waves is the quadrapolar deformation: the space is elongated in a direction while it is compressed in the orthogonal direction. Laser light interferometers with freely suspended mirrors are ideally suited device for the detection of these orthogonal minute distortions of space induced by gravitational waves. The current main gravitational wave detectors are sophisticated and very sensitive interferometers; they are the most sensitive position measurement devices ever operated and currently capable of measuring distance changes of the order of 10^{-18} m rms (about one-thousandth of the diameter of a proton) over separations of few kilometres (124).

The distortion of space is function of the amplitude of the gravitational wave, its polarisation and the orientation of the detector with respect to the source. However, in relation to the sensitivity of the detector itself, an interferometric measurement translates the question *how small a gravitational wave amplitude can be detected?* into *how small a change in optical power can be measured?* At the time of writing this document the design and research of second generation detectors (advanced detectors) is well advanced. They will start operation in 2014 and are expected to improve the current sensitivity tenfold.

The disturbances seen by the interferometer are the combination of the action of the gravitational waves in the space and extraneous displacements of the test masses provoked by external agents: seismic vibration, thermal excitation, gravity gradients, etc. There is also an intrinsic noise source, in the measuring process of space distortions, caused by the use of laser light. This arises from the quantum nature of the light-particles (i.e. photons), and the resulting randomness associated with their detection and with the corresponding random momenta they transfer to the test masses. Since the output light power is used to monitor the test mass positions, the statistical fluctuations of the light may be interpreted as equivalent position fluctuations.

The sensitivity of gravitational wave detectors is often quoted by the 'Amplitude Spectral Density' (ASD) of the noise – the minute relative displacements between test masses when the interferometer is in the linear regime, or locked (see

Section 6.4.4 for a more detailed explanation of the locked state). The sensitivity of the laser interferometric detectors is limited by different factors depending the frequency considered: seismic vibrations at low frequencies (< 10 Hz), thermal random displacements of test masses, mirror coatings, suspensions, etc. at mid-frequencies (< 200 Hz) and the shot-noise at the higher frequencies. A detailed derivation of the spectral density of the strain $h(f)$ due to the shot-noise from the photon arrival uncertainty is given in (29).

The theoretical understanding and calculation of the shot-noise level in the case of a perfectly coherent and monochromatic light is sound. However, this is not the case for modulated laser light induced in the gravitational wave detectors for which a main frequency and other subsidiary frequencies may exist. Thus the interest of measuring the shot noise level for different modulation/demodulation schemes and comparison with theory. The ultimate aim of this experiment was to shed some light upon modulated light shot noise levels.

6.1.1 Standard quantum limit: shot-noise and radiation pressure noise

The quantum nature of light reveals itself in two effects that limit the precision of any optical measurement: a) the photon shot noise, dominant at frequencies above 100 Hz, is linked to the uncertainty in the counting of the number of photons at the interferometer ports, and b) quantum radiation pressure noise, dominant at frequencies below 100 Hz, which arises from the mirror displacements induced by quantum radiation pressure fluctuations (124). The former is understood to be caused by quantum fluctuations of the vacuum electromagnetic field that enters the antisymmetric port of the interferometer (125). The joint limitation from shot noise and radiation pressure effects is called *Standard Quantum Limit* (SQL).

The use of *squeezed light*, in which much research is being done currently, is a promising technique to beat the SQL. The term makes reference to the squeezing of the circular uncertainty region of the two conjugate variables of light *amplitude* and *phase*. It is possible to reduce the uncertainty of one of the conjugate variables at the expense of the other. In our case, amplitude-squeezed light can have decreased phase fluctuations at the expense of increased amplitude fluctuations.

The quantum limit in the laser-interferometric gravitational wave detector can be overcome by the injection of squeezed states of light into the antisymmetric port of the interferometer (124). To understand how the squeeze light is implemented on an interferometer and the achievable sensitivity improvements see (51).

6.1.2 Photon shot-noise

The term shot-noise refers to the random generation and flow of mobile charge carriers. For a photodetector that converts photon-energy into electron-energy, the generation, subject to quantum randomness of mobile charges, introduces a degree of uncertainty on any light-power measurement. The quantum nature of the light is the underlaying reason for the non-uniform arrival of the photons to the photodetector. An uncertainty on the measurement is always present no matter how stable the power of the light to measure, as a combination of the random arrival of the photons and generation of charges by the photodetector.

Statistically, the expected shot-noise level of a light of arbitrary power can be calculated. For a detailed derivation from first principles see (126). The power spectral density function of the current arising from random generation and flow of charges is:

$$S(\nu) = 2\,e\,\bar{I} \tag{6.1}$$

where $\bar{I}$ is the average current measured and $e = 1.602 \times 10^{-19}\,\mathrm{C}$ is the charge of the electron. It is convenient to represent this power by an *equivalent noise generator* at frequency ν, with a mean-square current amplitude of $\bar{i_N^2} \equiv S(\nu)\Delta\nu = 2e\bar{I}\Delta\nu$.

6.2 Experiment

In the following, a general description of the experiment carried out is given: the components of the interferometer, the variable modulator to generate different types of modulation, the opto-electronic system to keep the interferometer stable and the electronics to take measurements of the shot-noise level. The interferometer was built inside a clean room, although not in vacuum. The components

were mounted on seismically isolated table and the laser used was amplitude estabilised.

6.2.1 General description of the experiment

It was decided that a Mach-Zehnder (see 6.2.2) was the most suitable interferometer for the execution of the experiment although slightly more complicated than the well-known Michelson-type interferometer, it provided a bigger flexibility with respect to permitting the conditioning of the light independently in the two arms, so that the phase modulation can be applied selectively to only one of the light beams. One of the arms of the interferometer contained the module to flexibly modulate the light in various forms (see 6.4.3), while the other arm was used to condition the light, in intensity and polarisation, and thus improve the interference conditions between the modulated and non-modulated beams.

The interferometer was locked, or maintained stable, by means of a piezoelectric transducer (PZT) acting on one of the corner mirrors of the interferometer (see 6.4.4). A servosystem, comprised of a locking photodiode (6.4.4.1) and the PZT actuator, worked together to compensate for changes in the relative arm lengths of the interferometer and to keep one of the ports of the interferometer in a dark fringe (destructive interference of the two beams) and the other in a bright fringe (constructive interference). The measurements of the shot-noise level were taken on the dark fringe with a sensitive photodetector similar to the one used in the GEO600 detector (see 6.4.5.1).

6.2.2 Mach-Zehnder interferometer (MZI)

The Mach-Zehnder interferometer is a rectangular-shaped optical set-up (see Fig. 6.1) that splits the incident light beam into two components by means of a beam-splitter (BS). After following two different L-shaped optical paths the beams are recombined on a second beam splitter. The phase difference accumulated by the two beams along their respective optical paths is a function of the arm's length and the number of internal/external reflections and transmissions that each beam is subjected to. The resulting phase difference between the two beams establishes the degree of constructive/destructive interference seen at

each port (see (127) for an enlightening discussion of the phase differences accumulated for general description of a Mach-Zehnder interferometer and the phase differences accumulated by each beam).

$$
\begin{aligned}
E_{in} &= E_0 e^{iw_0 t} \\
E_1 = \rho E_{in} &= \rho E_0 e^{i(w_o t - k l_1)} \\
E_2 = i\tau E_{in} &= i\tau E_0 e^{i(w_o t - k l_2)} \\
E_3 = r E_1 e^{-k l_3} &= r\rho E_0 e^{i[w_0 t - k(L_1 + l_3)]} \\
E_4 = r E_2 e^{-k l_4} &= ir\tau E_0 e^{i[w_0 t - k(L_2 + l_4)]}
\end{aligned}
$$

$$
\begin{aligned}
E_{P1} &= i\tau E_3 + \rho E_4 = ir\rho\tau E_o \left[e^{i[w_0 t - k(L_1 + L_3)]} + e^{i(w_0 t - k(L_2 + L_4))} \right] \\
E_{P2} &= i\tau E_4 + \rho E_3 = -r\tau^2 E_o e^{i[w_0 t - k(L_1 + L_3)]} + \rho^2 r E_o e^{i[w_0 t - k(L_2 + L_4)]}
\end{aligned}
$$

where $k = 2\pi/\lambda$ is the wave number and $L_i = f(l_i)$ are the physical distances between optical components. The amplitude reflection and transmission coefficients of the mirrors and beam splitters are (r, t) and (ρ, τ), respectively. Here two perfectly reflecting corner mirrors ($r = 1$ and $t = 0$) are considered and two ideal 50/50 beam splitters ($\rho = 1/\sqrt{2}$ and $\tau = i/\sqrt{2}$). We can simplify replacing $\phi_1 = k(L_1 + L_3)$ and $\phi_2 = k(L_2 + L_4)$ for the phases accumulated, and compute the electric fields and optical power of the beams at the output of the interferometer:

$$
\begin{aligned}
E_{P1} &= ir\rho^2 E_o \left[e^{i(w_0 t - \phi_1)} + e^{i(w_0 t - \phi_2)} \right] \\
E_{P2} &= r\rho^2 E_o \left[e^{i(w_0 t - \phi_2)} - e^{i(w_0 t - \phi_1)} \right]
\end{aligned}
$$

$$
\begin{aligned}
P_{P1} = E_{P1} E_{P1}^* &= 2\rho^4 r^2 E_0^2 (1 + \cos\Delta\phi) = \frac{E_0^2}{2}(1 + \cos\Delta\phi) \\
P_{P2} = E_{P2} E_{P2}^* &= 2\rho^4 r^2 E_0^2 (1 - \cos\Delta\phi) = \frac{E_0^2}{2}(1 - \cos\Delta\phi) \\
P_T &= P_{P1} + P_{P2} = E_0^2
\end{aligned}
$$

where the phase difference at the point where beams superpose is $\Delta\phi = \phi_2 - \phi_1$.

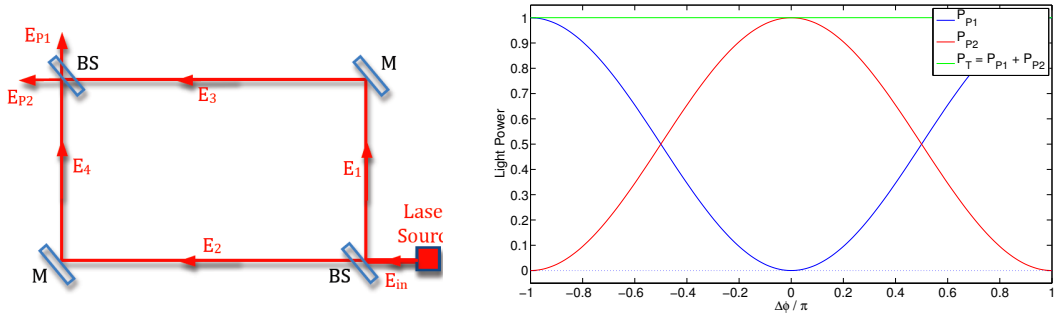

Figure 6.1: *Left:* Schematic diagram of the Mach-Zehnder interferometer. *Right:* Light power curves for each of the output ports as function of the phase difference between the combined beams, for input incident field $E_0 = 1$.

6.3 Modulation of Laser Light

In a similar fashion to low-frequency electromagnetic signals (e.g. broadcast radio signals) the light at high-frequencies can also be modulated. The result of modulating a monochromatic light (e.g. laser light) is a multi-frequency light where some of the energy is transferred from the carrier light into sidebands offset from the carrier by the modulation frequency.

6.3.1 Gravitational waves and modulation of laser light

Gravitational wave detectors are sophisticated interferometers that use modulated light to measure the contraction of space-time created by the gravitational waves and to keep the interferometer stable or locked (29). The expected frequency of the gravitational waves falls within the audio bandwidth and is hampered by high laser power and frequency noise level existing in this frequency range.

The modulation of the light is at a few tens of MHz, significantly higher than the sensitivity band for gravitational waves, which has its upper bound at approximately 10 MHz where the period of the gravitational wave drops below the storage time for photons in the interferometer. Modulation of the light allows the detection frequency for a signal to be above the range where laser amplitude

and frequency noise cause the problems, but low enough for photodetectors to measure both the amplitude and the phase of the modulated light exiting the interferometer relative to the modulation signal applied at the input.

A technique called *Heterodyne detection* allows for the electrical signal generated on the photodetector, and which encodes information of the signal to be lowered down in frequency. This process is called *demodulation* and is physically carried out by multiplying the photodetector signal with a reference frequency or *local oscillator*. The resulting signal shows components, and the original signal information can be recovered by low pass filtering.

6.3.2 Electro-optic modulation of laser beams

A beam of laser light can be modulated when forced to propagate through a medium where its polarization is altered in an oscillating manner; for example, a birefringent crystal in which an external and alternating electrical field is applied.

A birefringent crystal is one in which the speed of propagation of light depends on the direction of propagating of the light beam through the crystal and the polarization state of the light beam. A linearly polarized light beam entering the crystal in a certain direction can be decomposed into components parallel to and perpendicular to the optical axis of the crystal; these two components will travel at different speeds through the crystal, so by controlling the thickness of the crystal, an arbitrary rotation of the polarization vector can be achieved. In the case of waveplates, crystals are deliberately cut to a precise thickness in order to alter the polarization state of the laser light through the accumulation of the desired amount of retardation for a particular wavelength.

Electro-optic modulators are composed of birefringent crystals sandwiched between two electrodes, where the degree of birefringence depends on the electric field across the crystals. By changing the electric field (applying a voltage to the electrodes) one can alter the retardation of the beam along one crystal axis relative to the other. An alternating voltage will cause the light to be modulated at the output of the crystal.

6.4 Types of light modulation

Let us now consider different types of light modulation mathematically. For a graphical and mathematical representation of the modulation types and their corresponding carrier and sideband frequency and phase relations see Jun Mizuno's PhD thesis (128) and Gerhard Heinzel's PhD thesis (129).

The scalar representation of the electric field of unmodulated light at a fixed location in space is:

$$E(t) = E_0\, e^{i\, w_0 t}, \tag{6.2}$$

where $w_0 = 2\pi f_0$ is the angular frequency of the carrier light.

6.4.1 Amplitude Modulation

The intensity of the light and the power of the beam are characterised by the amplitude of its electric field. If the amplitude is modulated (i.e. changed periodically) amplitude-modulated light is obtained. The modulation can be expressed mathematically as follows:

$$\begin{aligned} E_{AM}(t) &= E_0\,(1 + m\cos w_m t)\exp(i w_0 t) \\ &= E_0\,\left[\exp(i w_0 t) + \frac{m}{2}\exp[i(w_0 + w_m)t] + \frac{m}{2}\exp[i(w_0 - w_m)t]\right], \end{aligned} \tag{6.3}$$

where m is the degree of modulation . Eq. 6.3 shows that the amplitude-modulated laser-light can be described by a pair of sidebands offset by the modulation-frequency w_m from the central frequency component or carrier w_0. The power carried by a modulated light beam –what would be measured on a photodetector with a conversion efficiency of 100%– can be inferred by calculating the square of the magnitude of the electric field by multiplying with its complex conjugate. Colloquially, this exercise is known as the "beating" between components. The photoconversion of amplitude-modulated light results in three components at DC and frequencies w_m and $2w_m$.

$$\begin{aligned} P_{AM}(t) &= E_{AM}(t)\, E^*_{AM}(t) \\ &= E_0^2\,\left[1 + \frac{m^2}{2} + 2m\cos(w_m t) + \frac{m^2}{2}\cos(2w_m t)\right]. \end{aligned} \tag{6.4}$$

There is no photodetector dynamically fast enough as to convert a laser light (frequency $w_0 = 1.77e15$ Hz) to an alternating electric signal. But modulation frequencies (mostly radio frequencies) are much lower than the frequency of the light and thus their photoconverted alternating electrical signals can be readily analysed on an oscilloscope. An alternative and equivalent expression to Eq. 6.3 can be derived by modulating the original optical signal of Eq. 6.2 with $\sin(w_m t)$ instead of $\cos(w_m t)$ [1]. The resulting average power carried by the modulated light beam is the same for both.

6.4.1.1 Physical implementation of Amplitude Modulation

If the polarisation of the incident light is not linear and parallel to one of the principal axes of the crystal, the two components travelling will be phase-shifted relative to each other. As a consequence, the polarisation state at the output will be different to before entering the crystal and the intensity allowed through may be controlled by means of a polarising beam-splitter. The change in polarisation state can be controlled by the external electric field applied onto the crystal.

To get a big enough polarisation state change the application of high voltages is often necessary. It is however possible to get the same net effect with a lower voltage, by biasing the system locating a quarter-wave plate just after the crystal. A detailed description of the amplitude modulation optical set up and its corresponding mathematical description can be found in (126).

6.4.2 Phase modulation

In a similar fashion to altering the amplitude sinusoidally, variation of the phase of the laser-light may be desired to produce phase-modulated light instead. Math-

[1]

$$\begin{aligned} E_{AM}(t) &= E_0\,(1+\sin w_m t)\exp(iw_0 t) \\ &= E_0\,\left[\exp(iw_0 t) - i\frac{m}{2}\exp[i(w_0+w_m)t] + i\frac{m}{2}\exp[i(w_0-w_m)t]\right] \end{aligned} \tag{6.5}$$

$$P_{AM}(t) = E_{AM}(t)\,E^*_{AM}(t) = E_0^2\left[1+\frac{m^2}{2}+2m\sin(w_m t)+\frac{m^2}{2}\cos(2w_m t)\right] \tag{6.6}$$

ematically, this can be represented as follows:

$$E_{PM}(t) = E_0 \exp[i(w_0 t + m \cos w_m t)], \tag{6.7}$$

where, again, m is the modulation index. We can transform Eq. 6.7 to an expression similar to Eq. 6.3 by developing the second exponential term, for this term can be expressed as an infinite series of Bessel functions of the first kind [1](see (130)). If the modulation index is small enough ($m \ll 1$) we can approximate the infinite series of terms by taking only the first two terms.

$$\begin{aligned} E_{PM}(t) &\approx E_0 \exp(i\, w_0 t)\, [J_0(m) + 2i\, J_1(m) \cos(w_m t)] \\ &\approx E_0 \exp(i\, w_0 t)[1 + i\, m \cos(w_m t)] \\ &\approx E_0 \left[\exp(i w_0 t) + i\frac{m}{2} \exp[i(w_0 + w_m)t] + i\frac{m}{2} \exp[i(w_0 - w_m)t]\right] \end{aligned} \tag{6.8}$$

where the approximations for small m have been used: $J_0(m) \approx 1$ and $J_1(m) \approx m/2$. Only the phase is modulated and there is no change in the overall light power at any frequency.

Again, an alternative equivalent expression to Eq. 6.8 can be derived by modulating the original optical signal of Eq. 6.2 with $\sin(w_m t)$ instead of $\cos(w_m t)$ [2]. The resulting power of the modulated light beam is the same for both.

6.4.2.1 Physical implementation of phase modulation

If the incident laser-light beam is polarised parallel to one the birefringent axes of the electro-optic crystal, phase modulation results. The application of an

[1]
$$\exp(im\cos\alpha) = \sum_{k=-\infty}^{\infty} i^k J_k(m) \exp(ik\alpha) = J_0(m) + 2\sum_{k=1}^{\infty} K_k(m)\cos(k\alpha)$$

[2]
$$\begin{aligned} E_{PM}(t) &= E_0 \exp[i(w_0 t + m \sin w_m t)] \\ &\approx E_0 \exp(i\, w_0 t)[J_0(m) + 2i\, J_1(m) \sin(w_m t)] \\ &\approx E_0 \exp(i\, w_0 t)[1 + i\, m \sin(w_m t)] \\ &\approx E_0 \left[\exp(i w_0 t) + \frac{m}{2} \exp[i(w_0 + w_m)t] - \frac{m}{2} \exp[i(w_0 - w_m)t]\right] \end{aligned} \tag{6.9}$$

sinusoidal electric field does not change the state of polarisation; it changes the refractive index of the crystal, the phase-velocity and thus the light phase at the output. The value of the phase modulation index m is a function of various parameters but depends predominantly on the value of the electric field applied. For more details, see (126).

6.4.3 Laser light electro-optical modulation

The variable modulator permitted achieving various types of modulation and the easy switch between different modulation schemes without needing to modify or relocate optical components.

The flexible modulating device was designed and had been tested by colleagues at the department previously. The core of the modulator is an electro-optic crystal modulator (EOM) sandwiched between ancillary wave plates; in turn, all this is confined between crossed polarizer beam splitters (PBS) (see Fig. 6.2). The incident beam is linearly polarized at 45° to the principal axes of the crystal and modulated when propagating along the crystal. The resulting modulated light contains the carrier and sidebands, which are successively rid of the undesired polarization components by using wave plates to filter them out. By rotating the quarter- and half-wave plates (QWP and HWP, respectively) located after the crystal, it is possible to obtain amplitude-modulation, phase-modulation, single sideband-modulation and unbalanced modulation (i.e. two sidebands of different size) at the output of the variable modulator. By rotating the quarter (QWP) we get a circularly polarised carrier and one horizontal and one vertical sidebands just after it. Then, by rotating the HWP this polarisation status is rotated as a whole to four different states, all with circular polarisation for the carrier and linear polarisation for the sidebands. The output last beam splitter extinguishes one of the sidebands or let partially the two depending for which of the four states the HWP has been positioned for. For clarity the optical set up from (131) have been duplicated in Fig. 6.2. The interested reader is encouraged to look up the original paper.

The described modulation system was included in the longer side of the lower arm, while the upper arm contained a polariser beam splitter (PBS) sandwiched

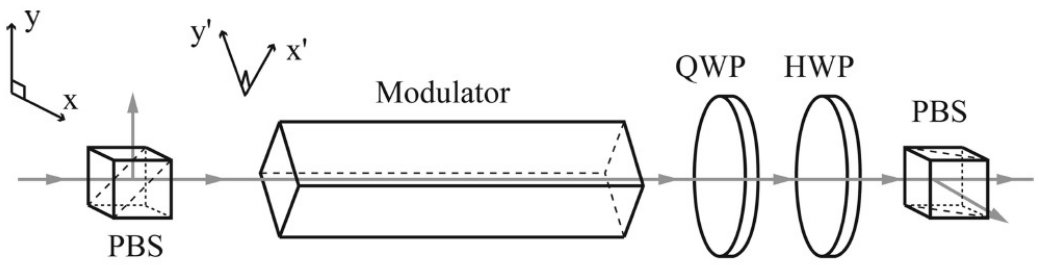

Figure 6.2: Set-up of the optical components of the flexible variable modulator used in the experiment. It was inserted on one of the arms of the Mach-Zehnder interferometer and allowed selecting from various modulation types and easy switching among them.

by two half-wave plates; this allowed the conditioning of the light power and polarisation to improve the interference of the beams. Optical componentry inserted in both arms can be seen in Fig. 6.2.

6.4.3.1 Electro-Optic crystal

The first electro-optic crystal tried proved not to be adequate for the experiment: the power of the sidebands obtained was only about $1/160^{th}$ of the power of the carrier and insufficient to proceed with the measurements. From theoretical calculations we established that the *half-wave voltage* V_π of this crystal was $\approx$ 4500V and that our resonant circuit could not get the high voltages required to get strong sidebands. Also, we observed that the modulation of the light was considerably affected by small fluctuations of the environment temperature, even inside the temperature-controlled laboratory. The lack of stable modulation, due to the temperature-dependent polarization changing continuously, was the main reason to replace the electro-optical crystal by a new one.

The new device comprised of two rectangular-shaped lithium niobate ($LiNO_3$) crystals, mounted in series within a U-shaped metallic support, and their principal axes were rotated 90° to compensate the temperature expansion. The electrical connections to the second crystal were cut off and the second-stage modulation was avoided while keeping the benefit of the temperature expansion/contraction compensation. Unfortunately, the EOM did not behave like a zeroth-order wave-plate and to compensate for this an auxiliary circuit which allowed adding a bias

voltage was fitted as a result later on. Two high-voltage generators were allowed applying a bias voltage range of $\pm 600\,\mathrm{V}$.

6.4.3.2 Resonant circuit for the electro optical modulator crystal

The electrical field across the electro-optic crystal is proportional to the voltage applied onto the crystal. To obtain the desired light modulation degree, a minimum modulation index, the electrical field necessary is often quite high and the voltage required can be up to several hundred volts. One practical way of obtaining the required high-voltage is to amplify a low voltage signal by means of a resonant circuit matched to the impedance which the source was designed to drive ($50\,\Omega$). The resonance circuit is in essence an autotransformer with a inductance that balances the capacitance of the crystal and minimises the overall impedance of the circuit. An schematic view is shown in see Fig. 6.3.

The resonant circuit and the crystal were mounted on a board. The manufacturing of the coil and the selection of the tapping point was a trial and error process until the measured RF power reflected by the resonant circuit was minimum. Our coil consisted of a big air-core copper solenoid of aspect ratio 1:1 with $\varnothing \approx L \approx 6$ cm and $N \approx 17$ turns. In combination with the EOM crystal and all the auxiliary resistors and capacitors the resonant circuit board, tested with the Spectrum Analyzer, presented a resonance frequency at approximately 15.44 MHz , see Fig. 6.3. The circuit was first tried outside the clean room on a provisional optic bench, where the tuning of the coil (moving tapping point of the autotransformer) was easier. For the new EOM crystal stronger sidebands were obtained with a power ratio to the carrier of 1/9. The power on the sidebands was measured by using an optical spectrum analyser (a confocal Fabry-Pérot cavity with a piezoelectric actuator on one mirror to scan the cavity length), where the sidebands were observed clearly and recorded with an oscilloscope, see Fig. 6.4.

Phase and amplitude modulated light show a very similar spectrum when scanned by the Fabry-Pérot cavity (carrier plus two sidebands) and if the second order sidebands are not visible they cannot be easily discerned. They can, however, easily distinguished with the help of a photodetector by comparing the frequency components of the electrical signal, for as it was shown by Eq. 6.4 the

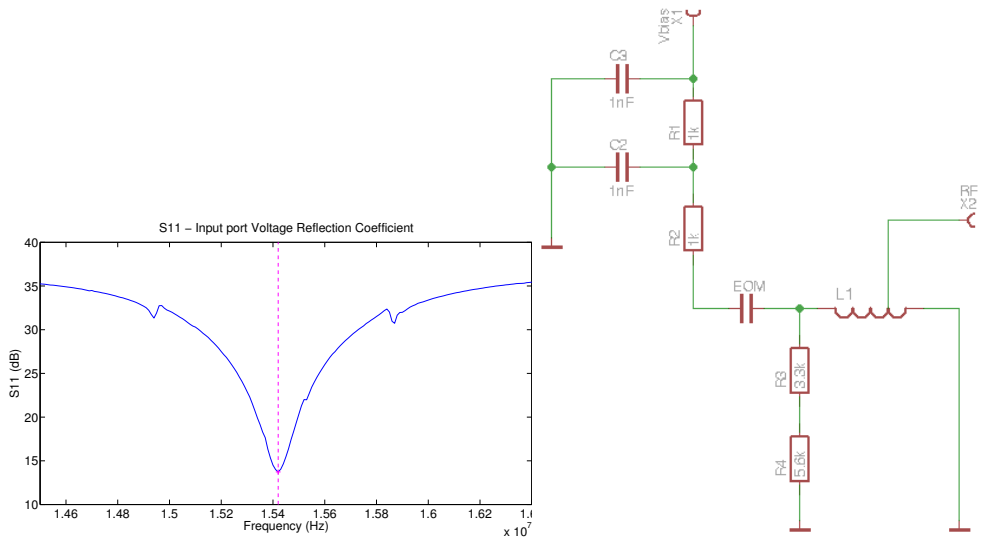

Figure 6.3: *Left*: Trace of the S11 (input port voltage reflection coefficient) for the board containing the resonant circuitry: EOM crystal, resonance coil and all the auxiliary resistors and capacitors. The resonance frequency measured in the spectrum analyser was $f_{res} \approx 15.44$ MHz with a scale factor $Q \approx 170$. The two small peak at both sides of the resonance frequency are the piezoelectric resonances of the crystal. *Right*: Schematic of the RF resonant circuit. The 2×1k resistors and 2×1nF capacitors were fitted to avoid interference between the Vbias (DC) and the modulation signal (RF). The other resistances to ground (split into two resistors in series to minimise their equivalent capacitance) add stability to the response of the circuitry.

purely phase-modulated light does not have a component at the modulation frequency. When the quarter wave-plate of the flexible modulator shown in Fig. 6.2 is oriented such as to get circular polarization of the carrier just after it, a rotation of the last half wave-plate by 22.5° switches alternately the output between phase and amplitude modulated light. Table 6.1 shows the orientation of the half-wave plate and the DC and RF measurements taken. When the RF value is extinguished light is being modulated in phase. The same modulation effect could be obtained by altering the voltage of the crystal. When just after the quarter wave plate the carrier is linearly polarised, it is possible to extinguish it (supressed carrier) and let only the sidebands through.

Switch between AM and PM by rotation of the HWP			
α_{HWP}	V_{DC} (V)	$V_{RF_{pk-pk}}$ (mV)	Modulation.
4°	3.65	550-590	AM
...	...	...	...
50°	3.96	550-590	AM
72°	3.88	~ 0	PM
95°	3.56	550-590	AM
117°	3.52	~ 0	PM
140°	3.8	550-590	AM
...	...	...	...
226°	3.64	550-590	AM
340°	3.76	~ 0	PM

Table 6.1: Angular values of the half-wave plate (HWV) to switch modulation between amplitude-modulation (AM) and phase-modulation (PM).

The source of the radio-frequency modulation signal was a signal generator. The signal was split in two and each branch amplified independently. The power of the RF signal applied to the crystal ($\approx$ 1 W) was carefully monitored by a power meter, which indicated both the power consumed and reflected by the resonant circuit of the electro-optic crystal. Moving the tapping-point on the coil the impedance was matched to the source impedance to ensure the power forward was approximately 1 W and the Standing Wave Ratio (SWR) was negligible, an

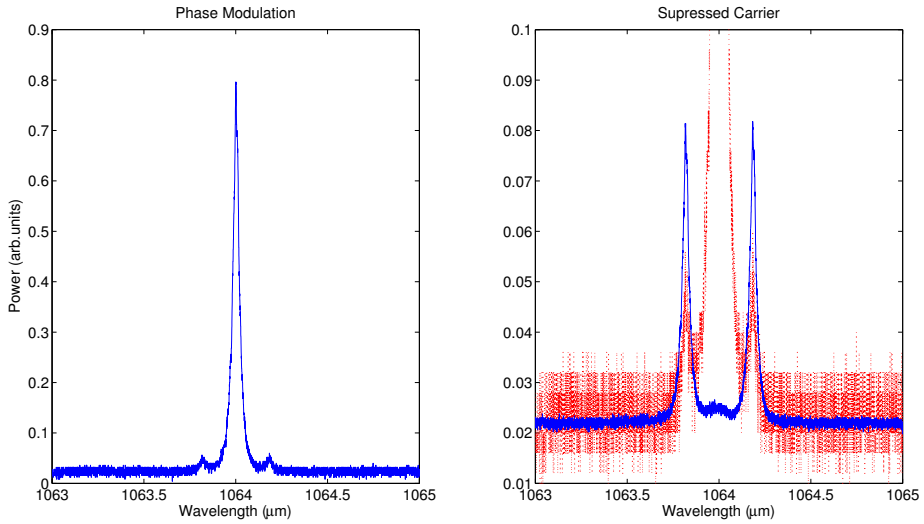

Figure 6.4: Oscilloscope traces showing spectrum of the light captured by the scanning Fabry-Perot cavity. *Left*: Carrier and sidebands for phase modulated light. The carrier and the sidebands are visible with a power ratio of ≈ 14 here and the second order sidebands are not visible. *Right*: Spectrum of the light with suppressed carrier: the carrier disappears and sideband power increases twofold. The supression of the carrier could be achieved by changing the bias voltage ($V_{bias} = 357V$). The same trace as on the left is shown in the background for comparison. For a particular position of HWP it is possible to cancel both sidebands.

indication of very little power being reflected back from the coil attached to the electro-optic coil.

The source of the modulation signal was a signal generator providing 10 dBm (10 mW) at a frequency of 14.57 MHz. This was split into two branches of 5 dBm and subsequently amplified independently; one branch was amplified 12 dB in order to get an adequate local oscillator signal level (17 dBm) for demodulation; the other branch was amplified to a level considered of strong enough sidebands ($\approx$ 30 dBm $\approx$ 1 W). The fact of having the same signal source for both ensured a synchrony between modulation and demodulation. The power of the RF signal applied to the crystal ($\approx$ 1 W) was carefully monitored by a power meter, which indicated both the power absorbed and reflected by the resonant circuit. By selecting the adequate tapping-point on the coil the impedance was matched to the source impedance to ensure that the power forward was approximately 1 W and that the standing wave ratio (SWR) was negligible, an indication of minimum power being reflected back from the resonance circuit.

6.4.4 Locking: the interferometer as a null instrument

Vibrations transmitted to the optical bench, air currents across the laser beams and other unwanted disturbances make the aligned beams of the interferometer to dither causing oscillating interference: light intensity at each of the two output ports of the interferometer swing through multiple bright and dark fringes. It is not possible to take measurements at the dark fringe without stabilising (*locking*) the interferometer first, locking the interferometer in such a manner as to get permanent dark fringe in one of the ports; if one is at the dark fringe the other would must be at the bright fringe, as required by the principle of conservation of energy. A servomechanism is used to measure any departure from the working point and drive the actuator, attached to one of the corner mirrors, to bring the interferometer back to the selected working point.

A variant of the Pound-Drever-Hall (PDH) control system was used to keep the interferometer locked. The PDH control system was originally devised for laser frequency stabilisation by locking the laser light to the cavity. By measuring the modulated light that gets reflected out of the cavity and comparing this

with the original modulation signal it is possible to know on which side of the resonance the cavity is, depending whether the signals are in phase or 180° out of phase (132). The comparison results in a bipolar error signal that can be used to correct for any deviations from resonance. A detailed explanation of the PDH technique can be found in (133) and (134).

Variants of the PDH control technique are equally applicable to the case of interferometers needing to be kept locked. In our case, the demodulated signal of a dedicated photodetector (*locking photodetector*), which received some light picked off the bright port to get the bipolar error signal, and was used to drive a piezo-electric-transducer (PZT) attached to one of the corner mirrors of the interferometer (see Fig. 6.5). The closed loop of the servomechanism continuously driving the actuator made it possible to keep the interferometer locked and to take measurements in the dark port.

6.4.4.1 Locking photodetector

The locking photodetector was designed to work as a current source into a low impedance circuit, in the photoconductive mode and with a reverse bias voltage of 15 V. In contrast to the photovoltaic mode, the photoconductive mode allows for a faster response and easily measurable amplified output voltage.

A part of the light from the bright port was picked off by a crystal slab and reduced in intensity with a grey filter before being focused to the locking photodetector. The photodetector was designed to provide DC and RF voltages proportional to the light frequency components detected. The DC signal helped to ensure that the light beam was correctly focused within the photodiode detection area, whereas the RF signal served to discern amplitude and phase modulation (for the phase modulated light does not have a component at the modulation frequency) and to provide an error signal after demodulating and low-pass filtering.

Fig. 6.6 shows the schematic of the locking photodetector circuitry with the DC and RF voltage output terminals. The size of the RF signal is proportional to the power contained in the sidebands, which is generally quite small and it needs to be amplified by a resonant circuit to be measured. The resonant circuit

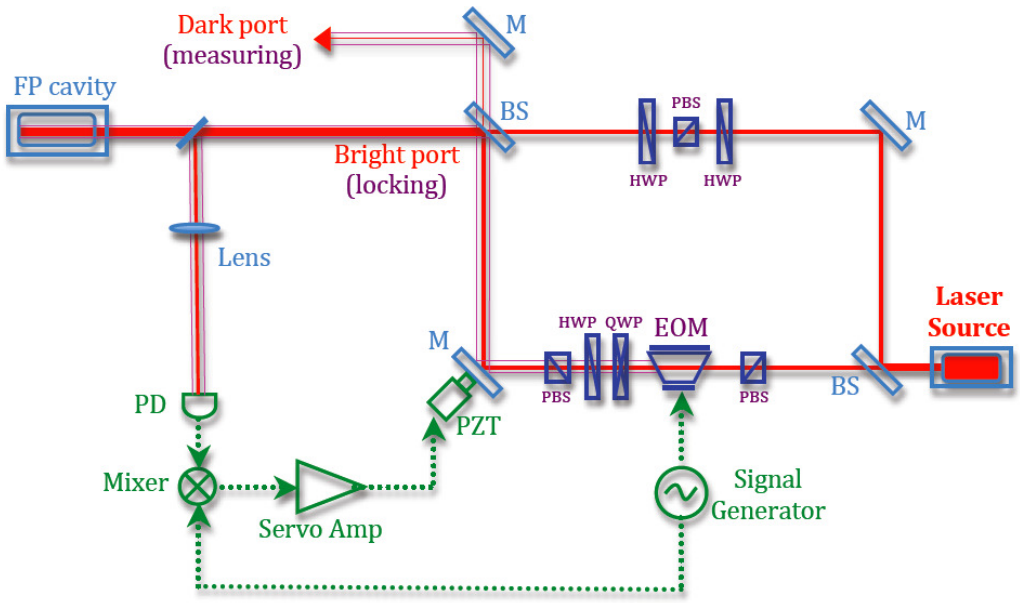

Figure 6.5: Locking set-up showing the electro-optic components of the servomechanism (green). A partially transmitting mirror along the bright port picks some light to the locking photodetector; its demodulated signal is the bipolar error signal that feeds the servomechanism driving the PZT attached to the corner mirror. The Fabry-Perot cavity located at the bright port allows visualization of the carrier and the sidebands in the oscilloscope.

comprises of a tunable inductor that resonates with the overall capacitance of the circuit plus that of the photodiode.

By adjusting the tunable inductor the circuitry was made to resonate at the desired modulation frequency. Checking the output voltage while adjusting the tunable inductor it was possible to resonate the circuit at our particular modulation frequency. The process consisted of measuring the amplified signal induced in the circuitry by a radiating air-coil connected to the signal generator and positioned close to the open box containing the photodiode circuitry. A mathematical description of the resonance condition for a similar photoconductive detector mode is analysed in (129).

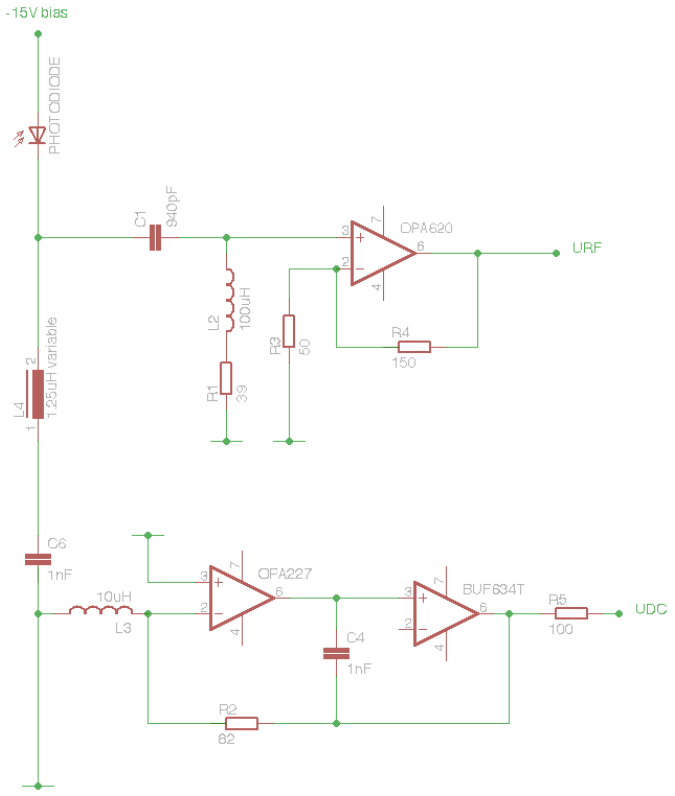

Figure 6.6: Schematic of the *Locking photodetector* circuit in the photoconductive mode with reverse bias. All this was fitted within a box with an aperture to receive the light. It includes two output terminals for DC and RF current measurements.

6.4.4.2 Heterodyne demodulation of the signal

The term demodulation refers to the act of recovering the information encoded in the modulated light. In the heterodyne technique the encoded modulated signal is multiplied with another of the same frequency as the modulation signal called local oscillator; i.e. the components on the modulated light are beat with the local oscillator. This action generates signals at frequencies of added and subtracted frequencies of the components mixed and proportional to their amplitudes, making it easier their recovery. Depending on the phase difference at which the signals are mixed, the demodulation phase, the result is different too.

In general, we can assume that a light beam (modulated or not) is altered by the interferometer (suppresed carrier, single sideband) and then detected in the photodetector. Let us assume we know the amplification/attenuation for each of the frequency components of the light in the interferometer, represented by the transfer function $T(w)$. Since, to first order, the electric field of the light is composed of three discrete frequencies we can use the corresponding particular complex values of the interferometer.

$$T_0 = T(w_0), \quad T_+ = T(w_0 + w_m), \quad T_- = T(w_0 - w_m) \tag{6.10}$$

The photocurrent generated is proportional to

$$I \propto E_o^2 + 2mE_0^2\Re[T_0(T_+^* - T_-^*)]\cos(w_m t) + \Im[T_0(T_+^* + T_-^*)]\sin(w_m t) \tag{6.11}$$

and this will be demodulated with a homodyne technique by mixing it with a local oscillator at the modulation frequency and phase α. After low-passing the signal the result is:

$$S = 2\Re[T_0(T_+^* - T_-^*)]\cos\alpha - 2\Im[T_0(T_+^* + T_-^*)]\sin\alpha. \tag{6.12}$$

The first term, proportional to $\cos\alpha$ is called the quadrature (Q) signal and the second component, proportional to $\sin\alpha$ is called the in-phase (I) signal. Fig. 6.7 depicts the DC signals obtained after demodulating the RF output of the photodiodes in both ports of the interferometers, obtained by the simulating software Finesse (135). The demodulated signal of the bright port was used as

an error signal for the locking control system, whereas the demodulated signal of the dark port was to take shot-noise level measurements. The error signal shows bipolar nature at the zero-crossing point, which permits the locking of the interferometer by means of a servomechanism acting on one of the corner mirrors. From the comparison of left and right plots we can observe the following points: a) light power splits into the two ports so that when one is in the bright fringe the other is in the dark; b) the signal presents the biggest slope at zero-crossing (this allows for more sensitive control) when the demodulation angle α is smallest; c) the slope is of opposite sign for the two ports.

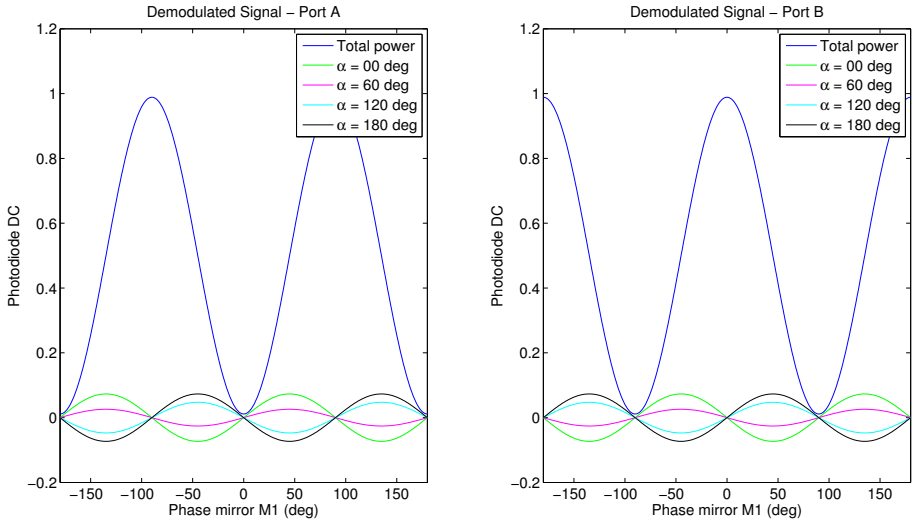

Figure 6.7: DC signals (simulated with Finesse) obtained in the photodiodes located in the dark (*left*) and bright (*right*) ports of the interferometer in function of the phase change obtained by moving one of the mirror corners, for example. The bigger signals correspond to the total light power detected, whereas the smaller sinusoids are the demodulated error signals, for various demodulation angles, used for locking the interferometer (bright port) and taking the shot-noise level measurements (dark port).

6.4.4.3 Locking servomechanism - PZT driving circuit

As mentioned in the introduction of this section a piezo electric actuator (PZT) attached to one of the corner mirrors of the MZI was used to keep the interferometer locked (ref. PZT: PI P-840.10, open-loop travel @ 0-100V of 15μm). The

corrective action of this actuator made possible to keep one of the ports in the dark fringe at which to measure the shot-noise level. The bipolar error signal out of the demodulated and low-pass filtered signal of the locking photodetectors was filtered and amplified by the servo-control to drive the actuator. The schematic of the electronic circuitry of the servomechanism are shown Fig. 6.8.

To infer the DC gain needed by the control system the optical and electrical gains were considered in combination. The stroke of the actuator necessary to swing the interferometer from dark to bright fringe was approximately half of the laser's wavelength (≈ 0.5 μm); this could be achieved by a change of 3.3 V on the signal to the actuator and measured out as a change of $\approx$ 1 V on the DC level of the locking photodetector. This relation yielded an optical gain of $K_{opt} = 0.3$ indicating that per 1V applied to the PZT there is a DC voltage change of 0.3V in the locking photodetector output. An electro-optic gain of about 2000 was chosen as necessary: an electric amplification of gain 6000 ($\approx$ 60 dB).

The servo-control circuitry shown in Fig. 6.8 was designed by Dr. Borja Sorazu and built enclosed in a metallic box. This was drilled on one side to permit the access of a small screwdriver to the tuning potentiometer controlling the gain and facilitate the locking. It is a proportional control system with a preliminary low-pass passive filter (first order and 10 kHz cutoff) and a successive first non-inverting amplification stage of gain $\times$6. The tuning potentiometer trims the signal out of the first stage before the second and main amplification stage (first order active low-pass filter with a gain of 20 dB) and the final passive filter (first order and 1.57 Hz cutoff). The overall design characteristics of the servomechanism control are a gain of 60 dB and cutoff frequency of 1.57 Hz, with roll-off of -20 dB/dec down to unity gain at 106 Hz.

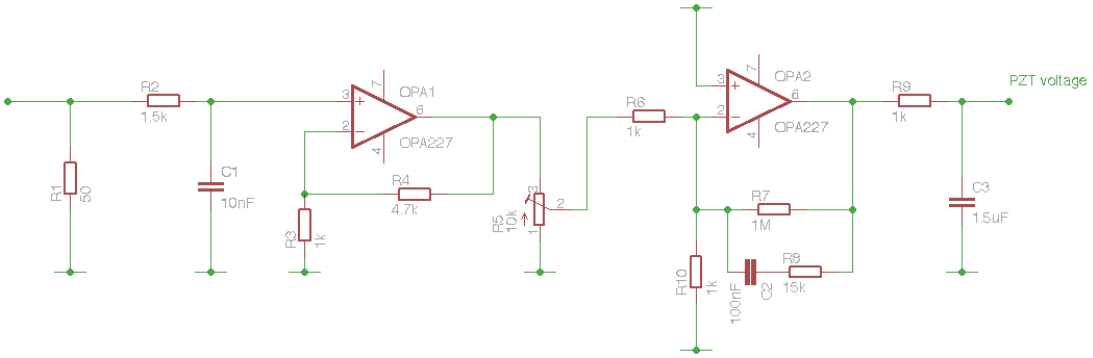

Figure 6.8: Schematic of the 50 Ω impedance matched servomechanism to lock the interferometer. It is comprised of various filtering stages and two amplification stages. The input to the servo-amplification is the error signal resulting from the demodulation of the signal given by the locking photodetector, and the output is the voltage to the PZT. The error signal is initially low-pass filtered and amplified moderately in the first amplification stage; a variable resistor (tuneable from the outside of the box with a screwdriver) allows for the adjusting of the second amplification stage and thus ensures the adequate amplification for driving the PZT to lock the interferometer.

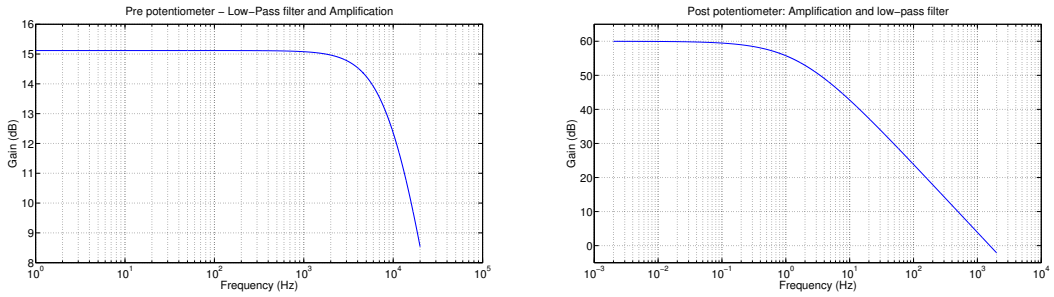

Figure 6.9: *Left*: Low-pass passive filter plus preliminary non-inverter amplification stage (gain ≈ 6) before the potentiometer. *Right*: Main amplification stage (gain ≈ 1000) and passive low-pass filter.

The frequency response, operation bandwidth, and stability of the servo control system were checked by interfering with the system and measuring its response. A sweeping sinusoidal signal was injected to the system (added to the error signal on a commercial pre-amplifier set with no gain and a cutoff frequency of 1 kHz) and the response of the system was measured at the same point as the injection on a spectrum analyser. Combining spectra acquired with locked and unlocked interferometer the open- and close-loop responses (see Fig. 6.10) that ultimately characterised our control system were obtained.

The phase margin analysis of the open-loop transfer function shows the fact that control loop is stable up to frequencies over 1kHz. This was considered to be good enough to provide long-term operation in our laboratory environment. The coincident valley in gain and phase around 330 Hz seems to be the "reaction resonance" of the support of the PZT to which the corner mirror was glued to and that absorbed energy out at a narrow frequency band around that frequency.

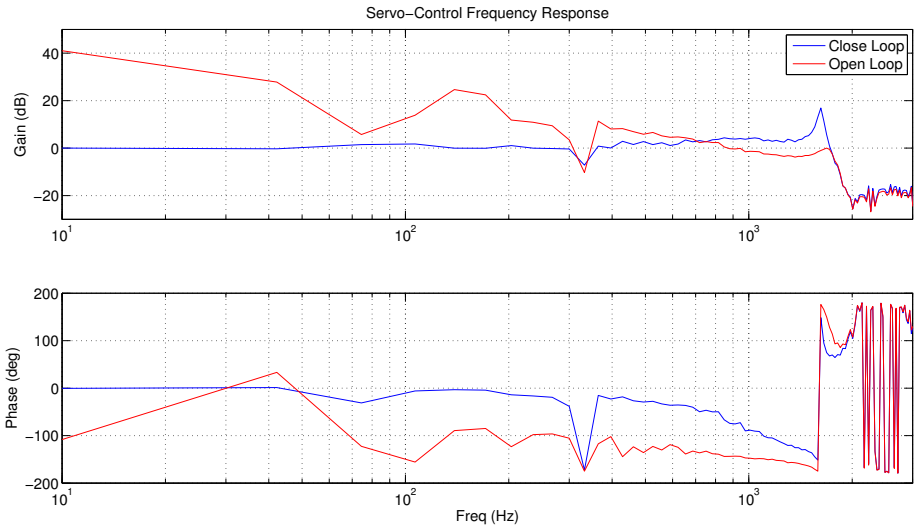

Figure 6.10: Frequency response of the servomechanism control system. Open- and close-loop systems have been overlaid on a Bode plot for comparison. Open-loop transfer function with unity gain at $\approx$ 880 Hz and phase margin of $\approx 32^\circ$ shows that the control system is stable for frequencies up to 1 kHz. Close-loop transfer function with bandwidth of $\approx$ 1.72 kHz and a resonance frequency at around 1.62 kHz.

6.4.5 Measuring the shot-noise level

Shot noise level measurements were carried out at the dark port of the interferometer by means of a sensitive photodetector (see section 6.4.5.1). The light at the dark port contained only the sidebands (the carrier was suppressed) and it was focused onto the sensitive photodiode. Similarly to the locking photodetector, the GEO600 like sensitive photodetector had a DC and a RF terminal; the former gave an indication of the light power falling onto it and the RF was the signal to demodulate and low-pass filter before taking the spectrum and measure the shot-noise level (see Fig. 6.11).

Although the locking of the interferometer was reliable for long periods of time a catastrophic failure of the photodetector happened once, after the sudden loss of lock, and after focusing more than 200 mW onto the photodiode; it got damaged as a result of the excessive heat generated that burnt the photodiode in a few seconds. A protection system for the safety of the photodetector was designed and implemented (see section 6.4.5.2) after the incident.

Once, however, an accidental loss of lock provoked the exposition of the photodiode to full light power;

6.4.5.1 GEO600 like photodetector

To emulate measurements of the GEO600 gravitational wave detector, a simplified replica of its photodetector was built and used for the measurements. Our photodetector differed from the original on the lack of resonance lines to measure higher harmonics of the modulation frequency. In a similar fashion to the locking photodetector it had a DC and RF output terminals and an input terminal to inject and emulate photocurrents generated by the photodiode; this allowed testing the circuitry and getting a transfer function of its response. The original schematic of the GEO600 photodiode and our simplified version can be compared side by side in Appendix L.

The response of the photodiode was tested with a spectrum analyser to verify that the resonance for the modulation frequency and the anti-resonances for its harmonics were at the desired frequencies. The original design had to be altered slightly for it included a tunable variable inductor that did not work for us; it did

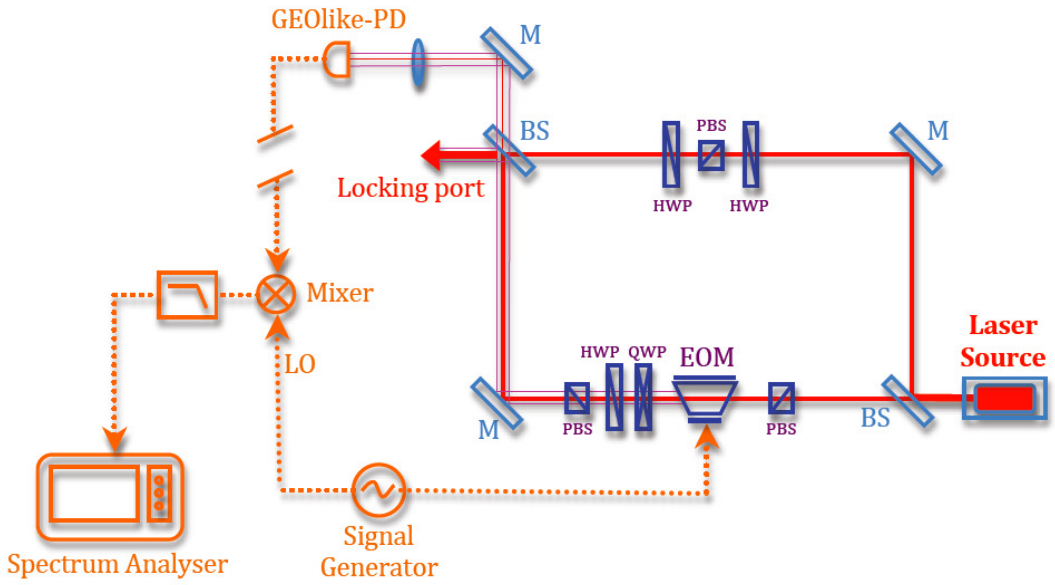

Figure 6.11: Shot noise level measuring set-up. The light on the dark fringe is focused to the GEO-like photodetector and filtered and demodulated. The ancillary components in the bright port and necessary to get the locking of the interferometer have been omitted in this diagram.

not permit obtaining the desired gain at the modulation frequency and thus was replaced with a fixed one of carefully calculated value. Fortunately this provided a much better response. Two spectra measurements of the RF output of the photodiode corresponding to the variable and fixed inductor are reproduced in Fig. 6.12. The reduced circuitry to calculate the value of the fixed inductor and the calculation of the inductor to get a resonance at the modulation frequency are reproduced in L.

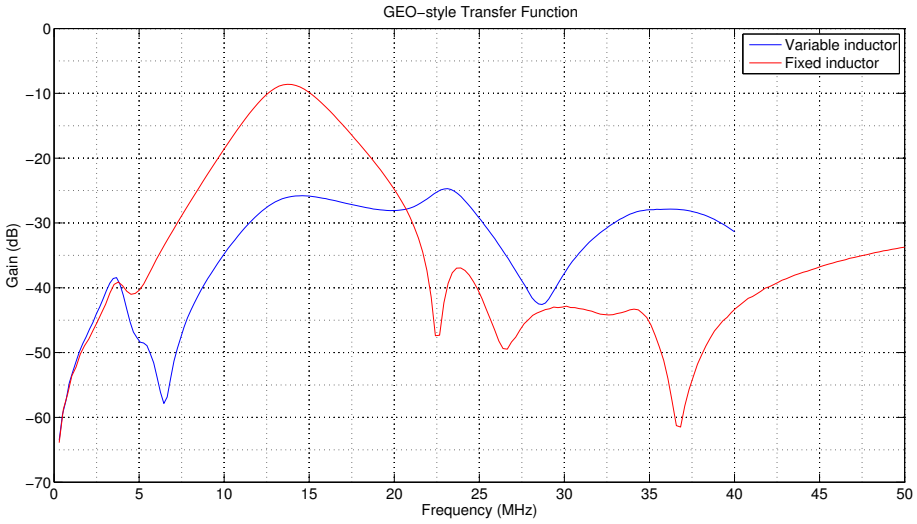

Figure 6.12: Comparison of the transfer functions of the GEO-style photodetector, with the preliminary tuneable variable inductance and the final fixed inductor of 1.35 μH. Note the better response of the resonance peak around the modulation frequency of 14.5 MHz and the attenuation of the second harmonic at $2 \times 14.5 \approx 29$ MHz with a gain 2 orders of magnitude smaller.

6.4.5.2 Photodiode protection system

Overall, the stability of the locked interferometer proved to be reliable and long lasting: it was capable to mantain itself locked for more than 30 minutes at a time, even when the optical bench was shaken accidentally. With the aim to safeguard the photodiode from another loss of lock, a protection system was designed and implemented. The protection allowed to switch off the reverse bias voltage when

the light power falling onto the detector was too big. The DC signal given out by the photodiode was continuously monitored by a voltage comparator that took action disconnecting the reverse bias from the photodetector whenever the DC voltage exceeded a previously set-up threshold. The safety circuit implemented is shown in Fig. 6.13.

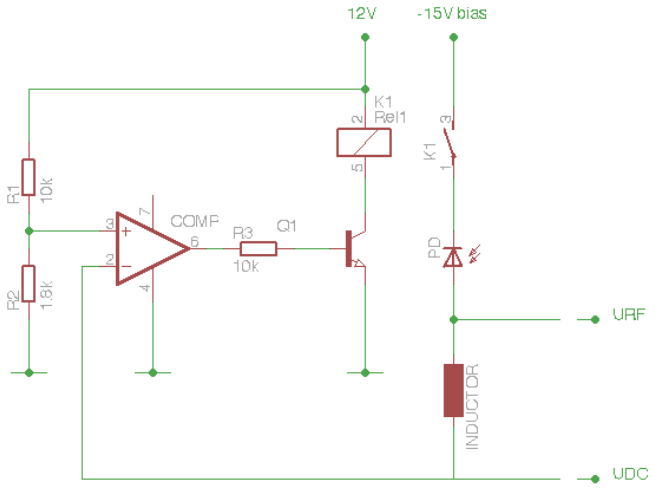

Figure 6.13: Protection circuit implemented to protect the GEOstyle photodiode for unexpected interferometer lock losses. The light power hitting the photodiode is monitored continuously and a comparator disconnects the bias voltage whenever the DC output of the photodetector surpasses the security threshold. The comparator triggers the normally-closed relay and opens the switch of the bias voltage in order to protect the photodiode from excessive heat generation.

The transfer function of the photodetector was tested again, after adding the external relay that permitted switching off the reverse bias, in order to check that the resonant peak around the modulation frequency and the attenuation around the second harmonic were not severely affected by the addition of ancilliary componentry. The response (transfer function) of the circuitry after adding the protection system can be observed in Fig. 6.14

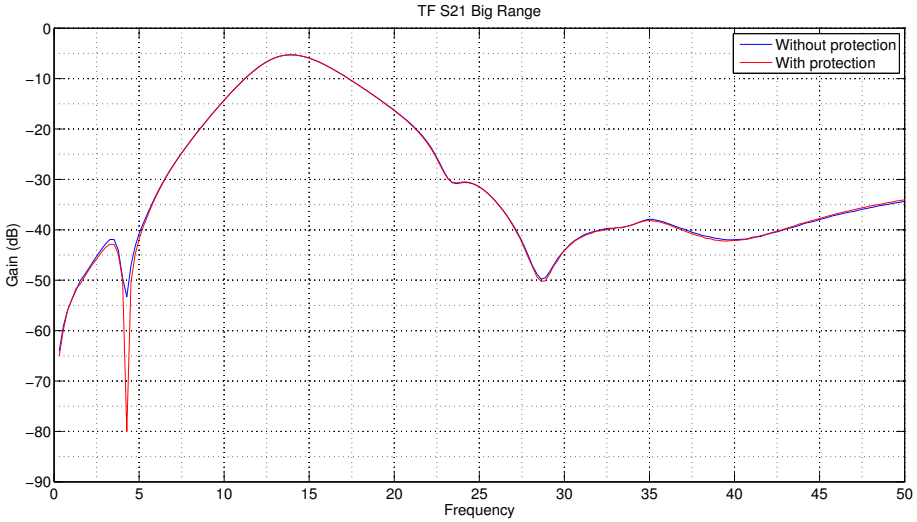

Figure 6.14: Comparison of the transfer function of the GEO-style photodetector before and after implementing the safety circuit to safeguard the photodiode from excessive light power in the accidental lock of loss.

6.4.5.3 Measurements

To ensure that a minimum level of light (and thus a measurable shot-noise level) existed in the dark port, the light power at the entrance of the interferometer was increased up to approximately 250 mW. This resulted in approximately 40 mW of light power in the dark port, which allowing for a photodiode efficiency of $\eta \approx 75\%$ provided a DC current out of $\bar{I} = \eta P \approx 30$mA. From Eq. 6.1 a rms current level for the shot-noise of $\bar{i_N^2} \approx 100$pA can be inferred. This is a minute current, which it needs to be amplified with care to ensure that the shot-noise level surpasses any electrical noise of the devices taking part in the measurement.

The measurements consisted on taking an averaged spectra of bandwidth 100 Hz at a frequency of about 10 kHz of the demodulated and low-passed signal out of the GEO-style photodetector. Different cable lengths between the photodetector and the mixer, where the demodulation takes place, allow for the RF signal to be combined with the local oscillator at different phase-differences (see Fig. 6.11). For a signal of frequency $w_m = 14.5$ MHz cables of length $\lambda_m = 20.8$ m are needed in order to change the demodulation phase 2π.

By trying different lengths of cables the critical phase at which the power of the spectrum is the lowest may be revealed; this is taken as a reference and corresponds to the demodulation in quadrature (Q). Conversely, the length for which the level is maximum will be for the in-phase (P) quadrature.

6.4.6 Results

All my measurements showed an electrical noise similar or higher than the shot noise level and, unfortunately, no conclusion could be extracted. Fig. 6.15 shows side by side one example of the spectra of the RF channel given by the GEO-style photodiode, taken of two measurements of bandwidth 800 Hz centered at 34.7kHz and 52.6 kHz. Each subplot presents three measurements: a) the lowest possible noise measurable by the spectrum analyser (when no cables were plugged to the analyser), b) with no light was projected to the photodiode (measurement of the electrical noise, only) and c) when the dark fringe light was projected to the photodiode (measurement of the modulated light). A notable difference was expected between the electrical noise and the dark fringe measurement; however, this could not be achieved. My inability of reducing the electric noise to levels considerably lower than the shot noise conditioned the extraction of conclusions in this experiment.

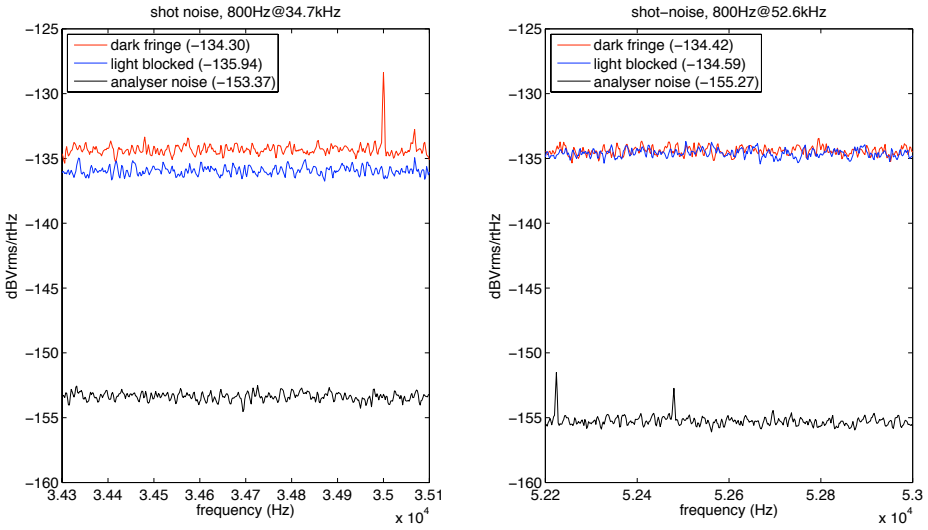

Figure 6.15: Spectrum of 800Hz@52.6kHz taken for $\sim$ 20mW of light power in the dark fringe.

Chapter 7

Summary and Future work

This thesis contains two separate sections focusing on gravitational wave detection. The main section is theoretical and summarises the Bayesian data analysis work, whereas the other describes some experimental work and is shorter. In the following, a brief summary of the theoretical work is presented and the ways to take this forward.

A procedure for studying the detectability of burst gravitational wave signals from galactic neutron stars has been presented in this thesis, based on the calculation of the time- and polarisation-averaged antenna pattern and power values. The results of this research could be taken further by considering more realistic galactic populations of neutron stars and including the exact location of the potential detector, which will be likely built in the southern hemisphere in the near future.

The modeling of the signal in the frequency domain using the closed form DTFT (rather than the computationally more demanding DFT) allows for a quicker computation of the likelihood for the Bayesian inference. Also, it provides the additional benefit of focusing the attention on those relevant frequency bandwidths where the signal power is concentrated. The use of the z-transform and its relation to the DTFT has proved to be very convenient for the computation of the likelihood for combined data stretches recorded by detectors at different locations that will receive the time-shifted signal. This work has presented a useful framework that can easily be applied to real data recorded by a network of detectors. Although it is partially dependent on the information

provided by the spectrogram of a potential detection candidate, the framework allows for the efficient modeling of the signal in the frequency domain in order to carry out model comparison and parameter estimation.

Bayesian inference for model comparison and parameter estimation can be computationally very demanding, in particular the calculation of the evidence for models with multiple parameters in combination with long stretches of data, for example, highly resolved simultaneously acquired data from several detectors. Hence the importance of efficient programming and modularity of the code to handle different models (number of oscillations) in combination with data from several detectors. In this work, the significant computation time required to calculate the evidence of each hypothesis using the nested sampling technique has been a major limitation to a) taking decisions dynamically in order to improve the performance of the code and b) getting enough scenarios and having enough trials in order to average results and compare different hypotheses. An ever more efficient way of computing the evidence and conducting Bayesian inference would open new horizons for some of the investigations carried out in this work. There follows a few ideas to assist in the reduction of computation time:

- Efficiently programmed code for the multinest algorithm has been made freely available (136) (tips for the installation of the freely available software can be found in Matthew Pitkin's blog (137)). The use of *multinest sampling* will facilitate the more in depth and faster study of multimode parameter spaces and relations between the model parameters. A relatively big parameter space has been searched in this work but analysis of an even bigger volume may be required for real data.

- The computation of the likelihood has been carried out using the real and imaginary coefficients of the analytic expression of the DTFT of the signal, evaluated at uniformly distributed frequency points. Limiting the frequency points to within bandwidths where most of the signal power is expected is a practical way of reducing the computation time. Another possibility, which has not been considered in this work, would be to use the whole detection bandwidth focusing on the regions where the signal power is concentrated. A practical way of achieving this would be to increase the frequency point

density in the regions where the signal power is concentrated: this could be done with the Warped Discrete Fourier Transform (WDFT) by means of a variable change of the z-transform(see Section 5.1).

Appendix A

Antenna Pattern study

A.1 Probability density function of F_+ and $F_\times$

The probability density functions of the antenna pattern functions F_+ and $F_\times$ for sources isotropically distributed around the detector are derived in this appendix. For a source of known location (given by the spherical angles θ, ϕ in the local frame of the detector) and radiating gravitational waves of polarisation angle ψ, the antenna pattern functions F_+ and $F_\times$ are functions of the angles (θ, ϕ, ψ). However, the probability density function of the antenna patterns function is independent of the polarisation angle ψ. This is to say:

$$F_+ = f(\theta, \phi, \psi) \quad \text{and} \quad F_\times = f(\theta, \phi, \psi), \quad \text{but}$$
$$p(F_+)\, dF_+ = p(F_\times)\, dF_\times = f(\theta, \phi).$$

For a particular direction specified on the local frame, the antenna pattern values can be readily calculated with:

$$F_+(\theta, \phi, \psi) = \frac{1}{2}(1 + \cos^2\theta)\cos 2\phi \cos 2\psi - \cos\theta \sin 2\phi \sin 2\psi \tag{A.1a}$$
$$F_\times(\theta, \phi, \psi) = \frac{1}{2}(1 + \cos^2\theta)\cos 2\phi \sin 2\psi + \cos\theta \sin 2\phi \cos 2\psi. \tag{A.1b}$$

Taking $A = \frac{1}{2}(1 + \cos^2\theta)\cos 2\phi$ and $B = \cos\theta \sin 2\phi$, we can write:

$$F_+ = A\cos 2\psi - B\sin 2\psi \tag{A.2a}$$
$$F_\times = A\sin 2\psi + B\cos 2\psi \tag{A.2b}$$

where $A \leq 1$ and $B \leq 1$. Obliging $A = C\cos\alpha$ and $B = C\sin\alpha$ (so that $C = \sqrt{A^2 + B^2}$ and $\alpha = \arctan B/A$), expressions in Eq. A.2 can be written as:

$$F_+ = C\left[\cos\alpha\cos 2\psi - \sin\alpha\sin 2\psi\right] = C\cos(2\psi + \alpha) \tag{A.3a}$$
$$F_\times = C\left[\cos\alpha\sin 2\psi + \sin\alpha\cos 2\psi\right] = C\sin(2\psi + \alpha) \tag{A.3b}$$

where $C \leq \sqrt{2}$. The pdf of F_+ and $F_\times$ can be derived from the pdf of ψ. In general, for a function $y = f(x)$ the probability density distributions of x and y can be related by equating probability volumes as follows:

$$p(y)dy = p(x)dx, \quad \text{so that} \quad p(y) = \frac{p(x)}{|dy/dx|},$$

where the absolute values of the differentials are taken for the probabilities to be always positive. Transcribing this to the case which concerns us here, we can write:

$$p(F_+)\,dF_+ = p(F_\times)\,dF_\times = p(\psi)\,d\psi.$$

The probability density function of the polarisation angle ψ is uniform in the range $[0, \pi/2)$, so that $p(\psi) = 2/\pi$ under the normalisation condition of $\int p(\psi)d\psi = 1$.

$$\left|\frac{dF_+}{d\psi}\right| = |-2C\sin(2\psi + \alpha)| = 2\sqrt{C^2 - F_+^2}$$
$$\left|\frac{dF_\times}{d\psi}\right| = |2C\cos(2\psi + \alpha) = 2\sqrt{C^2 - F_\times^2},$$

and putting things together we get:

$$p(F_+) = p(\psi)\left|\frac{d\psi}{dF_+}\right| = \frac{1}{\pi}\frac{1}{\sqrt{C^2 - F_+^2}} \tag{A.4a}$$
$$p(F_\times) = p(\psi)\left|\frac{d\psi}{dF_\times}\right| = \frac{1}{\pi}\frac{1}{\sqrt{C^2 - F_\times^2}}, \tag{A.4b}$$

Given a probability density function for ψ, an analytic expression for the probability density functions of F_+ and $F_\times$ can be obtained, where $C = f(\theta, \phi)$ because $C = \sqrt{A^2 + B^2}$ and $A = f(\theta, \phi)$ and $B = f(\theta, \phi)$. Fig. A.1 shows the pdf curves calculated with Eq. A.4 for different values of θ and ϕ.

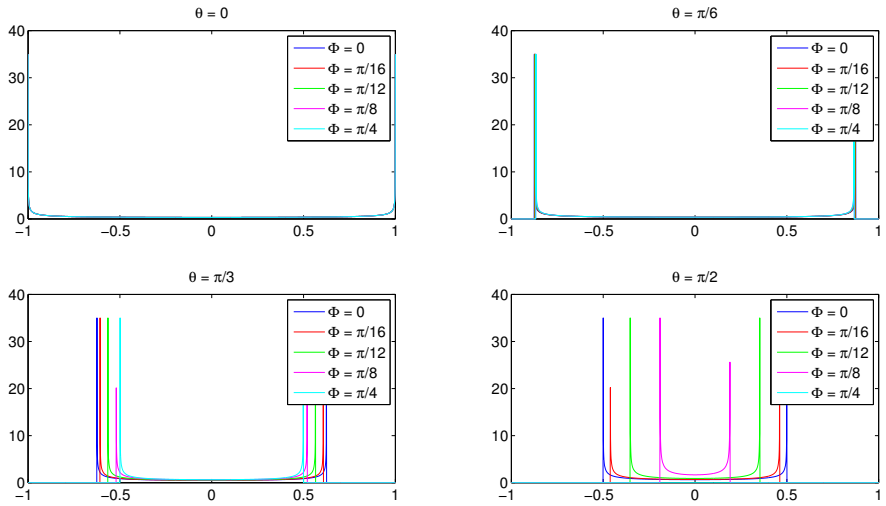

Figure A.1: F_+ and $F_\times$ pdf curves for various directions (θ, ϕ values measured in the local frame of the detector).

A.2 Probability density function of $\bar{F}$

It is straightforward to express $\bar{F}$ as a function of A and B, hence as a function of θ and ϕ:

$$\bar{F} = \sqrt{\frac{F_+^2 + F_\times^2}{2}} = \sqrt{\frac{A^2 + B^2}{2}} = \sqrt{\frac{\left[1/2(1 + \cos^2\theta)\cos 2\phi\ \right]^2 + \left[\cos\theta \sin 2\phi\right]^2}{2}}. \tag{A.5}$$

For isotropically distributed sourcess the pdfs of θ and ϕ are independent: $p(u) = p(\cos\theta) = 1/2$ (for $u \sim \mathcal{U}$[-1,1]) and $p(\phi) = 1/2\pi$. The combined pdf is thus $p(u, \phi) = 1/4\pi$. $p(\bar{F})$ can be obtained from the combined probability distribution

$p(u, \bar{F})$ by marginalising with respect to u. Since $\bar{F} = f(\theta, \phi)$ probability volumes can be equated to write:

$$|p(u, \bar{F})\, du\, d\bar{F}| = |p(\theta, \phi)\, d\theta\, d\phi|$$

which can be written as:

$$|p(u, \bar{F})\, du\, d\bar{F}| = p(\theta, \phi) \times |J| \tag{A.6}$$

where $|J|$ is the determinant of the *Jacobian* matrix that relates the differentials.

$$|J| = \left|\frac{\partial(u, \bar{F})}{\partial(\theta, \phi)}\right| = \left|\frac{\partial(\theta, \phi)}{\partial(u, \bar{F})}\right|^{-1}$$

$$|J| = \frac{(1-u^2)^{3/2}}{2\bar{F}} \frac{[2\bar{F}^2 - 1/4(1+u^2)^2][u^2 - 2\bar{F}^2]}{u^2 - 1/4(1+u^2)^2},$$

and substituting this in Eq. A.6 we obtain:

$$p(u, \bar{F}) = \frac{1}{4\pi} \frac{(1-u^2)^{3/2}}{2\bar{F}} \frac{[2\bar{F}^2 - 1/4(1+u^2)^2][u^2 - 2\bar{F}^2]}{u^2 - 1/4(1+u^2)^2}.$$

Marginalising this with respect to u, which takes values in the range [-1,1], we obtain the desired probability density function for $\bar{F}$:

$$p(\bar{F}) = \int_{\cos\theta=-1}^{\cos\theta=1} p(u, \bar{F})\, du. \tag{A.7}$$

It is not an easy job to marginalise this expression and find the analytic expression for $p(\bar{F})$. In Fig. A.2 we show the pdf curve computed numerically as a normalised histogram of occurrences of $\bar{F}$ values when considering all directions with equal probability.

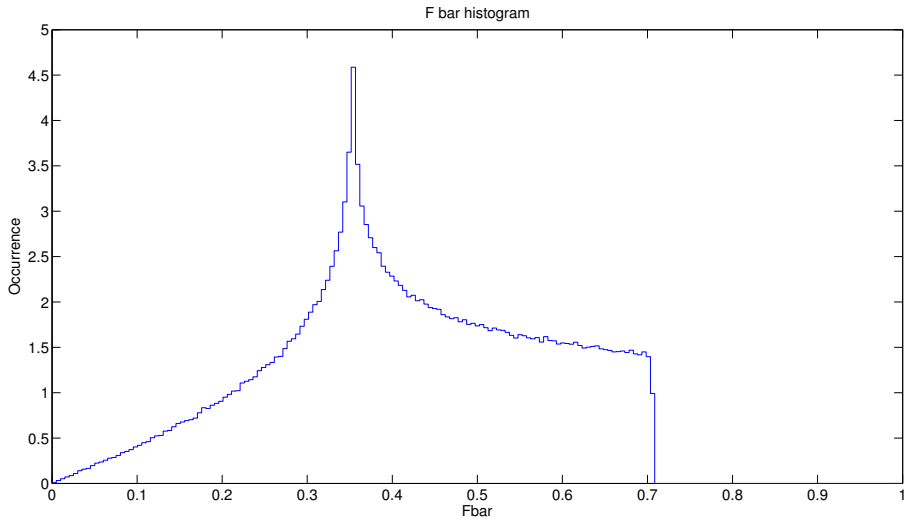

Figure A.2: Normalised histogram of $\bar{F}$ values obtained for random directions of incoming gravitational waves. This plot has been obtained numerically by computing and histogramming $\bar{F}$ values for 10^5 sources isotropically distributed ($u = \cos(\theta) \sim \mathcal{U}$[-1,1] and $\phi = \mathcal{U}[0,2\pi)$. The maximum value for a fully open L-shaped detector is $\sqrt{2}/2$ and the most frequent value is 0.352. (c.f. Fig. 2.7 on section 2.3).

Appendix B

Polarisation degree λ study

B.1 Unknown direction of angular momentum

To infer the probability of detection of a signal is necessary to know the probability of its degree of polarisation λ. In this section the probability density function $p(\lambda)$ of gravitational radiation emitted by a binary system of compact objects is derived. A neutron star lying in isolation with its angular momentum pointing in any direction with the same probability has some resemblance with a binary system randomly oriented in space. In the case of a binary system the polarisation degree can be calculated as:

$$\lambda = \frac{2\cos\iota}{1+\cos^2\iota} = \frac{2v}{1+v^2}, \tag{B.1}$$

where $\iota \in [0, \pi]$ is the angle subtended between the angular momentum of the system and the line of sight and $v = \cos\iota$. If we consider that the angular momentum vector of the source/system points in any direction with equal probability then its probability distribution is $p(v) = 1/2$, because $v = \cos\iota \sim \mathcal{U}$[-1,1]. Solving Eq. B.1 for v we get:

$$v = \frac{1}{\lambda} \pm \sqrt{\frac{1}{\lambda^2} - 1} \tag{B.2}$$

where "+" should be taken for values of $\lambda \in [-1, 0]$ and "−" for $\lambda \in [0, 1]$. Equating probability volumes:

$$p(\lambda)\, d\lambda = p(v)\, dv \tag{B.3}$$

we get:

$$p(\lambda) = p(v) \left|\frac{dv}{d\lambda}\right| = \frac{1}{2} \cdot \left|\frac{(1+u^2)^2}{2(1-u^2)}\right| = \frac{1}{2} \cdot \left| \frac{\left[1 + \left[\frac{1}{\lambda} \pm \sqrt{\frac{1}{\lambda^2} - 1}\right]^2\right]^2}{2\left[1 - \left[\frac{1}{\lambda} \pm \sqrt{\frac{1}{\lambda^2} - 1}\right]^2\right]} \right|, \tag{B.4}$$

which is already a normalised expression. Fig. B.1 shows the curve corresponding to the analytical expression in Eq. B.4. It has been compared with the result obtained by normalising the histogram of 10^5 trials.

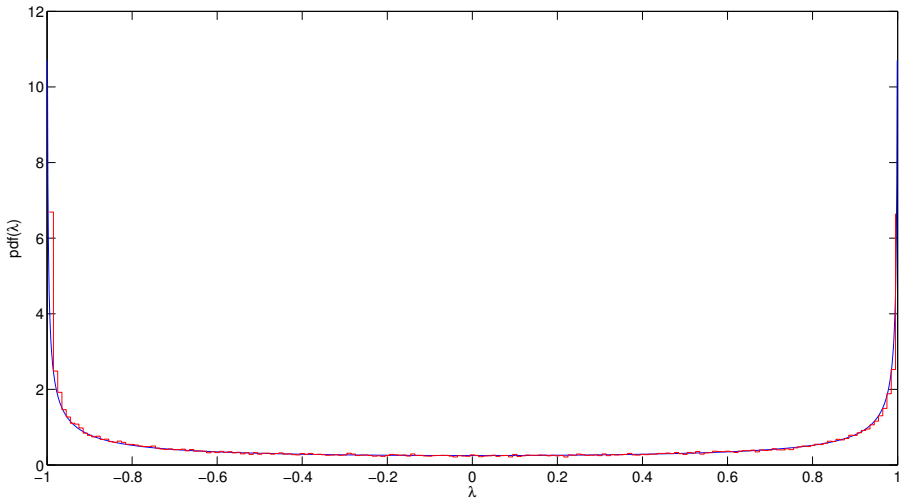

Figure B.1: Comparison of the analytical expression of the probability density function of λ given by Eq. B.4 and the normalised histogram of 10^5 trials. The lowest probability is for linearly polarised signals ($\lambda = 0$), whereas the highest probability is for circularly polarised signals ($\lambda = -1, \lambda = 1$).

B.2 Known direction of angular momentum

Electromanetic observations of nebulae around pulsars can sometimes help identifying the direction of the angular momentum and the angle with respect to the line of sight ι. What can be said about the polarisation degree λ then? Let us assume here that the value of ι has been constrained and it is represented by a gaussian probability distribution function:

$$p(\iota) = \frac{1}{\sigma_\iota \sqrt{2\pi}} \exp\left[-\frac{(\iota - \mu_\iota)^2}{2\sigma_\iota^2}\right]. \tag{B.5}$$

It is not easy to infer an analytic expression of $p(\lambda)$ given the probability distribution of ι in Eq. B.5 and their relation in Eq. B.1. Fig. B.2 (left) shows a numerical example to show the relation between the two distributions. For $\iota \sim \mathcal{N}(\mu_\iota, \sigma_\iota) \equiv \mathcal{N}(1.1501, 0.0873)$ (the uncertainty corresponds to the 95% of probability mass in the interval $\iota = \mu_\iota \pm 5°$ in radians). The normalized histogram of the resulting values of λ (10^6 trials) and its gaussian fit $\lambda \sim \mathcal{N}(\mu_\lambda, \sigma_\lambda) = \mathcal{N}(0.6891, 0.099)$ are shown in the right. The mode of the histogram is at $\lambda = 0.7162$.

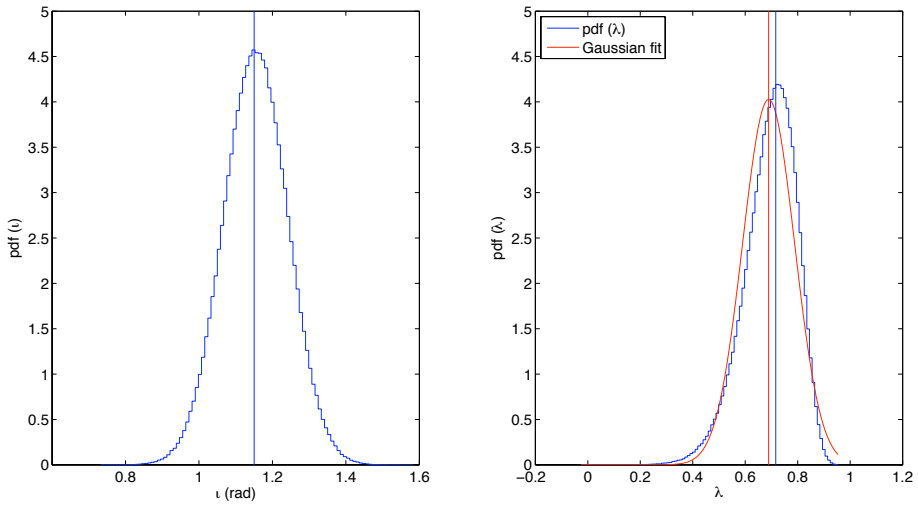

Figure B.2: Example of the probability distribution of λ and its gaussian fit (right) given the distribution of ι (left).

Appendix C

Comparing Histograms: The mean value of a histogram

This appendix provides insight into the procedure for quantitative comparison of histograms of comparable populations. This is a way, for example, to decide which of two countries with the same number of inhabitants is "taller" based only on their corresponding histograms, which were obtained by binning all the individual height values. The method is very simple and consists in calculating the mean value (called $\bar{x}$-value thereon) of each histogram and sorting them out by this value. Once the histogram has been created the $\bar{x}$-value can be calculated by adding all the individual results of the multiplications of the bin values (not the bin widths) with the number of occurrences for each bin. For a population of N values, organised in M bins, the mean or $\bar{x}$-value can be calculated as follows:

$$\bar{x} = \frac{1}{N} \sum_{m=1}^{M} n_m x_m,$$

where x_m is the value of the m^{th} bin and n_m is the number of counts of that same bin. The set of possible $\bar{x}$-values is analogous to the different ways of arranging N balls into M buckets, where the number of possible combinations is $\binom{N+M-1}{N}$.

Table C.1 shows a simple example to illustrate the procedure, in which 3 values have been arranged into 3 bins. Each possible arrangement is represented by a different row in the table.

N = 3 values into M = 3 bins				
Set No.	**Bin 1**	**Bin 2**	**Bin 3**	$\bar{x}$ **value**
1	[3	0	0]	1.000
2	[2	1	0]	1.333
3	[2	0	1]	1.666
4	[1	2	0]	1.666
5	[1	1	1]	2.000
6	[1	0	2]	2.333
7	[0	3	0]	2.000
8	[0	2	1]	2.333
9	[0	1	2]	2.666
10	[0	0	3]	3.000

Table C.1: List of all the possibilities to arrange 3 values into 3 bins and the $\bar{x}$-value of each arrangement. In total, there are $\binom{5}{3} = 10$ possibilities.

All the $\bar{x}$-values have been plotted in Fig. C.1. It can be observed that the mean values of subsequent histograms do not form a strictly increasing monotonic function, and that:

- Two arrangements/histograms can have the same $\bar{x}$-value. The outcomes [0 3 0] and [1 1 1] result on the same value $\bar{x} = 6$ (written as [0 3 0; 6] and [1 1 1; 6] thereon). Similarly, the arrangements [1 2 0; 5] and [2 0 1; 5]. The lesson here is that two histograms with the same $\bar{x}$-value are not necessarily the same histogram, for it is degenerate.

- Overall, $\bar{x}$-values present an increasing trend (given that the binning starts from the left) but it may decrease at points. For example, [1 0 2; 7], and the next one is [0 3 0; 6].

One conclusion drawn from the above points is that the $\bar{x}$-value is a subjective way of comparing histograms. For example, let us think we want to measure the degree of obesity in two groups of $N = 10$ children by using their histogramed

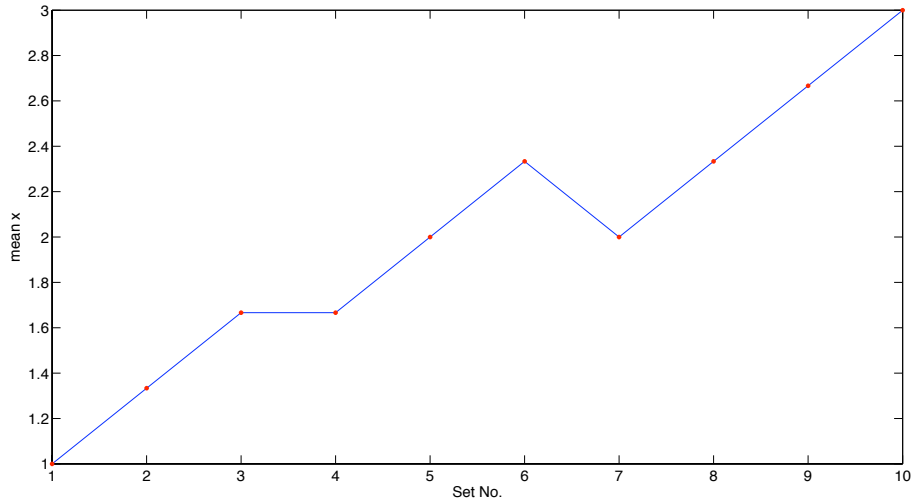

Figure C.1: Normalised $\bar{x}$-values corresponding to table C.1.

weights (to decide who of the two groups should go on a diet...) using $M = 3$ bins. Studying all the possible outcomes it is found that [0 9 1; 6], [1 7 2; 6], [2 5 3; 6], [3 3 4; 6],[4 1 5; 6] (see Fig. C.1) result in the same $\bar{x}$-value. That is to say that using only the $\bar{x}$-value as an indicator the same degree of obesity would be assigned to very different groups. Arguably, this is not fairest but it is a way of quantifying group of values/histograms nevertheless.

C.1 Extracting information from histograms

The fact that the $\bar{x}$ function is not a monotonically increasing can cause some uncertainty on decisions taken based solely on the mean value. One example is to infer which of two groups has a bigger mean value. Fortunately, the uncertainty of the decision reduces bigger is the number of values and bins considered. A simple example was devised to enlighten this and it is presented in the following.

The exercise consisted in sorting the mean $\bar{x}$ and the scale factor θ of 50 populations, generated by sampling from gaussian and gamma distributions of known mean and scale factor, respectively, using only the $\bar{x}$ of their histograms. For the gaussian populations the mean was randomly chosen from an uniform distribution

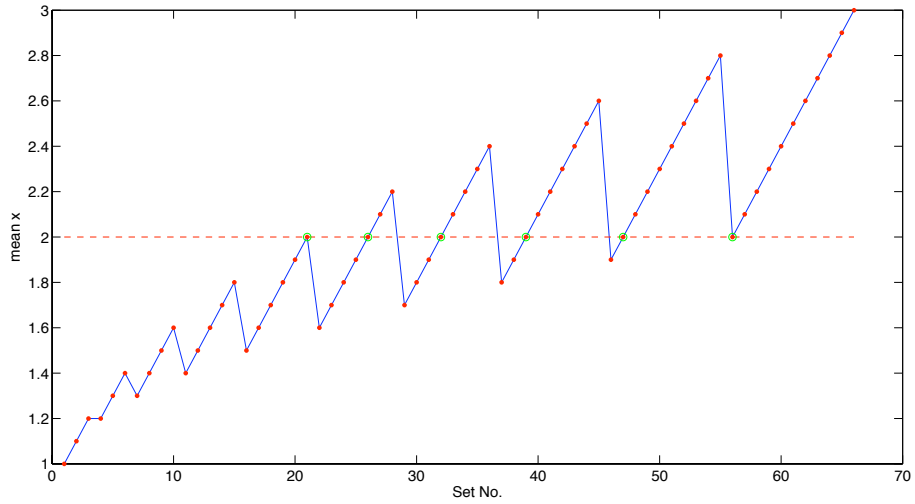

Figure C.2: Evolution of the normalised $\bar{x}$-values for all the possible arrangements of $N = 10$ values into $M = 3$ bins.

$\mu \sim \mathcal{U}[20{,}25]$ and the standard deviation is $\sigma = 5$. For the gamma distributions the scale factor was chosen from a uniform distribution $\theta \sim \mathcal{U}[5{,}8]$ with fixed shape factor $k = 2$. All the randomly chosen mean and scale factor values were recorded to later establish the fraction of correctly ordered populations using $\bar{x}$. A different number of samples and bins were tried in order to check how this affects the results: combinations of $N = 10^3, 10^4, 10^5$ and 10^6 values arranged into $M =$ 50, 100, 150 and 200 bins were tried. The exercise was repeated 500 times for each combination (N, M) and the fraction of successes (populations' mean and scale factors sorted out correctly) have been plotted. Fig. C.3 and Fig. C.4 show (N, M) trials each, with 50 gaussian (left) and 50 gamma (right) distributions. The need of a systematic way of quantifying histograms is shown clearly in the figures, for it is not easy to establish the order of the means or of the scale factors visually. Fig. C.5 shows the statistics of inferring the order of means and scale factors correctly using the $\bar{x}$-value of the histograms. As expected, bigger are N and M, the rate for which order is guessed correctly increases.

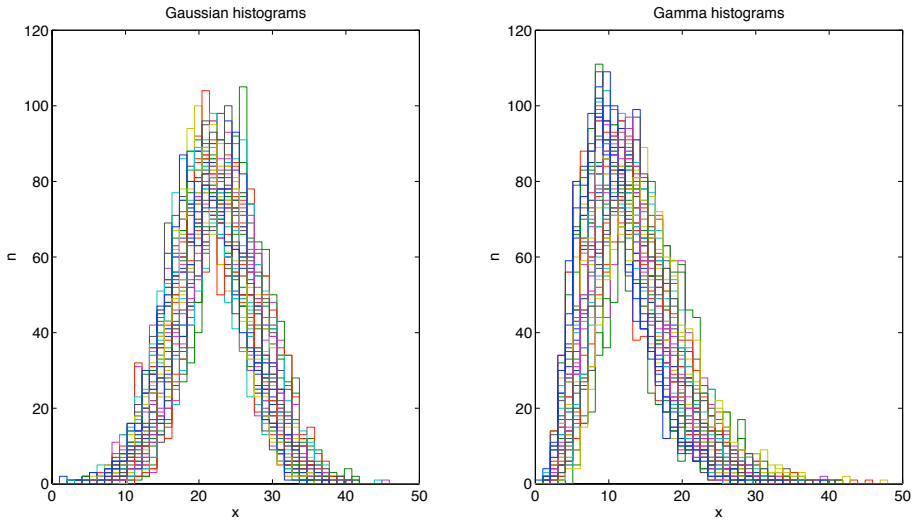

Figure C.3: 50 histograms ($M = 50$ bins) of ($N = 10^3$) samples values withdrawn from gaussian and gamma distributions, with random mean and scale factors, respectively.

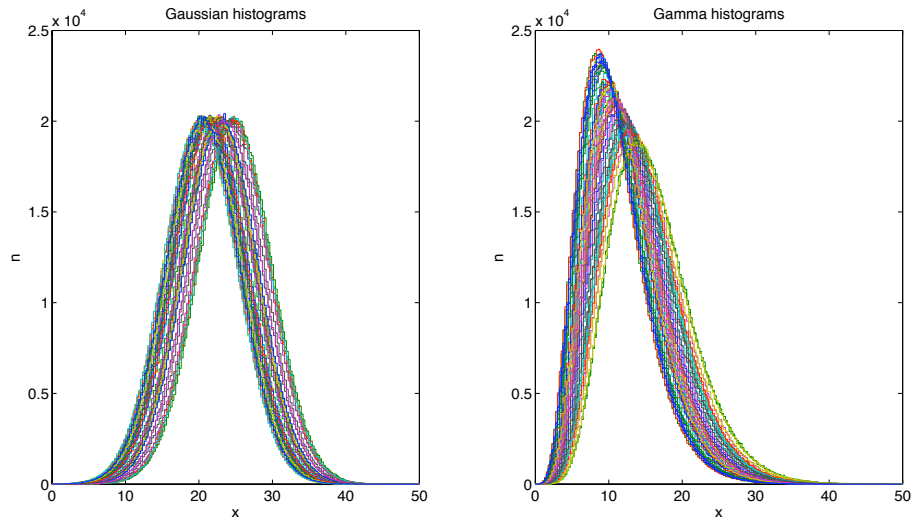

Figure C.4: 50 histograms ($M = 200$ bins) of ($N = 10^6$) samples values withdrawn from gaussian and gamma distributions, with random mean and scale factors, respectively.

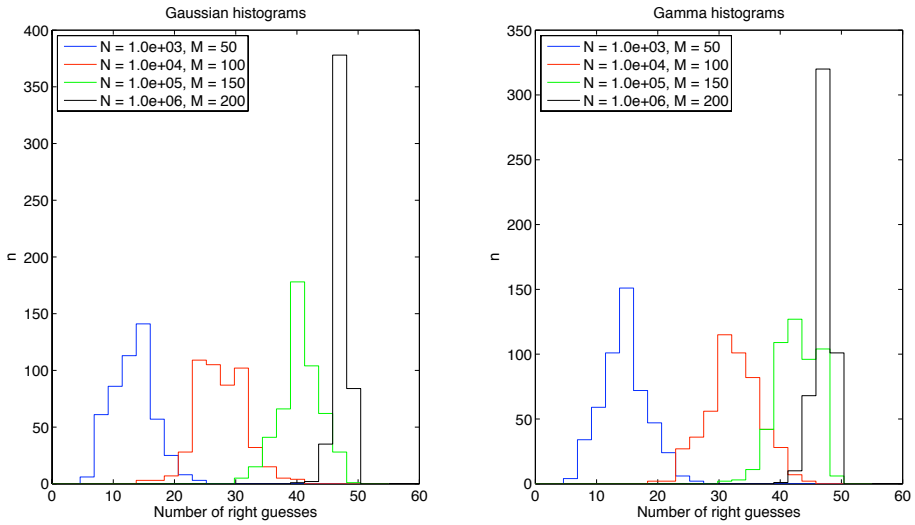

Figure C.5: Histograms of the 500 trials showing the number of histograms guessed in the right order. The bigger the number of values N and the number of bins M, the higher is the number of histograms ordered correctly using the $\bar{x}$ is higher.

Appendix D

Calculation of antenna pattern functions

It is straightforward to calculate the antenna function patterns, F_+ and $F_\times$, in the local frame of the detector with the Eqs. D.1:

$$F_+(\theta,\phi,\psi) = \frac{1}{2}(1+\cos^2\theta)\cos 2\phi\cos 2\psi - \cos\theta\sin 2\phi\sin 2\psi \tag{D.1a}$$

$$F_\times(\theta,\phi,\psi) = \frac{1}{2}(1+\cos^2\theta)\cos 2\phi\sin 2\psi + \cos\theta\sin 2\phi\cos 2\psi \tag{D.1b}$$

Eqs. D.1 have been taken from p.417 of Ref. (90) where the direction to the source (i.e. incoming direction of the gravitational wave) is given by the spherical angles (θ,ϕ) in the detector frame (see Fig. 9.2 in p. 366 or Fig. 9.9 in p. 416). Note that θ (i.e. the co-altitude) is measured from the direction perpendicular to the detector plane (a source located overhead has $\theta = 0$ and on the horizon has $\theta = \pi/2$), ϕ (i.e. the azimuth) is measured from the first to the second arm and ψ is the polarisation angle measured from the plane of constant ϕ (through the source) and the polarisation ellipse axis.

Eqs. D.1 are derived for a fully open L-shape detector (that is, the angle between arms $2\Omega = \pi/2$ rad). So, more generically, we can write:

$$F_+(\theta,\phi,\psi) = \frac{1}{2}\sin 2\Omega\left[(1+\cos^2\theta)\cos 2\phi\cos 2\psi - \cos\theta\sin 2\phi\sin 2\psi\right] \quad \text{(D.2a)}$$

$$F_\times(\theta,\phi,\psi) = \frac{1}{2}\sin 2\Omega\left[(1+\cos^2\theta)\cos 2\phi\sin 2\psi + \cos\theta\sin 2\phi\cos 2\psi\right]. \quad \text{(D.2b)}$$

Schutz - Tinto devised an equivalent and very flexible method to calculate the antenna patterns F_+ and $F_\times$. We refer the reader to Ref. (91) and note the derivation of Eq. 2.14 there (reproduced below in Eqs. D.3) to calculate the strain produced by the gravitational wave on the detector.

$$\frac{\delta l_n}{l_0} = -\frac{1}{2}\sin 2\Omega\left[(A_X^x A_X^y - A_Y^x A_Y^y)h_+ + (A_X^x A_Y^y + A_Y^x A_X^y)\exp(i\delta)h_\times)\right] \quad \text{(D.3a)}$$

$$= -\frac{1}{2}\sin 2\Omega\left[(a_{11}a_{21} - a_{12}a_{22})h_+ + (a_{11}a_{22} + a_{12}A_{21})\exp(i\delta)h_\times)\right] \quad \text{(D.3b)}$$

$$= -\frac{1}{2}\sin 2\Omega\left[F_+h_+ + F_\times\exp(i\delta)h_\times)\right] \quad \text{(D.3c)}$$

where a_{ij} are the elements of matrix $\mathbf{A}$ corresponding to the rotation matrix of Eulerian angles (θ,ϕ,ψ). This rotation matrix allows us to transform strain coordinates defined in $\mathbf{XYZ}$ (i.e. the wave-frame) into $\mathbf{xyz}$ (i.e. the detector-frame), see Fig. D.1. To know the a_{ij} elements it is logical to calculate first the matrix $\mathbf{A^{-1}}$ corresponding to the opposite transformation (i.e from $\mathbf{xyz}$ into $\mathbf{XYZ}$). This matrix is obtained by the combination (orderly matrix multiplication) of three individual successive rotations $\mathbf{R_i}(\theta_\mathbf{i})$ around the axis $\mathbf{x},\mathbf{y},\mathbf{z}$, see Ref. (138):

$$\mathbf{A^{-1}} = \mathbf{R_z}(\phi)\mathbf{R_x}(\theta)\mathbf{R_z}(\psi) \quad \text{(D.4)}$$

$$= \begin{pmatrix} \cos\psi\cos\phi - \cos\theta\sin\phi\sin\psi & \cos\psi\sin\phi + \cos\theta\cos\phi\sin\psi & \sin\psi\sin\theta \\ -\sin\psi\cos\phi - \cos\theta\sin\phi\cos\psi & -\sin\psi\sin\phi + \cos\theta\cos\phi\cos\psi & \cos\psi\sin\theta \\ \sin\theta\sin\phi & -\sin\theta\cos\phi & \cos\theta \end{pmatrix}. \quad \text{(D.5)}$$

and remembering that for the rotation of orthogonal frames $\mathbf{A^t} = \mathbf{A^{-1}}$ we can see that the transpose of the above matrix is the same as $(A)^j_K$ in section 2

of Ref. (91). Note the usage of the Eulerian angles (ϕ, θ, ψ) on individual base rotation matrices of the form:

$$\mathbf{R_x}(\theta_\mathbf{x}) = \begin{pmatrix} 1 & 0 & 0 \\ 0 & \cos\theta_x & \sin\theta_x \\ 0 & -\sin\theta_x & \cos\theta_x \end{pmatrix}, \quad \mathbf{R_z}(\theta_\mathbf{z}) = \begin{pmatrix} \cos\theta_z & \sin\theta_z & 0 \\ -\sin\theta_z & \cos\theta_z & 0 \\ 0 & 0 & 1 \end{pmatrix}. \tag{D.6}$$

The multiplication order $\mathbf{R_z}(\phi)\mathbf{R_x}(\theta)\mathbf{R_z}(\psi) = \mathbf{A^{-1}}$ corresponds to first rotating ψ counterclockwise, then θ counterclockwise, and lastly ϕ counterclockwise again. The second rotation is around the $\mathbf{x}$ axis and hence this transformation is called a *x-convention* rotation/transformation.

The detector-frame **xyz** is defined, conveniently but unconventionally, such that the $\mathbf{x}$ and $\mathbf{y}$ are contained in the detector plane and $\mathbf{x}$ bisects the angle 2Ω between the detector arms, see Fig. D.1. An important implication is that ϕ is measured counterclockwise from the bisector, and not from the first arm of the detector as it is considered on Eqs. D.2.

From the generic expression to calculate the strain on the arms of the detector (given Eqs. D.3) we can readily calculate the antenna pattern functions as:

$$F_+ = -\sin 2\Omega \left(a_{11}a_{21} - a_{12}a_{22}\right) \tag{D.7a}$$
$$= -\sin 2\Omega \left[1/2\left(1+\cos^2\theta\right)\sin 2\phi\cos 2\psi + \cos\theta\cos 2\phi\sin 2\psi\right] \tag{D.7b}$$
$$F_\times = -\sin 2\Omega \left(a_{11}a_{22} + a_{12}a_{21}\right) \tag{D.7c}$$
$$= -\sin 2\Omega \left[-1/2\left(1+\cos^2\theta\right)\sin 2\phi\sin 2\psi + \cos\theta\cos 2\phi\cos 2\psi\right] \tag{D.7d}$$

Eqs. D.7 and Eqs. D.2 are equivalent, but not equal. If we were considering the average value of the antenna pattern $\bar{F} = \sqrt{1/2(F_+^2 + F_\times^2)}$ we would have easily overlooked the difference. To see their equivalency it is important to note a few subtle points:

- In Eqs. D.7 ϕ is measured from the bisector of the arms (see Fig. D.1), whereas in Eqs. D.2 ϕ is measured from the first arm to the second arm. For a detector of generic shape, there is a shift of Ω between the two systems.

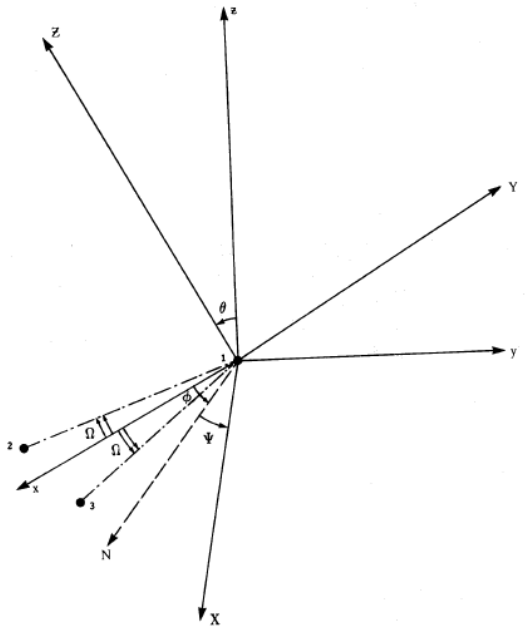

Figure D.1: The relation between the detector frame **xyz** and the wave frame **XYZ**. The angles θ and ϕ are the usual spherical polar coordinates of the wave's incoming direction, measured in the detector frame. The angle ψ is a measure of the polarisation angle of the wave, defined as a rotation about the **Z**-axis. N is the projection of the line of nodes of the polarisation ellipse onto the **xy** plane. Figure taken from Ref. (91).

- The angle θ is always measured from the perpendicular to the detector plane. However, on Eqs. D.7, θ is one of the Eulerian angles to tilt the detector frame toward the source, whereas in Eqs. D.2, θ is the rotation angle so that the propagation direction of the wave points to the detector (c.f. see Fig. 9.2 in Ref. (90)). This is why to show the equivalency between them we need to substitute θ for $\pi - \theta$. Sources in the Northern Celestial Hemisphere (NCH) have $\delta > 0$ and $\theta > \pi/2$, whereas sources in the South Celestial Hemisphere (SCH) have $\delta < 0$ and $\theta < \pi/2$. In general, $\theta = \pi/2 + \delta$, see Fig. D.3.

- It is important to be careful and keep in mind where the angles (θ, ϕ) are measured from. If we make the substitution $\theta \to \pi - \theta$ and $\phi \to \phi + \Omega$ in Eqs. D.7, these reduce to Eqs. D.2. This is shown graphically in Fig. D.2.

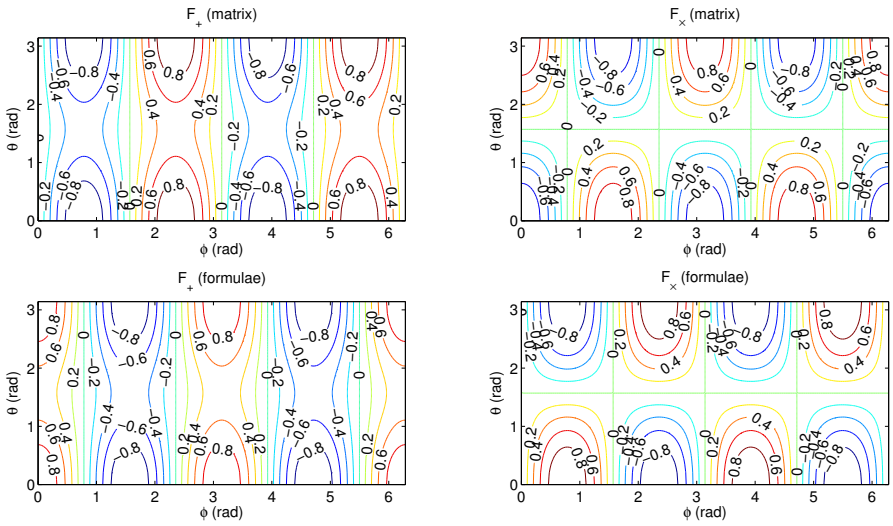

Figure D.2: Comparation of F_+ and $F_\times$ calculated with Eqs. D.2 (*two upper panels*) and Eqs. D.7 (*two lower panels*) for a L-shape detector. It is readily seen that both ways to calculate the antenna patterns are equivalent: if we take the two upper panels and first shift the patterns $\pi/4$ rad horizontally to the right (emulating $\phi \to \phi + \Omega$), and then flip the patterns with respect to an horizontal axis at $\theta = \pi/2$ (emulating the replacement $\theta \to \pi - \theta$) we obtain the two panels below.

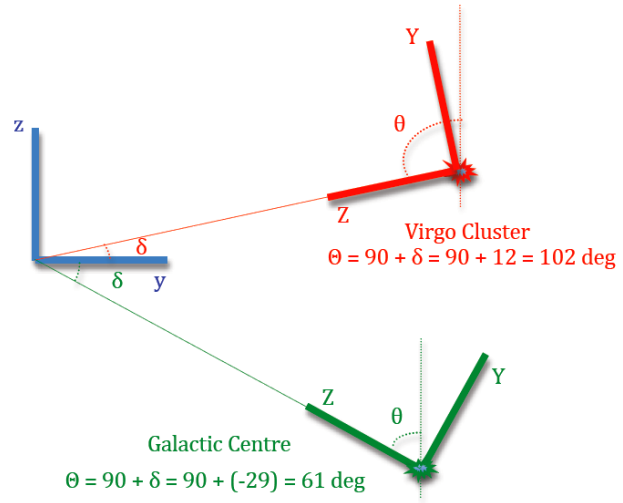

Figure D.3: θ calculation examples for two sources (Virgo Cluster and the Galactic Centre) where the relation $\theta = \pi/2 + \delta$ is obvious. Note that this figure shows only the partial rotation (of one Eulerian angle θ) on the **zy** plane; θ is the angle we need to rotate the wave frame to align it with the detector frame.

The calculation of the angles (θ, ϕ, ψ) for a particular instant and source location, given by equatorial coordinates (δ,RA), is not straightforward using spherical trigonometry. This rather intricate calculation may be alleviated by a systematic transformation (matrix multiplication) that takes the gravitational wave amplitude and projects it onto any detector of particular location and orientation on Earth. The conversion is done in two steps by means of an intermediate stepping frame.

Let us first define the new intermediate coordinate frame $\mathbf{x'y'z'}$ fixed to the centre of the Earth and rotating with it around $\mathbf{z'}$ (the axis going through the poles) so that $\mathbf{x'}$ pierces and follows the rotation of the Greenwich meridian as shown in Fig. D.4. Having defined an intermediate Earth-fixed frame (called Earth frame thereon) we are now in the position to compute a rotation matrix $\mathbf{B}$ that transforms coordinates from any detector's local frame **xyz** to the Earth frame. A straight-forward way of calculating $\mathbf{B}$ is to follow an analogue procedure to $\mathbf{A}$ and to combine, by orderly multiplication, three successive rotations of the Eulerian angles (α, β, γ) to rotate the Earth frame to the detector frame. β and

γ denote the latitude and longitude, respectively, of the geographical location of the detector and α, the angle subtended between the North-Sourth meridian of the location and the detector bisector, defines its orientation. Following the *y-convention* (the second rotation is with respect to the re-oriented **y** axis) and noting the rotation angle as the colatitude $\pi/2 - \beta$ we get:

$$\mathbf{B_1} = \mathbf{R_z}(\alpha)\mathbf{R_y}(\pi/\mathbf{2} - \beta)\mathbf{R_z}(\gamma) \tag{D.8}$$

$$= \begin{pmatrix} \cos\gamma\sin\beta\cos\alpha - \sin\gamma\sin\alpha & \cos\gamma\sin\beta\sin\alpha + \sin\gamma\cos\alpha & -\cos\gamma\cos\beta \\ -(\sin\gamma\sin\beta\cos\alpha + \cos\gamma\sin\alpha) & -\sin\gamma\sin\beta\sin\alpha + \cos\gamma\cos\alpha & \sin\gamma\cos\beta \\ \cos\beta\cos\alpha & \cos\beta\sin\alpha & \sin\beta \end{pmatrix} \tag{D.9}$$

Eq. D.8 is an alternative expression to **B** calculated in (91) departing from $\mathbf{A^t}$ in Eq. D.4 and doing the substitutions $\phi \to \gamma - 3\pi/2, \psi \to \alpha - \pi/2$ and $\theta \to \pi/2 - \beta$, as indicated in the paper. It is reproduced here for the benefit of the reader:

$$\mathbf{B_2} = \begin{pmatrix} \cos\alpha\sin\beta\cos\gamma - \sin\alpha\sin\gamma & \sin\alpha\cos\gamma + \cos\alpha\sin\beta\sin\gamma & -\cos\alpha\cos\beta \\ -(\cos\alpha\sin\gamma + \sin\alpha\sin\beta\cos\gamma) & -\sin\alpha\sin\beta\sin\gamma + \cos\alpha\cos\gamma & \sin\alpha\cos\beta \\ \cos\beta\cos\gamma & \cos\beta\sin\gamma & \sin\beta \end{pmatrix}$$

$\mathbf{B_1}$ and $\mathbf{B_2}$ look different but correspond to the same rotation: the multiplication with the coordinates of a randomly chosen spatial point yields the same result and probes that they are indeed equivalent. Also shows that α is measured from the North-South to the bisector of the detector and not from East-West, as it might be understood from Fig. 2 of (91). We take $\mathbf{B_1} = \mathbf{B_2} = \mathbf{B}$.

We can now work out the combined transformation $\mathbf{C} = \mathbf{BA}$ needed to convert coordinates from **XYZ** (wave frame) to **xyz** (detector frame). The relation between the three reference frames can be seen in Fig. D.4.

For clarity and reference, the meaning of the Eulerian angles partaking in the two rotation transformation matrices **A** and **B** are listed below.

- α angle between the bisector of the detector and the meridian (North-South line).

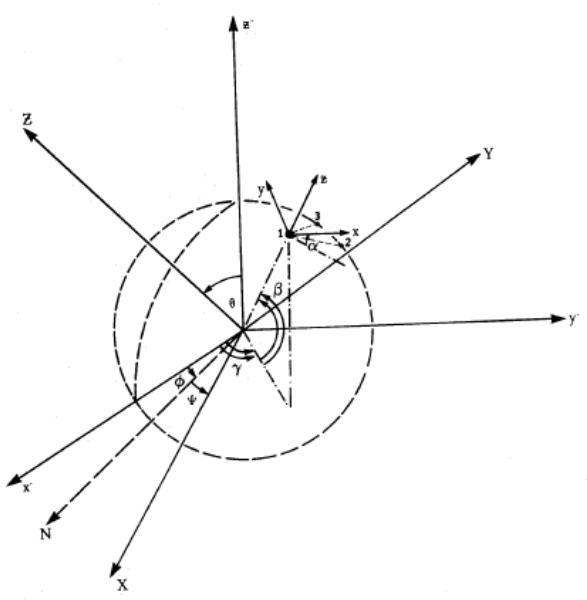

Figure D.4: The relation between the detector's axes **xyz**, the Earth's axes **x'y'z'** and the wave's axes **XYZ**. β and γ are the detector's latitude and longitude, respectively, and α is the orientation with respect to the local meridian (North-South line). The angles θ and ϕ are the usual spherical polar coordinates of the wave's propagation direction, which now are measured with respect to the Earth's axes. The angle ψ determines the polarisation orientation of the wave. ϕ and γ are angles measured on the **x'y'** plane.

- β latitude of detector's location.
- γ longitude of the detector's location.
- θ 'co-declination' of the source direction $\theta = \pi/2 + \delta$.
- ϕ Hour-angle of the source from Greenwich (GHA = GLST - RA), where GLST is the local sidereal time at Greenwich and RA is the right ascension of the source.
- ψ wave's polarisation angle.
- Ω half of the angle between arms.

Appendix E

Chebyshev polynomials

Curves in figures in Section 2.6 have been obtained empirically by calculating the proportion of the trials that fall over a particular threshold of the antenna pattern values. Following the custom of (92) the curves can be described by a linear combination of Chebyshev polynomials. The more polynomials we make use of the more accurate the description of the curve will be. The following is an excerpt from (139).

Typically, the Chebyshev polynomials of the first kind are defined in the range $-1 \leq x \leq 1$ and are of the form:

$$T_r = \cos r\theta, \quad \cos\theta = x, \quad -1 \leq x \leq 1. \tag{E.1}$$

Chebyshev polynomials can be generated from the recurrence system

$$T_0(x) = 1 \tag{E.2}$$

$$T_1(x) = x \tag{E.3}$$

$$T_{r+1}(x) = 2x\,T_r(x) - T_{r-1}(x). \tag{E.4}$$

The Chebyshev polynomials of the first kind defined in the range $0 \leq x \leq 1$ are more convenient for us here, since our threshold for the antenna power $X_*^{1/2}$ is defined in that range. Following the notation in (139) we use an asterisk to differentiate the polynomials defined in the range [0,1] from the more commonly used polynomials in the range [-1,1]. In general, any finite range $a \leq y \leq b$

can be transformed to the basic range $-1 \leq x \leq 1$ with the change of variable $y = 1/2(b-a)x + 1/2(b+a)$. By applying the corresponding change of variables the Chebyshev polynomials in the new range T^* can be defined as:

$$T_0^* = 1 \tag{E.5}$$
$$T_1^* = 2x - 1 \tag{E.6}$$
$$T_2^* = 8x^2 - 8x + 1 \tag{E.7}$$
$$T_3^* = 32x^3 - 48x^2 + 18x - 1 \tag{E.8}$$
$$... \tag{E.9}$$
$$T_{r+1}^* = 2(2x-1)\,T_r^*(x) - T_{r-1}^*(x) \tag{E.10}$$

Figure E.1: Chebyshev polynomials T_r^*, defined in the range [0,1].

The fitting of the curves was done by a linear combination of the orthogonal Chebyshev polynomials T_n^* by minimising the residuals S between the samples and the curve to fitted:

$$S = \sum_{k=0}^{N} w(x_k) \left[f(x_k) - \sum_{r=0}^{n} c_r T_r(x_k) \right]^2, \tag{E.11}$$

where we have $N+1$ samples ($k = 0, 1, 2, ...N$) and w_k is the weight given to each sample $f(x_k)$, and c_r is the coefficient of the Chebyshev polynomial of degree r.

The minimisation problem leads to the normal equations:

$$\mathbf{T'WTc} = \mathbf{T'Wf} \tag{E.12}$$

and for $\mathbf{W} = \mathbf{I_n}$, the identity matrix of dimension N, assuming all the samples have the same importance. $\mathbf{c}$ is the vector of constants, $\mathbf{f}$ is the vector of given values, $\mathbf{W}$ is the diagonal matrix with elements, and $\mathbf{T}$ is the $(N+1) \times (n+1)$ matrix whose r^{th} column is the vector with elements $T_r(x_0), ...T_r(x_N)$. The prime denotes matrix transposition. The equation system can be written as:

$$\begin{pmatrix} T_0(x_0) & T_1(x_0) & \dots & T_N(x_0) \\ T_0(x_1) & T_1(x_1) & \dots & T_N(x_1) \\ \vdots & \vdots & \ddots & \vdots \\ T_0(x_N) & T_1(x_N) & \dots & T_N(x_N) \end{pmatrix} \cdot \begin{pmatrix} c_0 \\ c_1 \\ \vdots \\ c_N \end{pmatrix} = \begin{pmatrix} f(x_0) \\ f(x_1) \\ \vdots \\ f(x_N) \end{pmatrix}. \tag{E.13}$$

This matrix-system is easily solved with a matrix computing program as Matlab.

Appendix F

Tables of Chebyshev coefficients

In the following tables the coefficients of the Chebyshev polynomials to fit the most relevant detection probability curves in Section 2.6 are presented. Results obtained by Monte Carlo simulations for single antennae or a network of detectors have been approximated for signals of different polarisation degree and when distance factor is and is not considered. Polynomials of fourth degree have been used to fit the curve in the range $0 \leq X_*^{1/2} \leq 0.5$.

Coefficients of Chebyshev Polynomials $T_r^*(x)$ for $x \in [0,1]$ (see Appendix E)						
		$\mathbf{c_0}$	$\mathbf{c_1}$	$\mathbf{c_2}$	$\mathbf{c_3}$	$\mathbf{c_4}$
DET.	**Factor**			**Disc-shaped**		
GEO600	DN	7.801e-03	-3.753e-04	-1.513e-02	-1.260e-01	-5.591e+00
	DY	7.817e-03	1.073e-04	-9.504e-03	2.574e-02	1.324e+00
LIGO-H	DN	7.798e-03	-3.599e-04	-9.600e-03	-9.152e-02	-6.748e+00
	DY	7.817e-03	2.048e-04	-2.727e-03	8.449e-02	1.076e+00
LIGO-L	DN	7.815e-03	-6.158e-05	-9.915e-03	-6.037e-02	-3.663e+00
	DY	7.827e-03	3.439e-04	-6.502e-03	3.807e-02	1.042e+00
VIRGO	DN	7.781e-03	-8.589e-04	-1.897e-02	-1.231e-01	-3.780e+00
	DY	7.791e-03	-5.477e-04	-1.691e-02	-4.312e-02	4.511e-01
TAMA300	DN	7.802e-03	-5.513e-04	-2.468e-02	-2.481e-01	-7.739e+00
	DY	7.807e-03	-3.502e-04	-2.442e-02	-1.996e-01	-4.502e+00
PERTH	DN	7.773e-03	-1.225e-03	-2.761e-02	-5.276e-01	-2.365e+01
	DY	7.799e-03	-3.700e-04	-1.519e-02	-2.501e-01	-1.248e+01
DET.	**Factor**			**Sph - GC**		
GEO600	DN	7.802e-03	-3.640e-04	-1.483e-02	-1.089e-01	-4.760e+00
	DY	7.815e-03	1.468e-05	-8.130e-03	3.220e-02	9.678e-01
LIGO-H	DN	7.798e-03	-3.685e-04	-9.103e-03	-8.635e-02	-6.830e+00
	DY	7.814e-03	1.051e-04	-7.496e-04	8.896e-02	2.101e-01
LIGO-L	DN	7.822e-03	1.164e-04	-7.409e-03	-3.140e-02	-3.023e+00
	DY	7.829e-03	3.256e-04	-3.618e-03	5.864e-02	8.929e-01
VIRGO	DN	7.774e-03	-1.058e-03	-2.158e-02	-1.515e-01	-4.341e+00
	DY	7.784e-03	-7.645e-04	-1.650e-02	-4.328e-02	1.045e-01
TAMA300	DN	7.799e-03	-6.870e-04	-2.728e-02	-2.793e-01	-8.201e+00
	DY	7.804e-03	-5.106e-04	-2.417e-02	-2.092e-01	-5.196e+00
PERTH	DN	7.767e-03	-1.414e-03	-2.989e-02	-5.772e-01	-2.571e+01
	DY	7.787e-03	-8.045e-04	-1.897e-02	-3.514e-01	-1.692e+01
DET.	**Factor**			**Sph-SE**		
GEO600	DN	7.800e-03	-3.713e-04	-1.354e-02	-1.481e-01	-7.068e+00
	DY	7.772e-03	2.013e-02	9.025e-02	7.199e-01	1.549e+01
LIGO-H	DN	7.801e-03	-3.499e-04	-1.308e-02	-1.398e-01	-6.726e+00
	DY	7.773e-03	2.009e-02	8.999e-02	7.180e-01	1.545e+01
LIGO-L	DN	7.801e-03	-3.415e-04	-1.281e-02	-1.343e-01	-6.527e+00
	DY	7.775e-03	2.008e-02	8.970e-02	7.127e-01	1.527e+01
VIRGO	DN	7.801e-03	-3.533e-04	-1.310e-02	-1.396e-01	-6.713e+00
	DY	7.773e-03	2.008e-02	8.981e-02	7.148e-01	1.535e+01
TAMA300	DN	7.801e-03	-3.545e-04	-1.327e-02	-1.426e-01	-6.802e+00
	DY	7.774e-03	2.010e-02	8.987e-02	7.147e-01	1.532e+01
PERTH	DN	7.800e-03	-3.617e-04	-1.318e-02	-1.420e-01	-6.819e+00
	DY	7.775e-03	2.008e-02	8.980e-02	7.140e-01	1.530e+01

Table F.1: Signals of $\lambda = 1$ in Fig. 2.28, Fig. 2.29, Fig. 2.30.

Coefficients of Chebyshev Polynomials $T_r^*(x)$ for $x \in [0,1]$ (see Appendix E)						
		c_0	c_1	c_2	c_3	c_4
DET.	**Factor**			**Disc-shaped**		
GEO600	DN	7.813e-03	5.884e-03	-7.457e-04	-1.664e-02	-2.331e-01
	DY	7.814e-03	6.222e-03	7.712e-04	-7.274e-03	5.463e-01
LIGO-H	DN	7.810e-03	5.287e-03	-5.690e-04	2.589e-02	1.123e+00
	DY	7.812e-03	5.672e-03	1.580e-03	4.662e-02	2.375e+00
LIGO-L	DN	7.818e-03	5.804e-03	1.480e-03	2.082e-02	9.134e-01
	DY	7.819e-03	6.188e-03	3.584e-03	3.470e-02	1.643e+00
VIRGO	DN	7.803e-03	5.466e-03	-7.041e-03	-1.048e-01	-2.547e+00
	DY	7.804e-03	5.803e-03	-5.694e-03	-1.028e-01	-2.177e+00
TAMA300	DN	7.819e-03	6.461e-03	-3.859e-04	-5.921e-02	-1.832e+00
	DY	7.818e-03	6.751e-03	1.906e-04	-7.273e-02	-2.085e+00
PERTH	DN	7.815e-03	4.910e-03	9.035e-04	1.937e-02	-6.714e-01
	DY	7.816e-03	5.342e-03	4.100e-03	6.587e-02	1.669e+00
GEO600	DN	7.812e-03	5.926e-03	-1.092e-03	-2.158e-02	-3.036e-01
	DY	7.814e-03	5.864e-03	-1.118e-04	-3.870e-03	6.954e-01
LIGO-H	DN	7.810e-03	5.254e-03	-5.350e-04	3.242e-02	1.378e+00
	DY	7.812e-03	5.221e-03	7.923e-04	5.780e-02	2.760e+00
LIGO-L	DN	7.821e-03	5.859e-03	3.045e-03	4.681e-02	1.716e+00
	DY	7.821e-03	5.757e-03	3.175e-03	4.910e-02	2.128e+00
VIRGO	DN	7.801e-03	5.395e-03	-8.646e-03	-1.300e-01	-3.300e+00
	DY	7.803e-03	5.320e-03	-7.887e-03	-1.169e-01	-2.517e+00
TAMA300	DN	7.819e-03	6.449e-03	-1.612e-03	-8.618e-02	-2.755e+00
	DY	7.819e-03	6.341e-03	-1.290e-03	-8.118e-02	-2.338e+00
PERTH	DN	7.814e-03	4.773e-03	1.888e-04	1.235e-02	-9.737e-01
	DY	7.817e-03	4.772e-03	1.901e-03	4.769e-02	8.701e-01
GEO600	DN	7.813e-03	5.466e-03	4.722e-05	1.684e-03	-4.364e-03
	DY	7.373e-03	3.185e-02	2.206e-01	2.321e+00	5.866e+01
LIGO-H	DN	7.813e-03	5.448e-03	-6.662e-07	9.041e-04	-2.491e-02
	DY	7.374e-03	3.180e-02	2.201e-01	2.315e+00	5.850e+01
LIGO-L	DN	7.812e-03	5.443e-03	1.350e-06	1.614e-03	1.265e-02
	DY	7.377e-03	3.182e-02	2.201e-01	2.315e+00	5.848e+01
VIRGO	DN	7.812e-03	5.443e-03	-6.119e-05	2.634e-04	-3.686e-02
	DY	7.375e-03	3.181e-02	2.201e-01	2.315e+00	5.850e+01
TAMA300	DN	7.813e-03	5.473e-03	1.685e-04	1.872e-03	-2.306e-02
	DY	7.375e-03	3.183e-02	2.203e-01	2.318e+00	5.858e+01
PERTH	DN	7.812e-03	5.428e-03	-9.538e-05	3.402e-04	-4.158e-02
	DY	7.377e-03	3.181e-02	2.200e-01	2.314e+00	5.845e+01

Table F.2: Signals of $\lambda = 0$ in Fig. 2.28, Fig. 2.29, Fig. 2.30.

Coefficients of Chebyshev Polynomials $T_r^*(x)$ for $x \in [0,1]$ (see Appendix E)						
		$\mathbf{c_0}$	$\mathbf{c_1}$	$\mathbf{c_2}$	$\mathbf{c_3}$	$\mathbf{c_4}$
DET.	**Factor**			**Disc-shaped**		
GEO600	DN	7.820e-03	4.128e-04	-2.604e-02	-1.634e-01	-2.983e+00
	DY	7.825e-03	6.887e-04	-2.756e-02	-1.874e-01	-2.509e+00
LIGO-H	DN	7.814e-03	1.782e-04	-1.912e-02	-2.920e-02	6.509e-01
	DY	7.820e-03	5.218e-04	-1.974e-02	-3.654e-02	1.831e+00
LIGO-L	DN	7.828e-03	5.865e-04	-2.106e-02	-9.599e-02	-1.053e+00
	DY	7.833e-03	9.215e-04	-2.193e-02	-1.181e-01	-8.484e-01
VIRGO	DN	7.803e-03	-2.021e-04	-3.513e-02	-2.842e-01	-5.954e+00
	DY	7.808e-03	8.306e-05	-3.681e-02	-3.194e-01	-6.134e+00
TAMA300	DN	7.831e-03	7.116e-04	-3.234e-02	-3.057e-01	-7.253e+00
	DY	7.834e-03	9.197e-04	-3.533e-02	-3.675e-01	-8.501e+00
PERTH	DN	7.819e-03	2.697e-04	-1.368e-02	-3.690e-02	-2.661e+00
	DY	7.826e-03	6.863e-04	-1.253e-02	-4.642e-04	3.366e-01
GEO600	DN	7.820e-03	3.769e-04	-2.740e-02	-1.798e-01	-3.317e+00
	DY	7.823e-03	4.853e-04	-2.581e-02	-1.522e-01	-1.627e+00
LIGO-H	DN	7.813e-03	1.415e-04	-1.873e-02	-1.578e-02	1.083e+00
	DY	7.817e-03	2.855e-04	-1.675e-02	2.190e-02	3.320e+00
LIGO-L	DN	7.832e-03	7.085e-04	-1.862e-02	-5.912e-02	3.483e-02
	DY	7.833e-03	7.386e-04	-1.856e-02	-5.927e-02	6.658e-01
VIRGO	DN	7.798e-03	-3.571e-04	-3.777e-02	-3.217e-01	-7.000e+00
	DY	7.801e-03	-2.729e-04	-3.665e-02	-3.045e-01	-5.791e+00
TAMA300	DN	7.830e-03	6.392e-04	-3.483e-02	-3.531e-01	-8.771e+00
	DY	7.831e-03	6.782e-04	-3.430e-02	-3.480e-01	-8.138e+00
PERTH	DN	7.817e-03	1.663e-04	-1.361e-02	-3.491e-02	-2.818e+00
	DY	7.822e-03	3.289e-04	-1.133e-02	1.559e-02	7.634e-02
GEO600	DN	7.819e-03	3.565e-04	-2.106e-02	-1.096e-01	-2.234e+00
	DY	7.680e-03	2.627e-02	1.498e-01	1.394e+00	3.275e+01
LIGO-H	DN	7.818e-03	3.505e-04	-2.100e-02	-1.096e-01	-2.241e+00
	DY	7.682e-03	2.623e-02	1.495e-01	1.392e+00	3.271e+01
LIGO-L	DN	7.819e-03	3.508e-04	-2.094e-02	-1.078e-01	-2.159e+00
	DY	7.684e-03	2.624e-02	1.495e-01	1.392e+00	3.270e+01
VIRGO	DN	7.819e-03	3.587e-04	-2.087e-02	-1.069e-01	-2.137e+00
	DY	7.682e-03	2.623e-02	1.495e-01	1.391e+00	3.269e+01
TAMA300	DN	7.819e-03	3.623e-04	-2.100e-02	-1.105e-01	-2.274e+00
	DY	7.683e-03	2.625e-02	1.496e-01	1.393e+00	3.272e+01
PERTH	DN	7.818e-03	3.502e-04	-2.088e-02	-1.079e-01	-2.203e+00
	DY	7.683e-03	2.623e-02	1.495e-01	1.391e+00	3.268e+01

Table F.3: Signals of $\lambda \sim \mathcal{U}[0,1]$ in Fig. 2.28, Fig. 2.29, Fig. 2.30.

Coefficients of Chebyshev Polynomials $T_r^*(x)$ for $x \in [0,1]$ (see Appendix E)						
		$\mathbf{c_0}$	$\mathbf{c_1}$	$\mathbf{c_2}$	$\mathbf{c_3}$	$\mathbf{c_4}$
DET.	**Factor**			**Disc-shaped**		
GEO600	DN	7.812e-03	5.342e-05	-2.076e-02	-1.306e-01	-3.732e+00
	DY	7.821e-03	3.968e-04	-1.959e-02	-8.008e-02	-2.313e-01
LIGO-H	DN	7.808e-03	-2.052e-05	-1.323e-02	-1.916e-02	-1.614e+00
	DY	7.820e-03	4.128e-04	-1.069e-02	5.826e-02	2.991e+00
LIGO-L	DN	7.823e-03	3.199e-04	-1.501e-02	-5.192e-02	-1.346e+00
	DY	7.831e-03	6.666e-04	-1.443e-02	-2.495e-02	9.221e-01
VIRGO	DN	7.792e-03	-5.557e-04	-2.847e-02	-2.120e-01	-5.055e+00
	DY	7.799e-03	-2.702e-04	-2.879e-02	-1.979e-01	-3.096e+00
TAMA300	DN	7.820e-03	1.604e-04	-2.860e-02	-2.674e-01	-7.105e+00
	DY	7.822e-03	3.319e-04	-3.093e-02	-2.926e-01	-6.633e+00
PERTH	DN	7.805e-03	-2.098e-04	-1.605e-02	-1.924e-01	-1.058e+01
	DY	7.820e-03	3.804e-04	-1.016e-02	-4.473e-02	-3.358e+00
DET.				**Spherical-GC**		
GEO600	DN	7.812e-03	3.165e-05	-2.150e-02	-1.335e-01	-3.575e+00
	DY	7.819e-03	2.595e-04	-1.763e-02	-5.172e-02	2.627e-01
LIGO-H	DN	7.808e-03	-4.212e-05	-1.270e-02	-7.238e-03	-1.335e+00
	DY	7.817e-03	2.605e-04	-7.583e-03	1.023e-01	3.703e+00
LIGO-L	DN	7.829e-03	4.831e-04	-1.225e-02	-1.347e-02	-2.834e-01
	DY	7.832e-03	5.781e-04	-1.078e-02	2.498e-02	1.928e+00
VIRGO	DN	7.786e-03	-7.376e-04	-3.139e-02	-2.519e-01	-6.113e+00
	DY	7.792e-03	-5.592e-04	-2.844e-02	-1.895e-01	-3.103e+00
TAMA300	DN	7.817e-03	3.882e-05	-3.158e-02	-3.167e-01	-8.493e+00
	DY	7.820e-03	1.281e-04	-3.009e-02	-2.839e-01	-6.710e+00
PERTH	DN	7.802e-03	-3.342e-04	-1.675e-02	-2.099e-01	-1.151e+01
	DY	7.813e-03	3.042e-05	-1.042e-02	-7.076e-02	-5.284e+00
DET.				**Spherical-SE**		
GEO600	DN	7.812e-03	5.986e-05	-1.670e-02	-1.046e-01	-3.904e+00
	DY	7.722e-03	2.381e-02	1.251e-01	1.111e+00	2.544e+01
LIGO-H	DN	7.811e-03	5.499e-05	-1.662e-02	-1.035e-01	-3.837e+00
	DY	7.723e-03	2.376e-02	1.248e-01	1.107e+00	2.534e+01
LIGO-L	DN	7.812e-03	5.292e-05	-1.651e-02	-1.005e-01	-3.715e+00
	DY	7.725e-03	2.375e-02	1.245e-01	1.102e+00	2.517e+01
VIRGO	DN	7.812e-03	6.019e-05	-1.651e-02	-1.014e-01	-3.769e+00
	DY	7.724e-03	2.375e-02	1.246e-01	1.104e+00	2.524e+01
TAMA300	DN	7.812e-03	6.640e-05	-1.658e-02	-1.033e-01	-3.826e+00
	DY	7.724e-03	2.377e-02	1.248e-01	1.106e+00	2.530e+01
PERTH	DN	7.811e-03	5.357e-05	-1.652e-02	-1.023e-01	-3.825e+00
	DY	7.725e-03	2.376e-02	1.247e-01	1.105e+00	2.527e+01

Table F.4: Signals of $\lambda = f(\iota)$ in Fig. 2.28, Fig. 2.29, Fig. 2.30.

Coefficients of Chebyshev Polynomials $T_r^*(x)$ for $x \in [0,1]$ (see Appendix E)							
DET	**Pop.**	**Factor**	$\mathbf{c_0}$	$\mathbf{c_1}$	$\mathbf{c_2}$	$\mathbf{c_3}$	$\mathbf{c_4}$
6	Disc	DN	7.805e-03	-2.098e-04	-1.605e-02	-1.924e-01	-1.058e+01
		DY	7.820e-03	3.804e-04	-1.016e-02	-4.473e-02	-3.358e+00
	Sph-SE	DN	7.811e-03	5.357e-05	-1.652e-02	-1.023e-01	-3.825e+00
		DY	7.725e-03	2.376e-02	1.247e-01	1.105e+00	2.527e+01
1-6	Disc	DN	7.822e-03	3.850e-04	-2.604e-02	-9.801e-02	-8.352e-01
		DY	7.830e-03	8.249e-04	-2.626e-02	-1.161e-01	-3.734e-02
	Sph-SE	DN	7.809e-03	6.114e-05	-3.426e-02	-2.201e-01	-3.695e+00
		DY	7.636e-03	2.985e-02	1.842e-01	1.782e+00	4.261e+01
1-2-6	Disc	DN	7.818e-03	4.282e-04	-3.642e-02	-6.271e-02	5.145e+00
		DY	7.826e-03	9.018e-04	-3.945e-02	-1.805e-01	1.940e+00
	Sph-SE	DN	7.814e-03	3.663e-04	-4.438e-02	-2.760e-01	-2.912e+00
		DY	7.566e-03	3.410e-02	2.271e-01	2.279e+00	5.555e+01
1-2-3-6	Disc	DN	7.789e-03	-3.782e-04	-7.119e-02	-4.607e-01	1.405e-02
		DY	7.812e-03	5.741e-04	-7.055e-02	-6.354e-01	-8.690e+00
	Sph-SE	DN	7.798e-03	6.389e-06	-6.805e-02	-5.061e-01	-4.018e+00
		DY	7.489e-03	3.746e-02	2.654e-01	2.750e+00	6.816e+01
1-2-3-4-6	Disc	DN	7.736e-03	-2.038e-03	-1.247e-01	-1.301e+00	-2.302e+01
		DY	7.776e-03	-6.098e-04	-1.151e-01	-1.340e+00	-2.856e+01
	Sph-SE	DN	7.781e-03	-4.798e-04	-9.706e-02	-9.521e-01	-1.517e+01
		DY	7.488e-03	3.796e-02	2.684e-01	2.772e+00	6.855e+01
1-2-3-4-5-6	Disc	DN	7.783e-03	-6.760e-04	-1.356e-01	-1.655e+00	-3.633e+01
		DY	7.832e-03	1.394e-03	-1.139e-01	-1.518e+00	-3.674e+01
	Sph-SE	DN	7.793e-03	-1.447e-04	-1.134e-01	-1.294e+00	-2.630e+01
		DY	7.361e-03	4.144e-02	3.145e-01	3.382e+00	8.556e+01

Table F.5: Signals of $\lambda = f(\iota)$ in Fig. 2.37.

Appendix G

Discrete signals

Continuous time signals are often discretised to be recorded and analysed digitally; the higher is the sampling frequency the better the resemblance between the analogical and reconstructed digital signals. A discrete-time signal is generated by sampling from a continuous signal $x(t)$ as follows:

$$x[n] \equiv x(t)|_{t=nT} = x(nT) \quad n = 0, 1, 2, ... \tag{G.1}$$

where T is the *sampling interval*, the time interval between two consecutive samples, and the inverse of the sampling interval $f_s = 1/T$ is the *sampling frequency*. The continuous time variable t is related to the discrete time variable n as follows:

$$t_n = nT = \frac{n}{f_s} = \frac{2\pi}{\Omega_s} n \quad \text{where} \quad n = 0, 1, 2, ... \tag{G.2}$$

where $\Omega_s = 2\pi f_s$ is the *angular sampling frequency*.

Let us now consider a generic continuous exponential sinusoidal signal defined in time as:

$$x(t) = A\ e^{-t/\tau} \sin(\Omega_0 t + \phi), \tag{G.3}$$

and the transformation of the parameters from the continuous to the discrete time-domain:

$$x[n] = A \exp\left[-\frac{nT}{\tau}\right] \sin(\Omega_0 nT + \phi) \tag{G.4a}$$

$$= A \exp\left[-\frac{2\pi}{\Omega_s \tau} n\right] \sin\left(\frac{2\pi\Omega_0}{\Omega_s} n + \phi\right) \tag{G.4b}$$

$$= A \exp[-an] \sin(w_0 n + \phi) \tag{G.4c}$$

where $a = 2\pi/(\Omega_s \tau)$ is the inverse of the discrete damping time (in units of samples^{-1}) and $w_0 = 2\pi\Omega_0/\Omega_s = \Omega_0 T$ is the normalised digital angular frequency (in units of rad sample^{-1}). Fig. G.1 compares the continuous time domain with its discretised version.

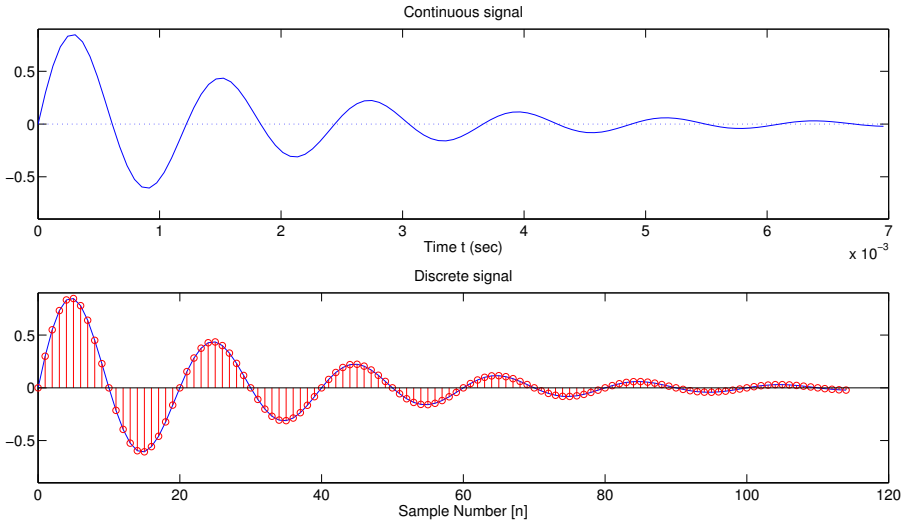

Figure G.1: Comparison of a continuous exponentially damped sinusoid (Eq. G.3) and its discretised version (Eq. G.4). The upper box shows the original continuous signal and the lower box shows the discrete version as a result of the sampling process. Parameters: $A = 1$, $\Omega_s/\Omega_0 = 20, w_0 = \pi/10$ rad sample^{-1}, a $= 1/30$ samples^{-1} and $\phi = 0$.

A discrete-time signal $\{x[n]\}$ is defined as a set of values uniformly distributed in time. It may be represented as a sequence of values in which the time variable takes integer values in the range $n \in (-\infty, \infty)$ as:

$$\{x[n]\} = \{..., x[-2], x[-1], x[0], x[1], x[2], ...\} \tag{G.5}$$

When only the values after the sample $n \geq k$ need to be considered, the signal can be multiplied with the unitary step function $\mu[n-k]$. Fig. G.2 shows an unconstrained signal defined for a different range of values.

$$\mu[n-k] = \begin{cases} 1 & n \geq k, \\ 0 & n < k. \end{cases} \tag{G.6}$$

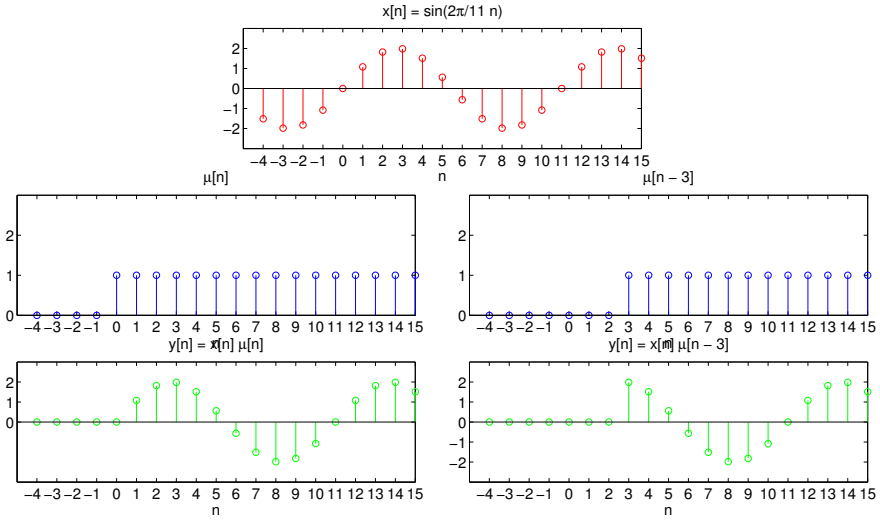

Figure G.2: Truncation of a signal by a step function of the form $\mu[n-k]$. The three panes on the left show the truncation of a sinusoidal signal by $\mu[n-0]$. The three panes on the right show the truncation of the signal at $k = 3$ by the unitary step function $\mu[n-k]$.

To consider signals the signal can be multiplied by the step function $\mu[n-0] = \mu[n]$.

Appendix H

Signal and noise in the frequency-domain

In this appendix the instrumental error probability distribution, both in the time and frequency domain, is studied. The instrumental noise is usually assumed to be stationary and gaussian of zero mean and thus, when a gravitational wave signal is suspect, is the same as to say that the most probable thing is to acquire the model-predicted value for each datum of the set.

The real-valued discrete time sequence $\{s[n]\}$ acquired can be transformed into the equivalent representation in the frequency domain $\{\tilde{s}[k]\}$ by means of the Discrete Fourier Transform (DFT). The transformation of a N-point discrete time sequence results in a sequence of N complex numbers, where each complex number represents one harmonic of the signal. Taking the generic symbol $\tilde{\square}$ for either $\tilde{s}$, $\tilde{h}$ or $\tilde{n}$:

$$\square_{\Re}[k] = \Re\{\tilde{\square}[k]\}, \quad \square_{\Im}[k] = \Im\{\tilde{\square}[k]\}, \quad k = 0, ..., N-1, \tag{H.1}$$

or represented in their phasor form as:

$$\tilde{n}_k \equiv N[k]\angle\theta_{\tilde{n}}[k], \quad \text{where} \quad N[k] = n^2_{\Re}[k] + n^2_{\Im}[k] \quad \text{and} \quad \theta_{\tilde{n}}[k] = \arctan(n_{\Im}/n_{\Re})$$
$$\tilde{s}_k \equiv S[k]\angle\theta_{\tilde{s}}[k], \quad \text{where} \quad S[k] = s^2_{\Re}[k] + s^2_{\Im}[k] \quad \text{and} \quad \theta_{\tilde{s}}[k] = \arctan(s_{\Im}/s_{\Re})$$
$$\tilde{h}_k \equiv H[k]\angle\theta_{\tilde{h}}[k], \quad \text{where} \quad H[k] = h^2_{\Re}[k] + h^2_{\Im}[k] \quad \text{and} \quad \theta_{\tilde{h}}[k] = \arctan(h_{\Im}/h_{\Re})$$

Assuming that the discrepancy between the signal and the data acquired is only the instrumental noise, for the kth frequency bin:

$$\tilde{n}[k] = \tilde{s}[k] - \tilde{h}[k] \begin{cases} n_{\Re}[k] = s_{\Re}[k] - h_{\Re}[k] \\ n_{\Im}[k] = s_{\Im}[k] - h_{\Im}[k] \end{cases} \qquad k = 0, ..., K-1. \tag{H.2}$$

H.1 Cartesian representation: Real and imaginary coefficients

The probability of getting the noise complex vector $\tilde{n}[k]$ is given by a bivariate normal probability distribution of variables $n_{\Re}[k]$ and $n_{\Im}[k]$:

$$p(\tilde{n}[k]|\tilde{\sigma}[k], I) = p(n_{\Re}[k], n_{\Im}[k]|\sigma_{\Re}[k], \sigma_{\Im}[k], I) \sim N(\mu[k], \mathbf{\Sigma}[k]), \tag{H.3}$$

$$\text{with} \quad \mu[k] = [0, 0] \quad \text{and} \quad \mathbf{\Sigma} = \begin{bmatrix} \sigma^2_{\Re}[k] & \sigma_{\Re}[k]\sigma_{\Im}[k] \\ \sigma_{\Re}[k]\sigma_{\Im}[k] & \sigma^2_{\Im}[k] \end{bmatrix}. \tag{H.4}$$

Generically, the bivariate normal distribution can be written as (see (140)):

$$p(n_{\Re}[k], n_{\Im}[k]|\sigma_{\Re}[k], \sigma_{\Im}[k], \rho, I) = \frac{1}{2\pi\sigma_{\Re}\sigma_{\Im}\sqrt{1-\rho^2}} \exp\left[-\frac{z[k]}{2(1-\rho^2)}\right] \tag{H.5}$$

where $\rho \equiv \text{cor}(n_{\Re}[k], n_{\Im}[k]) = \sigma_{\Re\Im}[k]/(\sigma_{\Re}[k]\sigma_{\Im}[k])$ is the correlation coefficient between the variables and

$$z[k] \equiv \frac{(s_{\Re}[k] - h_{\Re}[k])^2}{\sigma^2_{\Re}[k]} - \frac{2\rho\,(s_{\Re}[k] - h_{\Re}[k])(s_{\Im}[k] - h_{\Im}[k])}{\sigma_{\Re}[k]\sigma_{\Im}[k]} + \frac{(s_{\Im}[k] - h_{\Im}[k])^2}{\sigma^2_{\Im}[k]}. \tag{H.6}$$

For the case of gaussian and stationary noise in the time domain there is no correlation between the real and imaginary coefficients, so that $\sigma_{\Re\Im}[k] = 0$ and $\rho = 0$. The uncertainty is the same for the two variables $\sigma_{\Re}[k] = \sigma_{\Im}[k] = \sigma[k]$ and Eq. H.5 then reduces to:

$$p(n_{\Re}[k], n_{\Im}[k]|\sigma[k], I) = \frac{1}{2\pi\sigma^2[k]} \exp\left[-\frac{(s_{\Re}[k] - h_{\Re}[k])^2 + (s_{\Re}[k] - h_{\Im}[k])^2}{2\sigma^2[k]}\right]. \tag{H.7}$$

H.2 Polar representation: Magnitude and phase

A complex vector $\tilde{c}$ corresponding to the harmonic of the spectrum can be alternatively represented with cartesian coordinates $\tilde{c} \equiv (c_{\Re}, c_{\Im})$ or polar coordinates of magnitude and phase $C\angle\theta$, related by the equations $c_{\Re} = C\cos\theta$ and $c_{\Im} = C\sin\theta$. To transform the joint probability distribution of $p(c_{\Re}, c_{\Im})$ into $p(C, \theta)$ can be done by equating the volumes under the joint probability density curves:

$$p(C,\theta)\, dC\, d\theta = p(c_{\Re}, c_{\Im})\, dc_{\Re}\, dc_{\Im} \tag{H.8}$$

$$p(C,\theta) = p(c_{\Re}, c_{\Im}) \left| \frac{dc_{\Re}}{dC} \frac{dc_{\Im}}{d\theta} \right| = C\, p(c_{\Re}, c_{\Im}) \tag{H.9}$$

In the following, the magnitude and phase probability distribution densities are derived, in the absence and in the presence of the signal (see (141)).

H.2.1 Absence of the signal: noise only acquired

In the absence of signal ($\tilde{h}[k] = 0; h_{\Re}[k] = h_{\Im}[k] = 0$) the spectrum of the data acquired $\{\tilde{s}\}$ includes only noise $\{\tilde{n}\}$. The complex vector $\tilde{n}[k]$ corresponding to the kth frequency bin points in any direction and its most probable magnitude depends on the instrumental noise level. Eq. H.7 then reduces to:

$$p(\tilde{s}[k]|\sigma[k], I) = p(s_{\Re}[k], s_{\Im}[k]|\sigma[k], I) = \frac{1}{2\pi\sigma^2[k]} \exp\left[\frac{s^2_{\Re}[k] + s^2_{\Im}[k]}{\sigma^2[k]}\right] \tag{H.10}$$

which, following Eq. H.9, transforms into another bivariate distribution function of variables magnitude and phase $(S[k], \theta_{\tilde{s}}[k])$:

$$p(S[k], \theta_{\tilde{s}}[k]|\sigma[k], I) = \frac{S[k]}{2\pi\sigma^2[k]} \exp\left[-\frac{S^2[k]}{2\sigma^2[k]}\right]. \tag{H.11}$$

To find the univariate probability density functions $p(S[k]|\cdot)$ and $p(\theta_{\tilde{s}}[k]|\cdot)$, we can marginalise Eq. H.11 over all possible phases $\theta_{\tilde{s}}[k]$ in the range $[0, 2\pi)$ to get:

$$p(S[k]|\sigma[k], I) = \int_0^{2\pi} p(S[k], \theta_{\tilde{s}}[k])\, d(\theta_{\tilde{s}}[k]) = \frac{S[k]}{\sigma^2[k]} \exp\left[-\frac{S^2[k]}{2\sigma^2[k]}\right]. \tag{H.12}$$

This is called *Rayleigh* distribution and it is defined only for positive values. As $\sigma[k]$ increases, the distribution flattens out and the peak decreases moving to the right (see Fig. H.1); the most probable value (the mode) is $S[k] = \sigma[k]$. The distribution of the phase $\mathrm{p}(\theta_{\tilde{d}}[k]|\cdot)$ can be calculated similarly by marginalising Eq. H.11 over $S[k]$.

$$p(\theta_{\tilde{s}}[k]|\sigma_k, I) = \int_0^\infty p(S[k], \theta_{\tilde{s}}[k])\, dS[k] = \frac{1}{2\pi}. \tag{H.13}$$

This is an expected result: for purely gaussian noise, the phase of each one of the harmonics has a random phase distributed uniformly $\theta_{\tilde{s}}[k] \sim \mathcal{U}[0, 2\pi)$.

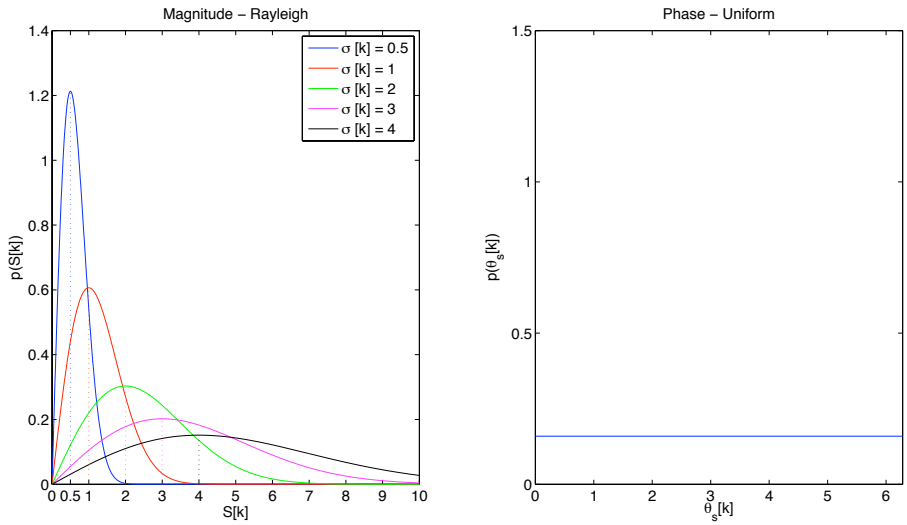

Figure H.1: When the signal is absent and only noise is measured the distribution of the magnitude $S[k]$ follows a *Rayleigh* distribution, whereas the phase distribution is uniform. The panel on the left shows various distributions for different values of $\sigma[k]$. The panel on the right is the uniform distribution for the phase $\theta_{\tilde{s}}[k]$.

H.2.2 Presence of the signal: signal + noise acquired

Let us consider now the case where the acquired data $\{\tilde{s}[k]\}$ is not only noise but includes a signal modeled as $\{\tilde{h}[k]\}$ too. What are the probability distributions of the magnitude and phase for a particular frequency bin? The likelihood of measuring $\tilde{s}[k]$ assuming that $\tilde{h}[k]$ is the true value is given by:

$$p(\tilde{s}[k]|\tilde{h}[k],\sigma[k]) = p(s_{\Re}[k], s_{\Im}[k]|h_{\Re}[k], h_{\Im}[k], \sigma[k]) \tag{H.14}$$

$$= \frac{1}{2\pi\sigma^2[k]} \exp\left[-\frac{(s_{\Re}[k]-h_{\Re}[k])^2 + (s_{\Im}[k]-h_{\Im}[k])^2}{2\sigma[k]^2}\right] \tag{H.15}$$

$$= \frac{1}{2\pi\sigma^2[k]} \exp\left[-\frac{s^2_{\Re}[k] + s^2_{\Im}[k] + h^2_{\Re}[k] + h^2_{\Im}[k] - 2(s_{\Re}[k]h_{\Re}[k] + s_{\Im}[k]h_{\Im}[k])}{2\sigma^2[k]}\right] \tag{H.16}$$

$$= \frac{1}{2\pi\sigma^2[k]} \exp\left[-\frac{S^2[k] + H^2[k] - 2(\tilde{s}[k]\cdot\tilde{h}[k])}{2\sigma^2[k]}\right] \tag{H.17}$$

$$= \frac{1}{2\pi\sigma^2[k]} \exp\left[-\frac{S^2[k] + H^2[k] - 2S[k]H[k]\cos(|\theta_{\tilde{h}}[k] - \theta_{\tilde{s}}[k]|)}{2\sigma^2[k]}\right]. \tag{H.18}$$

Introducing $\alpha[k] = |\theta_{\tilde{s}}[k] - \theta_{\tilde{h}}[k]|$ the joint probability is:

$$p(S[k],\alpha[k]|\tilde{h}[k],\tilde{\sigma}[k]) = p(\tilde{s}[k]|\tilde{h}[k],\sigma[k]) \tag{H.19}$$

$$= \frac{S[k]}{2\pi\sigma^2[k]} \exp\left[-\frac{S^2[k] + H^2[k] - 2S[k]H[k]\cos\alpha[k]}{2\sigma^2[k]}\right]. \tag{H.20}$$

To calculate the probability of only the magnitude, the above expression can be integrated out over all possible values of $\alpha[k]$ in the range $[0, 2\pi)$:

$$p(S[k]|\tilde{h}[k],\tilde{\sigma}[k]) = \int_0^{2\pi} p(S[k],\alpha[k]|\tilde{h}[k],\sigma[k])d(\alpha[k]) \tag{H.21}$$

$$= \frac{1}{2\pi}\frac{S[k]}{\sigma^2[k]} \exp\left[-\frac{S^2[k] + H^2[k]}{2\sigma^2[k]}\right] \int_0^{2\pi} \exp\left[\frac{S[k]H[k]}{\sigma[k]^2}\cos\alpha[k]\right] d(\alpha[k]). \tag{H.22}$$

Both variables are entangled in the exponential within the integral, which is related to the Bessel function of the first kind. In particular:

$$I_0(z) = \frac{1}{\pi}\int_0^{\pi} e^{\pm z\cos\theta}\, d\theta = \frac{1}{\pi}\int_0^{\pi} \cosh(z\cos\theta)\, d\theta, \tag{H.23}$$

is called the *modified* Bessel function of the first kind and zeroth order [1]. Then, Eq. H.21 reduces to:

$$p(S[k]|\tilde{h}[k],\sigma[k]) = \frac{S[k]}{\sigma^2[k]}\exp\left[-\frac{S^2[k]+H^2[k]}{2\sigma^2[k]}\right] I_0\left(\frac{S[k]H[k]}{\sigma^2[k]}\right). \tag{H.24}$$

This probability density function is called the *Rician* distribution in honour of S.O. Rice of Bell Telephone Laboratories, who developed and discussed the properties of this distribution in a pioneering series of papers on random noise (142; 143).

Expression of Eq. H.19 can be marginalised over $S[k]$ to get the probability distribution of $\alpha[k]$, which is the difference in phase between the measured and modeled complex vector. It is not expected to be a Gaussian probability function is not expected because phase values are the result of a non-linear function (arctan). In fact, the derivation to marginalise over $S[k]$ is not trivial and only the result is shown below:

$$p(\alpha[k]|\tilde{h}[k],\tilde{\sigma}[k]) = \int_0^\infty p(S[k],\alpha[k]|\tilde{h}[k],\tilde{\sigma}[k])d(S[k]) \tag{H.25}$$

$$= \frac{1}{2\pi}\exp\left(-\frac{S^2[k]}{2\sigma^2[k]}\right)\left[1+\frac{S[k]}{\sigma[k]}\sqrt{2\pi}\cos(\alpha[k])\exp\left(\frac{S^2[k]\cos^2(\alpha[k])}{2\sigma^2[k]}\right)\left[1-Q\left(\frac{S[k]\cos\alpha[k]}{\sigma[k]}\right)\right]\right], \tag{H.26}$$

where the function $Q(\cdot)$ is closely related to functions erf$(\cdot)$ and erfc$(\cdot)$:

$$Q(x) = \frac{1}{2}\text{erfc}\left(\frac{x}{\sqrt{2}}\right) = \frac{1}{2}\left[1-\text{erf}\left(\frac{x}{\sqrt{2}}\right)\right] \tag{H.27}$$

$$\text{erfc}(x) = \frac{2}{\sqrt{\pi}}\int_x^\infty e^{-y^2}\,dy = 2Q(x\sqrt{2}). \tag{H.28}$$

Fig. H.2 shows the Rician distribution for the magnitude in Eq. H.24 and the phase distribution given in Eq. H.25.

[1] The n^{th} order modified Bessel functions $I_n(x)$ are ordinary n^{th} order Bessel function $J_n(x)$ with a purely imaginary argument, see (**?**). The Bessel functions of the first kind are related to the modified Bessel functions of the first kind: $I_n(z) = i^{-n}J_n(iz)$. Unlike the ordinary Bessel functions J_n, which are oscillating as functions of a real argument, the modified Bessel functions I_n are exponentially growing functions.

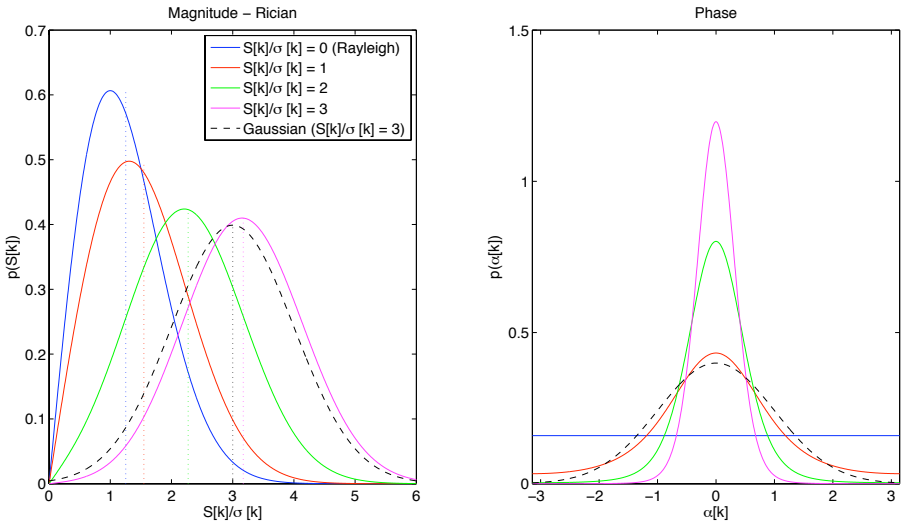

Figure H.2: For the kth frequency bin of spectra containing noise and signal, the magnitude $S[k]$ of each complex vector ($\tilde{s}[k] \equiv S[k]\angle\theta_{\tilde{s}}[k]$) follows a Rician probability density distribution. When the signal is very weak the distribution of $S[k]$ reduces to the *Rayleigh* distribution and the phase distribution reduces to an uniform one. For a signal of intensity $S[k]/\sigma[k] = 3$ the magnitude and phase distributions have been compared against a gaussian distribution of the same SNR.

(H.29)

The general expression for the distribution $p(\alpha[k]|\tilde{h}[k], \tilde{\sigma}[k])$ given in H.21 is complicated but it can be simplified for two limits, when the signal in comparison with the noise is a) considerably smaller, $S[k] \ll \sigma[k]$, and b) considerably bigger, $S[k] \gg \sigma[k]$ (144).

In the first one, when the measurement hardly contains any signal, $S[k] \approx 0$, Eq. H.25 reduces to:

$$p(\alpha[k]|0, \sigma[k]) = \begin{cases} \frac{1}{2\pi} & -\pi < \alpha[k] < \pi, \\ 0 & \text{otherwise}, \end{cases} \tag{H.30}$$

showing that in the absence of signal, as in Eq. H.13, the complex vector of the noise 'points in all directions' with the same probability.

When the signal is much bigger than the noise, $S[k] \gg \sigma[k]$ (very large SNR), the deviation in phase $\alpha[k]$ will be very small. The term $[1 - Q(\cdot)]$ in Eq. H.25 will approximate to 1 and the second term in the brackets will dominate the first term, reducing the equation to:

$$p(\alpha[k]|\tilde{h}[k], \tilde{\sigma}[k]) \approx \frac{S[k]\cos(\alpha[k])}{\sigma[k]\sqrt{2\pi}} \exp\left[\frac{-S^2[k](1-\cos^2(\alpha[k]))}{2\sigma^2[k]}\right] \tag{H.31}$$

$$\approx \frac{1}{\sqrt{2\pi}(\sigma[k]/S[k])} \exp\left[-\frac{\alpha[k]^2}{2(\sigma[k]/S[k])^2}\right]. \tag{H.32}$$

The probability distribution of the phase difference can then be considered as a zero mean Gaussian when $S[k] \gg \sigma[k]$. This is not surprising, because when the signal value is large, deviations parallel to the complex coefficient can be ignored.

Appendix I

MATLAB code - Nested Sampling Algorithm

The procedural steps of the nested sampling algorithm are standard and well defined. Adapting them efficiently to the problem at hand, however, is not always easy. The accuracy required and the dimensions of the parameter space P dictate the number of necessary objects N and the length of the Markov chains to look for new object candidates. The crux of the algorithm is the procedure to find a new object to replace the one with the lowest likelihood. This can be done in many ways, but choosing an efficient one that will sweep all the relevant regions of the parameter space where the evidence is concentrated while keeping the computation time to a minimum, is desired. In this work, a standard procedure has been followed: one of the objects, save the one with lowest likelihood, is chosen and evolved through a Markov chain to find a suitable candidate with a higher likelihood.

In the following the steps of the nested sampling algorithm are presented as pseudo Matlab code language used throughout this work. The core of the code is based on the section 9.2.4 of 'Programming nested sampling in C' of (114). See also Appendix in (115).

For real applications evidence and likelihood values can range various orders of magnitude. It is convenient to work with the logarithms of those values instead. A repeateadly used function to add to numbers through their logarithms is presented at the end.

I.1 Matlab pseudo-code - working with logarithms

The huge range of values for the likelihood and the prior mass make the use of logarithms necessary to handle the calculations; operations like multiplications simplify and become additions, whereas other simple operations like additions become more complicated. In the following, the steps of the nested sampling algorithm followed in this work are presented as Matlab pseudo-code.

1. *Define number of objects N, where $n \in [1, N]$.*

   ```
   N = 200; \% for example
   ```

2. *Define number of variables P, where $p \in [1, P]$.*

   ```
   P = 10; \% for example
   ```

3. *Define number of links of the Markov Chain M, where $m \in [1, M]$.*

   ```
   M = 20; \% for example
   ```

4. *Allocate memory for speed - it is convenient to define each object as a structure of fields (variables, log likelihood, log weight) in order to replace, interchange and restore original values during the implementation of the algorithm.*

   ```
   Obj(N).Theta(P) = 0;
   Obj(N).logL = 0;
   Obj(N).logW = 0;
   ```

5. *Draw a set of N points $\{\boldsymbol{\Theta}_n\}$ from prior $\pi(\boldsymbol{\Theta})$ and calculate their log likelihood $\{\log \mathcal{L}(\boldsymbol{\Theta}_n)\}$. For the case of variables with independent priors:*

   ```
   for n = 1:N
   \% draw a point from the P-dimensional space.
   [Obj(n).Theta] = priorpdf(pdf parameters); \% customize prior pdf
   \% calculate the log likelihood of that point
   Obj(n).logL = loglkh([Obj(n).Theta]);
   end
   ```

6. *Initialise variables*

```
logZ = -1e-30; \% so that $Z = 0$
logw = 0; \% weight of the worst object at each iteration
c = 0.1; \% The covariance matrix of proposal is
             \% the covariance matrix of the objects
t = 0; \% number of iterations
notfound = true;
```

7. *Compute outermost interval of prior mass:*

```
logw = log(1 - exp(-1/N));
```

8. *NESTED SAMPLING LOOP - continue for a fixed number of iterations or until the evidence contribution for a new iteration is negligible. The algorithm is stopped when the new contribution to the evidence is smaller than a fraction 1/e^5 $\approx$ 1/150 of the evidence value accumulated so far.*

```
WHILE max([Obj.logL]) + logw < Z * exp(-5)
```

   - Find the object with the lowest likelihood value

```
worst = find([Obj.logL] == min([Obj.logL]);
\% we save the object to be replaced in case candidates
\% are not successful and need to revert back to original situation
keep = Obj(worst);
```

   - Compute weight of the worst object in collection (W = L * w)

```
Obj(worst).logW = Obj(worst).logL + logw;
```

   - Update evidence ($Z = Z + W$)

```
logZ = AddUsingLogarithms(logZ,Obj(worst).logW);
```

   - Record the worst object to produce posterior samples if necessary

```
Samples(k) = Obj(worst);
```

   - Replace worst object by a copy of another random object

```
copy = unidrnd(N); \% choose any, apart from worst
Obj(worst) = Obj(copy);
```

   - Evolve object (through a Markov Chain, for example).

```
WHILE notfound
    for m = 1:M \% try M trials (links) of the Markov chain
      mu = Obj(worst);
      sigma = cov([Obj.Theta(1)',...,Obj.Theta(P)']);
      new = mvnrnd(mu,c*sigma);
      \% Replace worst with new only if conditions are fullfilled
      if [loglkh(new) > Obj(worst).logL] &...
       [prior(new)/prior(worst) > unifrnd(0,1,1,1)]
      Obj(worst) = Obj(new);
      notfound = false;
      end
    end
else \% means none of the M attemps/candidates have been accepted
    Obj(worst) = Keep; \% revert to situation before the M trials
    copy = unidrnd(N); \% choose another starting point
    Obj(worst) = Obj(copy);
 end
```

- Prior mass shrinks with factor $e^{-1/N}$ at each iteration

```
logw = logw - 1/N;
```

- Add iteration number

```
t = t + 1;
```

```
end
```

9. Add the contribution of the remaining points (if the algorithm has not been stopped prematurely this should be a very small contribution and therefore to consider the last tiny contribution is not crucial).

```
for n = 1:N
    Obj(n).logW = logw + Obj(n).logL;
    logZ = AddUsingLogarithms(logZ,Obj(n).logW);
    Samples(k+n) = Obj(n);
end
```

```
*********************************************************
function [c] = AddUsingLogarithms(a,b)
    if a > b
    c = a + log(1+exp(b-a));
    else
        c = b + log(1+exp(a-b));
    end
*********************************************************
```

I.2 Matlab code used for hypothesis comparison and parameter estimation - working with logarithms

In the following the Matlab code used for the parameter estimation and model comparison, for the case of 7 parameters in total corresponding to the H_{1U} hypothesis. First the main script is presented. The functions called are shown after.

```
% MODEL COMPARISON & PARAMETER ESTIMATION SCRIPT
% Unknown Source location (incoming direction)
% f-mode (N1): 5 parameters (VXN1)
% Source location: 2 parameters

% THE 5 PARAMETERS (h0,f0,tau,lambda,psi)
% h0 is the amplitude
% f0  is the oscillation frequency
% tau is the damping time
% lambda is the degree of elliptization
% psi is the polarisation angle

close all; clear all;
% In the following the type of calculation is chosen, for the same
% script could take a different number of parameters
jmode = 'k';  % source of known location (5 unknown)
% jmode = 'u'; % source of unknown location (7 unknown)
nNR = 1; % number of noise realisations
keepnoise = 1; % yes, keep the noise realisation used previously
% keepnoise = 0; % no, don't keep the noise realisation used previously
create = 1; % yes, create noise in the first iteration and use that later
% create = 0; % no, don't create noise in the first iteration

% CONSTANTS
fs = 16384; % Sampling frequency
fres = 0.05; % Frequency resolution
```

```
% Source towards Galactic Centre
SCE.RA = (17 + 45.6/60)/24 * 2*pi;
SCE.Dec = -(28 + 56/60)/180*pi;
SCE.r = 8.5; % in kpc
SCE.Name = 'Galactic Centre';

SCE.The = pi/2 + SCE.Dec;
GMSTrad = 0; GHAX = GMSTrad - SCE.RA;
SCE.Phi = GHAX;

% DETECTOR NETWORKS
% 1.GEO600 / 2.LIGO-H / 3.LIGO-L / 4.VIRGO / 5.TAMA300 / 6.PERTH
% Chose the detectors involved in the detection
NDET.dets = [2 3 4];
NDET.ndets = size(NDET.dets,2);
% Energy released in 1e-6 Ms c^2 (various SNR values)
Efs = [10 20 30 40 50] * 1e-3;
nE = length(Efs);

%-------------------------------------------------------------------
% Allocate memory - Create empty structures
AllocateMemory_N1;
%-------------------------------------------------------------------

for e = 1:nE
  % Eq.1 of MNRAS 299, 1059-1068
  Veval.V2N1 = 3090; Veval.V2N1f = 2*pi*Veval.V2N1/fs;
  Veval.V3N1 = 0.109; Veval.V3N1f = 1/(Veval.V3N1*fs);
  Veval.V4N1 = 0.7;
  Veval.V5N1 = 1.2;
  SCE.PsiN1 = Veval.V5N1;
  Veval.V1N1 = 2.2e-21 * Efs(e)^0.5 * (2000/Veval.V2N1)^0.5 * (50/SCE.r);

  Veval.S1 = pi/2 - SCE.Dec;
  Veval.S2 = SCE.RA;
```

```
%-----------------------------------------------------------------
% Defines the ranges of the parameter spaces
  Print_Calc_Ranges_N1_fixed;
%-----------------------------------------------------------------
  E(e).Vrmin = Vrmin;
  E(e).Vrmax = Vrmax;
  E(e).Veval = Veval;
%-----------------------------------------------------------------
% Calculates order at which the signal arrives to ALL detectors
  ArrivalOrderALL;
%-----------------------------------------------------------------
% Calculates/prints order at which the signal arrives to ALL detectors
  Print_Calc_Antenna_Patterns_N1;
%-----------------------------------------------------------------
% Calculate arrival order and time shifts between detectors
  ArrivalOrderSEL;
%-----------------------------------------------------------------
% Defines the bandwidth to use for the likelihood calculation
  Print_Calc_Frequency_Bandwidth_N1;
%-----------------------------------------------------------------
  Calc_DTFT_N1;
%-----------------------------------------------------------------

  for r = 1:nNR
    switch keepnoise
      case 1
        if e==1 && r==1 && create==1
          [NoiseN1] = NoiseCurves(af,fminN1,fmaxN1);
          Calc_Noise_ALL_N1;
          save ./tosave/NoiseN1 NoiseN1
        else
          load ./tosave/NoiseN1ref
        end
      case 0
        [NoiseN1] = NoiseCurves(af,fminN1,fmaxN1);
        Calc_Noise_ALL_N1;
```

```
     end
     Calc_Add_Noise_N1;

logLN1 = 0;
CN = 0; C1N1 = 0; C2N1 = 0;

for j = 1:nseList
  k = seList(j);
  C1N1 = -N1p * log(2*pi) - 2*sum(log(NoiseN1(k).sig));
  C2N1 = - sum(((NWSCN1(k).r).^2 + (NWSCN1(k).i).^2) ./(2*NoiseN1(k).sig.^2));
  logLN1 = logLN1 + C1N1 + C2N1;
end

Calc_SNR_N1;
     E(e).NR(r).DE = DE;
     E(e).NR(r).NE = NE;

switch jmode
  case 'k'
    NestedSamplingN1;
    logZN1 = logZ;
    logBN1 = logZ - logLN1;
    display(sprintf('H1K: log B = log(p(HS)) - log(p(HN)) = ...
    %1.6e - %1.6e = %1.6e (%1.6e)',logZN1,logLN1,logBN1,exp(logBN1)));
  case 'u'
    NestedSamplingN1S;
    logZN1S = logZ;
    logBN1S = logZN1S - logLN1;
    display(sprintf('H1U: log B = log(p(HS)) - log(p(HN)) = ...
    %1.6e - %1.6e = %1.6e (%1.6e)',logZN1S,logLN1,logBN1S,exp(logBN1S)));
end

NR(r).Vmean = Vmean;
NR(r).Vstd = Vstd;
NR(r).Sam = Sam;
NR(r).Xs = Xs;
```

```
NR(r).Hlist = Hlist;
NR(r).stepVsN1 = stepVsN1;
NR(r).wks = wks;
NR(r).kn = kn;
NR(r).logLN1 = logLN1;

switch jmode
  case 'k'
    NR(r).logZN1 = logZN1;
    NR(r).logBN1 = logBN1;
  case 'u'
    NR(r).logZN1S = logZN1S;
    NR(r).logBN1S = logBN1S;
  end
 end
E(e).NR = NR;
end
```

```
%------------------ AllocateMemory_N1.m --------------------

E(nE).NR(nNR).Vmean.V1N1 = 0;
E(nE).NR(nNR).Vmean.V2N1 = 0;
E(nE).NR(nNR).Vmean.V3N1 = 0;
E(nE).NR(nNR).Vmean.V4N1 = 0;
E(nE).NR(nNR).Vmean.V5N1 = 0;

E(nE).NR(nNR).Vstd.V1N1 = 0;
E(nE).NR(nNR).Vstd.V2N1 = 0;
E(nE).NR(nNR).Vstd.V3N1 = 0;
E(nE).NR(nNR).Vstd.V4N1 = 0;
E(nE).NR(nNR).Vstd.V5N1 = 0;

E(nE).NR(nNR).Vstd.S1 = 0;
E(nE).NR(nNR).Vstd.S2 = 0;

logBN1Ss = zeros(nE,nNR);

E(nE).Vrmin = 0;
E(nE).Vrmax = 0;
E(nE).Veval = 0;

E(nE).NR(nNR).DE = 0;
E(nE).NR(nNR).NE = 0;
```

```
%------------------ Print_Calc_Ranges_N1_fixed.m --------------------

% Selecting ranges of values
Ef_min = 1e-3 * 1e-6;
Ef_max = 1e2 * 1e-6;
% Eq.1 of MNRAS 299, 1059-1068
Vrmin.V1N1 = fmodeEtoA(Ef_min,Veval.V2N1,Veval.V3N1,rpc);
Vrmax.V1N1 = fmodeEtoA(Ef_max,Veval.V2N1,Veval.V3N1,rpc);

Vrmin.V2N1 = Veval.V2N1 - 20; Vrmax.V2N1 = Veval.V2N1 + 20;
Vrmin.V3N1 = 0.01; Vrmax.V3N1 = 1;
Vrmin.V4N1 = 0.01; Vrmax.V4N1 = 0.99;
Vrmin.V5N1 = 0; Vrmax.V5N1 = pi;

Vrmin.S1 = 0; Vrmax.S1 = pi;
Vrmin.S2 = 0; Vrmax.S2 = 2*pi;

display('------------- RANGES N1  ---------------');
display(sprintf('%s:  Range: [%1.5e / %1.5e], Exact: %1.5e',...
Vname.V1N1,Vrmin.V1N1,Vrmax.V1N1,Veval.V1N1));
display(sprintf('%s:  Range: [%1.5e / %1.5e], Exact: %1.5e',...
Vname.V2N1,Vrmin.V2N1,Vrmax.V2N1,Veval.V2N1));
display(sprintf('%s:  Range: [%1.5e / %1.5e], Exact: %1.5e',...
Vname.V3N1,Vrmin.V3N1,Vrmax.V3N1,Veval.V3N1));
display(sprintf('%s:  Range: [%1.5e / %1.5e], Exact: %1.5e',...
Vname.V4N1,Vrmin.V4N1,Vrmax.V4N1,Veval.V4N1));
display(sprintf('%s:  Range: [%1.5e / %1.5e], Exact: %1.5e',...
Vname.V5N1,Vrmin.V5N1,Vrmax.V5N1,Veval.V5N1));
```

```
%------------------ fmodeEtoA.m --------------------

function A = fmodeEtoA(E,f,tau,r)
% convert energy in units of Ms c^2 to gravitational wave amplitude
% for f modes
% from MNRAS 299, 1059-1068
% E(Ms c^2), f (Hz), tau (sec) and r(kpc)

heff = 2.2e-21 * (E/1e-6)^0.5 * (2000/f)^0.5 * (50/r);
A = heff / sqrt(f*tau);
```

```
%------------------ ArrivalOrderALL.m --------------------

% This script calculates the order of the detectors at signal arrival.
nDET = 6;
DET(nDET).kr = 0; DET(nDET).di = 0; DET(nDET).No = 0;
DET(nDET).name = 'namehere';

c = 3e8; % Speed of light
REarth = 6.5e6; % Earth radius

% k vector points to the source
[SCE.kx,SCE.ky,SCE.kz] = sph2cart(SCE.Phi, SCE.Dec,1);
SCE.k = [SCE.kx SCE.ky SCE.kz];

for j = 1:nDET
% Detector's position vector on Earth (from Latitude and Longitude)
  [ONE] = LatLongBisXiC(j);
  [kx,ky,kz] = sph2cart(ONE.Long,ONE.Lat,1);
  DET(j).kr = [kx ky kz];
  DET(j).No = ONE.No;
  DET(j).name = ONE.name;
% calculate d distance from Earth centre
  DET(j).di = dot(SCE.k,DET(j).kr);
end

% Ordering and Assigning numbers to all available detectors
% Create two columns with distance and detector number (to sort)
List = zeros(nDET,2);
for j = 1:nDET
  List(j,1) = DET(j).di;
  List(j,2) = DET(j).No;
end

% Detector location (North Pole) would have DET(NP).d = 1
% Detector location (South Pole) would have DET(SP).d = -1
```

```
soList = sortrows(List,-1);

% printing arrival order to ALL detectors
display('-----------------------------------------------------------------');
display(sprintf('At instant: GMST (rad): %1.2f, GHAX (rad) = %1.2f',...
GMSTrad,GHAX));
display('Signal order arrival to (ALL) detectors');
for j = 1:nDET
  display(sprintf('Detection %1.0f @ D%1.0f: %s',...
  j,soList(j,2),DET(soList(j,2)).name));
end

% time shifts between ALL detectors
Veval.Tall(nDET) = 0;
% soList(1,2) is the number of the detector seeing the signal first
for j= 2:nDET
  tsh = dot(SCE.k,(DET(soList(1,2)).kr - DET(soList(j,2)).kr))*REarth/c;
  atsh = abs(tsh);
  cnsh = round(atsh*fs);
  display(sprintf('T1%1.0f: Time lapse: %1.1f ms (%1.0f samples)',...
  j,atsh*1000,cnsh));
  Veval.Tall(j) = cnsh + Veval.Tall(1);
end
```

```
%------------------ Print_Calc_Antenna_Patterns_N1.m --------------------

% Antenna Function Patterns calculation
DET(nDET).Omega = 0;
DET(nDET).Alpha = 0;
DET(nDET).Beta = 0;
DET(nDET).Gamma = 0;
DET(nDET).FpN1 = 0;
DET(nDET).FcN1 = 0;

display('----------------------------------------------------------------------');
for j = 1:nDET
  [RST] = LatLongBisXiC(j);
  DET(j).Omega = RST.Xi / 2;
  DET(j).Alpha = RST.Bis;
  DET(j).Beta = RST.Lat;
  DET(j).Gamma = RST.Long;
  [DET(j).FpN1,DET(j).FcN1] = FpFcST(SCE.The,SCE.Phi,SCE.PsiN1,...
  DET(j).Alpha,DET(j).Beta,DET(j).Gamma,DET(j).Omega);
  display(sprintf('@ D%1.0f: FpN1 = %1.3f, FcN1 = %1.3f',...
  j,DET(j).FpN1,DET(j).FcN1));
end
```

```
%------------------ LatLongBisXiC.m --------------------

function[DETrad] = LatLongBisXiC(det)
% this script is just to do the code more concise.
% just choose the number that idenfies the detector and get out
% the location/orientation parameters that define that detector.
% Detrad contains: Detrad.name, Detrad.Lat,...
% Detrad.Long, Detrad.Bis, Detrad.Xi

% from PRD 58, 063001
% Detrad.Lat = latitude of Detector
% Detrad.Long = longitude of Detector
% Detrad.Bis = from East to bisector (counterclockwise)
% Detrad.Xi = angle between arms

% 1. GEO600
% 2. LIGO Handford;
% 3. LIGO Livingston
% 4. VIRGO
% 5. TAMA300
% 6. Customized 1


switch det
    case 1
% GEO-600
DETdeg.Lat = 52.3; DETdeg.Long = -9.8; DETdeg.Bis = 158.8; DETdeg.Xi = 94.3;
DETdeg.name = 'GEO600';
DETdeg.No = 1;
    case 2
% LIGO Hanford
DETdeg.Lat = 46.5; DETdeg.Long = 119.4; DETdeg.Bis = 261.8; DETdeg.Xi = 90;
DETdeg.name = 'LIGO-H';
DETdeg.No = 2;
    case 3
```

```
% LIGO Livingston
DETdeg.Lat = 30.6; DETdeg.Long = 90.8; DETdeg.Bis = 333.0; DETdeg.Xi = 90;
DETdeg.name = 'LIGO-L';
DETdeg.No = 3;
    case 4
% VIRGO
DETdeg.Lat = 43.6; DETdeg.Long = -10.5; DETdeg.Bis = 206.5; DETdeg.Xi = 90;
DETdeg.name = 'VIRGO';
DETdeg.No = 4;
    case 5
% TAMA300
DETdeg.Lat = 35.7; DETdeg.Long = -139.5; DETdeg.Bis = 315; DETdeg.Xi = 90;
DETdeg.name = 'TAMA300';
DETdeg.No = 5;
    case 6
% Custom (PERTH)
DETdeg.Lat = -31.9; DETdeg.Long = 116; DETdeg.Bis = 0; DETdeg.Xi = 90;
DETdeg.name = 'PERTH';
DETdeg.No = 6;
end

DETrad.Lat = DETdeg.Lat/180*pi;
DETrad.Long = DETdeg.Long/180*pi;
DETrad.Bis = DETdeg.Bis/180*pi;
DETrad.Xi = DETdeg.Xi/180*pi;
DETrad.name = DETdeg.name;
DETrad.No = DETdeg.No;
```

```
%------------------ FpFcST.m --------------------

function[Ep,Ec] = FpFcST(the,phi,psi,alpha,beta,gamma,omega)

% DETECTOR LOCATION/ORIENTATION
% alpha - orientation (bisector to E-W line)
% beta - latitude
% gamma - longitude

% SOURCE LOCATION
% the - co-declination
% phi - GHA (HA in Greenwich)
% psi - so to get '+' and 'x' dephased pi/2

% see MNRAS 224, 131-154

% Rotation matrix A to go from 'Wave' to 'Earth' frame
[A] = RotMatA(the,phi,psi);

% Rotation matrix B to go from 'Earth' to 'Detector' frame
[B] = RotMatB(alpha,beta,gamma);

% Combined rotation C to go from 'Wave' to 'Detector'
C = B*A;

Ep = sin(2*omega) * (C(1,1)*C(2,1) - C(1,2)*C(2,2));
Ec = sin(2*omega) * (C(1,1)*C(2,2) + C(1,2)*C(2,1));
```

```
%------------------ RotMatA.m --------------------

function[A] = RotMatA(the,phi,psi)
% Rotation matrix
% Wave frame to Detector frame
% matrix A in MNRAS 224, 131 (page 136)
% from (X,Y,Z) to (x,y,z), see fig.3

A11 = cos(psi)*cos(phi) - cos(the)*sin(phi)*sin(psi);
A12 = -(sin(psi)*cos(phi) + cos(the)*sin(phi)*cos(psi));
A13 = sin(the)*sin(phi);

A21 = cos(psi)*sin(phi) + cos(the)*cos(phi)*sin(psi);
A22 = -sin(psi)*sin(phi) + cos(the)*cos(phi)*cos(psi);
A23 = -sin(the)*cos(phi);

A31 = sin(the)*sin(psi);
A32 = sin(the)*cos(psi);
A33 = cos(the);


A = [A11 A12 A13; A21 A22 A23; A31 A32 A33];
```

```
%------------------ RotMatB.m --------------------

function[B] = RotMatB(alpha,beta,gamma)
% Rotation matrix from 'Earth' to 'Detector' frame
% matrix B in MNRAS 224, 131 (page 141)
% from (x',y',z') to (x,y,z), see fig.3

B11 = cos(alpha)*sin(beta)*cos(gamma) - sin(alpha)*sin(gamma);
B12 = sin(alpha)*cos(gamma) + cos(alpha)*sin(beta)*sin(gamma);
B13 = -cos(alpha)*cos(beta);

B21 = -(cos(alpha)*sin(gamma)+sin(alpha)*sin(beta)*cos(gamma));
B22 = -sin(alpha)*sin(beta)*sin(gamma) + cos(alpha)*cos(gamma);
B23 = sin(alpha)*cos(beta);

B31 = cos(beta)*cos(gamma);
B32 = cos(beta)*sin(gamma);
B33 = sin(beta);


B = [B11 B12 B13; B21 B22 B23; B31 B32 B33];
```

```
%------------------ Print_Calc_Frequency_Bandwidth_N1.m --------------------

N = fs/fres; S2 = N;
aw = 0:2*pi/N:2*pi*(1-1/N);
af = aw/(2*pi)*fs;

% select bandwidth
bdwN1 = 200;
fminN1 = Veval.V2N1 - bdwN1;
fmaxN1 = Veval.V2N1 + bdwN1;
takefN1 = (af >= fminN1 & af <= fmaxN1);
fN1 = af(takefN1);
wN1 = aw(takefN1);
N1p = length(fN1);

display('---------------- FREQUENCY DOMAIN FEATURES --------------');
display(sprintf('Freq. Resolution: %1.2f Hz',fres));
display(sprintf('Bandwidth: %1.0f Hz [%1.0f - %1.0f]',bdwN1,fminN1,fmaxN1));
```

```
%------------------ Calc_DTFT_N1.m --------------------

%% DTFT Calculations
WN1(nDET).Zsin = zeros(1,N1p);
WN1(nDET).Zcos = zeros(1,N1p);
WN1(nDET).Cs = 0;
WN1(nDET).Cc = 0;

WSCN1(nseList).Zsincos = zeros(1,N1p);
WSCN1(nseList).r = zeros(1,N1p);
WSCN1(nseList).i = zeros(1,N1p);
WSCN1(nseList).m = zeros(1,N1p);

for j = 1:nseList
  k = seList(j);
  WN1(k).Zsin = Zreimsinsh(Veval.V2N1f,Veval.V3N1f,Veval.Tsh(j),wN1);
  WN1(k).Zcos = Zreimcossh(Veval.V2N1f,Veval.V3N1f,Veval.Tsh(j),wN1);
  WN1(k).Cs = DET(k).FpN1 * E(e).Veval.V1N1;
  WN1(k).Cc = DET(k).FcN1 * E(e).Veval.V1N1 * Veval.V4N1;
  WSCN1(k).Zsincos = WN1(k).Cs * WN1(k).Zsin + WN1(k).Cc * WN1(k).Zcos;
  WSCN1(k).r = real(WSCN1(k).Zsincos);
  WSCN1(k).i = imag(WSCN1(k).Zsincos);
  WSCN1(k).m = abs(complex(WSCN1(k).r,WSCN1(k).i));
  WSCN1(k).psd = 2* abs(WSCN1(k).Zsincos).^2/fs;
end
```

```
%------------------ NestedSamplingN1.m --------------------

% NESTED SAMPLING
constVN = [1 2 3 4 5];

% Declare
kn = 0; KN = 1e4;
n = 100; % number of objects
mmax = 20; % number of trials to find a new object
nVN1 = 7; % number of variables
H = 0;
logZ = -1e30;

logmax = -1e31;
cV = 0.1; % to reduce covariance

% To stop loop at
f = exp(-5);

% Memory allocation
stepVsN1 = zeros(nVN1);
Hlist = zeros(1,KN);
Xs = zeros(1,KN);

Obj(n).V1N1 = 0; Obj(n).V2N1 = 0; Obj(n).V3N1 = 0;
Obj(n).V4N1 = 0; Obj(n).V5N1 = 0; Obj(n).V2fN1 = 0; Obj(n).V3fN1 = 0;
Obj(n).S1 = 0; Obj(n).S2 = 0; Obj(n).Dec = 0; Obj(n).RA = 0;
Obj(n).logL = 0; Obj(n).logWt = 0;

Try.V1N1 = 0; Try.V2N1 = 0; Try.V3N1 = 0; Try.V4N1 = 0;
Try.V5N1 = 0; Try.V2fN1 = 0; Try.V3fN1 = 0;
Try.S1 = 0; Try.S2 = 0; Try.Dec = 0; Try.RA = 0;
Try.logL = 0; Try.logWt = 0;

Keep.V1N1 = 0; Keep.V2N1 = 0; Keep.V3N1 = 0; Keep.V4N1 = 0;
Keep.V5N1 = 0; Keep.V2fN1 = 0; Keep.V3fN1 = 0;
```

```
Keep.S1 = 0; Keep.S2 = 0; Keep.Dec = 0; Keep.RA = 0;
Keep.logL = 0; Keep.logWt = 0;

Sam(KN).V1N1 = 0; Sam(KN).V2N1 = 0; Sam(KN).V3N1 = 0;
Sam(KN).V4N1 = 0; Sam(KN).V5N1 = 0; Sam(KN).V2fN1 = 0;
Sam(KN).V3fN1 = 0;
Sam(KN).S1 = 0; Sam(KN).S2 = 0; Sam(KN).Dec = 0; Sam(KN).RA = 0;
Sam(KN).logL = 0; Sam(KN).logWt = 0;


% Set priors for n objects
for i = 1:n
  if sum(constVN==1)==0;
    Obj(i).V1N1 = unifrnd(E(e).Vrmin.V1N1,E(e).Vrmax.V1N1,1,1);
  else Obj(i).V1N1 = E(e).Veval.V1N1; end
  if sum(constVN==2)==0;
    Obj(i).V2N1 = unifrnd(E(e).Vrmin.V2N1,E(e).Vrmax.V2N1,1,1);
  else Obj(i).V2N1 = E(e).Veval.V2N1; end
  if sum(constVN==3)==0;
    Obj(i).V3N1 = unifrnd(E(e).Vrmin.V3N1,E(e).Vrmax.V3N1,1,1);
  else Obj(i).V3N1 = E(e).Veval.V3N1; end
  if sum(constVN==4)==0;
    Obj(i).V4N1 = unifrnd(E(e).Vrmin.V4N1,E(e).Vrmax.V4N1,1,1);
  else Obj(i).V4N1 = E(e).Veval.V4N1; end
  if sum(constVN==5)==0;
    Obj(i).V5N1 = unifrnd(E(e).Vrmin.V5N1,E(e).Vrmax.V5N1,1,1);
  else Obj(i).V5N1 = E(e).Veval.V5N1; end

  if sum(constVN==6)==0;
    Obj(i).S1 = unifrnd(E(e).Vrmin.S1,E(e).Vrmax.S1,1,1);
  else Obj(i).S1 = E(e).Veval.S1; end
  if sum(constVN==7)==0;
    Obj(i).S2 = unifrnd(E(e).Vrmin.S2,E(e).Vrmax.S2,1,1);
  else Obj(i).S2 = E(e).Veval.S2; end

  Obj(i).V2fN1 = Obj(i).V2N1 * 2*pi/fs;
```

```
  Obj(i).V3fN1 = 1/(Obj(i).V3N1 * fs);
  Obj(i).Dec = pi/2 - Obj(i).S1;
  Obj(i).RA = mod(Obj(i).S2,2*pi);

  [Tsh,seList] = ArrivalOrderTimeShifts(DET,NDET,...
  Obj(i).Dec,Obj(i).RA,GMSTrad,fs);

  CN = 0; C1N1 = 0; C2N1 = 0;
  for j = 1:nseList
    k = seList(j);
    cWSN1 = Zreimsinsh(Obj(i).V2fN1,Obj(i).V3fN1,Veval.Tsh(j),wN1);
    cWCN1 = Zreimcossh(Obj(i).V2fN1,Obj(i).V3fN1,Veval.Tsh(j),wN1);
    cThe = pi/2 + Obj(i).Dec;
    cPhi = GMSTrad - Obj(i).RA;
    [cFpN1,cFcN1] = FpFcST(cThe,cPhi,Obj(i).V5N1,DET(k).Alpha,...
    DET(k).Beta,DET(k).Gamma,DET(k).Omega);

    CpN1 = cFpN1 * Obj(i).V1N1;
    CcN1 = cFcN1 * Obj(i).V1N1 * Obj(i).V4N1;
    cWSCN1 = 1/1 * (CpN1 * cWSN1 + CcN1 * cWCN1);
    cWSCN1r = real(cWSCN1);
    cWSCN1i = imag(cWSCN1);

    C1N1 = -N1p * log(2*pi) - 2*sum(log(NoiseN1(k).sig));
    C2N1 = - sum(((cWSCN1r - NWSCN1(k).r).^2 +...
     (cWSCN1i - NWSCN1(k).i).^2) ./(2*NoiseN1(k).sig.^2));
    CN = CN + C1N1 + C2N1;
  end
  Obj(i).logL = CN;
end

% Outermost interval of prior mass
% because \xi_k = exp(-k/n), thus logw = log(1 - \xi_k)
logw = log(1 - exp(-1/n));
w = exp(logw); X = 1 - w; log10X = log10(X);
display('%-----------------------------------------------%');
```

```
display('NESTED SAMPLING RUNNING...');
display(sprintf('Number of Objects = %1.0f',n));
display(sprintf('Stop when exp(%1.2f) Evidence to stop',log(f)));
display(sprintf('logw = %1.3f (w = %1.5e), ...
so X = %1.5e (log10X = %1.3f)',logw,w,X,log10X));

% NESTED SAMPLING LOOP
% continue while the contribution to evidence is bigger than f
while (kn==0) || (az > log(f) + bz)
  kn = kn + 1;
  worst = find(min([Obj.logL]) == [Obj.logL]);
  % in case two or more objects are found...
  worst = worst(unidrnd(length(worst)));
  Obj(worst).logWt = logw + Obj(worst).logL;

  % Update evidence Z and information H
  logZnew = aplusb(logZ,Obj(worst).logWt);
  Hlist(kn) = H; H = exp(Obj(worst).logWt - logZnew) * Obj(worst).logL + ...
  exp(logZ - logZnew) * (H + logZ) - logZnew;
  logZ = logZnew;

  % save the worst sample before replacing it (for posterior samples)
  Sam(kn) = Obj(worst);
  display(sprintf('N1 values: [%1.6e, %1.6e, %1.6e, %1.6e,... 1.6e]',...
  Sam(kn).V1N1,Sam(kn).V2N1,Sam(kn).V3N1,...
  Sam(kn).V4N1,Sam(kn).V5N1));
  display(sprintf('N1 values: [%1.6e, %1.6e]',Sam(kn).S1,Sam(kn).S2));
  inm = false;
  ntrial = 0;

  while ~inm
  copy = unidrnd(n); while (copy==worst); copy = unidrnd(n); end
    Keep = Obj(worst); % in case we a replacement is not found
    Obj(worst) = Obj(copy);
    am = 0;
```

```
for m = 1:mmax
  isin = false;
  while ~isin
  if (mod(kn,1)==0 || kn==1)
    Calc_Mu_Sigma_N1S;
    TryVN1 = mvnrnd(muVN1,cV*CCVN1);
    Try.V1N1 = TryVN1(1); Try.V2N1 = TryVN1(2); Try.V3N1 = TryVN1(3);
    Try.V4N1 = TryVN1(4); Try.V5N1 = TryVN1(5);
    Try.S1 = TryVN1(6); Try.S2 = TryVN1(7);
  end

  if sum(constVN==1) == 0;
    isV1N1in = (Try.V1N1 > E(e).Vrmin.V1N1) & (Try.V1N1 < E(e).Vrmax.V1N1);
  else isV1N1in = 1; end;
  if sum(constVN==2) == 0;
    isV2N1in = (Try.V2N1 > E(e).Vrmin.V2N1) & (Try.V2N1 < E(e).Vrmax.V2N1);
  else isV2N1in = 1; end;
  if sum(constVN==3) == 0;
    isV3N1in = (Try.V3N1 > E(e).Vrmin.V3N1) & (Try.V3N1 < E(e).Vrmax.V3N1);
  else isV3N1in = 1; end;
  if sum(constVN==4) == 0;
    isV4N1in = (Try.V4N1 > E(e).Vrmin.V4N1) & (Try.V4N1 < E(e).Vrmax.V4N1);
  else isV4N1in = 1; end;
  if sum(constVN==5) == 0;
    isV5N1in = (Try.V5N1 > E(e).Vrmin.V5N1) & (Try.V5N1 < E(e).Vrmax.V5N1);
  else isV5N1in = 1; end;

  if sum(constVN==6) == 0;
    isS1in = (Try.S1 > E(e).Vrmin.S1) & (Try.S1 < E(e).Vrmax.S1);
  else isS1in = 1; end;
  if sum(constVN==7) == 0;
    isS2in = (Try.S2 > E(e).Vrmin.S2) & (Try.S2 < E(e).Vrmax.S2);
  else isS2in = 1; end;

  isinN1 = isV1N1in .* isV2N1in .* isV3N1in .* isV4N1in ...
  * isV5N1in * isS1in * isS2in;
```

```
isin = isinN1;
end

Try.V2fN1 = Try.V2N1 *2*pi/fs;
Try.V3fN1 = 1/(Try.V3N1 * fs);
Try.Dec = pi/2 - Try.S1;
Try.RA = mod(Try.S2,2*pi);

[Tsh,seList] = ArrivalOrderTimeShifts(DET,NDET,...
Try.Dec,Try.RA,GMSTrad,fs);

CN = 0; C1N1 = 0; C2N1 = 0;
for j = 1:nseList
  k = seList(j);
  cWSN1 = Zreimsinsh(Try.V2fN1,Try.V3fN1,Veval.Tsh(j),wN1);
  cWCN1= Zreimcossh(Try.V2fN1,Try.V3fN1,Veval.Tsh(j),wN1);
  cThe = pi/2 + Try.Dec;
  cPhi = GMSTrad - Try.RA;
  [cFpN1,cFcN1] = FpFcST(cThe,cPhi,Try.V5N1,DET(k).Alpha,...
  DET(k).Beta,DET(k).Gamma,DET(k).Omega);

  CpN1 = cFpN1 * Try.V1N1;
  CcN1 = cFcN1 * Try.V1N1 * Try.V4N1;
  cWSCN1 = 1/1 * (CpN1 * cWSN1 + CcN1 * cWCN1);
  cWSCN1r = real(cWSCN1);
  cWSCN1i = imag(cWSCN1);

  C1N1 = -N1p * log(2*pi) - 2*sum(log(NoiseN1(k).sig));
  C2N1 = - sum(((cWSCN1r - NWSCN1(k).r).^2 + ...
  (cWSCN1i - NWSCN1(k).i).^2) ./(2*NoiseN1(k).sig.^2));

  CN = CN + C1N1 + C2N1;
  end
  Try.logL = CN;

  if Try.logL > Keep.logL
```

```
          alpha = Obj(worst).V1N1 / Try.V1N1;
          u = rand;
          if alpha > u
            Obj(worst) = Try;
            inm = true;
            am = am + 1;
          end
         end
        end
        ntrial = ntrial + 1;
        if ~inm; Obj(worst) = Keep; end
    end

    % Shrink interval
    logw = logw - 1/n; w = exp(logw);
    logX = -kn/n; X = 10^logX; Xs(kn) = X;

    % from Eq.16 of Skilling's document on Nested Sampling
    az = max([Obj.logL]) + (-kn/n);
    bz = logZ;
    factor = exp(az - bz);

    if mod(kn,5)==0 || kn==1
      display(sprintf('Run type: %s',jmode));
      display(sprintf('E = %1.0f/%1.0f, NR = %1.0f/%1.0f,...
       Iteration No. = %1.0f, Trials = %1.0f, Accepted: %1.0f/%1.0f',...
       e,nE,r,nNR,kn,ntrial,am,mmax));
       display(sprintf('logw = %1.3f (w = %1.5e), so X = %1.5e (log10X = %1.3f)',...
       logw,w,X,logX));
       display(sprintf('logZ = %1.5e, H = %1.5e',logZ,H));
       display(sprintf('Contribution to Z is %1.5e (stop at %1.5e)',...
       log(factor),log(f)));
    end
end

% Add remaining
```

```
for i = 1:n
    Obj(i).logWt = logw + Obj(i).logL;
    logZnew = aplusb(logZ,Obj(i).logWt);
    H = exp(Obj(i).logWt - logZnew) * Obj(i).logL + exp(logZ - logZnew)...
     * (H + logZ) - logZnew;
    logZ = logZnew;
    Sam(kn+1) = Obj(i);
end

% RESULTS
% take only the relevant part (kn iterations recorded)
Sam = Sam(1:kn);
Xs = Xs(1:kn);
Hlist = Hlist(1:kn);
stepVsN1 = stepVsN1(:,1:kn);

wks = exp([Sam.logWt] - logZ);
Vmean.V1N1 = sum(wks .* [Sam.V1N1]);
Vmean.V2N1 = sum(wks .* [Sam.V2N1]);
Vmean.V3N1 = sum(wks .* [Sam.V3N1]);
Vmean.V4N1 = sum(wks .* [Sam.V4N1]);
Vmean.V5N1 = sum(wks .* [Sam.V5N1]);

Vstd.V1N1 = sqrt(sum(wks .* ([Sam.V1N1] - Vmean.V1N1).^2));
Vstd.V2N1 = sqrt(sum(wks .* ([Sam.V2N1] - Vmean.V2N1).^2));
Vstd.V3N1 = sqrt(sum(wks .* ([Sam.V3N1] - Vmean.V3N1).^2));
Vstd.V4N1 = sqrt(sum(wks .* ([Sam.V4N1] - Vmean.V4N1).^2));
Vstd.V5N1 = sqrt(sum(wks .* ([Sam.V5N1] - Vmean.V5N1).^2));

display('****************** Results ***********************');
display(sprintf('Number of iterates = %1.0f',kn));
display(sprintf('Evidence: ln(Z) = %1.5e +/- %1.5f',logZ,sqrt(H/n)));
display('%------------------------------------------------------------');
display(sprintf(' Exact/Mean/Std V1N1 = %1.5e/%1.5e/%1.5e',...
E(e).Veval.V1N1,Vmean.V1N1,Vstd.V1N1));
display(sprintf(' Exact/Mean/Std V2N1 = %1.5f/%1.5f/%1.5f',...
```

```
Veval.V2N1,Vmean.V2N1,Vstd.V2N1));
display(sprintf(' Exact/Mean/Std V3N1 = %1.5f/%1.5f/%1.5f',...
Veval.V3N1,Vmean.V3N1,Vstd.V3N1));
display(sprintf(' Exact/Mean/Std V4N1 = %1.5f/%1.5f/%1.5f',...
Veval.V4N1,Vmean.V4N1,Vstd.V4N1));
display(sprintf(' Exact/Mean/Std V5N1 = %1.5f/%1.5f/%1.5f',...
Veval.V5N1,Vmean.V5N1,Vstd.V5N1));
display('%------------------------------------------------------------');
toc
```

```
%------------------ ArrivalOrderTimeShifts.m --------------------

function [Tsh,seList] = ArrivalOrderTimeShifts(DET,NDET,TDec,TRA,GMSTrad,fs)
% script to calculate arrival order and time shifts between sel. detectors

c = 3e8; % Speed of light
REarth = 6.5e6; % Earth radius
nDET = size(DET,2);

% [X,Y,Z] = SPH2CART(TH,PHI,R)
% TH is the counterclockwise angle in the xy plane
% measured from the positive x axis.
% PHI is the elevation angle from the xy plane.

TSCE.Phi = GMSTrad - TRA;
TSCE.Dec = TDec;

[TSCE.kx,TSCE.ky,TSCE.kz] = sph2cart(TSCE.Phi, TSCE.Dec,1);
TSCE.k = [TSCE.kx TSCE.ky TSCE.kz];

for j = 1:nDET; DET(j).di = dot(TSCE.k,DET(j).kr); end

% Ordering and Assigning numbers to all available detectors
% Create two columns with distance and detector number (to sort)

List(:,1) = [DET.di];
List(:,2) = 1:nDET;
soList = sortrows(List,-1);

% time shifts between selected detectors
seList = [];
%display('---------- Arrival Order -------------');
for k = 1:size(soList,1)
    if sum(soList(k,2)==NDET.dets)==1
       seList = [seList soList(k,2)];
    end
```

```
end

% display('---------- Time Delays -------------');
Tsh(nDET) = 0;
for k = 1:length(seList)
    tsh = dot(TSCE.k,(DET(seList(1)).kr - DET(seList(k)).kr))*REarth/c;
    atsh = abs(tsh);
    Tsh(k) = round(atsh*fs);
end
```

```
%------------------ Calc_SNR_N1.m --------------------
% SNR calculation

for j = 1:nDET
  DE(j).SNRN1 = 0;
end

for j = 1:nseList
  k = seList(j);
  DE(k).SNRN1 = SNRSchutz(WSCN1(k).m,NoiseN1(k).PSD,fs,fres);
  display(sprintf('SNR (Schutz) for N1 on Det %1.0f (%s) is %1.2f',...
  k,DET(k).name,DE(k).SNRN1));
end

NE.SNRN1 = sqrt(sum([DE.SNRN1].^2));
display(sprintf('SNR (Schutz) for N1 on Network SNRN1: %1.2f',...
NE.SNRN1));
```

Appendix J

Signal arrival order to detectors

Gravitational wave signals are expected to travel at the speed of light. Hence, if a signal is detected in a network of various antennae logically there will be a signal arrival order to the detectors. This order is important in the implementation of our algorithms, in order to include the time-shifts between the detectors. To determine the arrival order the following procedure was used:

- Define a reference frame $\mathbf{x}, \mathbf{y}, \mathbf{z}$ fixed to the Earth and rotating with it (it is the same reference as $\mathbf{x'y'z'}$ defined in Appendix D) so that $\mathbf{z}$ is the axis going through the north-pole and $\mathbf{x}$ pierces the intersection point between the equator and the Greenwich meridian.

- Determine the unit vectors $\hat{\mathbf{k}}$ that point from the centre of the Earth to each of the ground-based detectors defined. (e.g. a detector located in the north pole is [0,0,1]). In general, $\hat{\mathbf{k}} = [k_x, k_y, k_z] = sph2cart(\gamma, \beta, 1)$, where γ is the longitude and β the latitude of the detector's location. Note: "sph2cart" is a matlab command to convert spherical angles into cartesian coordinates.

- Determine the unit vector pointing at the source $\hat{\mathbf{s}} = [s_x, s_y, s_z] = \text{sph2cart}(\phi, \delta, 1)$, where ϕ = GLST - RA is the hour-angle in Greenwich of the source at the particular instant and δ is its declination.

- Determine the projection of each detector unitary vector $\hat{\mathbf{k_i}}$ onto the direction toward the source: $d_i = \hat{\mathbf{k_i}} \cdot \hat{\mathbf{s}}$ (e.g. for two detectors in antipodal

points with a source overhead d will be 1 and -1). We just need to sort out d_i values to infer the arrival order of the signal to the detectors considered.

- Time-shifts between detectors can be readily calculated by considering that the gravitational wave signal is a plane wave by the time it reaches the network. The time shift between detector i and j is given in seconds by $\Delta t_{ij} = R_e/c \left[(\hat{\mathbf{k_i}} - \hat{\mathbf{k_j}} \cdot \hat{\mathbf{s}}\right]$, where the speed of light is $c = 3 \times 10^8$ m/s and the mean radius for the Earth $R_e = 6.5 \times 10^6$ m. Time shift is measured in number of samples by rounding to the closest integer the operation $\Delta n_{ij} = f_s \, \Delta t_{ij}$.

  As an example, Table J.1 shows the arrival order for the six detectors considered, together with the time shifts, in milliseconds and number of samples, for a signal coming from the galactic centre at the instant GLST = 0h. The antenna pattern functions for each oscillation mode and detector are included here for reference.

DET	**Name**	**Arrival**		
		Pos.	**Time (ms)**	**Samples***
1	GEO600	5	31.4	515
2	Adv-LIGO-H	3	16.3	267
3	Adv-LIGO-L	2	9.5	155
4	Adv-VIRGO	4	31	508
5	TAMA300	6	35.8	586
6	PERTH	1	0	0

Signal incoming from the galactic centre at GLST = 0h.
* Assuming sampling frequency $f_s = 16384$ Hz.

Table J.1: Arrival order and antenna patterns of the detectors for f- and p-modes.

Fig. J.1 shows a time-shift contour-map for a grid of geographical location on Earth for the particular time instant of GLST = 0h. The geographical position of each detector is pinpointed and it is easy to establish the arrival order of the signal from the graph. The order of signal detection varies as the Earth turns (sidereal day periodicity) depending the source's sky-location. Fig. J.2 depicts

the detection time differences between each of the detector and the centre of the Earth during a sidereal day.

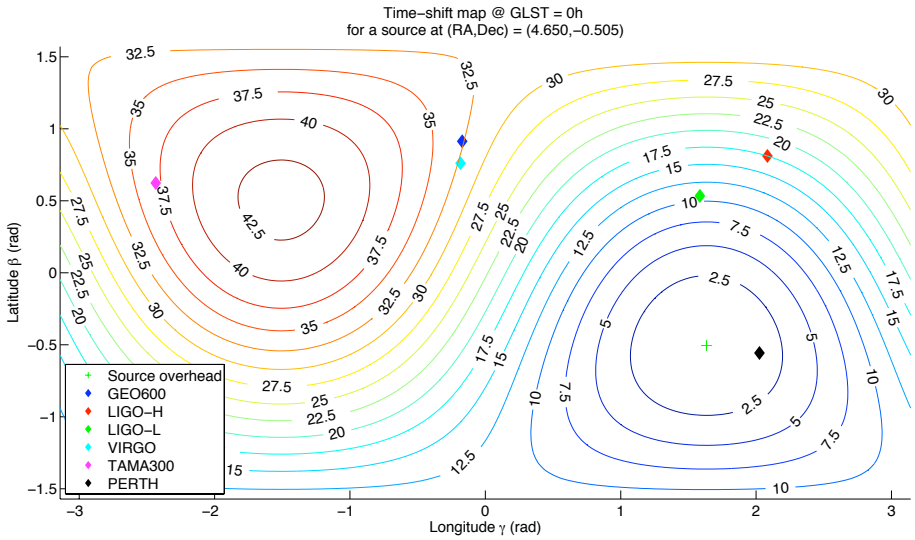

Figure J.1: Time-shift map for a grid of locations on Earth for a signal coming from the galactic centre (δ_{GC} = -0.51 rad, RA = 4.65 rad). The green cross marks the location for zero time-shift, a position corresponding to a detector located at latitude $\beta = \delta_{GC}$ and longitude $\gamma = \phi_{GC}$ = GLST - RA_{GC} = 1.63 rad. Contour levels depict time shifts in seconds.

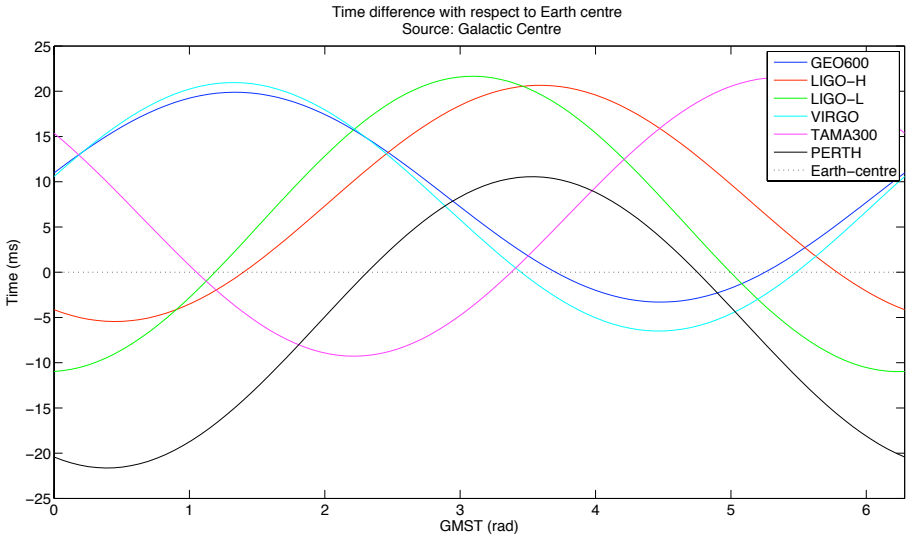

Figure J.2: Arrival time differences for the detectors considered for a signal coming from the galactic centre (δ_{GC} = -0.51 rad, RA = 4.65 rad) during one rotation of the Earth. The horizontal dotted line at zero marks the reference of arrival time at the Earth centre. Times are positive for those detector which see the signal before the centre of the Earth, and negative for those who see it later.

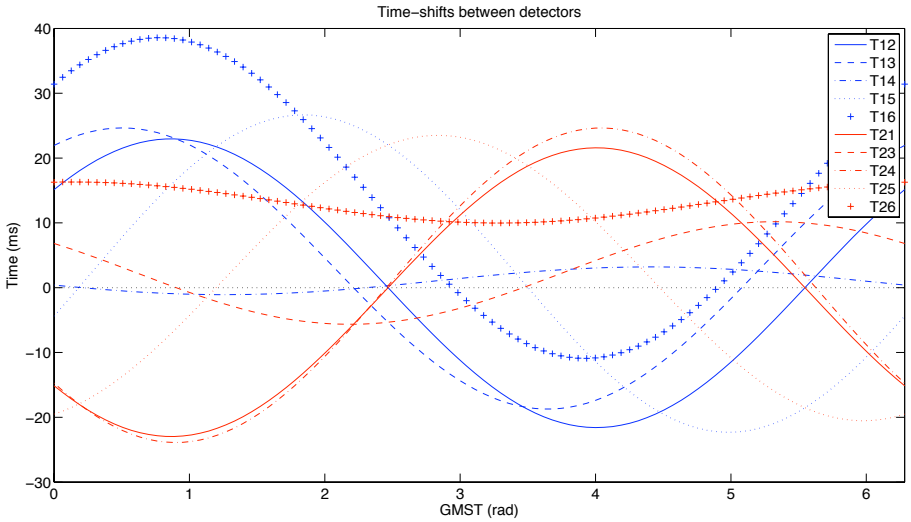

Figure J.3: Time differences between detectors considered for a signal coming from the galactic centre (δ_{GC} = -0.51 rad, RA = 4.65 rad) during one rotation of the Earth. Time differences between two detectors T_{ij} and T_{ji} are the same but with different sign, as expected.

Appendix K

Parameter Estimation Results

This appendix groups the parameter estimation results in tabulated form for the scenarios and hypothesis considered in Chapter 5. Each table reports the mode of the probability distribution and 95 % credibility interval for each of the parameters depending the strength of the signal (SNR).

Parameter Estimation H_{1K}					
SNR	**P**	**Exact**	**Mode**	**Range**	**Diff. %**
8	h_0	9.2597e-22	7.2561e-22	[2.9534e-22 - 1.3471e-21]	%-21.64
	f_0	3.0900e+03	3.0895e+03	[3.0878e+03 - 3.0908e+03]	%-0.01
	τ	1.0900e-01	8.9573e-02	[2.4920e-02 - 2.5369e-01]	%-17.82
	λ	7.0000e-01	2.1000e-01	[3.0000e-02 - 9.1000e-01]	%-70.00
	ψ	1.2000e+00	1.0794e+00	[5.6857e-01 - 1.4845e+00]	%-10.05
10	h_0	1.1570e-21	1.0125e-21	[5.3438e-22 - 1.5383e-21]	%-12.49
	f_0	3.0900e+03	3.0896e+03	[3.0883e+03 - 3.0906e+03]	%-0.01
	τ	1.0900e-01	9.4546e-02	[4.9786e-02 - 1.8407e-01]	%-13.26
	λ	7.0000e-01	7.3000e-01	[3.0000e-02 - 9.5000e-01]	%4.29
	ψ	1.2000e+00	1.1178e+00	[7.4575e-01 - 1.4367e+00]	%-6.85
12	h_0	1.3891e-21	1.2374e-21	[8.5967e-22 - 1.8513e-21]	%-10.91
	f_0	3.0900e+03	3.0897e+03	[3.0888e+03 - 3.0906e+03]	%-0.01
	τ	1.0900e-01	9.4546e-02	[5.4760e-02 - 1.5423e-01]	%-13.26
	λ	7.0000e-01	6.3000e-01	[7.0000e-02 - 9.7000e-01]	%-10.00
	ψ	1.2000e+00	1.1412e+00	[8.7491e-01 - 1.3898e+00]	%-4.90
20	h_0	2.3152e-21	2.2677e-21	[1.7955e-21 - 2.7872e-21]	%-2.05
	f_0	3.0900e+03	3.0899e+03	[3.0894e+03 - 3.0903e+03]	%-0.00
	τ	1.0900e-01	1.0092e-01	[7.5663e-02 - 1.3122e-01]	%-7.41
	λ	7.0000e-01	6.7000e-01	[4.1000e-01 - 9.7000e-01]	%-4.29
	ψ	1.2000e+00	1.1630e+00	[1.0556e+00 - 1.3061e+00]	%-3.08

Table K.1: Parameter estimation from the posterior probability density distribution in Fig. 5.5 corresponding to the hypothesis H_{1K} in Scenario 1.

Parameter Estimation H_{1G}					
SNR	**P**	**Exact**	**Mode**	**Range**	**Diff. %**
8	h_0	9.2597e-22	7.3517e-22	[3.0132e-22 - 1.3268e-21]	%-20.61
	f_0	3.0900e+03	3.0899e+03	[3.0888e+03 - 3.0909e+03]	%-0.00
	τ	1.0900e-01	8.9573e-02	[3.4867e-02 - 2.2883e-01]	%-17.82
	λ	7.0000e-01	6.7000e-01	[5.0158e-01 - 8.5526e-01]	%-4.29
	ψ	1.2000e+00	1.1898e+00	[1.1183e+00 - 1.2742e+00]	%-0.85
10	h_0	1.1570e-21	1.0390e-21	[6.1052e-22 - 1.5454e-21]	%-10.20
	f_0	3.0900e+03	3.0899e+03	[3.0891e+03 - 3.0907e+03]	%-0.00
	τ	1.0900e-01	9.4546e-02	[4.9786e-02 - 1.7412e-01]	%-13.26
	λ	7.0000e-01	6.8368e-01	[5.1526e-01 - 8.6895e-01]	%-2.33
	ψ	1.2000e+00	1.1898e+00	[1.1183e+00 - 1.2807e+00]	%-0.85
12	h_0	1.3891e-21	1.2414e-21	[8.1004e-22 - 1.7513e-21]	%-10.63
	f_0	3.0900e+03	3.0899e+03	[3.0893e+03 - 3.0905e+03]	%-0.00
	τ	1.0900e-01	1.0452e-01	[5.9749e-02 - 1.5925e-01]	%-4.11
	λ	7.0000e-01	6.8368e-01	[5.1526e-01 - 8.6895e-01]	%-2.33
	ψ	1.2000e+00	1.1898e+00	[1.1183e+00 - 1.2677e+00]	%-0.85
20	h_0	2.3152e-21	2.1687e-21	[1.7791e-21 - 2.7140e-21]	%-6.33
	f_0	3.0900e+03	3.0898e+03	[3.0895e+03 - 3.0903e+03]	%-0.01
	τ	1.0900e-01	1.0092e-01	[7.5663e-02 - 1.3122e-01]	%-7.41
	λ	7.0000e-01	6.8143e-01	[5.1000e-01 - 8.3571e-01]	%-2.65
	ψ	1.2000e+00	1.1768e+00	[1.1248e+00 - 1.2612e+00]	%-1.94

Table K.2: Parameter estimation from the posterior probability density distribution in Fig. 5.8 corresponding to the hypothesis H_{1G} in Scenario 1.

Parameter Estimation H_{1U}					
SNR	**P**	**Exact**	**Mode**	**Range**	**Diff. %**
8	h_0	9.2597e-22	5.1031e-22	[1.0411e-22 - 1.0906e-21]	%-44.89
	f_0	3.0900e+03	3.0893e+03	[3.0874e+03 - 3.0909e+03]	%-0.02
	τ	1.0900e-01	7.6607e-02	[2.3321e-02 - 2.2980e-01]	%-29.72
	λ	7.0000e-01	1.6077e-01	[1.0000e-02 - 8.1410e-01]	%-77.03
	ψ	1.2000e+00	1.1107e+00	[9.5200e-02 - 3.1099e+00]	%-7.44
	δ	2.0758e+00	2.1085e+00	[1.0542e-01 - 3.0994e+00]	%1.57
	RA	4.6496e+00	4.7229e+00	[4.2169e-01 - 6.1988e+00]	%1.58
10	h_0	1.1570e-21	5.6307e-22	[2.1885e-22 - 1.2515e-21]	%-51.34
	f_0	3.0900e+03	3.0893e+03	[3.0884e+03 - 3.0903e+03]	%-0.02
	τ	1.0900e-01	9.0816e-02	[5.0408e-02 - 2.1204e-01]	%-16.68
	λ	7.0000e-01	1.1051e-01	[1.0000e-02 - 7.6385e-01]	%-84.21
	ψ	1.2000e+00	1.1741e+00	[0.0000e+00 - 3.1099e+00]	%-2.16
	δ	2.0758e+00	2.9097e+00	[8.4338e-02 - 3.0994e+00]	%40.17
	RA	4.6496e+00	4.7229e+00	[2.3615e+00 - 6.2410e+00]	%1.58
12	h_0	1.3891e-21	9.1397e-22	[5.0904e-22 - 1.6660e-21]	%-34.20
	f_0	3.0900e+03	3.0893e+03	[3.0886e+03 - 3.0902e+03]	%-0.02
	τ	1.0900e-01	9.7551e-02	[5.7143e-02 - 1.5816e-01]	%-10.50
	λ	7.0000e-01	1.6077e-01	[1.0000e-02 - 7.6385e-01]	%-77.03
	ψ	1.2000e+00	1.1741e+00	[6.3467e-02 - 3.0147e+00]	%-2.16
	δ	2.0758e+00	2.0452e+00	[1.9187e+00 - 3.0783e+00]	%-1.47
	RA	4.6496e+00	4.6808e+00	[2.3193e+00 - 5.1868e+00]	%0.67
20	h_0	2.3152e-21	2.3503e-21	[1.2094e-21 - 2.9777e-21]	%1.51
	f_0	3.0900e+03	3.0897e+03	[3.0892e+03 - 3.0902e+03]	%-0.01
	τ	1.0900e-01	9.7551e-02	[7.7347e-02 - 1.3122e-01]	%-10.50
	λ	7.0000e-01	4.6231e-01	[1.1051e-01 - 9.1462e-01]	%-33.96
	ψ	1.2000e+00	1.2376e+00	[7.9333e-01 - 2.9195e+00]	%3.13
	δ	2.0758e+00	2.0452e+00	[1.9187e+00 - 3.0783e+00]	%-1.47
	RA	4.6496e+00	4.6808e+00	[2.3193e+00 - 4.9338e+00]	%0.67

Table K.3: Parameter estimation from the posterior probability density distribution in Fig. 5.9 corresponding to the hypothesis H_{1U} in Scenario 1.

Parameter Estimation H_{2U}					
SNR	**P**	**Exact**	**Mode**	**Range**	**Diff. %**
20	h_{0f}	2.0689e-21	1.8468e-21	[1.4443e-21 - 2.3498e-21]	%-10.74
	f_{0f}	3.0900e+03	3.0899e+03	[3.0893e+03 - 3.0906e+03]	%-0.00
	τ_f	1.0900e-01	9.4490e-02	[6.8493e-02 - 1.2699e-01]	%-13.31
	λ_f	7.0000e-01	8.7286e-01	[4.0429e-01 - 9.7327e-01]	%24.69
	ψ_f	1.2000e+00	1.1249e+00	[9.8503e-01 - 1.2881e+00]	%-6.26
	h_{0p}	4.1378e-22	2.6903e-22	[3.5880e-24 - 4.3493e-22]	%-34.98
	f_{0p}	7.8380e+03	7.8380e+03	[7.8380e+03 - 7.8380e+03]	%-0.00
	τ_p	4.6400e+00	6.1152e+00	[3.4835e+00 - 9.7494e+00]	%31.79
	λ_p	3.0000e-01	1.9271e-01	[1.0000e-02 - 8.7373e-01]	%-35.76
	ψ_p	2.3000e+00	2.3800e+00	[5.3947e-01 - 2.9195e+00]	%3.48
30	h_{0f}	3.0969e-21	2.8854e-21	[2.4830e-21 - 3.3885e-21]	%-6.83
	f_{0f}	3.0900e+03	3.0900e+03	[3.0896e+03 - 3.0903e+03]	%-0.00
	τ_f	1.0900e-01	9.4583e-02	[7.5064e-02 - 1.1410e-01]	%-13.23
	λ_f	7.0000e-01	7.9000e-01	[5.7333e-01 - 9.7333e-01]	%12.86
	ψ_f	1.2000e+00	1.1281e+00	[1.0375e+00 - 1.2415e+00]	%-5.99
	h_{0p}	6.1938e-22	4.9088e-22	[3.2417e-22 - 6.9092e-22]	%-20.75
	f_{0p}	7.8380e+03	7.8380e+03	[7.8380e+03 - 7.8380e+03]	%-0.00
	τ_p	4.6400e+00	5.4387e+00	[3.5381e+00 - 8.6063e+00]	%17.21
	λ_p	3.0000e-01	2.5915e-01	[1.0000e-02 - 7.5746e-01]	%-13.62
	ψ_p	2.3000e+00	2.3722e+00	[2.1478e+00 - 2.5966e+00]	%3.14
40	h_{0f}	4.1300e-21	3.9597e-21	[3.4566e-21 - 4.4124e-21]	%-4.13
	f_{0f}	3.0900e+03	3.0899e+03	[3.0897e+03 - 3.0902e+03]	%-0.00
	τ_f	1.0900e-01	9.7551e-02	[8.4082e-02 - 1.1102e-01]	%-10.50
	λ_f	7.0000e-01	8.4000e-01	[6.0667e-01 - 9.7333e-01]	%20.00
	ψ_f	1.2000e+00	1.1307e+00	[1.0841e+00 - 1.2240e+00]	%-5.77
	h_{0p}	8.2601e-22	7.0079e-22	[5.3507e-22 - 9.3279e-22]	%-15.16
	f_{0p}	7.8380e+03	7.8380e+03	[7.8380e+03 - 7.8380e+03]	%-0.00
	τ_p	4.6400e+00	5.3394e+00	[3.8189e+00 - 7.3666e+00]	%15.07
	λ_p	3.0000e-01	2.2593e-01	[1.0000e-02 - 6.0797e-01]	%-24.69
	ψ_p	2.3000e+00	2.3402e+00	[2.1478e+00 - 2.5325e+00]	%1.75

Table K.4: Parameter estimation from the posterior probability density distribution in Fig. 5.12 and Fig. 5.13 corresponding to the hypothesis H_{22K} in Scenario 2.

Parameter Estimation H_{2U}					
SNR	**P**	**Exact**	**Mode**	**Range**	**Diff. %**
20	h_{0f}	2.0689e-21	8.7056e-22	[7.0098e-22 - 2.2272e-21]	%-57.92
	f_{0f}	3.0900e+03	3.0896e+03	[3.0892e+03 - 3.0902e+03]	%-0.01
	τ_f	1.0900e-01	9.4330e-02	[7.3248e-02 - 1.4704e-01]	%-13.46
	λ_f	7.0000e-01	4.0895e-01	[2.0684e-01 - 8.6368e-01]	%-41.58
	ψ_f	1.2000e+00	1.2059e+00	[2.8560e-01 - 3.1099e+00]	%0.49
	h_{0p}	4.1378e-22	3.5880e-24	[3.5880e-24 - 3.5424e-22]	%-99.13
	f_{0p}	7.8380e+03	7.8380e+03	[7.8380e+03 - 7.8380e+03]	%-0.00
	τ_p	4.6400e+00	6.4000e+00	[5.0000e-01 - 9.4000e+00]	%37.93
	ψ_p	3.0000e-01	2.6128e-01	[1.0000e-02 - 8.3923e-01]	%-12.91
	λ_p	2.3000e+00	2.4435e+00	[4.7600e-01 - 3.1099e+00]	%6.24
	δ	2.0758e+00	2.1261e+00	[2.0309e+00 - 3.0781e+00]	%2.43
	RA	4.6496e+00	4.6965e+00	[2.4117e+00 - 5.0139e+00]	%1.01
30	h_{0f}	3.0969e-21	2.8152e-21	[1.4537e-21 - 3.6661e-21]	%-9.10
	f_{0f}	3.0900e+03	3.0898e+03	[3.0894e+03 - 3.0902e+03]	%-0.01
	τ_f	1.0900e-01	9.6204e-02	7.4653e-02 - 1.1776e-01]	%-11.74
	λ_f	7.0000e-01	3.6143e-01	[2.3571e-01 - 8.8943e-01]	%-48.37
	ψ_f	1.2000e+00	1.1489e+00	[1.0224e+00 - 3.0783e+00]	%-4.26
	h_{0p}	6.1938e-22	4.2689e-22	[2.3363e-22 - 6.3033e-22]	%-31.08
	f_{0p}	7.8380e+03	7.8380e+03	[7.8380e+03 - 7.8380e+03]	%-0.00
	τ_p	4.6400e+00	5.1127e+00	[3.7163e+00 - 9.1023e+00]	%10.19
	λ_p	3.0000e-01	8.5385e-02	[1.0000e-02 - 6.3821e-01]	%-71.54
	ψ_p	2.3000e+00	2.4128e+00	[7.0157e-01 - 2.8247e+00]	%4.90
	δ	2.0758e+00	2.0944e+00	[2.0309e+00 - 3.0781e+00]	%0.90
	RA	4.6496e+00	4.6331e+00	[2.4752e+00 - 4.8235e+00]	%-0.35
40	h_{0f}	4.1300e-21	3.9419e-21	[3.3648e-21 - 4.5767e-21]	%-4.56
	f_{0f}	3.0900e+03	3.0899e+03	[3.0897e+03 - 3.0902e+03]	%-0.00
	τ_f	1.0900e-01	1.0019e-01	[8.0194e-02 - 1.1019e-01]	%-8.08
	λ_f	7.0000e-01	6.3276e-01	[4.2862e-01 - 9.3897e-01]	%-9.61
	ψ_f	1.2000e+00	1.1693e+00	[1.0686e+00 - 1.3372e+00]	%-2.56
	h_{0p}	8.2601e-22	6.8079e-22	[5.0787e-22 - 8.6389e-22]	%-17.58
	f_{0p}	7.8380e+03	7.8380e+03	[7.8380e+03 - 7.8380e+03]	%-0.00
	τ_p	4.6400e+00	5.3531e+00	[3.7367e+00 - 7.0704e+00]	%15.37
	λ_p	3.0000e-01	2.1103e-01	[1.0000e-02 - 5.6282e-01]	%-29.66
	ψ_p	2.3000e+00	2.4043e+00	[2.2119e+00 - 2.6928e+00]	%4.53
	δ	2.0758e+00	2.0944e+00	[2.0309e+00 - 2.1896e+00]	%0.90
	RA	4.6496e+00	4.6331e+00	[4.5696e+00 - 4.6965e+00]	%-0.35

Table K.5: Parameter estimation from the posterior probability density distribution in Fig. 5.14 and Fig. 5.15 corresponding to the hypothesis H_{22U} in Scenario 2.

Appendix L

Schematics of the GEO600 photodetector

Fig. L.1 shows the schematic corresponding to the original design of the photodetector. It presents two main outputs for the measurement of DC and RF voltages: a high inductive impedance filters out the signal at the modulation frequency for the DC line and a high capacitive impedance filters out low frequencies for the RF line. The signals need to be amplified so that they can be measured clearly for the amount of light projected onto the photodetector at the dark fringe, which is very small. The RF line presents a resonant circuit to amplify the voltage response of the photocurrent at the modulation frequency. At the same time it combines a notch filter at twice the modulation frequency, which is aimed to filter out the second harmonic of the modulation frequency. Fig. L.2 our simplified version.

L.1 Calculation of the inductance value for the RF resonant line within the GEO style PD version

In the following, we present the reduced circuitry of the RF line used to calculate the value of the fixed value inductor to so that the resonance frequency approximates the modulation frequency. Equivalent impedances are inferred operational

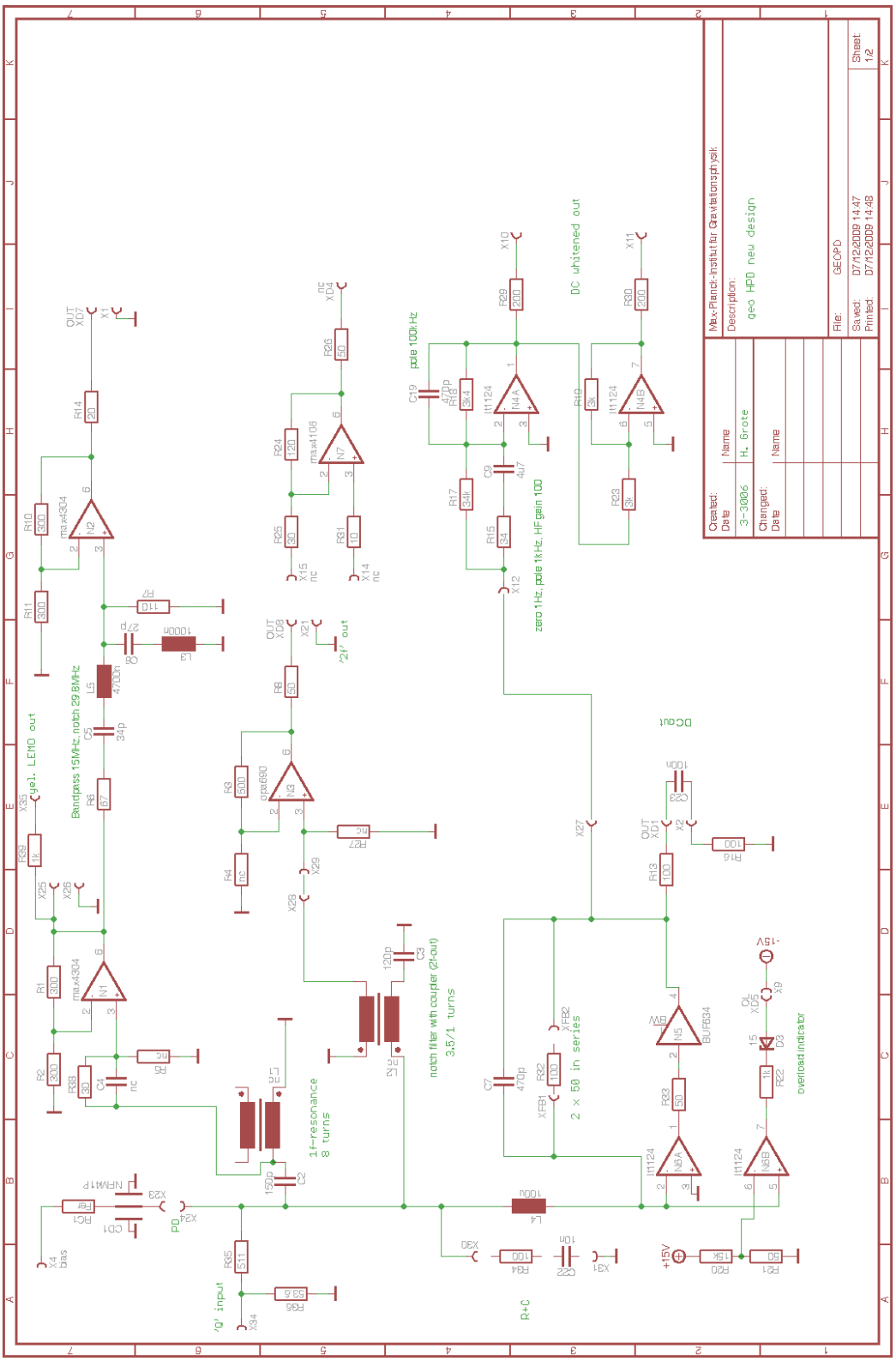

Figure L.1: Schematics corresponding to the original GEO600 photodetector.

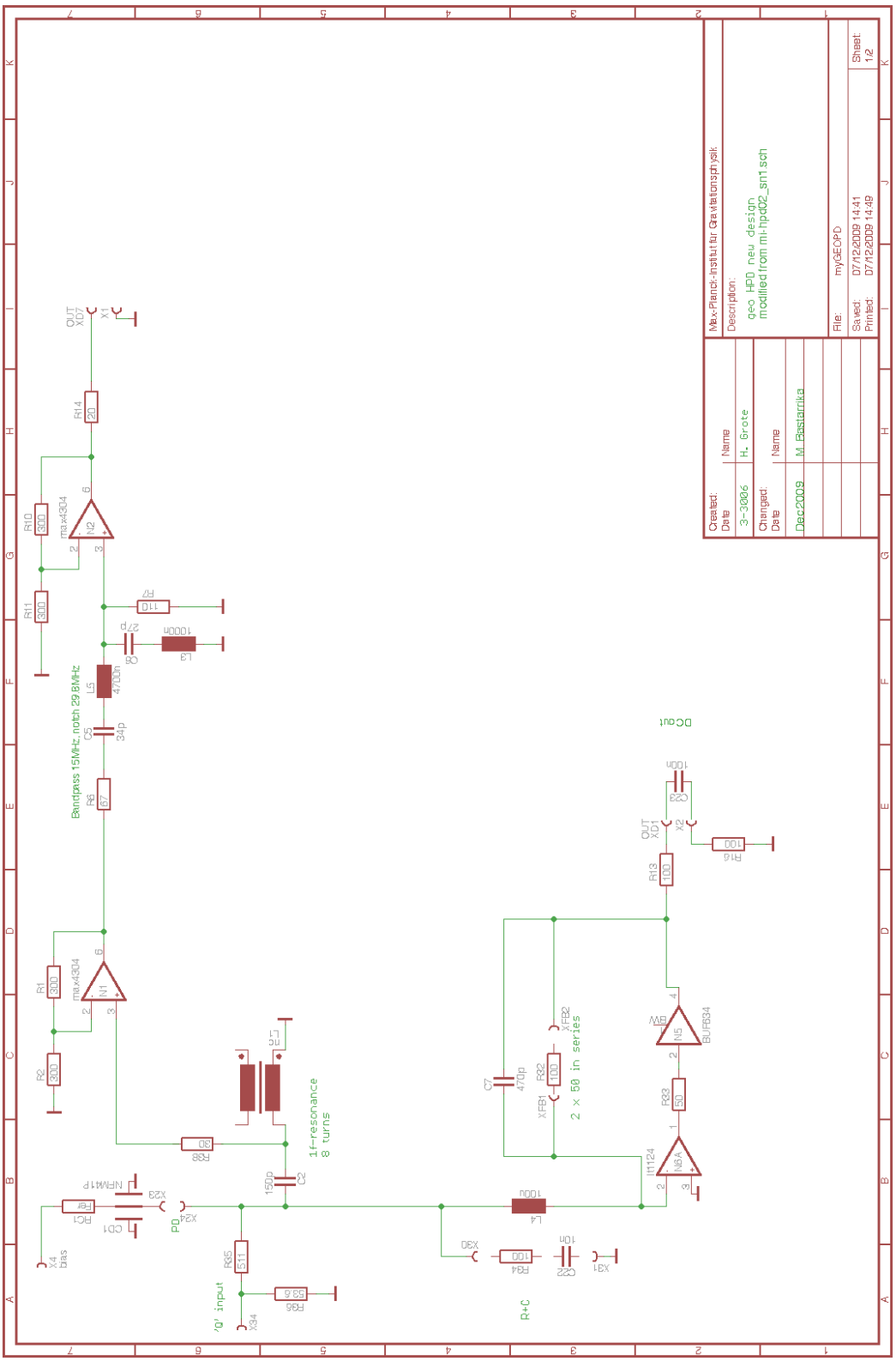

Figure L.2: Schematics corresponding to the modified version of the original photodiode of the GEO600 detector.

amplifiers, which ideally don't consume any current through their inverting/non-inverting pins, omitted.

At high frequencies (∼10 MHz) the input impedance of the RF part of the circuit can be simplified to Fig. L.3.

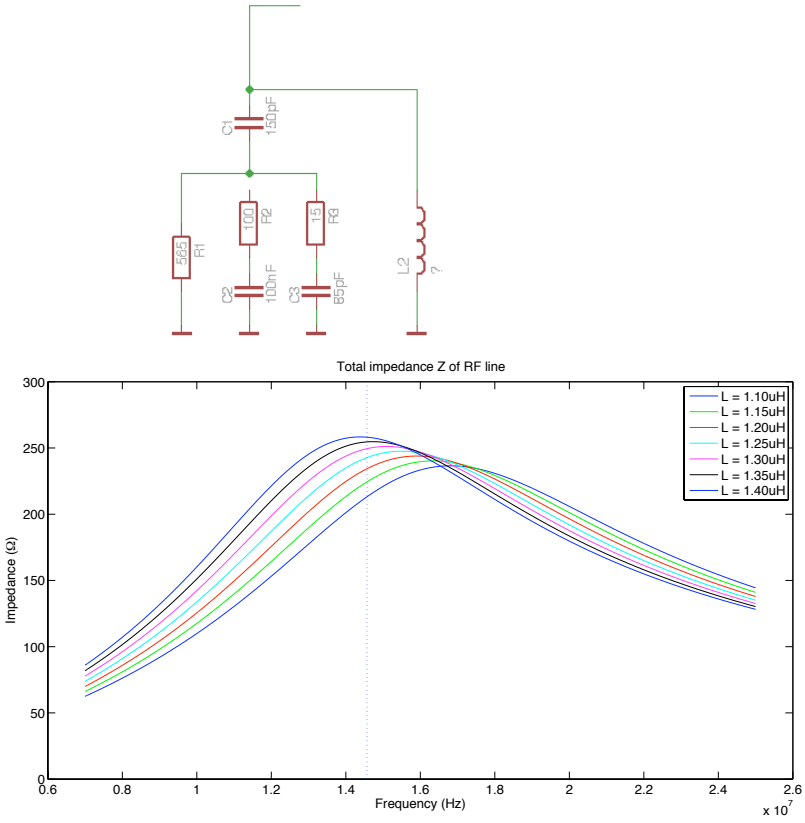

Figure L.3: *Up*: Equivalent reduced schematic of RF line to calculate the value of the inductor to get resonance at the modulation frequency. *Down*: Equivalent impedance calculation for different inductance values. The maximum impedance of $Z_{max} = 255\ \Omega$ for the inductance value L = 1.35 μH at the modulation frequency of $f_{mod} = 14.57$ MHz was inferred.

Bibliography

[1] B. F. Schutz. *A First Course in General Relativity*. February 1985.

[2] I. Chakrabarty. Gravitational Waves: An Introduction. *ArXiv Physics e-prints*, August 1999.

[3] R. A. Hulse and H. J. Taylor. Discovery of a Pulsar in a Close Binary System. In *Bulletin of the American Astronomical Society*, volume 6 of *Bulletin of the American Astronomical Society*, pages 453–+, September 1974.

[4] R. A. Hulse and J. H. Taylor. Discovery of a pulsar in a binary system. *The Astrophysical Journall*, 195:L51–L53, January 1975.

[5] Ingrid H. Stairs. Testing general relativity with pulsar timing. *Living Reviews in Relativity*, 6(5), 2003.

[6] M. Burgay, N. D'Amico, A. Possenti, R. N. Manchester, A. G. Lyne, B. C. Joshi, M. A. McLaughlin, M. Kramer, J. M. Sarkissian, F. Camilo, V. Kalogera, C. Kim, and D. R. Lorimer. An increased estimate of the merger rate of double neutron stars from observations of a highly relativistic system. *Nature*, 426:531–533, December 2003.

[7] B.S. Sathyaprakash Bernard F. Schutz. Physics, astrophysics and cosmology with gravitational waves. *Living Reviews in Relativity*, 12(2), 2009.

[8] Gravitational Radiation - A new window onto the universe, Kip S.Thorne. http://www.its.caltech.edu/~kip/scripts/publications.html.

[9] K. S. Thorne. Gravitational Radiation – A New Window Onto the Universe. *ArXiv General Relativity and Quantum Cosmology e-prints*, April 1997.

[10] B. P. Abbott et al. An upper limit on the stochastic gravitational-wave background of cosmological origin. *Nature*, 460:990–994, August 2009.

[11] B. Abbott et al. Setting upper limits on the strength of periodic gravitational waves from PSR J1939+2134 using the first science data from the GEO 600 and LIGO detectors. *Physical Review D*, 69(8):082004–+, April 2004.

[12] B. Abbott et al. Upper limits on gravitational wave emission from 78 radio pulsars. *Physical Review D*, 76(4):042001–+, August 2007.

[13] B. Abbott et al. Beating the Spin-Down Limit on Gravitational Wave Emission from the Crab Pulsar. *The Astrophysical Journall*, 683:L45–L49, August 2008.

[14] J. Abadie et al. All-sky search for gravitational-wave bursts in the first joint LIGO-GEO-Virgo run. *Physical Review D*, 81(10):102001–+, May 2010.

[15] M. Punturo et al. The Einstein Telescope: a third-generation gravitational wave observatory. *Classical and Quantum Gravity*, 27(19):194002–+, October 2010.

[16] B. F. Schutz. Gravitational wave astronomy. *Classical and Quantum Gravity*, 16:A131–A156, December 1999.

[17] C. Hanna, t. LIGO, and Virgo Scientific Collaborations. Gravitational-wave data analysis overview of compact binary searches using waveforms inspired by numerical relativity. *Classical and Quantum Gravity*, 27(11):114003–+, June 2010.

[18] S. A. Hughes. Gravitational Waves from Merging Compact Binaries. *Annual Review of Astronomy and Astrophysics*, 47:107–157, September 2009.

[19] B. F. Schutz. Gravitational wave sources and their detectability. *Classical and Quantum Gravity*, 6:1761–1780, December 1989.

[20] S. E. Woosley. Gamma-ray bursts from stellar mass accretion disks around black holes. *The Astrophysical Journal*, 405:273–277, March 1993.

[21] H. Dimmelmeier, C. D. Ott, A. Marek, and H.-T. Janka. Gravitational wave burst signal from core collapse of rotating stars. *Physical Review D*, 78(6):064056–+, September 2008.

[22] K. N Yakunin, P. Marronetti, A. Mezzacappa, S. W Bruenn, C.-T. Lee, M. A Chertkow, W. Hix, J. M Blondin, E. J Lentz, O. Bronson Messer, and S. Yoshida. Gravitational Waves from Core Collapse Supernovae. *ArXiv e-prints*, May 2010.

[23] C. Röver, M.-A. Bizouard, N. Christensen, H. Dimmelmeier, I. S. Heng, and R. Meyer. Bayesian reconstruction of gravitational wave burst signals from simulations of rotating stellar core collapse and bounce. *Physical Review D*, 80(10):102004–+, November 2009.

[24] B. Allen and J. D. Romano. Detecting a stochastic background of gravitational radiation: Signal processing strategies and sensitivities. *Physical Review D*, 59(10):102001–+, May 1999.

[25] J. Weber. Evidence for Discovery of Gravitational Radiation. *Physical Review Letters*, 22:1320–1324, June 1969.

[26] J. Weber. Gravitational Radiation Experiments. *Physical Review Letters*, 24:276–279, February 1970.

[27] International Gravitational Event Collaboration (IGEC). http://igec.lnl.infn.it/.

[28] A. M. Sintes. The Search for Gravitational Waves: Opening a New Window into the Universe. In J. M. Diego, L. J. Goicoechea, J. I. González-Serrano, & J. Gorgas, editor, *Highlights of Spanish Astrophysics V*, pages 65–+, 2010.

[29] P. R. Saulson. *Fundamentals of interferometric gravitational wave detectors*. 1994.

[30] D. G. Blair, editor. *The Detection of Gravitational Waves*, July 1991.

[31] F. J. Raab. The LIGO project: progress and prospects. In *Gravitational Wave Experiments*, pages 70–85, 1995.

[32] B. Caron et al. The VIRGO experiment: status of the art. In *Gravitational Wave Experiments*, pages 86–99, 1995.

[33] B. Willke et al. Status of GEO 600. *Classical and Quantum Gravity*, 21:417–+, March 2004.

[34] R. Takahashi and the TAMA Collaboration. Status of TAMA300. *Classical and Quantum Gravity*, 21:403–+, March 2004.

[35] LIGO Scientific Collaboration (LSC). http://ligo.org/.

[36] VIRGO website. http://www.virgo.infn.it/.

[37] European Gravitational Observatory (EGO). http://www.ego-gw.it/.

[38] T. Uchiyama et al. Present status of large-scale cryogenic gravitational wave telescope. *Classical and Quantum Gravity*, 21:1161–+, March 2004.

[39] P. Barriga et al. AIGO: a southern hemisphere detector for the worldwide array of ground-based interferometric gravitational wave detectors. *Classical and Quantum Gravity*, 27(8):084005–+, April 2010.

[40] The Australian International Gravitational Research Centre. http://www.gravity.uwa.edu.au/.

[41] Australian Consortium for Interferometric Gravitational Astronomy (ACIGA). http://www.anu.edu.au/Physics/ACIGA/#.

[42] J. R. Smith and LIGO Scientific Collaboration. The path to the enhanced and advanced LIGO gravitational-wave detectors. *Classical and Quantum Gravity*, 26(11):114013–+, June 2009.

[43] the LIGO Scientific Collaboration and the Virgo Collaboration. Search for Gravitational Waves from Compact Binary Coalescence in LIGO and Virgo Data from S5 and VSR1. *ArXiv e-prints*, May 2010.

[44] B. P. Abbott et al. Searches for Gravitational Waves from Known Pulsars with Science Run 5 LIGO Data. *The Astrophysical Journal*, 713:671–685, April 2010.

[45] B. P. Abbott et al. All-Sky LIGO Search for Periodic Gravitational Waves in the Early Fifth-Science-Run Data. *Physical Review Letters*, 102(11):111102–+, March 2009.

[46] B. P. Abbott et al. Einstein@Home search for periodic gravitational waves in early S5 LIGO data. *Physical Review D*, 80(4):042003–+, August 2009.

[47] R. Adhikari, P. Fritschel, and S. Waldman. Enhanced ligo. Technical Report T060156-01, LIGO Scientific Collaboration (LSC), November 2006.

[48] B. Willke et al. The GEO-HF project. *Classical and Quantum Gravity*, 23:207–+, April 2006.

[49] H. Vahlbruch, S. Chelkowski, B. Hage, A. Franzen, K. Danzmann, and R. Schnabel. Demonstration of a Squeezed-Light-Enhanced Power- and Signal-Recycled Michelson Interferometer. *Physical Review Letters*, 95(21):211102–+, November 2005.

[50] H. Vahlbruch, A. Khalaidovski, N. Lastzka, C. Gräf, K. Danzmann, and R. Schnabel. The GEO 600 squeezed light source. *Classical and Quantum Gravity*, 27(8):084027–+, April 2010.

[51] R. Schnabel, J. Harms, K. A. Strain, and K. Danzmann. Squeezed light for the interferometric detection of high-frequency gravitational waves. *Classical and Quantum Gravity*, 21:1045–+, March 2004.

[52] G. M. Harry and the LIGO Scientific Collaboration. Advanced LIGO: the next generation of gravitational wave detectors. *Classical and Quantum Gravity*, 27(8):084006–+, April 2010.

[53] Eric Gustafson, David Shoemaker, K.A. Strain, and Rai Weiss. Lsc white paper on detector research and development. Technical Report T990080-00-D, LIGO Scientific Collaboration (LSC), November 1999.

[54] T. Creighton. Advanced LIGO: sources and astrophysics. *Classical and Quantum Gravity*, 20:853–+, September 2003.

[55] A. Freise, S. Chelkowski, S. Hild, W. Del Pozzo, A. Perreca, and A. Vecchio. Triple Michelson interferometer for a third-generation gravitational wave detector. *Classical and Quantum Gravity*, 26(8):085012–+, April 2009.

[56] S. Hild, S. Chelkowski, and A. Freise. Pushing towards the ET sensitivity using 'conventional' technology. *ArXiv e-prints*, October 2008.

[57] Einstein Telescope (ET). http://www.et-gw.eu/index.php.

[58] Einstein Telescope Design Study: Vision Document. https://workarea.et-gw.eu/et/WG4-Astrophysics/visdoc/VisDoc-090616.pdf.

[59] Advanced Virgo White Paper, VIR–NOT–DIR–1390–304. http://wwwcascina.virgo.infn.it/advirgo/docs/whitepaper.pdf.

[60] Laser Interferometric Gravitational-Wave Observatory (LIGO). http://www.ligo.caltech.edu/.

[61] E. Chassande-Mottin, M. Hendry, P. J. Sutton, and S. Márka. Multimessenger astronomy with the Einstein Telescope. *General Relativity and Gravitation*, pages 109–+, June 2010.

[62] W. Baade and F. Zwicky. Remarks on Super-Novae and Cosmic Rays. *Physical Review*, 46:76–77, July 1934.

[63] A. Hewish, S. J. Bell, J. D. H. Pilkington, P. F. Scott, and R. A. Collins. Observation of a Rapidly Pulsating Radio Source. , 217:709–713, February 1968.

[64] J. D. H. Pilkington, A. Hewish, S. J. Bell, and T. W. Cole. Observations of some further Pulsed Radio Sources. , 218:126–129, April 1968.

[65] A. G. Lyne and F. Graham-Smith. Pulsar astronomy. *Cambridge Astrophysics Series*, 31, 1998.

[66] The Australia Telescope National Facility (ATNF) catalogue of pulsars. http://www.atnf.csiro.au/research/pulsar/psrcat/.

[67] R. N. Manchester, G. B. Hobbs, A. Teoh, and M. Hobbs. ATNF Pulsar Catalog (Manchester+, 2005). *VizieR Online Data Catalog*, 7245:0–+, August 2005.

[68] James Clark. *An Evidence Based Search For Transient Gravitational Waves From Neutron Stars*. PhD thesis, University of Glasgow, 2009.

[69] Magnetars. Scientific American (2003). http://solomon.as.utexas.edu/~duncan/sciam.pdf.

[70] P. M. Woods and C. Thompson. *Soft gamma repeaters and anomalous X-ray pulsars: magnetar candidates*, pages 547–586. April 2006.

[71] H.-P. Nollert. TOPICAL REVIEW: Quasinormal modes: the characteristic 'sound' of black holes and neutron stars. *Classical and Quantum Gravity*, 16:159–+, December 1999.

[72] K. Kokkotas and B. Schmidt. Quasi-Normal Modes of Stars and Black Holes. *Living Reviews in Relativity*, 2:2–+, September 1999.

[73] N. Andersson, Y. Kojima, and K. D. Kokkotas. On the Oscillation Spectra of Ultracompact Stars: an Extensive Survey of Gravitational-Wave Modes. *The Astrophysical Journal*, 462:855–+, May 1996.

[74] Nils Andersson. Excitation of schwarzschild black-hole quasinormal modes. *Phys. Rev. D*, 51(2):353–363, Jan 1995.

[75] N. Andersson and K. D. Kokkotas. Towards gravitational wave asteroseismology. *Monthly Notices of the Royal Astronomical Society*, 299:1059–1068, October 1998.

[76] Nils Andersson and Staffan Linnæus. Quasinormal modes of a schwarzschild black hole: Improved phase-integral treatment. *Phys. Rev. D*, 46(10):4179–4187, Nov 1992.

[77] T. G. Cowling. The non-radial oscillations of polytropic stars. *Monthly Notices of the Royal Astronomical Society*, 101:367–+, 1941.

[78] Bernd Schmidt Kostas D. Kokkotas. Quasi-normal modes of stars and black holes. *Living Reviews in Relativity*, 2(2), 1999.

[79] L. Lindblom and S. L. Detweiler. The quadrupole oscillations of neutron stars. *The Astrophysical Journals*, 53:73–92, September 1983.

[80] K. D. Kokkotas and B. F. Schutz. W-modes - A new family of normal modes of pulsating relativistic stars. *Monthly Notices of the Royal Astronomical Society*, 255:119–128, March 1992.

[81] J. G. Davies, A. G. Lyne, and J. H. Seiradakis. Pulsars-Thirteen new ones discovered. , 244:84–+, August 1973.

[82] C. Palomba. Simulation of a population of isolated neutron stars evolving through the emission of gravitational waves. *Monthly Notices of the Royal Astronomical Society*, 359:1150–1164, May 2005.

[83] C. Palomba. Simulation of a population of gravitational wave-driven neutron stars. *Classical and Quantum Gravity*, 22:1027–+, September 2005.

[84] J. W. Hartman, D. Bhattacharya, R. Wijers, and F. Verbunt. A study of the evolution of radio pulsars through improved population synthesis. *Astronomy and Astrophysics*, 322:477–488, June 1997.

[85] S. Johnston. Evidence for a Deficit of Pulsars in the Inner Galaxy. *Monthly Notices of the Royal Astronomical Society*, 268:595–+, May 1994.

[86] G. Woan. *The Cambridge Handbook of Physics Formulas*. June 2000.

[87] P. Jaranowski, A. Królak, and B. F. Schutz. Data analysis of gravitational-wave signals from spinning neutron stars: The signal and its detection. *Physical Review D*, 58(6):063001–+, September 1998.

[88] Nicolas Arnaud, Matteo Barsuglia, Marie-Anne Bizouard, Philippe Canitrot, Fabien Cavalier, Michel Davier, Patrice Hello, and Thierry Pradier. Detection in coincidence of gravitational wave bursts with a network of interferometric detectors: Geometric acceptance and timing. *Phys. Rev. D*, 65(4):042004, Jan 2002.

[89] J. Marx et al. Expanding the ligo network: The case for installing an advanced ligo detector in australia. Technical Report M1000115-v6, LIGO Scientific Collaboration (LSC), July 2010.

[90] S. W. Hawking and W. Israel. *Three hundred years of gravitation*. 1987.

[91] B. F. Schutz and M. Tinto. Antenna patterns of interferometric detectors of gravitational waves. I - Linearly polarized waves. *Monthly Notices of the Royal Astronomical Society*, 224:131–154, January 1987.

[92] M. Tinto. Coincidence probabilities for a network of interferometric detectors of gravitational waves. *Monthly Notices of the Royal Astronomical Society*, 229:315–332, November 1987.

[93] S. K. Mitra. *Digital signal processing : a computer-based approach*. 2001.

[94] MATLAB (a Mathworks product). http://www.mathworks.com/.

[95] F. Guglielmetti, R. Fischer, and V. Dose. Background-source separation in astronomical images with Bayesian probability theory - I. The method. *Monthly Notices of the Royal Astronomical Society*, 396:165–190, June 2009.

[96] R. Trotta. Bayes in the sky: Bayesian inference and model selection in cosmology. *Contemporary Physics*, 49:71–104, March 2008.

[97] A. H. Jaffe. *Bayesian analysis of cosmic microwave background data*, pages 229–+. 2010.

[98] E. B. Ford and P. C. Gregory. Bayesian Model Selection and Extrasolar Planet Detection. In G. J. Babu & E. D. Feigelson, editor, *Statistical Challenges in Modern Astronomy IV*, volume 371 of *Astronomical Society of the Pacific Conference Series*, pages 189–+, November 2007.

[99] T. B. Littenberg and N. J. Cornish. Bayesian approach to the detection problem in gravitational wave astronomy. , 80(6):063007–+, September 2009.

[100] C. Röver, R. Meyer, and N. Christensen. Coherent Bayesian inference on compact binary inspirals using a network of interferometric gravitational wave detectors. *Phys. Rev. D*, 75(6):062004–+, March 2007.

[101] J. Veitch and A. Vecchio. Bayesian coherent analysis of in-spiral gravitational wave signals with a detector network. *Phys. Rev. D*, 81(6):062003–+, March 2010.

[102] J. Veitch and A. Vecchio. Assigning confidence to inspiral gravitational wave candidates with Bayesian model selection. *Classical and Quantum Gravity*, 25(18):184010–+, September 2008.

[103] A. Stroeer and J. Veitch. Bayesian approach to the study of white dwarf binaries in LISA data: The application of a reversible jump Markov chain MonteCarlo method. *Phys. Rev. D*, 80(6):064032–+, September 2009.

[104] R. J. Dupuis and G. Woan. Bayesian estimation of pulsar parameters from gravitational wave data. *Phys. Rev. D*, 72(10):102002–+, November 2005.

[105] A. C. Searle, P. J. Sutton, and M. Tinto. Bayesian detection of unmodeled bursts of gravitational waves. *Classical and Quantum Gravity*, 26(15):155017–+, August 2009.

[106] B. Aylott, J. Veitch, and A. Vecchio. Bayesian inference on the Numerical INJection Analysis (NINJA) data set using a nested sampling algorithm. *Classical and Quantum Gravity*, 26(11):114011–+, June 2009.

[107] E. T. Jaynes. *Probability Theory: The Logic of Science*. 1994.

[108] Richard Umstätter, Nelson Christensen, Martin Hendry, Renate Meyer, Vimal Simha, John Veitch, Sarah Vigeland, and Graham Woan. Bayesian modeling of source confusion in lisa data. *Phys. Rev. D*, 72(2):022001, Jul 2005.

[109] Joel N. Franklin. Numerical simulation of stationary and non-stationary gaussian random processes. *SIAM Review*, 7(1):68–80, 1965.

[110] Gerhard Heinzel. Random noise generator. Technical Report S2-AEI-TN-3034, Albert Einstein Institut, 2006.

[111] LTPDA: a MATLAB toolbox for accountable and reproducible data analysis.
http://www.lisa.aei-hannover.de/ltpda/.

[112] Gerhard Heinzel, Albrecht Rdiger, and Roland Schilling. Spectrum and spectral density estimation by the discrete fourier transform (dft), including a comprehensive list of window functions and some new at-top windows. Technical Report 395068, Albert Einstein Institut, November 1999.

[113] J. Skilling. Nested Sampling. In R. Fischer, R. Preuss, and U. V. Toussaint, editors, *American Institute of Physics Conference Series*, pages 395–405, November 2004.

[114] D. S. Sivia. *Data Analysis: A Bayesian Tutorial*. Clarendon (Oxford Univ. Press), Oxford, 1996 (ISBN: 0-19-851762-9 or 0-19-851889-7 in paperback). Divinder Sivia presents a very straightforward account of Bayesian analysis. Rather than going for mathematical rigor and an axiomatic approach, he introduces concepts as they are needed to solve a sequence of increasingly complex analysis problems. Very readable and informative.

[115] J. Skilling. Nested Sampling for Bayesian Computations. In *ISBA 8th World Meeting in Bayesian Statistics*, 2006.

[116] Jun S. Liu. *Monte Carlo Strategies in Scientific Computing*. Springer, October 2002.

[117] P. C. Gregory. *Bayesian Logical Data Analysis for the Physical Sciences: A Comparative Approach with 'Mathematica' Support*. Cambridge University Press, 2005.

[118] J. Veitch and A. Vecchio. Bayesian coherent analysis of in-spiral gravitational wave signals with a detector network. *Phys. Rev. D*, 81(6):062003, Mar 2010.

[119] Stefan Franz, Sanjit K. Mitra, and Gerhard Doblinger. Frequency estimation using warped discrete fourier transform. *Signal Processing*, 83(8):1661 – 1671, 2003.

[120] A. Makur and S.K. Mitra. Warped discrete-fourier transform: Theory and applications. *Circuits and Systems I: Fundamental Theory and Applications, IEEE Transactions on*, 48(9):1086–1093, Sep 2001.

[121] Nils Andersson and Kostas D. Kokkotas. Gravitational waves and pulsating stars: What can we learn from future observations? *Phys. Rev. Lett.*, 77(20):4134–4137, Nov 1996.

[122] C.-Y. Ng and R. W. Romani. Fitting Pulsar Wind Tori. *The Astrophysical Journal*, 601:479–484, January 2004.

[123] C.-Y. Ng and R. W. Romani. Fitting Pulsar Wind Tori. II. Error Analysis and Applications. *The Astrophysical Journal*, 673:411–417, January 2008.

[124] K. Goda, O. Miyakawa, E. E. Mikhailov, S. Saraf, R. Adhikari, K. McKenzie, R. Ward, S. Vass, A. J. Weinstein, and N. Mavalvala. A quantum-enhanced prototype gravitational-wave detector. *Nature Physics*, 4:472–476, March 2008.

[125] C. M. Caves. Quantum-mechanical noise in an interferometer. *PRD*, 23:1693–1708, April 1981.

[126] Amnon Yariv. *Optical Electronics in Modern Communications (Oxford Series in Electrical & Computer Engineering)*. Oxford University Press Inc, USA, 5th revised edition edition, April 1997.

[127] K P Zetie, S F Adams, and R M Tocknell. How does a mach-zehnder interferometer work? *Physics Education*, 35(1):46, 2000.

[128] Jun. Mizuno. Comparison of optical configurations for laser interferometric gravitational wave detectors /. 1995.

[129] Gerhard Heinzel. *Advanced optical techniques for laser-interferometric gravitational-wave detectors*. PhD thesis, Universität Hannover, February 1999.

[130] G. B. Arfken and H. J. Weber. *Mathematical methods for physicists 6th ed.* 2005.

[131] B. W. Barr, S. H. Huttner, J. R. Taylor, B. Sorazu, M. V. Plissi, and K. A. Strain. Optical modulation techniques for length sensing and control of optical cavities. *Appl. Opt.*, 46(31):7739–7745, 2007.

[132] R. W. P. Drever, J. L. Hall, F. V. Kowalski, J. Hough, G. M. Ford, A. J. Munley, and H. Ward. Laser phase and frequency stabilization using an optical resonator. *Applied Physics B: Lasers and Optics*, 31(2):97–105, June 1983.

[133] E. D. Black. An introduction to pound-drever-hall laser frequency stabilization. *American Journal of Physics*, 69(1):79–87, January 2001.

[134] Eric Black. Notes on pound-drever-hall technique. Technical report, April 1998.

[135] Andreas Freise. FINESSE: Frequency domain interferometer simulation software. Technical report, January 2010.

[136] MultiNest: Efficient and Robust Bayesian Inference. http://ccpforge.cse.rl.ac.uk/projects/multinest/.

[137] Astrophysicists at work: Installing and running MultiNest http://www.astro.gla.ac.uk/~matthew/blog/?p=342.

[138] H. Goldstein, C. Poole, and J. Safko. *Classical mechanics*. 2002.

[139] L. Fox and I. B. Parker. *Chebyshev Polynomials in Numerical Analysis*. 1968.

[140] Wolfram MathWorld. http://mathworld.wolfram.com/.

[141] H. Gudbjartsson and S. Patz. The Rician Distribution of Noisy MRI Data. *Magn. Reson. Med.*, 34(6):319–914, December 1995.

[142] S. O. Rice. Mathematical Analysis of Random Noise. *Bell Systems Tech. J., Volume 23, p. 282-332*, 23:282–332, 1944.

[143] S. O. Rice. Mathematical Analysis of Random Noise-Conclusion. *Bell Systems Tech. J., Volume 24, p. 46-156*, 24:46–156, 1945.

[144] HáKon Gudbjartsson and Samuel Patz. The rician distribution of noisy mri data. *Magnetic Resonance in Medicine*, 34(6):910–914, 1995.